

The contribution of proteins associated with cell adhesion and survival to tissue integrity in the mammary gland

Dissertation

zur Erlangung des Doktorgrades

der Naturwissenschaften

vorgelegt beim Fachbereich Biowissenschaften

der Johann Wolfgang Goethe-Universität

in Frankfurt am Main

von

Isabell Julia Smyrek

aus Offenbach am Main

Frankfurt am Main, 2017

(D30)

vom Fachbereich Biowissenschaften der Johann Wolfgang Goethe-Universität als Dissertation
angenommen.

Dekanin: Prof. Dr. Meike Piepenbring

Erster Gutachter: Prof. Dr. Ernst H. K. Stelzer

Zweiter Gutachter: Prof. Dr. Anna Starzinski-Powitz

Datum der Disputation: _____

Danksagung

Sehr herzlich möchte ich mich bei Herrn Prof. Dr. Ernst H. K. Stelzer bedanken für die Unterstützung während meiner gesamten Promotion. Ich bedanke mich vor allem für sein Vertrauen und die wissenschaftliche Freiheit.

Frau Prof. Dr. Anna Starzinski-Powitz danke ich für die freundliche Bereitschaft zur Begutachtung meiner Arbeit und die jahrelange Begleitung meiner fachlichen aber auch persönlichen Entwicklung.

Ich möchte mich herzlich bei Dr. Francesco Pampaloni, Dr. Sabine Fischer und Katharina Hötte für das Korrekturlesen bedanken. Ich habe mit ihnen zahlreiche inspirierende und konstruktive Diskussionen führen konnten. Sabine Fischer danke ich vor allem auch für die Hilfe bei Fragen der Statistik und für das Fitting des Computermodells. Ich bedanke mich bei Biena Mathew für die produktive Zusammenarbeit im Projekt *Spheroid Formation* und bei Alexander Schmitz für die Zusammenarbeit und Analyse der *Squeezoids*. Durch solche Zusammenarbeiten zeigen wir, dass Interdisziplinarität essentiell für das Voranschreiten der Wissenschaft ist.

Ich danke den Praktikanten und Absolventen, die ich betreut habe dafür, dass ich selber viel für die Entwicklung meines Lehrstils lernen durfte: Melisa Merdan-Desik, Sanam Saeifar, Julia Tarnick, Diana Müller, Elena Gosau, Susanna Lissek, Carolin Fix, Katharina Hötte und Lotta Hof. Großer Dank geht an Sigrun Becker für die Unterstützung im Labor und die immer guten Worte. Dem gesamten Arbeitskreis Physikalische Biologie danke ich für die gute Stimmung während der letzten Jahre. Besonders seien hier auch die Jungs des HRZ erwähnt, Kai Richter und Sascha Rodzies.

Ich danke meinen Eltern, Irene und Erich, meinem Bruder Christopher und auch meinen Großeltern für die immerwährende Unterstützung und Förderung.

Zum Abschluss danke ich Alexander Schmitz für die stete moralische Unterstützung, die mich aufgebaut aber vor allem auch gestärkt hat.

Zusammenfassung

Die Zusammensetzung und der Zusammenhalt von Zellen definiert die Integrität von Geweben und Organen und bedingt deren Struktur und Funktion. Gleichwohl handelt es sich bei Geweben nicht um starre Komplexe aus Zellen, sondern sie unterliegen einer stetigen Dynamik. Es gibt eine Vielzahl von wichtigen Faktoren und Prozessen, die Einfluss auf die Integrität eines Gewebes haben. Die Differenzierung, das Überleben und auch das kontrollierte Absterben von Zellen, sowie das Zusammenspiel von Zelladhäsion und -migration sind wichtige gewebeeigene Faktoren. Als ein sehr wichtiger, v.a. externer Faktor werden physikalische Kräfte angesehen, die durch äußere Einflüsse aber auch durch die Zellen im Zellverband entstehen. Die Identifizierung und Charakterisierung einflussnehmender Prozesse und Faktoren, sowie der daran beteiligten Moleküle dient einem generellen Verständnis der Physiologie und hilft Krankheiten zu verstehen, die auf einer Zerstörung der Gewebeintegrität basieren.

Die Brustdrüse ist ein Organ, das postnatal und im Verlaufe der reproduktiven Phase drastischen morphologischen und funktionellen Veränderungen unterliegt. Hierbei lassen sich sehr gut die Faktoren und Prozesse untersuchen, die zur Gewebeintegrität beitragen oder diese auflösen. Beispielsweise entwickelt die Brustdrüse während der Schwangerschaft durch Proliferation und Differenzierung die Funktion eines sekretorischen Organs. Neben diesen beiden Prozessen ist die Zell-Adhäsion zu Nachbarzellen und zur Extrazellulären Matrix (EZM) wichtig für den Erhalt der Struktur und Funktion. Adhäsions- und adhäsionsassoziierte Moleküle, wie zum Beispiel Cadherine oder auch das Aktin Zytoskelett, sind essentiell für eine intakte Verknüpfung der Zellen. Die beim Entstehen und Etablieren von Adhäsionsverbindungen unterliegende Dynamik ist im physiologischen Kontext nur wenig erforscht.

Während des Abstillens durchläuft die Brustdrüse eine vollständige Rekonstruktion in Form einer Rückbildung des Organs. Dieser komplexe Prozess wird Involution genannt und besteht aus zwei Phasen. In der ersten Phase treten bereits die ersten Anzeichen für den einsetzenden kontrollierten Zelltod auf. Jedoch kann die Brustdrüse unter Fortsetzung des Saugstimulus in die Laktation zurückkehren. Mechanismen, die das Überleben der Zellen sichern, sind hier vermutlich von Bedeutung. Mit Eintritt in die zweite Phase der Involution wird ein Status erreicht, von dem aus die Rekonstruktion der Brustdrüse unaufhörlich voranschreitet und eine Rückkehr zur Laktation unmöglich wird. Studien deuten darauf hin, dass ein erhöhter Milchstau Mechanismen induzieren kann, die zur Involution führen. Durch welche Reize und zelluläre Signalwege dieser Prozess initiiert wird und welche Mechanismen die Reversibilität der ersten Phase der Involution begründen, ist weitestgehend unklar. Möglicherweise fungiert die Autophagie als

Schutzmechanismus vor einem frühzeitigen Absterben der Zellen. Durch mechanische Einwirkung geschädigte Proteine werden markiert und dadurch von Chaperonen erkannt und abgebaut. In dieser besonderen Form der selektiven Autophagie (englisch: *chaperone assisted selective autophagy*, CASA) ist BAG3 das Schlüsselprotein und initiiert zusätzlich die Gentranskription, um geschädigte Proteine zu ersetzen. BAG3 ist aber vor allem dadurch bekannt, dass es mit dem Überlebensfaktor Bcl-2 interagiert und dadurch eine essentielle Rolle bei der Erhaltung von Zellen spielt. Inwiefern BAG3 beim kontrollierten Zelltod während der Rekonstruktion der Brustdrüse eine Funktion innehat und welcher Mechanismus diese Funktion reguliert, ist bisher nicht bekannt.

In dieser Arbeit wurden verschiedene Aspekte der Gewebeintegrität anhand dreidimensionaler Zellkulturen und des Brustdrüsenmodells untersucht. Weitestgehend wurde mit dreidimensionalen Sphäroidkulturen und Fluoreszenzmikroskopie gearbeitet. (1) Es wurde ein verlässliches Immunfärbeprotokoll und dessen Evaluation erarbeitet. (2) Das Sphäroidmodell aus Brustepithelzellen wurde auf strukturelle und funktionelle Ähnlichkeit zum Gewebe *in vivo* untersucht. Weiterhin wurde geprüft, (3) welche Rolle das von BAG3 abhängige Überleben der Zellen in der Involution der Brustdrüse spielt, (4) ob auf Zellverbände einwirkende physikalische Kräfte die Gewebeintegrität beeinflussen, und (5) welche Rolle Proteine, die mit Adhäsion oder Wachstum assoziiert sind, bei der Regulierung von Gewebeintegrität spielen.

Durch eine Expressionsanalyse konnte gezeigt werden, dass BAG3 während der Schwangerschaft gering exprimiert wurde. Im Verlauf der Laktation stieg die Expression an. Eine Induktion der Involution führte zu einem weiteren Anstieg der Expression von BAG3 und erreichte am dritten Tag der Involution das Expressionsmaximum. Ergänzend zu den Analysen *in vivo* wurde in einem zweidimensionalen Zellkulturexperiment festgestellt, dass BAG3 in Brustepithelzellen einen Einfluss auf das Überleben der Zellen hat. Somit lässt sich ein Anstieg der Expression von BAG3 zu Beginn der Involution mit einer zunächst erhöhten Überlebensrate der Zellen in Verbindung bringen.

Die moderne Zellbiologie bestrebt Experimente zu entwickeln, in denen der dreidimensionale, physiologische Zustand möglichst gut abgebildet wird. Bei der Aufnahme von dreidimensionalen Zellkulturen mit Hilfe der Fluoreszenzmikroskopie ist es Herausforderung, die dreidimensionale Struktur von großen Sphäroiden *in toto* abzubilden. Bisweilen gestaltet sich die Immunfärbung solcher Proben bezüglich der Verteilung der mit Fluorophoren markierten Antikörper und der Intensität der Färbung als schwierig. In dieser Arbeit wurde eine Evaluation von Immunfärbungen in großen Sphäroiden *in toto* durchgeführt. In dieser Evaluation wurden die Spezifität, die Intensität und die Homogenität der Färbung bewertet. Anhand dieser Eckpfeiler wurde ein Färbeprotokoll für den Gebrauch in Sphäroiden erarbeitet, das in einer Vielzahl nachfolgender Projekte Anwendung findet. Das Protokoll wurde im Fachjournal *Biomedical Optics Express* publiziert.

Mithilfe der Immunofluoreszenz wurde anschließend überprüft, ob Sphäroide aus Brustepithelzellen geeignete Modelle für das Brustgewebe sind. Dafür wurden die morphologischen und funktionalen Eigenschaften der Sphäroide geprüft. Zellen, die sich zu einem Sphäroid zusammenschließen, sekretieren EZM. Dabei kann die Haftung der Zellen an die EZM sowohl für die Sphäroidformierung, als auch für das Entstehen morphologischer Besonderheiten der Sphäroide eine Rolle spielen. In Sphäroiden verschiedener Brustepithelzelllinien und unterschiedlicher Invasivität wurde die zeitabhängige Synthese und Organisation der EZM untersucht. Es wurden die Komponenten Collagen Typ IV, Fibronectin und Laminin, die in der Basallamina präsent sind, und Collagen Typ I, welches vor allem im Stroma vorhanden ist, untersucht. Es wurde gezeigt, dass die Sphäroide spätestens 24 Stunden nach Beginn der Formierung EZM synthetisieren. Die in der Basallamina vorkommenden Proteine wurden von allen Zelllinien exprimiert, während die invasiven Zellen zusätzlich eine erhöhte Synthese des stromalen Collagen Typ I zeigten. Im Verlauf der Sphäroidformierung änderte sich die Lokalisation mancher EZM Proteine. Beispielsweise war in Sphäroiden invasiver Zellen Fibronectin nach sieben Tagen vorwiegend in einer innenliegenden Schicht auf ca. $\frac{3}{4}$ der Distanz zwischen Zentrum und Sphäroidoberfläche vorzufinden. Übereinstimmend mit der bestehenden Literatur deutet dies auf eine physikalische Abgrenzung zweier Zellpopulationen hin, bestehend aus einer an der Oberfläche befindlichen teilungsaktiven Zellschicht und einer im Inneren liegenden teilungsinaktiven Zellschicht. Neben der Organisation der EZM bildeten die Sphäroide morphologische Strukturen, die azinaren Strukturen in der Brustdrüse ähnelten. Die Zellen zeigten eine Polarisierung der Membranproteine, jedoch keine Polarisierung des Golgi Apparates. Diese Ergebnisse zeigen, dass verschiedene Mechanismen zu einer Polarität führen können und eine Membranpolarisierung unabhängig von einer Polarisierung des sekretorischen Apparates erzeugt werden kann. Im weiteren Verlauf wurde gezeigt, dass die Sphäroide durch eine hormonelle Induktion auf Basis des laktotrophen Hormons Prolaktin differenzieren. Zusammenfassend zeigen diese Ergebnisse, dass Sphäroide komplexe Strukturen bilden, die Parallelen zur Struktur und Funktion des Gewebes *in vivo* aufweisen.

Im nächsten Teil wurde der Einfluss mechanischen Stresses auf die Brustepithelzellen untersucht. Sphäroide wurden deformiert, indem sie in Agarosekapillaren eingebettet wurden, deren Durchmesser kleiner als der Durchmesser der Sphäroide war. Eine morphologische Analyse zeigte, dass die Kompression im Verlauf von vier Tagen keinen Einfluss auf das Volumen der Sphäroide und die Zellzahl hatte. Allerdings zeigte sich eine aktive Anpassung des Zellkernvolumens. Das Zellkernvolumen war nach einer einstündigen Kompression vergleichbar zur nicht deformierten Kontrolle. Interessanterweise war das Zellkernvolumen im Vergleich zur Kontrolle nach einer 24-stündigen Kompression um ca. 20% geringer. Nach 96-stündiger Kompression war nur noch ein Unterschied von ungefähr 7% messbar. Zusätzlich zu den morphologischen Eigenschaften wurde

die Induktion des kontrollierten Zelltods über die Aktivierung von Caspasen gemessen. Eine kurzfristig einwirkende Kompression bewirkte eine ansteigende Aktivierung von Caspasen. Im weiteren Verlauf der Zeit passten sich die Zellen der Kompression durch eine Reduktion der Caspaseaktivität an, sodass das Überleben der Zellen gesichert wurde. Zuletzt wurde untersucht, ob die Kompression der Sphäroide die selektive Autophagie (CASA) aktiviert. Nach 24-stündiger Kompression war keine Induktion der Autophagie messbar und die Expression von BAG3 war, entgegen der Annahme, um 20% reduziert. Diese Ergebnisse deuten darauf hin, dass die Kompression der Sphäroide CASA nicht aktivierte. In Bezug auf die Induktion der Involution in der Brustdrüse bleibt es dennoch offen, ob CASA eine Rolle spielt, da die Zellkulturexperimente die enormen physikalischen Kräfte, die zu diesem Zeitpunkt in der Brustdrüse herrschen, nicht widerspiegeln. Die hier angewandten Experimente betrachteten vielmehr eine moderate Verformung und zeigten, dass Brustepithelzellen auf eine Verformung reagieren, indem sie sich auf morphologischer Ebene anpassen und bei lang anhaltendem Stress Überlebensmechanismen zur Verringerung von Zelltod aktivieren.

Neben Zellüberlebensmechanismen, Zelltod und physikalische Kräften hat auch die Etablierung von Zellkontakten und das Zellwachstum Einfluss auf die Gewebeintegrität. Diese wurden in einem Versuch zur Sphäroidformierung untersucht. In diesem System können Zellen ohne externe Störfaktoren interagieren und ein Zellaggregat bilden. Die Formierung von Sphäroiden unterliegt einer Dynamik, die in drei Phasen aufgeteilt werden kann: (1) die Aggregationsphase, (2) die Phase der Verdichtung, und (3) die Wachstumsphase. Diese Phasen konnten durch lichtmikroskopische Langzeitaufnahmen und der Messung der Aggregationsdynamik identifiziert und analysiert werden. Es wurde gezeigt, dass der Ablauf der Sphäroidformierung ein reaktionskontrollierter Prozess ist. Zellen gehen nicht notwendigerweise eine Verbindung ein, wenn sie sich zufällig berühren. Im Weiteren wurde ein computergestütztes Modell verwendet, um die Bindewahrscheinlichkeit und die Bruchwahrscheinlichkeit der Zellen zu bestimmen. Mithilfe der Aggregationsdynamik und der Wahrscheinlichkeit des Bildens und Brechens von Bindungen konnte festgestellt werden, inwiefern die Manipulation bestimmter Proteine die Sphäroidformierung beeinflusst. Im Zuge dessen wurde nicht nur BAG3, sondern auch andere, an der Adhäsion beteiligte Proteine untersucht. Diese waren E-Cadherin, Aktinfilamente, Mikrotubuli und die fokale Adhäsionskinase (FAK). Bei Funktionsverlust von E-Cadherin oder Aktin wurden keine kompakten Sphäroide gebildet. E-Cadherin ist ein membrangängiges Protein, das mit Cadherinen benachbarter Zellen Verbindungen eingehen kann. Aktinfilamente knüpfen intrazellulär an Adhäsionskontakte und stabilisieren diese. Tendenziell hatte keine der beiden Komponenten eine Auswirkung auf die Bindewahrscheinlichkeit, sondern bewirkten in zwei der drei untersuchten Zelllinien eine Zunahme der Bruchwahrscheinlichkeit. Dies zeigt, dass weder E-Cadherin noch Aktin die initialen Proteine beim Eingehen von Verbindungen zweier Zellen sind,

sondern dass andere Proteine daran beteiligt sein müssen. Wenn die Mikrotubuli depolymerisiert wurden, bildeten sich intakte Sphäroide. Allerdings war die Sphäroidformierung verlangsamt und das Wachstum massiv beeinträchtigt, da die Mikrotubuli während der Zellteilung den Spindelapparat bilden. Unterschiedliche Werte für die Binde- und Bruchwahrscheinlichkeit bei den untersuchten Zelllinien deuten darauf hin, dass Mikrotubuli durch unterschiedliche Mechanismen einen Einfluss auf die Zelladhäsion haben können. Diese Ergebnisse deuten auch auf eine Beteiligung der Mikrotubuli in der Reorganisation von Zellen hin, sodass sich die Zellen entgegen der Schwerkraft bewegen, um einen Sphäroiden zu formen. Da die Sphäroide EZM exprimieren und sekretieren, liegt es nahe, dass Zell-EZM Verbindungen aufgebaut werden. Die Bindung von Zellen an EZM wird meist über Integrine vermittelt, an die intrazellulär die Tyrosinkinase FAK bindet. Diese beeinflusst eine Vielzahl von Signalwegen. Im Allgemeinen hatte eine Inhibierung einer Phosphorylierungsstelle (Y397) von FAK geringe Wirkung auf die Aggregationsdynamik und die Bindewahrscheinlichkeit. Dies wurde dadurch bekräftigt, dass die Phosphorylierung von FAK in der dreidimensionalen Zellkultur im Vergleich zur zweidimensionalen Zellkultur abnimmt, da weniger Zell-EZM Verbindungen aufgebaut werden müssen. FAK spielt daher in einem dreidimensionalen Kontext eine eher untergeordnete Rolle. Es ist jedoch so, dass in Krebszellen FAK oft konstitutiv phosphoryliert vorliegt. Dann hat eine Inhibierung der FAK Aktivität auch eine Auswirkung auf das Zellwachstum, wie im Falle von 4T1 Zellen gezeigt werden konnte. Die Ergebnisse dieser Arbeit wurden in einem Manuskript zusammengefasst und befinden sich derzeit bei einem Fachjournal in der fortgeschrittenen Bewertungsphase.

Im Weiteren wurde BAG3 in der Sphäroidformierung untersucht. Hierfür wurde jeweils eine Zelllinie, in der BAG3 herunterreguliert wurde und eine Zelllinie, in der BAG3 deletiert wurde, verwendet. Eine Herunterregulation von BAG3 hatte einen leichten Einfluss auf die Verdichtung der Sphäroide. Wenn jedoch BAG3 in den Zellen deletiert wurde, war in dieser Phase kein messbarer Effekt nachzuweisen. Dies deutet darauf hin, dass BAG3 Einfluss auf die Prozesse der Sphäroidformierung hat, jedoch nicht essentielle Funktion ausübt, da ein Verlust des Proteins kompensiert werden kann. Nach siebentägiger Sphäroidkultur zeigte sich, dass die Sterberate der Zellen erhöht war, wenn BAG3 deletiert wurde. Das war bei der Zelllinie mit der Herunterregulation von BAG3 nicht der Fall. Das deutet darauf hin, dass nicht nur die Präsenz oder Abwesenheit eines Proteins Auswirkungen hat, sondern vor allem auch die Menge der Moleküle, die in der Zelle vorhanden ist. Zudem kann dies für vielseitig aktive Proteine wie BAG3 bedeuten, dass eine veränderte Anzahl der Moleküle in einem Signalweg keinerlei Auswirkung hat, während ein anderer Signalweg von einer schwankenden Anzahl der Moleküle massiv betroffen sein kann.

Mithilfe eines dreidimensionalen Zellkulturmodells wurden Fragen der Gewebeintegrität in der Brustdrüse beantwortet. Es wurden die Methoden entwickelt, um Sphäroide verlässlich mit bildgebenden Methoden darstellen zu können, und das Sphäroidmodell charakterisiert. Anhand von

in vivo und *in vitro* Experimenten wurde die Relevanz des Proteins BAG3 während der Involution aufgezeigt. Weiterhin wurde der Einfluss physikalischer Kräfte auf die Gewebeintegrität untersucht und welche Proteine beim Eingehen und Festigen von Adhäsionsverbindungen von Bedeutung sind. Die Ergebnisse dieser Arbeit helfen besser zu verstehen, was Zellen in einem Verband zusammenhält und wie Zellen auf Veränderungen in ihrer Umgebung reagieren. In dieser Arbeit wurde gezeigt, dass von BAG3 abhängige Überlebensmechanismen in der Anfangsphase der Involution der Brustdrüse aktiv sind. Basierend darauf können zukünftige Arbeiten Faktoren identifizieren, die im weiteren Verlauf einen Verlust der Gewebeintegrität herbeiführen. Dadurch kann auch der Schlüsselmechanismus der Einleitung der Involution und der damit verbundenen Aktivierung der Überlebensmechanismen in der Brustdrüse identifiziert werden. Das ist wichtig um die Physiologie dieses Organs und dessen Erkrankung zu verstehen. Zusätzlich tragen die Ergebnisse dieser Arbeit dazu bei, ein besseres Verständnis von spontaner Zellaggregation und Organisation zu schaffen. Die Ergebnisse dieser Arbeit werfen die Frage nach einer Beteiligung der dreidimensionalen Zellmigration in der Organisation von Gewebestrukturen auf.

Summary

Tissue integrity is defined by the composition and connection of cells as a structural and functional unit. It is modulated by a magnitude of processes including differentiation, survival, controlled death and adhesion of cells. Besides, external factors such as physical forces are also involved. A suitable model system to study all modalities of tissue integrity is the mammary gland. Postnatally and within the reproductive phase, the mammary gland undergoes morphological and functional modifications that periodically loosen or strengthen tissue integrity. An important point in the development of the mammary gland is the regression during weaning, also termed involution. The transition from lactation to involution is important for a controlled loss of tissue integrity. In this transition, collective cell death is initiated but not yet prominent enabling the mammary gland to fully recover lactation.

In this thesis, modalities of tissue integrity were investigated using three-dimensional cell cultures (i.e. spheroids) and the mammary gland as model systems. In the context of this thesis, I established (1) an immunofluorescence staining protocol and its detailed evaluation. Furthermore, I studied (2) the role of cell survival during mammary gland development, (3) the effect of physical forces that modulate tissue integrity and (4) the contribution of proteins to cell adhesion and growth.

Since a homogeneous fluorescence stain of the specimen is necessary for quantitative analysis, an immunofluorescence staining protocol was established to stain large spheroids *in toto*. The evaluation contributes qualitative and quantitative criteria that judge the specificity, intensity and homogeneity of the stain. Based on this approach, it was possible to demonstrate the morphological and functional characteristics that spheroids share with the mammary gland *in vivo*. These characteristics included the synthesis of extracellular matrix, the development of polarized acinar structures and lactogenic differentiation.

The role of cell survival during mammary gland development was analyzed by means of the expression profile of the pro-survival protein BAG3. The expression of BAG3 differed in the progress of mammary gland development. While the expression was low during pregnancy, it rose in the lactation phase and peaked within the first days of involution, indicating that BAG3 is associated with early involution in the mammary gland. *In vitro* experiments related the expression of BAG3 to cell survival in mammary epithelial cells.

Physical forces naturally occur during developmental processes influence tissue integrity during the initiation of mammary gland involution. The influence of physical force applied as compression on mammary epithelial spheroids was investigated. A morphological analysis showed that following a lag, the cell nuclei volume changed upon compression. A short-term compression induced the

activation of caspases. A prolonged compression reduced the activity of caspases. This suggests the induction of a process that allows cells the adaptation to changing environmental conditions. BAG3 is known to be involved in mechanical stress-induced autophagy, also known as chaperone assisted selective autophagy (CASA). Compression of spheroids did not induce CASA. The experimentally applied strain was not comparable to the strain found in the alveolar cells during involution *in vivo*. Thus, whether or not CASA is activated during mammary gland involution remains elusive. Nevertheless, the methodical approach to apply compression on spheroids *in vitro* is a model to study the influence of physical forces on cell aggregates.

Apart from cell survival and physical forces, growth and adhesion of cells affect tissue integrity. A spheroid formation assay and subsequent data analysis and computational modeling enabled the investigation of these processes in a non-adhesive environment. The analysis suggested that spheroid formation follows a reaction-controlled process, in which cells do not necessarily form a connection when they collide. The loss of function of either E-cadherin or actin strongly inhibited the formation of a spheroid. The analysis further revealed that neither E-cadherin nor actin influence the chance of the cells to form a connection when they collide. Both molecules are more important in stabilizing established connections. Depolymerization of microtubules still allowed spheroids to form, but the formation was decelerated and growth of the final spheroids was inhibited. The results from computational modeling suggested that microtubules act on cell adhesion through different mechanisms, which also vary among different cell types. The inhibition of FAK phosphorylation at Y397, a downstream target of integrin signaling, and the analysis of FAK protein levels in spheroids showed that integrin-mediated signaling is not prominent in three-dimensional spheroids formed from non-invasive cells. A deletion of BAG3 gene expression increased the number of dead cells in forming spheroids suggesting that BAG3 predominantly affects cell survival.

The results of this thesis identified and characterized adhesion- and survival-associated proteins that are important for tissue integrity. This thesis suggests that a BAG3-dependent cell survival mechanism is prominent at the beginning of mammary gland involution. Future studies will have to identify the related factors and inducers of tissue integrity loss in the mammary gland. This will shed light on the physiology of the organ and could explain the disorders that destroy its integrity. In addition, this thesis contributes to a better understanding of spontaneous cell aggregation, the aggregate organization and implies a role of cell migration in these processes. Future studies that focus on three-dimensional cell migration could explain, how cell migration is promoted and to which extent it supports tissue integrity.

Table of Contents

Danksagung	i
Zusammenfassung	ii
Summary	viii
List of Figures	xiv
List of Tables.....	xvi
List of abbreviations.....	xvii
1 Introduction	1
1.1 Motivation and scope	1
1.2 Studying tissue integrity based on the mammary gland	2
1.2.1 The mammary gland.....	2
1.2.2 Tissue organization of epithelia.....	7
1.2.3 Anchoring junctions coupled with actin filaments	8
1.2.4 The co-chaperone BAG3.....	11
1.3 Three-dimensional cell culture	13
1.3.1 Cellular spheroids.....	14
1.3.2 Spheroid formation.....	14
1.3.3 Physical forces applied to spheroids.....	16
1.4 Advanced light microscopy	16
1.4.1 Three-dimensional specimens require appropriate imaging systems	16
1.4.2 The limitations of imaging large specimens with LSM	18
1.4.3 The limitations of immunofluorescence staining in large specimens.....	20
1.5 Main contributions of this thesis	21
2 Materials and Methods	22
2.1 Materials	22
2.1.1 Chemicals	22
2.1.2 Enzymes	23
2.1.3 Special devices and consumable materials.....	23
2.1.4 Buffers and solutions.....	24
2.1.5 Commercial kits and products.....	25
2.1.6 Plasmids.....	25
2.1.7 Oligonucleotides.....	26
2.1.8 Antibodies	27
2.1.9 Chemical dyes for fluorescence microscopy	28
2.1.10 Bacterial strain.....	28
2.1.11 Cell lines and culture media	28
2.1.12 Mice.....	29
2.2 Molecular biology methods.....	29
2.2.1 Plasmid transformation in chemically competent <i>E. coli</i>	29
2.2.2 Isolation of plasmid DNA	29

2.2.3 Isolation of genomic DNA	29
2.2.4 Isolation of total RNA	30
2.2.5 DNA and RNA concentration measurement	30
2.2.6 Agarose gel electrophoresis.....	31
2.2.7 Quantitative real-time reverse transcription polymerase chain reaction (qPCR)	31
2.2.8 Protein isolation.....	31
2.2.9 Protein concentration measurement	31
2.2.10 Sodium dodecyl sulfate polyacrylamide gel electrophoresis (SDS-PAGE).....	32
2.2.11 Western (immuno-) blot analysis	32
2.2.12 Immunofluorescence staining.....	33
2.2.13 Immunohistochemistry	34
2.3 Lentivirus production	34
2.4 Cell culture methods.....	35
2.4.1 Cell culture	35
2.4.2 HC11 lactogenesis assay	35
2.4.3 Spheroid formation.....	36
2.4.4 Spheroid compression	36
2.4.5 Lentivirus transduction.....	36
2.4.6 Generation of knockout clones.....	36
2.4.7 Live-dead assay (LDA)	37
2.4.8 Cell adhesion assay.....	38
2.4.9 Cell proliferation assay.....	38
2.4.10 Cell migration assay	38
2.5 Optical clearing	39
2.6 Microscopy.....	39
2.6.1 Wide-field fluorescence microscopy.....	39
2.6.2 Confocal laser scanning microscopy.....	39
2.6.3 Light sheet-based fluorescence microscopy.....	39
2.7 Analysis of the projected area	41
2.8 Statistical analyses.....	41
2.9 Agent-based computational model.....	41
3 Results	43
3.1 BAG3 is associated with cell survival and differently expressed during mammary gland development	43
3.1.1 The expression of BAG3 mRNA changes during mouse mammary gland development	44
3.1.2 The CRISPR/Cas9 technology introduces a stable BAG3 knockout in mammary epithelial cells.....	45
3.1.3 BAG3 is dispensable for lactogenic differentiation of mammary epithelial cells.....	46
3.1.4 Short hairpin RNA (shRNA) introduces a stable BAG3 knockdown in mammary epithelial cells.....	48
3.1.5 BAG3 knockout and knockdown cells develop different phenotypes.....	49

3.2	Fluorescence microscopy of large spheroids <i>in toto</i>	51
3.2.1	<i>In toto</i> immunostaining of large spheroids	51
3.2.2	A comparison between multi-view image fusion and optical clearing.....	61
3.3	Mammary epithelial cell spheroids display morphological and functional characteristics of epithelial tissue	64
3.3.1	Morphological features of spheroids formed from different mammary epithelial cell lines	65
3.3.2	Type I collagen and fibronectin mRNA are expressed in mammary epithelial cell spheroids.....	66
3.3.3	HC11 spheroids synthesize type IV collagen, fibronectin and laminin but low amounts of collagen I.....	68
3.3.4	4T1 spheroids accumulate high amounts of ECM proteins and rearrange ECM	70
3.3.5	T47D spheroids synthesize laminin, fibronectin and type IV collagen but low amounts of type I collagen.....	72
3.3.6	Non-malignant mammary epithelial cell spheroids form polarized structures and express lactation-associated genes upon cell differentiation.....	75
3.4	Mechanical stress modulates tissue integrity.....	76
3.4.1	Strain in two-dimensional cell cultures	77
3.4.2	Spheroids adapt to compression by morphological and functional alterations of cells.....	80
3.5	A spheroid formation assay reproduces modalities of tissue integrity	86
3.5.1	Aggregation, compaction and growth are phases in spheroid formation	87
3.5.2	E-cadherin is required for tight aggregation of mammary epithelial cells	88
3.5.3	Actin is indispensable for spheroid formation and reinforces cell adhesion	90
3.5.4	Microtubule depolymerization decelerates spheroid formation and inhibits spheroid growth.....	93
3.5.5	FAK activity is crucial for spheroid growth but not for spheroid formation.....	94
3.5.6	BAG3 knockdown decelerates the aggregation phase and BAG3 knockout reduces cell viability in spheroids	97
4	Discussion	100
4.1	Imaging large spheroids requires high labeling performance and an adapted imaging approach	100
4.1.1	Evaluation of the immunofluorescence staining performance in large specimens.....	100
4.1.2	An increased antibody incubation temperature improves the staining	101
4.1.3	The advantages of optical clearing over multi-view image fusion.....	102
4.2	Spheroids with epithelial characteristics are a reliable tissue model system.....	104
4.3	ECM in mammary epithelial cell spheroids is differently synthesized and distributed	105
4.4	The differential expression of BAG3 implies an important role in mammary gland development	107
4.5	Mechanical stress activates caspases and alters the morphology in spheroids.....	109
4.6	A spheroid formation assay reveals proteins that modulate tissue integrity.....	112
4.6.1	Spheroid formation is a reaction-controlled mechanism and is distinguishable into three phases	113

4.6.2 Cadherins are important to reinforce cell contacts	114
4.6.3 Actin stabilizes existing cell contacts.....	115
4.6.4 Microtubules strengthen cell adhesion, promote cell rearrangement and facilitate cell proliferation.....	116
4.6.5 Levels of FAK protein synthesis and activity vary among cell lines	117
4.6.6 BAG3 promotes cell survival in spheroids.....	119
4.6.7 Phases of spheroid formation reflect modalities of tissue integrity.....	119
5 Outlook and Conclusion.....	122
5.1 Future research topics.....	122
5.1.1 Imaging large volumes of tissues will reveal cellular networks <i>in vivo</i>	122
5.1.2 The mechanism of BAG3 function in mammary gland development.....	123
5.1.3 The effect of ECM on the diffusion of small molecules in spheroids	124
5.1.4 The influence of mechanical stress on mammary gland involution	124
5.1.5 Cell migration and agility during spheroid formation and in mature spheroids.....	124
5.1.6 Proteins involved in the formation of cell contacts upon collision of cells.....	125
5.2 Concluding remarks.....	125
6 References	126
7 Supplement.....	139
7.1 BAG3 in the mammary gland and in mammary epithelial cells	139
7.2 Immunofluorescence staining and optical clearing	143
7.3 Characterization of mammary epithelial cell spheroids	146
7.4 Mechanical stress	147
7.5 Spheroid formation.....	148
Publications	161
Erklärung.....	162
Versicherung	162

List of Figures

Figure 1-1 Biological and methodical aspects of tissue integrity studied in this thesis.	2
Figure 1-2 Mammary gland development in mouse (<i>Mus musculus</i>) and human (<i>Homo sapiens</i>).	3
Figure 1-3 Alveolar cell morphology changes when involution is initiated.	5
Figure 1-4 Mammary gland involution (described in the murine context).	5
Figure 1-5 Schematic of epithelial anchoring junctions coupled with actin.	11
Figure 1-6 Comparison between confocal laser scanning microscopy (CLSM) and light sheet-based fluorescence microscopy (LSFM).	17
Figure 1-7 LSFM image quality can be improved with multi-view image fusion and optical clearing.	19
Figure 2-1 Spheroid mounting onto a pinhole sample holder.	40
Figure 2-2 Mounting of optically cleared spheroids.	40
Figure 3-1 Gene expression analysis of BAG3 in the developing mammary gland.	45
Figure 3-2 Generation and analysis of BAG3 knockout (KO) clones in HC11 cells.	47
Figure 3-3 Generation of a BAG3 knockdown cell line.	49
Figure 3-4 BAG3 affects cell viability and cell migration in mammary epithelial cells.	50
Figure 3-5 Schematic of the evaluation procedure.	52
Figure 3-6 Schematic of the tested immunostaining protocols.	54
Figure 3-7 Immunohistochemistry analysis of U343 spheroid center sections shows a nearly homogeneous stain for α -tubulin and β -catenin.	55
Figure 3-8 Inspection of the antibody stain in U343 spheroids reveals differences in the specificity due to the use of different staining protocols.	56
Figure 3-9 Overview of the signal intensities in spheroids obtained from different immunostaining conditions.	57
Figure 3-10 Antibody diffusion into spheroids varies between the different immunostaining protocols.	60
Figure 3-11 Illustration of the suggested immunofluorescence protocol for large spheroids.	61
Figure 3-12 Approaches to obtain insight into biological specimens with LSFM.	62
Figure 3-13 Comparison of image quality and of spheroid morphology using different LSFM imaging techniques.	63
Figure 3-14 Optical clearing reduces the spheroid volume.	64
Figure 3-15 Spheroids formed from mammary epithelial cells show morphological differences.	66
Figure 3-16 Type I collagen and fibronectin are present in cellular spheroids.	67
Figure 3-17 Cellular spheroids from HC11 cells synthesize ECM proteins.	69
Figure 3-18 Cellular spheroids from 4T1 cells synthesize ECM proteins.	71
Figure 3-19 Spheroids from highly invasive cancer cells rearrange fibronectin into a pattern.	72
Figure 3-20 Cellular spheroids from T47D cells synthesize ECM proteins.	73
Figure 3-21 Spheroids formed from HC11 cells develop mammary epithelial-specific characteristics.	76
Figure 3-22 Hydrostatic pressure on mammary epithelial cells increases autophagy when cells are additionally treated with the autophagy stimulating agent rapamycin.	78
Figure 3-23 Application of radial strain on cells cultured on flexible membranes.	79
Figure 3-24 Spheroid integrity is preserved under confinement in the long-term.	81
Figure 3-25 Compression of mammary epithelial cell spheroids alters the cell nuclei volume.	82
Figure 3-26 The amount of apoptotic cells differs in compressed spheroids.	83
Figure 3-27 Autophagic flux does not increase upon compression of mammary epithelial cell spheroids. ...	86

Figure 3-28 Cell lines have different spheroid formation dynamics.	88
Figure 3-29 Mammary epithelial cells require E-cadherin to form spheroids.	90
Figure 3-30 The cytoskeleton and FAK activity influence spheroid formation dynamics.	92
Figure 3-31 FAK synthesis and phosphorylation differs between cell lines and culturing methods.	96
Figure 3-32 BAG3 knockdown but not knockout affects spheroid formation in the aggregation phase and BAG3 knockout but not knockdown induces cell death in spheroids in the long term.	98
Figure 4-1 Results obtained from spheroid formation can be extrapolated to the tissue level.	120
Supplemental Figure 7-1 BAG3 localization in the mammary gland.	139
Supplemental Figure 7-2 Gene expression analysis of c-Fos in the developing mammary gland.	139
Supplemental Figure 7-3 Efficiency of Taqman primer for qPCR.	140
Supplemental Figure 7-4 Standard curve for the protein concentration determination.	141
Supplemental Figure 7-5 FACS gating strategy for sorting HC11 EGFP ⁺ cells.	142
Supplemental Figure 7-6 Semi-automated image analysis pipeline for wound-healing assays.	143
Supplemental Figure 7-7 The detection objective focus shift in a BABB optical clearing microscope setup follows a linear equation.	143
Supplemental Figure 7-8 Identification of the appropriate bead concentration for bead-based registration.	145
Supplemental Figure 7-9 Axial resolution is improved when a thinner light sheet is used.	145
Supplemental Figure 7-10 Single planes of central spheroid regions indicate the performance of cell nuclei segmentation for fused and optically cleared data sets.	146
Supplemental Figure 7-11 Phalloidin cross-reacts with extracellular matrix. HC11 spheroids differentiate regardless external collagen addition.	146
Supplemental Figure 7-12 BAG3 transcript variants with alternative exon usage between exon 1 and exon 4 are not present in murine mammary epithelial cells.	147
Supplemental Figure 7-13 Pairwise ratios between the principal directions p1, p2 and p3 along the spheroids.	147
Supplemental Figure 7-14 FACS gating strategy for sorting HC11 GFP ⁺ and mRFP ⁺ cells.	148
Supplemental Figure 7-15 Spheroid formation is analyzed by segmentation of the projected area of the cells.	150
Supplemental Figure 7-16 Determination of PF-573228 and DECMA-1 concentration.	151
Supplemental Figure 7-17 Cells require E-cadherin to form compact spheroids.	152
Supplemental Figure 7-18 Fit of the computational model simulations to the experimental data.	153
Supplemental Figure 7-19 Determination of cytochalasin D concentration.	154
Supplemental Figure 7-20 Determination of blebbistatin and para-nitroblebbistatin concentration.	155
Supplemental Figure 7-21 Determination of nocodazole concentration.	156
Supplemental Figure 7-22 Actin disruption inhibits spheroid formation and affects cell nuclei volume.	157
Supplemental Figure 7-23 The effect of drug treatment on cell death and cell viability.	157
Supplemental Figure 7-24 Optical properties of blebbistatin and para-nitroblebbistatin.	158
Supplemental Figure 7-25 Blebbistatin and para-nitroblebbistatin are cytotoxic upon illumination with blue light.	159
Supplemental Figure 7-26 Area segmentation differs between transmission and fluorescence image data.	160

List of Tables

Table 2-1: List of chemicals used in this thesis.	22
Table 2-2 List of enzymes used in this work.	23
Table 2-3 List of special devices and consumables.	23
Table 2-4 List of homemade buffers and other solutions.	24
Table 2-5: Commercially available kits and products.	25
Table 2-6 Plasmids, which were already available or purchased.	25
Table 2-7: Plasmids generated during this thesis.	26
Table 2-8 List of oligonucleotides used in this thesis.	26
Table 2-9 List of primary and secondary antibodies used for protein detection on membranes, immunofluorescence and functional studies.	27
Table 2-10: List of organic dyes for fluorescence microscopy.	28
Table 2-11: Cell lines.	28
Table 2-12: Composition of cell culture media.	28
Table 2-13: Polyacrylamide gel composition and pipetting scheme.	32
Table 3-1 Overview of the immunofluorescence quality evaluation from different staining protocols.	58
Table 3-2 Comparison of ECM distribution patterns in cellular spheroids of different cell types.	74
Table 4-1 Comparison between multi-view image fusion and optical clearing.	103
Supplemental Table 7-1 Descriptive statistics of the relative mRNA expression data from murine mammary glands.	141
Supplemental Table 7-2 Immunofluorescence staining protocols used to improve the stain quality in spheroids <i>in toto</i>	144
Supplemental Table 7-3 Raw data from antibody dispersion measurement.	144
Supplemental Table 7-4 Sample number for spheroid compression experiments.	148
Supplemental Table 7-5 The effect of light exposure on the projected area during the time-lapse.	148
Supplemental Table 7-6 Spheroid formation sample numbers.	149
Supplemental Table 7-7 Sample numbers of the live-dead assay performed with HC11 BAG3 knockdown and knockout cells.	150
Supplemental Table 7-8 Spheroid formation upon myosin-II inhibition.	158

List of abbreviations

2D	two-dimensional
3D	three-dimensional
A	Ampere
Ac	acetone
BABB	benzyl alcohol and benzyl benzoate
BAG	Bcl-2-associated athanogene
BiP	binding immunoglobulin protein
BM	basement membrane
BSA	bovine serum albumin
CCD	charged-coupled device
cDNA	complementary DNA
CLSM	confocal laser scanning fluorescence microscopy
Da	Dalton
DAPI	4',6-diamidin-2-phenylindol
dehyd.	dehydration
DNA	deoxyribonucleic acid
DR	death receptor
dsDNA	double-stranded DNA
E	efficiency
ECL	enhanced chemiluminescence
ECM	extracellular matrix
EGFP	enhanced Green fluorescent protein
EtOH	ethanol
EMT	Epithelial-mesenchymal transition
FACS	fluorescent activated cell sorting
FAK	focal adhesion kinase
FOV	field of view
<i>g</i>	gravitation
GAPDH	glyceraldehyde-3-phosphate dehydrogenase
GTPase	guanosine triphosphate hydrolase
h	hour(s)
HBS	Hepes-buffered saline (buffer)
HRP	horseradish peroxidase
Hs	<i>Homo sapiens</i>
IgG	immunoglobulin G
LB	lysogeny broth (medium)
LC3	microtubule-associated protein 1A/1B-light chain 3
LeGO	lentiviral gene ontology
LIF	leukemia inhibitory factor
LMP	lysosomal membrane permeabilization
LSFM	light sheet-based fluorescence microscopy
LTR	long terminal repeat
MAPK	mitogen-activated protein kinase
mDSLMM	monolithic digital scanned light sheet-based fluorescence microscope
MetOH	methanol
Mm	<i>Mus musculus</i>
MMP	matrix metalloproteinase
mRNA	messenger RNA

MTS	3-(4,5-dimethylthiazol-2-yl)-5-(3-carboxymethoxyphenyl)-2-(4-sulfophenyl)-2H-tetrazolium
MVR	Multi-view Reconstruction
N	Newton
NA	numerical aperture
o.n.	overnight
Pa	Pascal
PAGE	polyacrylamide gel electrophoresis
PBS	phosphate-buffered saline (buffer)
PDZGEF2	PDZ domain containing guanine nucleotide exchange factor 2
PFA	paraformaldehyde
PRL	prolactin
PVDF	polyvinylidene fluoride
qPCR	quantitative real-time polymerase chain reaction
r.p.m.	rounds per minute
RFP	red fluorescent protein
RFU	relative fluorescence unit
RI	refractive index
RIPA	radioimmunoprecipitation (buffer)
RNA	ribonucleic acid
RT	room temperature
SDS	sodium dodecyl sulfate
sgRNA	single guide RNA
shRNA	short hairpin RNA
SIN	self-inactivation
SNB	signal-to-background (ratio)
SPIM	single plane illumination microscopy
TAE	Tris acetic acid EDTA (buffer)
TBS	Tris-buffered saline (buffer)
TDE	2,2'-thiodiethanol
TDLU	terminal ductal lobulo-alveolar units
V	Volt
V _H H	variable heavy domain of antibodies
VSV-G	vesicular stomatitis virus glycoprotein G

1 Introduction

1.1 Motivation and scope

Tissue integrity involves all aspects that contribute to the maintenance of a functional tissue. All physical and biochemical interactions of a cell with its environment affect tissue integrity. A tissue is a dynamic system that, depending on internal or external stimuli, may undergo remodeling in order to build or break its integrity. These dynamics are therefore fundamental in developmental processes, such as embryonic development, or remodeling of adult tissue. Malfunction in the perception of internal or external stimuli can distort developmental processes or tissue function, which may support pathological conditions such as cancer.

Physical cues, such as mechanical stress exerted by external factors or cells interacting physically with each other, affect tissue integrity. Biochemical cues include molecules involved in cellular processes like cell adhesion and survival. How these cues contribute to tissue integrity and to which extent they interplay with each other is not well understood.

The mammary gland is the model system to study tissue integrity in a physiological, non-pathogenic context. The mammary gland is an organ capable to undergo multiple rounds of differentiation, has secretory function and undergoes post-lactational regression during adulthood. These changes require coordinated signaling events to process cues into the appropriate response. In the mammary gland, environmental changes affect tissue integrity dramatically on the level of cell proliferation, adhesion, differentiation and cell death.

In this thesis, I studied the processes involved in establishing and modulating tissue integrity of the mammary epithelium. I investigated the contribution of intracellular molecules such as the cytoskeleton and cytoskeleton-associated proteins in cell adhesion with a spheroid-based formation assay. Further, I investigated the influence of mechanical stress on tissue architecture. The focus was set on the morphological alterations of cells within spheroids that experienced physical force by compression for different periods of time. In this context, I investigated whether a compression influences autophagy and apoptosis in spheroids. This was accomplished using an *in vitro* three-dimensional (3D) spheroid model system generated from murine mammary epithelial cells. I highlighted the contribution of the pro-survival co-chaperone BAG3 in all studied aspects of tissue integrity and identified its expression pattern in the developing mammary gland.

Most results were based on imaging data from fixed and immunostained specimens. Labeling and imaging of intact, large three-dimensional specimens is challenging and, therefore, one part of my work focused on the optimization of the imaging conditions of large spheroids (Figure 1-1).

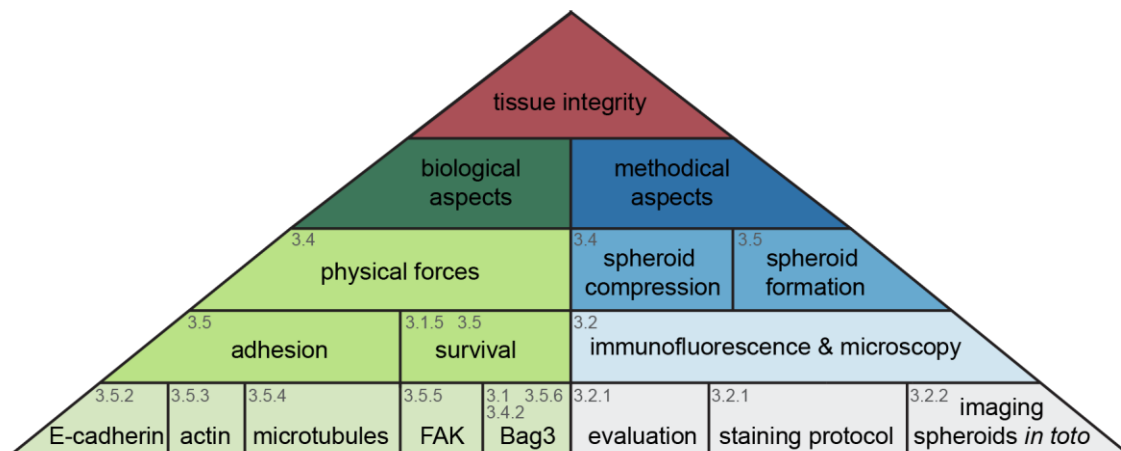


Figure 1-1 Biological and methodical aspects of tissue integrity studied in this thesis. The pyramid consists of two halves. The left half shows the biological aspects of studying tissue integrity. It focuses on adhesion and survival of cells, as well as physical forces. Within these contexts, the role of several proteins was studied. The methodical approaches to study these factors are shown in the right half of the pyramid. Three-dimensional cell culture was predominantly used as a culture model. The biological aspects were mainly studied in a spheroid compression assay and a spheroid formation assay. The main tool to study three-dimensional aggregates was three-dimensional microscopy, for which an immunofluorescence staining protocol and evaluation were developed. The grey numbers indicate the sections that deal with the according topic.

1.2 Studying tissue integrity based on the mammary gland

1.2.1 The mammary gland

The mammary gland is composed of compartments made from various cell types. The ducts form from luminal epithelial cells and contractile myoepithelial cells. The basement membrane (BM) underlies the epithelium and thereby surrounds the ducts. Adjacent is the stroma with mesenchymal cells, such as fibroblasts, blood cells, leukocytes, and the extracellular matrix (ECM). The composition of the stromal ECM and BM changes during development and differences in ECM composition can influence the behavior of the mammary epithelial cells (Fata et al., 2004; Kass et al., 2007).

In both, human and rodents, the mammary gland is a highly dynamic organ, which not only undergoes embryonic developmental processes, but also postnatal modifications. In general, mammary gland development can be classified into three major stages: the embryonic, the pubertal, and the reproductive stage (Watson and Khaled, 2008). Thus, the mammary gland is the appropriate model to study dynamic processes that foster and disrupt tissue integrity under non-pathological as well as under pathological conditions.

Anatomically, humans have only one pair of mammary glands. Terminal ductal lobulo-alveolar units (TDLUs) exist in spatially defined regions (Smalley et al., 2008), which are dominated by lobules of type 1 or type 2. During pregnancy, type 3 lobules develop and type 4 lobules are only present during lactation (Figure 1-2a). In comparison, rodents have ventrolateral five pairs in case of mice, and six pairs in case of rats. In mice, one pair lies in the cervical, two in the thoracic, and two in the abdominal-inguinal region. Compared to human, alveolar structures do not exist in the virgin glands of mice. There, alveogenesis occurs during pregnancy and lactation. In mice, alveoli distribute uniformly throughout the gland. On the cellular detail, in both, human and rodent, the bilayer composition of the tubular system is similar (Russo and Russo, 1996).

The rodent mammary gland shares important similarities with the human mammary gland making it a valuable model system to study breast development and neoplasia (Russo and Russo, 1996).

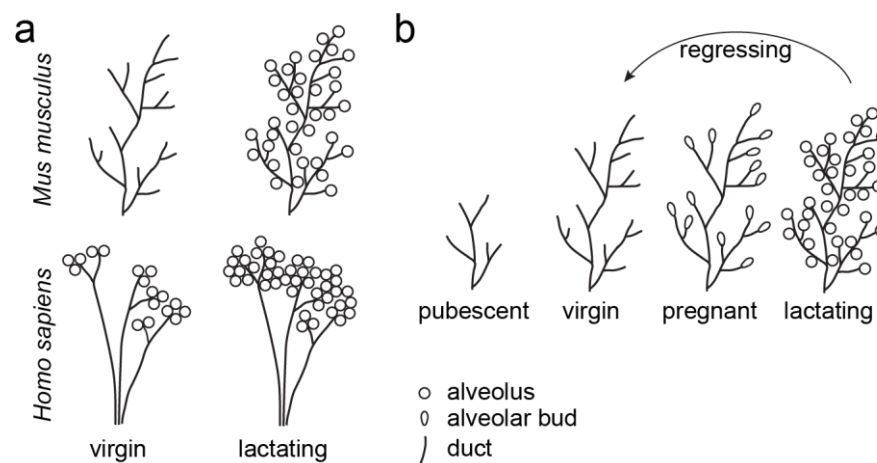


Figure 1-2 Mammary gland development in mouse (*Mus musculus*) and human (*Homo sapiens*). (a) Macroscopic structure of the mouse and human mammary epithelium in the virgin and lactating state. In mice, alveolar development is restricted to pregnancy. Alveoli distribute uniformly within the gland. In human, TDLUs are clusters of alveoli with spatial restriction. TDLUs further develop during pregnancy to produce milk. (b) Different stages of mouse mammary gland development. During puberty, the ductal tree grows out to fill the entire fat pad in mature virgin mice. At the onset of pregnancy, hormonal changes induce proliferation and formation of alveolar buds. Fully mature alveoli secrete milk during the lactation phase. Cessation of milking induces the regression phase (involution), where remodeling processes rearrange the mammary gland into a state comparable to the virgin mouse (based on Smalley *et al.* 2008, Hennighausen and Robinson 2005).

Mouse mammary gland development during embryogenesis, puberty and pregnancy

The mammary anlagen, which are the primordia of this organ, form during embryonic development. Before birth, a rudimental duct proliferates and invades the mammary fat pad precursor. This primitive epithelial structure remains dormant until the ovaries begin to secrete hormones. Then, the duct bifurcates and associates with the subdermal fat pad to form a small ductal system with terminal end buds (TEBs) at the dead end of the ducts. In this developmental stage, massive collective cell migration and proliferation are present (Richert et al., 2000; Friedl and Gilmour, 2009).

During pregnancy, the peptide hormone prolactin (PRL) produced in the anterior pituitary gland induces the ductal cells to proliferate and differentiate into secretory alveolar cells (Hennighausen and Robinson, 2005). Alveoli comprise the majority of the gland and secrete milk proteins and lipids approximately from day 18 of pregnancy on (Richert et al., 2000). Following parturition, milk secretion continues for about three weeks until weaning. Then, the mammary gland undergoes a complete remodeling process. This post-lactational regression, termed involution, lasts for two to three weeks, after which a status comparable to pre-pregnancy is reached. The cycle of strong cell proliferation and differentiation during pregnancy, followed by cell death and tissue remodeling in the involution process can be repeated many times (Figure 1-2b) (Richert et al., 2000). This makes the mouse mammary gland a suitable organ to study all phases of epithelial development and tissue integrity.

Mouse mammary gland development during involution

Post-lactational regression (involution) of the mammary gland results in a loss of the major portion of secretory cells and the degradation of the ECM (Quarrie et al., 1996). In general, a lacking suckling stimulus initiates the involution process. The whole process is distinguishable into two phases. The first phase is reversible, such that the lactation process resumes when the suckling stimulus restores within a certain time span. When this time span exceeds a critical time point, the remodeling process becomes irreversible, which marks the transition to the second phase (reviewed in Macias and Hinck, 2012). In animal studies, involution is studied by the abrupt removal of the offspring. This results in forced involution, a process that differs from natural weaning (Silanikove, 2014).

The shedding of apoptotic cells into the alveolar lumen indicates the first phase of forced involution. Teat-sealing experiments have revealed that this phase is regulated by local factors and is not under systemic control since the unaffected glands do not show the signs for involution (Watson and Kreuzaler, 2011). Milk stasis changes the morphology of the alveolar cells from a columnar towards an elongated shape with the elongated sides facing the lumen (Figure 1-3). The features exhibited by the cells do not match the appearances of classical apoptosis. In this first phase, cleaved caspase-3 and -6 are only detectable in the shed cells, but not in the surrounding alveolar cells (Watson, 2006). Caspase activation in the alveolar cells begins with the onset of the irreversible phase of involution. A depletion of executioner caspases from the mouse mammary gland does not abrogate involution. In contrast, markers for lysosomal activity, among them cathepsins and LC3, are expressed 24 hours post-weaning (Monks and Henson, 2009; Gajewska et al., 2013). Therewith, a lysosomal-mediated programmed cell death (LM-PCD) is present in the first phase of involution (Kreuzaler et al., 2011). Besides increased lysosomal leakage, autophagy is increased during the early phase of involution. At this stage, autophagy has been proposed a pro-survival role (Pensa et

al., 2014). From 48 hours on, autophagy declines (Pensa et al., 2014; Teplova et al., 2013). This rapid decline may be caused by the increase of LM-PCD, which causes a deficient fusion of lysosomes with autophagosomes due to leaky lysosomes (Pensa et al., 2014).

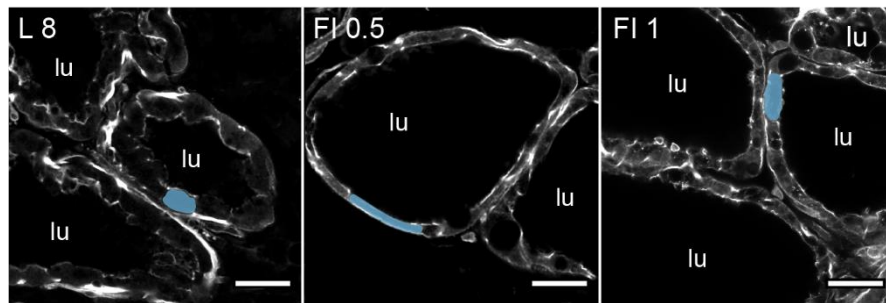


Figure 1-3 Alveolar cell morphology changes when involution is initiated. During lactation (here: 8 days) the alveolar cell shape is columnar. Upon

involution initiation, the accumulation of milk within the alveoli causes their dilatation. The alveolar cells flatten and have an increased surface facing the lumen. Two states of involution are shown: 0.5 days and 1 day following pup removal. The cell circumferences are shown by an F-actin stain (phalloidin AF488). The blue area shows the cell shape of individual. Microscope: Zeiss LSM780, objective lens: 63x/NA 1.4, scale bar: 25 μ m. FI: forced involution, L: lactation, lu: lumen.

The transition to the second, irreversible phase of involution occurs in mice after approximately 48 hours. Systemic factors regulate this phase (Watson and Kreuzaler, 2011). It is accompanied by the architectural change of the mammary gland. Alveoli begin to collapse, adipocytes re-emerge to fill the gland and massive ECM remodeling takes place. Matrix removal induces detachment-triggered apoptosis of epithelial cells. Invading macrophages remove the resulting debris (Figure 1-4) (Watson, 2006).

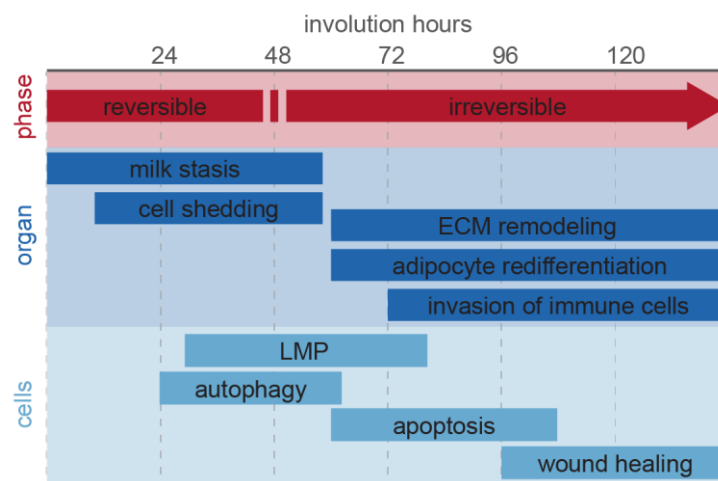


Figure 1-4 Mammary gland involution (described in the murine context). Mammary gland involution is separable into two distinct phases – a reversible and an irreversible phase. On the organ level, milks stasis and cell shedding of alveolar cells into the alveolar lumen mark the reversible phase. The irreversible phase is marked by cell death of alveolar cells, ECM remodeling, adipocyte dedifferentiation and immune reactions. On the cellular level, LMP and autophagy are upregulated in the

reversible phase. They decline with the onset of the irreversible phase. Apoptosis is a hallmark of the early irreversible phase, and wound healing processes in the late irreversible phase.

Characterizing the relationship between cancer development and mammary gland involution

There is incidence from several epidemiological studies that early termination of breastfeeding increases the risk of developing breast cancer at later age (summarized in Silanikove, 2014). The

world health organization (WHO) recommends to breastfeed infants for the first two years of life (Dewey, 2003), and the German Ministry for Nutrition and Agriculture (BMEL) advises to exclusively breastfeed for the first six months of life (BMEL, 2013). However, the Center for Disease Control and Prevention (CDC) reported that the actual rate of women breastfeeding their offspring at an age of 12 months was only 30% of infants born in 2013. The rate of exclusively breast fed infants at an age of six months was only 22% (CDC, 2013). Therefore, studying forced involution in the mouse model organism is not only important to understand the general processes occurring during this tissue remodeling process but also to get insight into its contribution to cancer development.

The role of mechanical stress in mammary gland involution

Cells in all tissues cope with a variety of mechanical forces, such as hydrostatic pressure, tensile, compressive, and shear stress (Butcher et al., 2009; DuFort et al., 2011). Mechanical input can occur in a passive, by the stiffening of the environment, or in an active manner, by the application of physical forces, which at least partially deform the cells. The mechanical stress is quantified in Pascal (Pa) as a measure of the force per unit area, which is equivalent to Newton (N) per m². The Young's modulus, or elastic modulus, is a measure of the stiffness of a solid material (i.e. cells or tissue). It is defined as the ratio between the stress and the strain. Strain is a dimensionless quantity and describes the change of length in relation to the original length of the specimen upon application of force. Biological tissues exhibit properties of solid material and viscous fluid, and thus can be described as viscoelastic materials (Fung, 1993). Therefore, not only the Young's modulus applies to characterize biological tissue, but also the shear modulus, which is the ratio between the shear stress and the shear strain (Butcher et al., 2009; DuFort et al., 2011).

In general, cells react to mechanical input by changing cell or organelle shape (Philip and Dahl, 2008; Guilak et al., 2000), remodeling of the cytoskeleton (Luo et al., 2013) or by the activation of signaling pathways (Ricca et al., 2013). The conversion of mechanical stimuli into biochemical signals termed mechanotransduction.

Different types of mechanosensors exist, which in turn activate downstream signaling effectors to induce the appropriate response. Most widely, mechanosensing is initiated by focal adhesion, in which integrin receptors transmit the information (Butcher et al., 2009). Further, stretch-activated ion-channels can act as mechanosensors (Iqbal and Zaidi, 2005). Intracellularly, the actin cytoskeleton in conjunction with its associated proteins acts as a mechanosensor by transmitting forces within and among neighboring cells. The actin cytoskeleton responds to mechanical input by self-remodeling and by activation of associated signaling pathways (Ehrlicher et al., 2011; Ulbricht et al., 2013b).

Changes of the local environment can have dramatic effects on the cellular behavior and phenotype. Thus, mechanical forces play a key role in many fundamental processes during development and pathogenesis (DuFort et al., 2011). Moreover, the influence of mechanical stresses has gained importance in dynamic systems such as the reproductive tissues (Jorge et al., 2014) and in tumor development (Paszek et al., 2005).

The actual mechanism that initiates the involution process in the mammary gland is still unknown. It seems that milk stasis is one of the first trigger of involution and that mainly local factors drive involution. One hypothesis is that apoptotic factors accumulate in the milk and at a certain point induce apoptosis.

Another hypothesis is, and certainly, both hypotheses could act in synergy, that the milk stasis causes mechanical stress by distension of alveolar cells and compromises the integrity of the alveolar cells. Thus, stimulated stress-sensing mechanisms result in involution (Macias and Hinck, 2012). This is supported by the finding that involution-associated genes are upregulated upon application of mechanical stretch (Quaglino et al., 2009). Different pathways have become popular as possible mechanisms (Oldenhof et al., 2002). The mechanical stretch hypothesis is further supported by the downregulation of the milk calcium-transporting plasma membrane calcium-ATPase2 (PMCA2) during involution. This results in an increase of intracellular Ca^{2+} and thereby initiates cell death (Monks and Henson, 2009). PMCA2 expression is regulated by the shape of the secretory cells (Watson and Kreuzaler, 2011). However, the mechanisms by which the mechanical forces are transduced to induce the involution answer are not known. Related to this context is the question how tissues adapt morphologically and physiologically to spontaneous mechanical stresses. Taking advantage of three-dimensional cell cultures would help to investigate the morphology of cells in an aggregate.

1.2.2 Tissue organization of epithelia

The epithelium is supported by the underlying connective tissue and contributes to the function of the mammary gland as a secretory organ. Epithelia line the body cavities, cover the body surface, and form various glands. Their main functions are protection, absorption and secretion. A hallmark of epithelial tissue is that its cells form tight connections to form a physical barrier. This results in specialized characteristics: (1) Cells from an epithelium are polar. Polarity is characterized by the asymmetrical distribution of molecules in a cell. All epithelia have an apical side and a basolateral side, which differ in structure and function. At the apical side, small membranous extensions called microvilli emerge to increase the surface for enhancing absorption or secretion. The basal side faces the BM, a supporting sheet of ECM. Epithelial cells have a polarized trafficking machinery with the secretory organelles (endoplasmic reticulum and Golgi apparatus) and endosomal compartment facing the apical side of the cells (reviewed in Rodriguez-Boulan and Macara, 2014). (2) Epithelia

are avascular, but they are (3) highly innervated by nerve fibers. (4) Epithelia have a high capacity for regeneration. A population of stem cells, which gives rise to daughter progenitor cells, intermingles with the other epithelial cells. In the mammary gland, stem cells are required to renew the epithelial cells after subsequent pregnancies (Watson and Khaled, 2008). (5) To fulfill their function as a physical barrier, epithelia develop specialized contacts, termed junctions. Junctions are classified according to four main functions: (a) anchoring junctions facilitate adhesion to other cells or the ECM and transmit physical forces, (b) occluding junctions form a tight connection between cells to generate an impermeable barrier, (c) channel-forming junctions connect the cytoplasm of adjacent cells for an exchange of small molecules and ions, (d) signal relaying junctions transmit signals among cells (Alberts et al., 2008).

1.2.3 Anchoring junctions coupled with actin filaments

Cell-cell contacts

Anchoring junctions that link cells mechanically with another are adherens junctions. Adhesion proteins span the membrane into the extracellular space to form contacts with proteins of opposing cells. These proteins belong to the cadherin superfamily. Via the outermost sub-domain, stabilized by Ca^{2+} , cadherins typically form hemophilic interactions with cadherin molecules of the same class. Cadherin molecules within the same cell cluster form patches consisting of multiple cadherin-cadherin bonds to enforce the connections (Alberts et al., 2008; Brasch et al., 2012).

The C-terminus of cadherins extends into the cytosol, where it connects to an entire protein machinery. Their direct binding partners are collectively termed catenins, among which are p120-catenin, β -catenin and γ -catenin, which associate with a variety of other molecules, such as cytoskeletal proteins and their regulators (Figure 1-5) (Meng and Takeichi, 2009). The connection to the actin cytoskeleton is important for the stability of adherens junctions as cell contacts dissociate upon actin depolymerization or upon loss of the proteins that connect actin filaments with cadherins (Ratheesh and Yap, 2012). The formation of adherens junctions is promoted by actin in two subsequent steps. It is suggested that actin brings juxtaposed membranes into proximity by the formation of filopodial, cadherin-rich extensions, which slide along each other when opposing cells make contact. Once initial contacts have been made, actin stabilizes the adherens junctions (Vasioukhin and Fuchs, 2001). In addition, cadherin-mediated cell contacts influence the morphology of the actin cytoskeleton by triggering its reorganization. Actin filaments and actin-binding proteins bundle into an adhesion belt localized at the borders of contacting epithelial cells (Bershadsky, 2004). The connection of the actin cytoskeleton of neighboring cells generates tension. Myosin motor proteins move actin filaments to contract or loosen the adhesion belt and

thereby modulate the tension in and between the cells (Alberts et al., 2008; Ouderkirk and Krendel, 2014).

Microtubules have been implicated in the modulation of cell-cell adhesion. Depolymerization of microtubules disrupts the integrity of adherens junctions (Waterman-Storer et al., 2000). Although microtubules do not concentrate at adhesion sites as actin does, they extend fibers towards adherens junctions with either end, plus or minus. Furthermore, the minus-ends of microtubules have been suggested to be involved in adherens junction assembly by an association with p120-catenin (reviewed in Meng and Takeichi, 2009). Recently, a study has unveiled that microtubules maintain phosphorylated p120-catenin and thereby keep it dissociated from E-cadherin, which leads to inhibition of the adhesiveness of E-cadherin (Maiden et al., 2016). However, microtubules have been reported to influence adherens junctions also by supporting the vesicular traffic of cadherin to the cell surface (Mary et al., 2002) and by influencing the local concentration of cadherin at the cell adhesion sites (Stehbens et al., 2006).

Cell-ECM contacts

The ECM is the principal extracellular component of all tissues. It consists of three classes of molecules: (1) structural (glyco-)proteins (i.e. collagens and elastins), (2) protein-polysaccharide complexes to embed the structural proteins (i.e. proteoglycans), and (3) adhesive glycoproteins to attach the cells to the matrix (i.e. fibronectins and laminins) (Alberts et al., 2008).

In epithelial tissues, the ECM organizes into the BM to determine cell polarity, to provide a scaffold for the epithelial cells and to connect the epithelial and the connective tissue mechanically. In addition, the BM influences a magnitude of cellular processes like cell survival, differentiation, proliferation and it serves as a scaffold for cell migration (Alberts et al., 2008). Epithelial cells as well as the underlying stromal cells synthesize and secrete proteins of the BM. The composition of the BM varies among the different tissues. In the mammary gland, for example, the BM is composed of fibronectin, laminin, type IV collagen and heparan sulfate proteoglycans (Richert et al., 2000).

The composition of the ECM of the connective tissue differs from the BM. It is synthesized by the stromal cells, mainly by fibroblasts. High amounts of glycosaminoglycan form hydrated gels. Embedded in this gel-like structures are collagen fibers, especially the fibrillar type I collagen (Alberts et al., 2008). Cells are able to remodel the ECM by degrading existing proteins and secreting new proteins into the extracellular space. This is an important feature to facilitate morphogenetic processes, in which cells have to rearrange spatially (i.e. following cell division) or have to migrate to a distinct location (reviewed in Page-McCaw et al., 2007).

Cells use different adhesion receptors to attach to the ECM. The most prominent molecules that make contact with the ECM are the family of integrin receptors. Like cadherins, integrins have a

relatively low affinity to their ligands, but a strong adhesion is facilitated by an accumulation of multiple such receptors at the cell surface (Alberts et al., 2008). Integrins have the ability to transmit signals along both directions across the membrane. Integrins form heterodimers that consist of an α - and β -subunit (reviewed in Humphries et al., 2006). Through conformational changes, integrin receptors switch between an inactive and active state. Active integrin receptors have high affinity to extracellular ligand binding and exhibit strong binding to their intracellular partners. Proteins that engage in the adhesion complex connect integrins to the actin cytoskeleton and induce its assembly and rearrangement (Figure 1-5). In addition, these proteins transmit signals into the cell that influence migration, survival, differentiation and motility (reviewed in Berrier and Yamada, 2007). The controlled turnover and establishment of adhesion complexes is necessary for cell migration. Either single cells or groups of cells perform cell migration. Collective cell migration is important for development, tissue organization, and plays a role in tissue repair and cancer. In the mammary gland for example, collective migration occurs during terminal end bud sprouting in branching morphogenesis (Friedl and Gilmour, 2009). For both, single cell as well as collective cell migration, the connection of the cells to the ECM via integrins is important to facilitate a forward movement (Ridley et al., 2003; Friedl and Gilmour, 2009; Frantz et al., 2010). Intracellularly, actin cytoskeleton remodeling and movement of actin filaments via myosins are the driving forces of pushing the cell over the substrate (Ridley et al., 2003). Microtubules are involved in cell migration by influencing the assembling, maintenance and disassembly of cell-ECM adhesion sites (Etienne-Manneville, 2013).

The turnover of cell-ECM adhesion promotes the activation of several signaling pathways (Vicente-Manzanares and Horwitz, 2011). An integrin-associated signaling molecule is the focal adhesion kinase (FAK). The canonical way of FAK activation is through adhesion of integrins to the substratum (Mitra et al., 2005). FAK contains multiple phosphorylation sites, of which the tyrosine (Tyr, Y) phosphorylation at position 397 within the kinase domain is well studied. This phosphorylation creates a binding site for several proteins such as Src and others (Mitra et al., 2005). Thus, FAK is involved in the regulation of a magnitude of cellular processes like cell migration, adhesion, polarity, proliferation and differentiation (Figure 1-5) (Millard et al., 2011). FAK influences cell proliferation in both, an integrin-dependent and integrin-independent manner. Integrin-mediated activation of FAK influences cell proliferation by activation of mitogen-activated protein kinases (MAPKs). Upon cell detachment from the substrate, pro-inflammatory signaling or stress signals such as chemical or oxidative stress, FAK dissociates from the adhesion complex and translocates into the cell nucleus, where it interacts with other proteins (i.e. p53) to influence cell proliferation (Lim, 2013). FAK promotes cell migration and invasion upon activation through integrins (Slack et al., 2001; Mitra et al., 2006) mainly by remodeling the actin cytoskeleton (Mitra et al., 2005). An opposing effect of FAK on cell migration is by modulating cell-cell interactions

(Yano et al., 2004). FAK transiently associates with cell-cell contacts and is required for the formation of adherens junctions by regulating Rho activity (Playford et al., 2008). Its involvement in multiple cellular processes and the fact that FAK is frequently overexpressed and active in malignant cells, makes FAK a potential target for cancer treatment (McLean et al., 2005; Tanjoni et al., 2010; Tancioni et al., 2015).

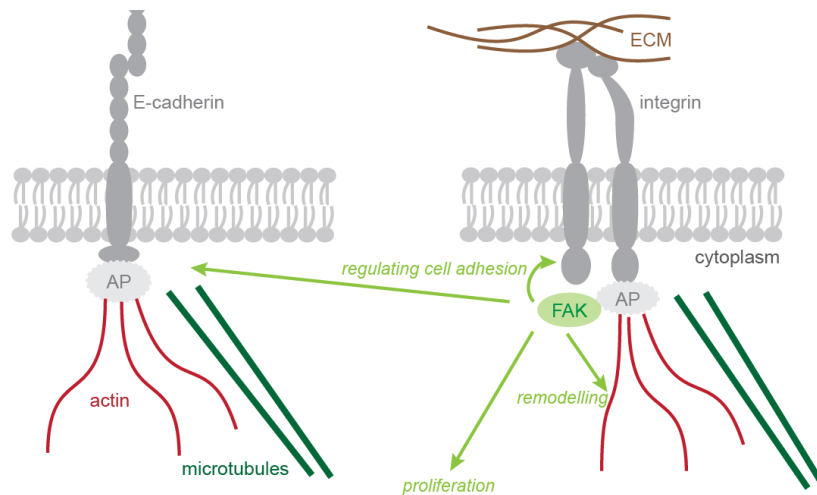


Figure 1-5 Schematic of epithelial anchoring junctions coupled with actin. Left: Cell-cell adhesion sites consist of transmembrane E-cadherin forming homophilic contacts with neighboring cells. Inside the cells, adaptor proteins (AP) bind E-cadherin and connect it to the actin cytoskeleton. Microtubules influence the adhesive capacity of

cadherins. Right: Cell-ECM adhesion sites consist of integrin receptors, which bind specific motifs in the ECM. Intracellularly, adaptor proteins (AP) bind integrin receptors and connect them to the actin cytoskeleton. Microtubules are involved in the turnover of cell-ECM adhesion sites. Integrin-matrix interactions activate FAK by phosphorylation. Active FAK influences cytoskeleton remodeling, regulates cell adhesion sites (to other cells and to the matrix) and is involved in cell proliferation and survival.

In a three-dimensional context, cells construct different types of cell-ECM adhesion, termed focal adhesion, fibrillar adhesion, and three-dimensional-matrix adhesion. These three types of cell-ECM adhesion engage the matrix-integrin-actin complex but differ in their morphology, their molecular composition and thus might control cell signaling differently (Cukierman et al., 2001; Yamada et al., 2003). FAK, for example, is highly tyrosine phosphorylated in focal adhesions, but less phosphorylated in fibrillar and three-dimensional-matrix adhesions (Yamada et al., 2003). Another example is the assembly of integrin receptors in the three adhesion types (Cukierman et al., 2001). This strongly indicates that integrin signaling can differ substantially in three-dimensional compared to two-dimensional environments.

1.2.4 The co-chaperone BAG3

The Bcl-2-associated athanogene (BAG) proteins are evolutionary highly conserved, implying an important biological role in cell physiology. BAG proteins are nucleotide exchange factors and share cell survival-promoting activity under stress conditions. Six homologues (BAG1-6) exist in the human and murine context, while the focus will be on BAG3.

BAG3 (also known as Bis and CAIR-1) has two isoforms with a molecular weight of 75 kDa and 40 kDa. While the short isoform mainly localizes to synaptosomes, the full-length isoform is

predominantly cytoplasmic. Full-length BAG3, from now on referred to as BAG3, consists of four exons. It carries a proline-rich domain, which facilitates interaction with Src homology (SH3) domain-containing sequences. At its C-terminal region, it has a BAG domain, which is conserved among all BAG proteins. This domain facilitates binding to the ATPase domain of Hsc70 or Hsp70. On its N-terminus, BAG3 has a tryptophan-tryptophan domain, which facilitates binding to proline-rich protein sequences. A prominent binding partner of BAG3 is Bcl-2, thus BAG3 is regarded as an anti-apoptotic protein. The modular composition of BAG3 facilitates a plethora of interactions with other proteins than Bcl-2. Hence, BAG3 is involved in several key signaling pathways in the cell, making it a protein with wide regulatory capacities, not only in apoptosis, but also in many other biological and cellular processes like development, arrangement of the cytoskeleton, and autophagy (reviewed in Behl, 2016).

In many cell types like epithelial cells, BAG3 expression can be induced by a variety of stressors (Behl, 2016). An upregulation has been shown for several types of tumors, including pancreatic cancer (Liao et al., 2001), thyroid carcinoma (Chiappetta et al., 2007), ovarian carcinoma (Suzuki et al., 2011), lung carcinoma (Chiappetta et al., 2014), and breast cancer (Nourashrafeddin et al., 2015).

In vitro experiments have confirmed that an overexpression of BAG3 inhibits both, spontaneous and drug-induced apoptosis, and that a BAG3 knockdown enhances apoptosis (reviewed in Rosati et al., 2011). Recently, BAG3 expression has been analyzed in bovine mammary gland development and has been found to be increased during the lactation phase compared to the late pregnancy phase. It has been suggested that this and the co-expression of other pro-survival markers maintains alveolar function during the lactation phase (Paten et al., 2015).

Besides the pro-survival function, BAG3 is associated with the regulation of adhesion and migration, and thereby contributes to invasion during tumorigenesis and metastasis of malignant tumors (Kassis et al., 2006; Iwasaki et al., 2007; Suzuki et al., 2011). It has been shown in various cancer cells that BAG3 overexpression increases cell migration and invasion, while a knockdown reduces cell motility (Iwasaki et al., 2007; Suzuki et al., 2011; Fontanella et al., 2010; Shi et al., 2016). However, the effect of BAG3 on cell motility is controversial as other studies have reported that BAG3 knockdown promotes cell migration and epithelial-mesenchymal transition (EMT)-like processes (Meng et al., 2014). Another study has reported that that BAG3 overexpression results in poor migration of breast carcinoma cells by reducing the formation of focal adhesions in a FAK-dependent manner (Kassis et al., 2006).

Via its WW domain and proline-rich domain, BAG3 is able to interact with a variety of proteins that are involved in signal transduction and are associated with the cytoskeleton (Pawson and Schlessinger, 1993; Bork and Sudol, 1994). BAG3 has been shown to regulate cell motility and actin cytoskeletal integrity in both, cancerous and non-cancerous cells via multiple interaction

partners like Rho GTPases (Iwasaki et al., 2007, 2010), FAK (Iorio et al., 2015; Antonietti et al., 2017), chaperonins (Fontanella et al., 2010) and transcriptional regulation (Kassis et al., 2006, 2009). From this, the question raises, whether BAG3 modulates cell motility under normal, physiological circumstances.

More recently, BAG3 has been demonstrated to be crucial for tissue integrity of skeletal muscles. In these cells, BAG3 acts through tension-induced chaperone-assisted selective autophagy (CASA) (Ulbricht et al., 2013a, 2013b). The CASA protein machinery is associated closely with the actin cytoskeleton, especially with actin-linking proteins like filamin. Filamin is a flexible linker between actin filaments. Upon tension, filamin unfolds and may get damaged and thus has to be degraded and replaced (Ulbricht et al., 2013b). BAG3 induces the complex formation of the chaperones HspA8/Hsc70 and HspB8/Hsp22, and the Hsc70-associated ubiquitin ligase CHIP/Stub1 (Arndt et al., 2010). BAG3 recruits the CASA machinery to the damaged proteins and facilitates their autophagic degradation (Ulbricht et al., 2013a). Moreover, BAG3 induces the transcription of filamin by activation of the transcription activators YAP and TAZ (Ulbricht et al., 2013b). Yet, it remains elusive whether the activity of the CASA machinery is restricted to muscle tissue or whether it becomes active in other tissue, which are exposed to extreme and spontaneous stresses, like, for example the mammary gland during post-lactational regression.

1.3 Three-dimensional cell culture

Three-dimensional cell culture offers an alternative *ex vivo* approach. Other than two-dimensional cell culture on plastic or glass surfaces, it provides an environment where cells reside and behave in a more close-to-natural condition. Thus, three-dimensional cell cultures enhance the physiological relevance of performed experiments (Pampaloni et al., 2007).

Three-dimensional cell culture comes in different flavors often classified by the test system, using either scaffold-based or scaffold-free techniques. For example, cysts (Debnath et al., 2003) or organoids (Lancaster and Knoblich, 2014; Broutier et al., 2016) are frequently produced by seeding single cells or tissue-like aggregates sparsely into or on top of a hydrogel matrix, where they self-organize, form lumen and functional units. Another example are multicellular tumor spheroids, which are often, but not exclusively (Semino et al., 2003), cultured in an adhesive-free environment. Different culturing techniques can be used to produce spheroids, i.e. hanging-drop, low adhesion U-well shaped scaffolds (also referred as liquid-overlay culture), or rotating bioreactors (Pampaloni et al., 2007; Weiswald et al., 2015). In the following sections, I will focus on cellular spheroids as a three-dimensional cell culture model.

1.3.1 Cellular spheroids

Spheroids are aggregates that can be formed from different cell types - cell line-based as well as primary cell-based.

Multicellular tumor spheroids, for example, resemble characteristics of *in vivo* tumor tissue very well. They develop a concentric layering with zones defined as proliferative, quiescent and necrotic (Bell et al., 2001; Sutherland et al., 1986). When spheroids reach a certain size, an inhomogeneous supply of the cells with nutrients and oxygen eventually leads to a reduction of cell survival in the core of the spheroid (Groebe and Mueller-Klieser, 1996; Nichols and Foster, 1994; Mueller-Klieser, 1984). This zone formation is frequently found in avascular tumors *in vivo*. Thus, multicellular tumor spheroids serve well as a model system to study tumor biology.

Apart from studying tumor or cancer biology, spheroids can serve for a better understanding of tissue integrity when non-tumorigenic cells are used. Apart from the zone formation namely, cellular spheroids exhibit ECM protein synthesis. Collagens, fibronectin, laminin, and glucosaminoglycans are just a few examples for matrix proteins, which have been found to be synthesized in spheroids (Nederman et al., 1984; Bjerkvig et al., 1989). Yet, it is not clear how cells in spheroids organize the expression and rearrangement of ECM over time. It is not known whether the cells rearrange the ECM to generate, for example, a physical or morphological barrier.

Following spheroid maturation, structural characteristics develop, which resemble *in vivo*-like structures. Glandular cells, such as mammary epithelial cells or colon adenocarcinoma cells, have often the capability to form polarized pseudo-glandular structures within the spheroids (Sutherland, 1988; Estrada et al., 2016). Further, it has been shown that cells within spheroids formed from primary cells or cell lines have the capability to undergo functional differentiation. Hepatocytes grown as spheroids differentiate to form functional bile canaliculi (Abu-Absi et al., 2002). In the context of the mammary gland, spheroids generated from primary murine mammary epithelial cells have been directed successfully to lactogenic differentiation in a matrix-free environment with PRL as inducing hormone (Timmins et al., 2005). It is not known whether mammary epithelial cell lines are able to undergo lactogenic differentiation when grown as spheroids. Most mammary epithelial cell lines require co-cultivation with other cell types or exogenously added ECM, and only few cell lines such as HC11 (Ball et al., 1988) or KIM-2 (Gordon et al., 2000) cells have been shown to differentiate without these factors grown as two-dimensional cell cultures.

1.3.2 Spheroid formation

Recent studies mainly explore the properties of mature spheroids - once they are formed. The dynamic processes that drive the self-assembly of isolated cells to form a spheroid are not intensively studied. However, they provide information about important biological processes such

as adhesion. The contribution of proteins in the contact formation of cells can be investigated with an analysis of spheroid formation. The conditions (i.e. a non-adhesive environment) generate a system devoid of external bias. Further, time-lapse imaging provides a high temporal resolution of the spheroid formation process. It reveals the involvement of molecules, cell movement and the dynamics of reorganizing cells.

Investigation of the participation and timing of integrins and cadherins in spheroid formation of human hepatoma cell lines using an image-based quantitative approach have shown that the formation process is complex and can be described as a multiphase process in which the adhesion molecules are of varying importance. Spheroid formation consists of distinguishable phases. In the initial phase, which is referred to as the aggregation phase, isolated cells begin to form a loose aggregate. The second phase is the compaction phase, in which the aggregated cells form a compact spheroid, and the third phase is the growth phase, in which cell proliferation results in spheroid growth (Enmon et al., 2001; Lin et al., 2006). Lin and colleagues have described an intermediate phase between the aggregation and compaction phase. It describes as a delay of compaction probably due to the rearrangement of E-cadherin at the cell surfaces (Lin et al., 2006). It has been shown that the majority of the studied cell lines form compact spheroids sufficiently when either E-cadherin or N-cadherin is expressed. Garg and colleagues have shown the role of N-cadherin clustering in junction stabilization with a spheroid-based formation assay and a computational approach. Cells lacking the ability to cluster cadherin molecules at the cell surface form contacts with neighboring cells but this interaction is weak and already formed connections tend to break (Garg et al., 2015). Integrins have been found to be important in spheroid formation of several cell lines, acting complementary to the formation process even without the involvement of cadherins (Casey et al., 2001; Ivascu and Kubbies, 2007). Saias and colleagues have reported different results. They have shown that integrins are dispensable for the formation of colon cancer spheroids. While an inhibition of integrin activity with RGD-containing peptides does not affect the formation process, inhibition of E-cadherin slows down spheroid formation without perturbing it. Furthermore, they have shown that other adhesion molecules contribute to spheroid formation (i.e. desmosomal DSG2 and DSC2) (Saias et al., 2015). A few studies have aimed to investigate the role of the cytoskeleton in spheroid formation. Tzanakakis and colleagues have concluded that an intact actin network is required for spheroid self-assembly (Tzanakakis et al., 2001). Opposing opinions exist for the microtubule network (Tzanakakis et al., 2001; Yoshii et al., 2011).

Knowledge to which extent other molecules contribute to the formation of three-dimensional cell aggregates barely exists. However, how cells organize into three-dimensional cluster is of high importance to identify the factors contributing to tissue integrity, destabilize cell contacts and induce cell motility to promote severe conditions such as cancer.

1.3.3 Physical forces applied to spheroids

The work with spheroids allows investigating the influence of physical forces on tissue integrity. Previous studies have investigated the role of mechanical stress on spheroid morphology, cell proliferation and apoptosis predominantly in the context of cancer research. Different approaches exist to apply pressure on spheroids (Loessner et al., 2013; Delarue et al., 2014). An approach to apply compressive stress on spheroids is their embedment in hydrogels of varying stiffness (Sieminski et al., 2007; Helmlinger et al., 1997; Cheng et al., 2009; Loessner et al., 2013; Paszek et al., 2005). A second approach is the induction of compressive stress by increased osmotic pressure. Individual spheroids are incubated inside a dialysis bag and osmotic pressure is induced by the addition of dextran. Long-term compressive stress reduces or inhibits cell proliferation and induces apoptosis in colon and breast carcinoma cells (Montel et al., 2011, 2012; Delarue et al., 2014). A third approach of mechanical perturbation is to confine spheroid growth by a tube-like silicone device. Spheroids from colorectal cancer cells, which have been grown inside the device, adopt a rod-like shape. The confined growth conditions induce mitosis but the cells show spindle defects and enter mitotic arrest (Desmaison et al., 2013). Confinement of spheroid growth can also be applied by an encapsulation in alginate shells. It has been shown that spheroids generated from mouse colon carcinoma cells increase cell density, alter the cellular organization, restrict cell proliferation to the outer rim of the spheroid and increase apoptosis in the spheroid center upon compressive stress (Alessandri et al., 2013).

Although spheroids have been shown to address mechanical perturbation of aggregates well, most studies have focused on the forces present in tumor development and how they influence tumor growth. How tissues react upon rapid mechanical forces is not well documented, but it is suggested that forces are fundamental during diverse developmental processes. One outstanding example is the mammary gland, which passes postnatally through different developmental stages. Increased physical forces accompany the transition between these stages. To which extent these forces affect cell fate in the mammary gland is largely unknown, but might be studied by the compression of spheroids.

1.4 Advanced light microscopy

1.4.1 Three-dimensional specimens require appropriate imaging systems

In numerous research areas such as developmental biology, clinical research and cell biology, three-dimensional model systems are used to examine scientific questions. These model systems vary in size and complexity, ranging from monoclonal cysts over multicellular spheroids, organoids, and organs to whole animals. Biological samples are opaque and they scatter light, thus light microscopy approaches become more challenging with increasing sample size and complexity

(Huisken et al., 2004). Consequently, high quality information about the inner regions of such specimens cannot be obtained.

To comply the needs of complete spatial and temporal resolution of these three-dimensional specimens, light microscopy has rapidly developed within the past decades. In the following, I will give a conceptual outline of confocal laser scanning microscopy (CLSM) and light sheet-based fluorescence microscopy (LSFM).

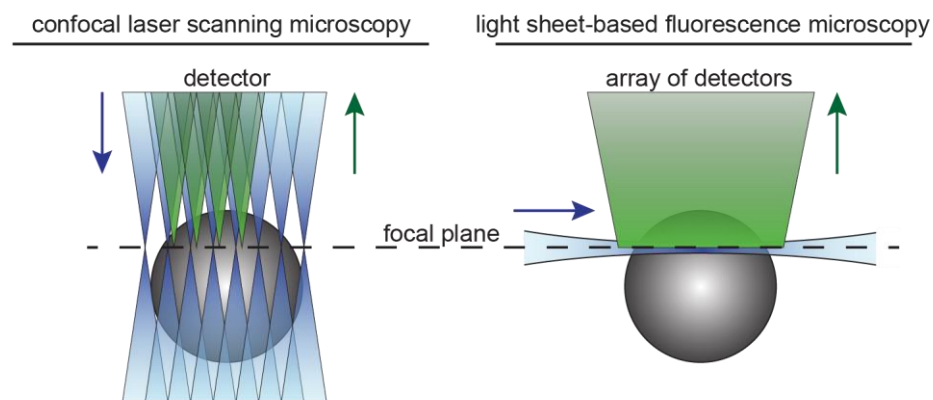


Figure 1-6 Comparison between confocal laser scanning microscopy (CLSM) and light sheet-based fluorescence microscopy (LSFM). In CLSM, the illumination and detection paths are arranged on the same axis. In LSFM, both paths are separated and orthogonally arranged to another. This allows the illumination of the part of the specimen, which is situated inside the focal plane. The point-detection in CLSM requires gradual scanning of the sample. A LSFM setup is equipped with a chip-containing camera, recording the entire focal plane at the same time.

Confocal laser scanning microscopy (CLSM)

In CLSM (and in other techniques, i.e. wide-field epifluorescence microscopy), the same objective lens is used for the illumination and the collection of the emitted fluorescent light (Stelzer, 2015). This results in the excitation of all fluorophores in a specimen. While wide-field epifluorescence microscopy techniques feature a point-illumination, the advancement of CLSM is a point-illumination and a point-detection. The latter one is an adjustable aperture, which facilitates the detection of only in-focus light (within the focal plane) by discriminating against out-of-focus light. However, this feature makes a time-consuming scanning process indispensable, in which the specimen is recorded in a step-wise manner (pixel by pixel) to obtain a whole image of the field of view (FOV) (Figure 1-6).

CLSM as well as other epifluorescence microscopy techniques combine the illumination and detection paths. Thus, all fluorophores in the specimen along the entire axial direction are excited although only the emitted light of the fluorophores in the focal plane are collected (Figure 1-6). This accounts for photo bleaching and, in living specimens, for photo toxicity (Stelzer, 2015).

Light sheet-based fluorescence microscopy (LSFM)

To cope with the challenges of confocal fluorescence microscopy, Ernst Stelzer and colleagues developed and later improved LSFM (Huisken et al., 2004; Keller et al., 2008, 2010).

LSFM provides high imaging speed, good penetration, low photo bleaching and photo toxicity, and the possibility to record multi-view image data to improve the axial resolution. This makes LSFM well suited for stable imaging of large and living specimens over a long period of time (Keller et al., 2008; Stelzer, 2015). This is achieved by the separation of the illumination and detection paths by an orthogonal alignment of the objective lenses. A camera allows the simultaneous detection of the entire focal plane (Pampaloni et al., 2013). A two-dimensional image of the focal plane at a certain position within the specimen can be recorded. To generate a three-dimensional dataset, the sample is moved with respect to the detection objective (along the z-axis) through a thin cuboid of laser light (Figure 1-6), thereby collecting additional single planes to produce an image z-stack. Thus, LSFM provides optical sectioning and has a true axial resolution (Huisken et al., 2004).

Spatial resolution itself not only consists of the within the focal plane lying lateral resolution, which is in a LSFM identical to a conventional fluorescence microscope, but also of the axial (along the optical axis, z) resolution. In an optical system, such as the wide-field fluorescence microscope, the axial resolution is considerably worse than the lateral resolution. In LSFM, the illumination and detection paths are separated and aligned orthogonally. This results in a three-dimensional point spread function (PSF), which has an axial limit determined by the thickness of the illuminating beam (Huisken et al., 2004; Keller et al., 2008). The axial resolution can be further improved by multi-view image fusion of image stacks along different view angles (section 1.4.2.).

Current developments in LSFM aim to improve the illumination to increase resolution, imaging depth and image quality. Examples are coherent structured illumination (Chang et al., 2017), Bessel beams (Fahrbach and Rohrbach, 2010), and two-photon illumination (Truong et al., 2011).

1.4.2 The limitations of imaging large specimens with LSFM

In LSFM, the image quality for a region of interest within the specimen depends on the location of the region relative to the illumination and the detection objective. The longer the distance of the region from the objective lenses, the longer the distance the excitation or emission light has to travel in order to reach the region of interest (or the detection objective in case of emission light). The longer the distance, the more the impact of light scattering and absorption by the specimen (Figure 1-7a) (Huisken et al., 2004).

In LSFM, two approaches exist to improve the image quality throughout the specimen: (1) multi-view image fusion and (2) optical clearing. Both accompany several advances and drawbacks, which are discussed in the following two sections. Although the main features of these two methods

are well documented, it has to be solved which approach is best suited for a specific scientific question when multicellular spheroids are used.

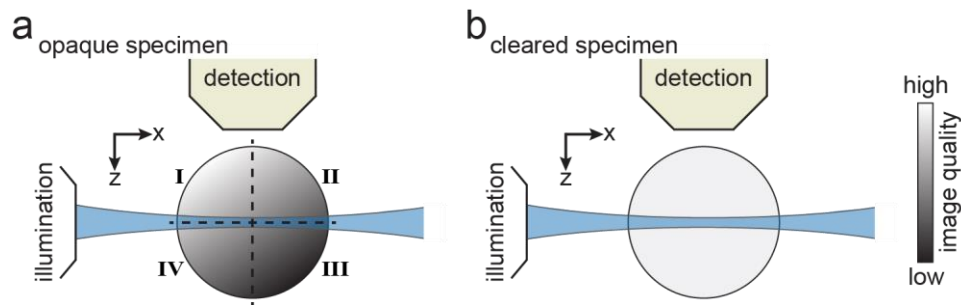


Figure 1-7 LSFM image quality can be improved with multi-view image fusion and optical clearing. (a) LSFM provides high image quality in the region, which is the closest to the illumination and detection objective (quadrant I). Regions farther away from the illumination and detection objective have decreased image quality due to the opacity of the specimen (quadrant II-IV). Image fusion combines the information of multiple view angles in one three-dimensional image. (b) Optically cleared specimens provide good image quality throughout the entire specimen. Transparency reduces light scattering and enhances contrast.

Multi-view image fusion

LSFM allows the rotation of the specimen around the y-axis. Therewith, image stacks from multiple view can be recorded and fused to obtain a data set with virtually isotropic resolution. This process is referred to as multi-view image fusion (Swoger et al., 2007).

To obtain a correctly fused image, algorithms use characteristics within the image stacks to compute the transformation matrix. For image reconstruction, potential registration approaches are intensity-based (Huisken et al., 2004; Preibisch et al., 2010; Swoger et al., 2007), segmentation-based (Keller et al., 2008), wavelet-based (Rubio-Guivernau et al., 2012) and fluorescent bead-based (Preibisch et al., 2010).

The bead-based registration uses landmarks (i.e. sub resolution fluorescent beads) in the images. It is fast, independent of the sample and allows an automatic evaluation of the registration error. However, the position of the fluorescent beads has to remain stable during the acquisition time, which often requires an embedment into a solid medium. Recently, the Stelzer laboratory has developed different techniques to uncouple bead and specimen mounting to move away from the embedment of the specimen into a rigid gel column (Strobl et al., 2015, 2017). Recently, the bead-based registration has also been improved by conjunction with subsequent multi-view deconvolution (Preibisch et al., 2014). All processes of bead-based registration, fusion and simultaneous deconvolution are implemented in the *ImageJ* plugin *Multiview Reconstruction*.

Optical clearing

Rendering a specimen transparent is referred to as optical clearing, thereby increasing light depth penetration and reducing light scattering, the principal cause of opaqueness in tissues (Figure 1-7b). Light scattering usually occurs at the transition between media of different refractive indices (RIs).

The refractive indices within tissues vary according to compartmentalization and their biomolecular composition (i.e., cytoplasm RI 1.35-1.37, cell nuclei RI 1.37-1.43, and fat RI >1.44 (Tuchin, 2015)). Transparency is achieved by matching the refractive index of the surrounding medium with that of the specimen and generating refractive uniformity throughout the specimen itself. Within the past decade, a magnitude of optical clearing techniques have been developed and improved.

The simplest way to obtain transparency is the adaption of the refractive index of the surrounding medium to that of the cellular component with the highest refractive index (i.e. lipids). This is achieved by replacing extracellular water with solutions of high refractive indices (D'Esposito et al., 2015; Seo et al., 2016). Other approaches remove the lipids from the specimens. They strongly vary in their complexity regarding applicability, duration and cost. To achieve the removal of lipids from the specimen, one fraction of procedures uses water-based agents such as denaturants or detergents (Hama et al., 2011; Susaki et al., 2014), while the other fraction uses organic solvents. Clearing methods based on organic solvents is for example Murray's clear. These exhibit strong clearing competence, but the use of harmful chemicals makes them less attractive. In addition, the morphology is harmed due to the dehydration of the specimens (Seo et al., 2016). Murray's clear uses an alcohol-based dehydration, which can be performed either with methanol or with ethanol, followed by an incubation in a mixture of benzyl alcohol and benzyl benzoate (BABB) to achieve transparency (Dent et al., 1989; Dodt et al., 2007). Although the general morphology seems to be conserved, the alcohol-based dehydration reduces specimen size dramatically. Further, BABB as well as the hydrophobic conditions harm fluorescent proteins making this approach incompatible with the use of fluorescent proteins (Seo et al., 2016).

Recently, sophisticated methods have been developed, which hybridize the specimen in a hydrogel before delipidation and refractive index matching. The delipidation is achieved by incubation in a solution with high concentration of the strong ionic detergent sodium dodecyl sulfate (SDS) (Chung and Deisseroth, 2013; Tomer et al., 2014).

1.4.3 The limitations of immunofluorescence staining in large specimens

Immunofluorescence is a technique, which is widely used to study protein distribution *in situ* (Coons and Kaplan, 1950). Antibodies of high epitope specificity enable a labeling of proteins of interest. By combining different antibodies and fluorophores, multiple labeling is possible. Classically, antibody staining measures the end-point of an experiment since the sample has to be fixed in order to allow the antibody to enter the cells (unless an extracellularly exposed epitope is labeled). Novel promising methods introduce heavy-chain antibodies, which were found in *Camelidae sp.* and shark, to target and label epitopes in living cells (Rothbauer et al., 2006).

Frequently, antibodies of the IgG class are used in immunofluorescence. These antibodies are relatively large having a molecular weight of approximately 150 kDa. Further, antibodies carry

charged amino acid residues, which may affect the diffusion of the antibody. Consequently, immunofluorescence staining of large specimens is challenging. Only cells at the surface are well labeled while cells in deeper regions show a poor fluorescence signal. Thus, providing an insight into the internal morphology of large specimens such as spheroids, traditional preparation techniques such as physical sectioning of paraffin-embedded or frozen specimens have been used (Brandtzaeg, 1998). However, upon this procedure, a reconstruction of the three-dimensional information is challenging.

So far, the quality of the immunofluorescence staining is rated subjectively by determining the specificity of the staining and according to the brightness of the fluorescence signal. However, this does not contribute to standardized practice and further produces an increased variability of the data. Data homogeneity is of special importance for downstream approaches such as quantitative analysis (Mathew et al., 2015; Schmitz et al., 2017). A previous study has tackled the issue to immunolabel spheroids *in toto*. Here, spheroids from colon cancer cells with diameters between 120 μm to 150 μm have been used. The researchers have aimed to obtain a homogeneous stain by rating the images qualitatively. Further, they have used fluorescent activated cell sorting (FACS) of dissociated spheroids to analyze the amount of labeled cells (Weiswald et al., 2010). However, tearing cells out of their spatial context is not the favorable way to evaluate a method that has been performed in a three-dimensional aggregate context. Instead, the future goal in three-dimensional cell biology and histology is to develop a standardized, applicable and objective quality evaluation.

1.5 Main contributions of this thesis

To understand tissue integrity, three-dimensional cell cultures and the mammary gland were chosen as models. In this context, the proteins involved in the two main processes (1) cell survival and growth, and (2) cell adhesion to cells and the ECM were studied.

The questions addressed in this thesis are:

- Are multicellular spheroids from mammary epithelial cells a suitable model system?
- To which extent can spheroids be immunolabeled *in toto* and how can the result be evaluated?
- Advances optical clearing multi-view image fusion applied to spheroids?
- Does BAG3 play a certain role in mammary gland development?
- In which cellular processes is BAG3 involved in mammary epithelial cells?
- What is the influence of mechanical stress on tissue integrity – on the morphological level and on the level of autophagy and apoptosis?
- What are the benefits of a spheroid formation assay to investigate cellular processes?
- What is the contribution of cytoskeletal, cytoskeleton-associated proteins and BAG3 in spheroid formation?

2 Materials and Methods

2.1 Materials

2.1.1 Chemicals

Table 2-1: List of chemicals used in this thesis.

name	manufacturer
(-)- blebbistatin	Sigma Aldrich
2,2'-thiodiethanol	Sigma Aldrich
2-mercapto ethanol	Carl Roth
2-propanol	Carl Roth
5-brom-4-chlor-3-indoxyl- β -D-galactopyranosid	Carl Roth
Acrylamide, 4K solution, 30% 29:1	Applichem
Agarose	Invitrogen
Agarose, low melt	Carl Roth
Albumin, fraction V	Applichem
Ampicillin	Carl Roth
APS	Applichem
Benzyl alcohol	Carl Roth
Benzyl benzoate	Merck
Chloroform	VWR
Collagen type I, bovine	ThermoFisher, Gibco
DABCO	Carl Roth
DEPC H ₂ O	Carl Roth
Dexamethasone	Sigma-Aldrich
DMSO	Carl Roth
dNTPs	Invitrogen
EDTA	Carl Roth
EGTA	Carl Roth
EtOH 100%	Sigma-Aldrich
EtOH 99.9%	Sigma-Aldrich
F-12 (HAM) medium	ThermoFisher, Gibco
FBS, Lot: 41G3420K	ThermoFisher, Gibco
Fibronectin (bovine plasma)	Sigma Aldrich
Geltrex	ThermoFisher, Gibco
Gentamicin	Sigma Aldrich
Glycerol	Carl Roth
Glycine	Carl Roth
Goat serum	ThermoFisher
H ₂ O ₂ 30%	VWR
HCl	Carl Roth
Hellmanex® II	Hellma Analytics
HEPES	Carl Roth
Insulin, human	Sigma Aldrich
IPTG	Carl Roth
KCl	Carl Roth

L-glutamine	ThermoFisher, Gibco
Luminol	VWR
mEGF	Peptotech
Methylcellulose	Sigma Aldrich
MetOH	Carl Roth
MgCl ₂	Carl Roth
Mowiol 4-88	Carl Roth
NaCl	Carl Roth
NaOH	Fluka
NP-40	Fluka
Nucleotides (dATP, dCTP, dGTP, dTTP)	ThermoFisher
Opti-MEM	ThermoFisher, Gibco
Paraformaldehyde	Sigma Aldrich
Para nitroblebbistatin	Opto Pharma
PBS buffer	ThermoFisher, Gibco
p-coumaric acid	Sigma Aldrich
Penicillin/Streptomycin	ThermoFisher, Gibco
PF-573228	Sigma Aldrich
phosStop	Roche
Prolactin, sheep pituitary	Sigma-Aldrich
Protease inhibitor cocktail	Sigma-Aldrich
RPMI 1640 medium	ThermoFisher, Gibco
Semi skimmed milk powder	Sigma Aldrich
Silicone SF33	Silikonfabrik.de
Sodium acetate	VWR
Sodium deoxycholate	Fluka
Sodium dodecyl sulfate	Carl Roth
TEMED	Carl Roth
Tetraspeck microspheres 1 µm	ThermoFisher
Tris	Carl Roth
Triton X-100	Carl Roth
Trypan blue 0.4%	Sigma Aldrich
Tween 20	Carl Roth

2.1.2 Enzymes

Table 2-2 List of enzymes used in this work.

name	manufacturer, catalogue number
Accutase	ThermoFisher, Gibco
Phusion Polymerase	New England Biolabs, <i>M0530</i>
Restriction enzymes	New England Biolabs
T4 DNA ligase	New England Biolabs, <i>M0202</i>
Taq DNA polymerase recombinant	ThermoFisher, <i>10342020</i>

2.1.3 Special devices and consumable materials

Table 2-3 List of special devices and consumables.

description	manufacturer
blotting chamber	Bio-Rad
cold plate	EG1150 C Cold Plate, Leica Biosystems
electrophoresis chamber, nucleic acids	Homemade from EMBL manufacturing shop
electrophoresis chamber, proteins	Mini-PROTEAN tetra electrophoresis system, Bio-Rad

embedding	Paraffin Embedding Station EG1140H, Leica Biosystems
filter	0.2 μm pore-size, Millipore
gel documentation system	Gel Stick "Touch", Intas
glass rod 200 μm	Hilgenberg, catalogue number 7347701
glass rod 300 μm	Hilgenberg, catalogue number 7347705
microplate photometer	Infinite M200, TECAN
microscope, confocal	LSM 780, Zeiss
microscope, light sheet-based	mDSLIM
microscope, wide-field	Axiovert CFL 40, Zeiss Axio Observer.Z1, Zeiss
microtome	RM2235, Leica Biosystems
nano-photometer	P300, Implen
PCR cycler	peqSTAR 96 Universal, Peqlab CFX-96 detection system, Bio-Rad
pH meter	Orion 3, Thermo Scientific
polypropylene tubes	0.2 ml, 0.5 ml, 1.5 ml, 2 ml, Eppendorf and Sarstedt
stereo microscope	SteREO, Zeiss
Western blot documentation system	Chemo Cam Imager, Intas

2.1.4 Buffers and solutions

Table 2-4 List of homemade buffers and other solutions.

name	ingredients
APS 10%	10% [w/v] ammonium persulfate in ddH ₂ O, store in dark at 4°C
BABB	1:2 benzyl alcohol : benzyl benzoate
Blocking solution (immunofluorescence)	0.1% [w/v] BSA, 0.2% [v/v] Triton X-100, 0.05% [v/v] Tween-20, 10% [v/v] goat serum in PBS
Blocking solution (Western blot)	5% [w/v] BSA in TBS-T or 5% [w/v] skimmed milk powder in TBS-T
DNA loading buffer (5x)	50% [w/v] sucrose, 0.25% [w/v] bromophenol blue, 0.25% [w/v] xylene cyanol
EDTA 0.5 M pH 7.6	0.5 M EDTA in ddH ₂ O, adjust pH to 7.6 with 37% HCl and/or 10 N NaOH
ECL solution	440 μl p-coumaric acid, 1 ml luminol, 100 mM Tris-HCl pH 8.5, add ddH ₂ O up to 200 ml, store in dark at 4°C add 0.5 $\mu\text{l}/\text{ml}$ 19.2% H ₂ O ₂ just prior to use
Citrate buffer 10 mM pH 6	10 mM sodium citrate, 0.05% [v/v] Tween-20, add ddH ₂ O to 1 l, adjust pH 6 with 1 N HCl, store at 4°C
HBS (2x)	281 mM NaCl, 100 mM HEPES, 1.5 mM Na ₂ HPO ₄ , pH 7.12, sterile filtered
RIPA buffer	0.5% [w/v] sodium deoxycholate, 1% [v/v] NP-40, 0.1% [w/v] SDS, 1 mM EDTA in PBS, filter sterile and store at 4°C
Mowiol	2.4 g Mowiol 4-88, 25 mg/ml DABCO, 6.97 g glycerin (86%), 5.03 ml ddH ₂ O
PBS (10x)	1,37 M NaCl, 26 mM KCl, 81 mM Na ₂ HPO ₄ , 15 mM KH ₂ PO ₄ , in ddH ₂ O, adjust pH 7.4 with HCl

Transfer buffer for nitrocellulose membranes (Western blot)	10% [v/v] MetOH, 25 mM Tris-HCL pH 8.8, 150 mM glycine
Paraformaldehyde fixation solution	4% [w/v] paraformaldehyde in PBS, pH 6.9
SDS-PAGE running buffer (1x)	25 mM Tris-HCl, 190 mM glycine, 0.1% [w/v] SDS
Sodium acetate 3 M pH 5.2	3 M sodium acetate, adjust pH to 5.2 with 96% acetic acid, sterile filtered and stored at 4°C
STET buffer	0.5% [v/v] Triton X-100, 50 mM EDTA, 8% [w/v] sucrose, 50 mM Tris-HCl pH 8.0, sterile filtered and stored at 4°C
TAE buffer (10x)	0.4 M Tris base, 0.2 M glacial acetic acid, 30.01 M EDTA-Na ₂ , in ddH ₂ O, pH 8.5
TBS buffer (1x)	150 mM NaCl, 10 mM Tris-HCl pH 7.5
TBS-T buffer	0.1% [v/v] Tween-20
Tris-HCL 0.62 M pH 6.9	0.62 M Tris in ddH ₂ O, adjust pH 6.9 with HCl
Tris-HCl 1 M pH 7.5	1 M Tris in ddH ₂ O, adjust pH 6.9 with HCl
Tris-HCl 1.88 M pH 8.8	1.88 M Tris in ddH ₂ O, adjust pH 6.9 with HCl

2.1.5 Commercial kits and products

Table 2-5: Commercially available kits and products.

name	manufacturer, catalogue number
CellTiter 96 Aqueous One Solution Cell Proliferation Assay (MTS)	Promega, G3580
DNeasy Blood and Tissue	Qiagen, 69504
Gene Ruler DNA ladder mix	Thermo Scientific, SM0331
Lipofectamine RNAiMax	Life Technologies, 13778030
Maxima First Strand cDNA Synthesis Kit for qPCR	Thermo Scientific, K1642
NucleoBond Xtra midi	Macherey-Nagel, 740410
NucleoSpin DNA prep (mini)	Macherey-Nagel, 740588
NucleoSpin Gel and PCR clean-up	Macherey-Nagel, 740609
NucleoSpin RNA	Macherey-Nagel, 740955
PageRuler pre-stained protein ladder	Thermo Scientific, 26616
Roti-Gel stain	Carl Roth, 3865.1
Roti-Load 1	Carl Roth, K929.1
Roti-Quant 5x Bradford	Carl Roth, K015.1
TaqMan Gene Expression Master Mix	ThermoFisher, 4369016
TaqMan Gene Expression Assay BAG3	ThermoFisher, Mm00443474_m1
TaqMan Gene Expression Assay filamin	ThermoFisher, Mm01187533_m1
TaqMan Gene Expression Assay c-Fos	ThermoFisher, Mm00487425_m1
TaqMan Gene Expression Assay Rpl13a	ThermoFisher, Mm01612987_g1
TRIzol® Reagent	Thermo Scientific, 15596018

2.1.6 Plasmids

Table 2-6 Plasmids, which were already available or purchased.

construct	description	vector backbone	reference
pBAG3sgRNACrispR/Cas9-T1	sgRNA BAG3 murine targeting TTT GAT CTC CCA GCC CG	pLenti-U6-sgRNA-SFFV-Cas9-2APuro	ABM
pBAG3sgRNACrispR/Cas9-T2	sgRNA BAG3 murine targeting GGA GCT CCC CCT ATA TG	pLenti-U6-sgRNA-SFFV-Cas9-2APuro	ABM

pBAG3sgRNACrispR/Cas9-T3	sgRNA BAG3 murine targeting GCA GCG ATT TCG TAC CG	pLenti-U6-sgRNA-SFFV-Cas9-2APuro	ABM
pCMV Δ R8.91 pLeGO-iC2	Gag/pol backbone only	pCMV pLeGO-iC2	GSH (Weber et al., 2008)
pLeGOiG2H2B	GFP-H2B	pLeGO-iG	Smyrek, Master thesis, 2013
pMD2.G psgscrRNACrispR/Cas9	VSV-G scr sgRNA	pMD2.G pLenti-U6-sgRNA-SFFV-Cas9-2APuro	GSH ABM
pGEM-T Easy			Promega, A1360

Table 2-7: Plasmids generated during this thesis.

construct	description	vector backbone	reference
pLeGO-iG shBAG3-1	shRNA-1 BAG3	pLeGO-iG2	this thesis (with L. Hof)
pLeGO-iG shBAG3-2	shRNA-2 BAG3	pLeGO-iG2	this thesis (with L. Hof)
pLeGO-iG shBAG3-3	shRNA-3 BAG3	pLeGO-iG2	this thesis (with L. Hof)
pLeGO-iG shscr	shRNA scrambled	pLeGO-iG2	this thesis (with L. Hof)
pLeGOiG2H2B-LifeAct-tagRFP	LifeAct-tagRFP	pLeGOiG2H2B	this thesis (with S. Becker)
pLeGO-tfLC3	tfLC3	pLeGO Δ iC2	this thesis (with S. Becker)

2.1.7 Oligonucleotides

Table 2-8 List of oligonucleotides used in this thesis. Forward oligonucleotides (primers) are marked with "F", reverse oligonucleotides with "R". Restriction enzymes for cloning purposes are part of the primer name. Corresponding restriction enzyme sequences are underlined.

oligonucleotide	sequence along 5' to 3' direction
F_ β -casein	AAT CTG TTG AAC ATA TCA ATG AG
F_BiP	TAC ACT TGG TAT TGA AAC TG
F_Hs_COL1A1	TGA CGA GAC CAA GAA CTG
F_Hs_FN1	CCG TGG GCA ACT CTG TC
F_Mm_BAG3-Acc65I	AAA TTT <u>GGT ACC</u> GGA CCC TAA CCC AGC ATG AG
F_Mm_Col1a1	CCT GGT AAA GAT GGT GCC
F_Mm_Fn1	ATG TGG ACC CCT CCT GAT AGT
F_PP1-T1_BAG3	GAC CCT AAC CCA GCA TGA GC
F_PP4-T3_BAG3	TGC TCA GCC TGA CTG AAG TG
F_RCAS-LifeAct-BsrGI	AGC <u>TGT ACA</u> TCG AGA TGG GTG TCG
F_TEasy-Mm_BAG3-Acc65I	AAA TTT <u>GGT ACC</u> AAC CCA GCA TGA GCG CCG
R_BiP	GGT GGC TTT CCA GCC ATT C
R_Hs_COL1A1	CCA TCC AAA CCA CTG AAA CC
R_Hs_FN1	TGC GGC AGT TGT CAC AG
R_Mm_BAG3-Acc65I	AAA TTT <u>GGT ACC</u> TCA TTG CAC CCA GAT AGC CC
R_Mm_Fn1	GCC CAG TGA TTT CAG CAA AGG
R_Mm-Col1a1	CAC CAG GTT CAC CTT TCG CAC C
R_PP1-T1_BAG3	CGT TCG AGG CGG ATA TGG TT
R_PP4-T3_BAG3	CTG AGC TGC TGC AGT TGT TG
R_RCAS-LifeAct-BsrGI	ACT <u>TGT ACA</u> CCC TTA TTC CTT TGA GAT
R_TEasy-Mm_BAG3-Acc65I	AAA TTT <u>GGT ACC</u> TCT ACA GCA TGG TCC CAG GG
R_ β -casein	CTG CAG AAA GTA CAG AAC TTT GGA C

2.1.8 Antibodies

Table 2-9 List of primary and secondary antibodies used for protein detection on membranes, immunofluorescence and functional studies. HRP: horseradish peroxidase, IgG: immunoglobulin G.

primary antibodies	species	clonality	stock concentration, dilution	manufacturer, catalogue number
α -tubulin	mouse	monoclonal	0.2 μ g/ μ l, 1:1,000	Molecular Probes, A11126
α -tubulin	rabbit	monoclonal	0.072 mg/ml, 1:1,000	Abcam, ab52866
BAG3	rabbit	polyclonal	1:2,000-1:5,000	Abnova, PAB0330
β -casein	goat	polyclonal	0.2 μ g/ml, 1:1,000	Santa Cruz, sc-17971
β -catenin	rabbit	polyclonal	0.2 μ g/ μ l, 1:100	Santa Cruz, sc-7199
Caspase-3 (active)	rabbit	polyclonal	0.2 μ g/ μ l, 1:100	Cell Signaling, #9661
Collagen I	rabbit	polyclonal	1 mg/ml, 1:100	Abcam, ab34710
Collagen IV	rabbit	polyclonal	1 mg/ml, 1:100	Abcam, ab6586
E-cadherin	mouse	monoclonal	250 μ g/ml, 1:100	BD, 610181
E-cadherin	rat	monoclonal	1 mg/ml, 10 μ g/ml	Abcam, ab11512
Ezrin	mouse	monoclonal	0.2 μ g/ μ l, 1:100	Santa Cruz, sc-58758
FAK	mouse	monoclonal	250 μ g/ml, 1:1,000	BD, 610088
Fibronectin	rabbit	polyclonal	1 mg/ml, 1:100	Abcam, ab23750
GAPDH	mouse	monoclonal	5.3 μ g/ μ l, 1:10,000	Ambion, AM4300
GM130	mouse	monoclonal	250 μ g/ml, 1:100	BD, 610822
IgG1	mouse	monoclonal	1 mg/ml, 10 μ g/ml	Abcam, ab18447
IgG1	rat	monoclonal	1 mg/ml, 10 μ g/ml	Abcam, ab18407
Integrin beta 1	mouse	monoclonal	1 mg/ml, 10 μ g/ml	Abcam, ab24693
Laminin	rabbit	polyclonal	0.68 mg/ml, 1:100	Sigma Aldrich, L9393
LC3	rabbit	polyclonal	1 μ g/ml, 1:1,000	Novus Biologicals, NB100-2220
RFP clone 5F8	rat	monoclonal	1 μ g/ μ l, 1:1,000	Chromotek, 5F8
p-FAK (Tyr397)	rabbit	polyclonal	1:500	Cell Signaling, #3283
secondary antibodies	species	stock concentration, dilution	manufacturer, catalogue number	
goat IgG HRP-conjugated	donkey	0.4 μ g/ μ l, 1:30,000	Jackson Immuno Research, 705-035-147	
mouse Alexa Fluor 568	donkey	2 μ g/ μ l, 1:400	Molecular Probes, A10037	
mouse Cy5	goat	2 μ g/ μ l, 1:400	Molecular Probes, A10524	
mouse IgG HRP-conjugated	goat	0.4 μ g/ μ l, 1:30,000	Jackson Immuno Research, 115-035-003	
rabbit Alexa Fluor 488	goat	2 μ g/ μ l, 1:400	Molecular Probes, A11008	
rabbit Alexa Fluor 568	goat	2 μ g/ μ l, 1:400	Molecular Probes, A11011	
rabbit Alexa Fluor 647	goat	2 μ g/ μ l, 1:400	Molecular Probes, A21244	

rabbit IgG HRP-conjugated	goat	0.4 µg/µl, 1:10,000	Jackson Immuno Research, 111-035-003
rat IgG HRP-conjugated	goat	0.4 µg/µl, 1:30,000	Jackson Immuno Research, 112-035-003

2.1.9 Chemical dyes for fluorescence microscopy

Table 2-10: List of organic dyes for fluorescence microscopy.

name	specificity	manufacturer
4',6-diamidin-2-phenylindol (DAPI)	DNA	Life Technologies
Hoechst 33342	DNA	Life Technologies
Alexa Fluor 488 Phalloidin, Alexa Fluor 546 Phalloidin	F-actin	Life Technologies
SYTOX Blue	DNA, dead cells only	Life Technologies
SYTOX Green	DNA, dead cells only	Life Technologies

2.1.10 Bacterial strain

The bacterial strain *E. coli* DH5α was used with the following phenotype:

fhuA2 Δ(argF-lacZ)U169 phoA glnV44 Φ80 Δ(lacZ)M15 gyrA96 recA1 relA1 endA1 thi-1 hsdR17

2.1.11 Cell lines and culture media

The cell lines listed in Table 2-11 were used for experiments. The appropriate culture media are listed in Table 2-12.

Table 2-11: Cell lines.

cell line	species	tissue origin	source / reference
4T1	<i>Mus musculus</i>	Mammary gland, epithelial tumor	ATCC
HEK 293T/17	<i>Homo sapiens</i>	Embryonic kidney	ATCC
HC11	<i>Mus musculus</i>	Mammary epithelial cells	gift from A. Starzinski-Powitz, (Ball et al., 1988)
T47D	<i>Homo sapiens</i>	Mammary gland, ductal carcinoma from metastatic site	ATCC, HTB-133
U343	<i>Homo sapiens</i>	Glioblastoma cell line	CLS, 300365

Table 2-12: Composition of cell culture media.

name	composition
HC11 growth medium	RPMI 1640 supplemented with 2 mM L-glutamine, 10% FBS, 10 ng/ml EGF, 5 µg/ml insulin
HC11 starvation medium	RPMI 1640 supplemented with 2 mM L-glutamine, 10% FBS, 10 ng/ml EGF
HC11 differentiation medium	RPMI 1640 supplemented with 2 mM L-glutamine, 10% FBS, 5 µg/ml insulin, 10 ⁻⁷ dexamethasone, 5 µg/ml prolactin
HEK 293T growth medium	DMEM high glucose supplemented with 10% FCS and 2 mM L-glutamine

T47D growth medium	RPMI 1640 supplemented with 2 mM L-glutamine, 10% FBS
4T1 growth medium	RPMI 1640 supplemented with 2 mM L-glutamine, 10% FBS
U343 growth medium	DMEM high glucose supplemented with 10% FCS and 2 mM L-glutamine

2.1.12 Mice

In this thesis, organs were extracted from female BALB/c mice (Harlan Laboratories). All mouse procedures were performed in compliance with the German animal welfare law, guidelines and policies.

2.2 Molecular biology methods

2.2.1 Plasmid transformation in chemically competent *E. coli*

Chemically competent *E. coli* DH5 α were used to amplify plasmids. An aliquot of competent *E. coli* was thawed on ice. 10 μ l vector DNA was added and mixed gently with the bacteria. Samples were incubated for 20 minutes on ice followed by a heat-shock at 42°C for 45 seconds. Subsequently, samples were incubated on ice for further 5 minutes. 900 μ l LB medium was added and the mixture was incubated shaking at 37°C for 1 hour. Bacteria were pelleted at 2,000 g for 2 minutes and plated on LB agar plates with the corresponding antibiotic for selection. The plates were incubated at 37°C overnight.

Clones grew as colonies and were picked with a 200 μ l pipet tip and inoculated into 5 ml LB medium with the corresponding antibiotic. The culture was incubated shaking at 37°C overnight.

2.2.2 Isolation of plasmid DNA

Highly purified vector DNA was required for Sanger sequencing and cell transfection. Therefore, DNA purification was performed with commercially available kits. For mini plasmid preparations the NucleoSpin DNA prep was used according to manufacturer's instructions. Midi plasmid preparations was achieved using the NucleoBond Xtra midi (Table 2-5). Here, plasmid precipitation duration was prolonged to 2 hours at -20°C. Further, all centrifugation steps were executed at 3,220 g. All other steps were performed following the manufacturer's manual.

2.2.3 Isolation of genomic DNA

Genomic DNA was isolated from culture cell lines with the DNeasy Blood & Tissue kit (Table 2-5). For this procedure, manufacturer's manual was followed. In brief, approximately 5x 10⁶ cells were pelleted at 400 g for 4 minutes. The cell pellet was dissolved in PBS and proteins were digested using proteinase K. genomic DNA was then bound to a silica membrane, where it was washed several times for purification. DNA was finally eluted and stored at -20°C.

2.2.4 Isolation of total RNA

For extraction of RNA from cultured cells or tissues, either the RNA kit or TRIzol® Reagent (Table 2-5) was used.

Adherent grown cells were washed once with ice-cold phosphate buffered saline (PBS) before addition of the 2-mercaptoethanol-containing lysis buffer, which at the same time inactivates RNases, breaks cells and provides optimal binding conditions for silica membrane binding. For a better homogenization, the cell lysate was passed through a shredder column. Contaminating DNA was removed by incubation of a DNase solution directly on the silica membrane. After several washing steps to remove salts, cell debris and metabolites, RNA was eluted with 20-50 µl RNase-free water.

RNA from whole mammary glands or cell cultures was isolated using TRIzol® Reagent. Therefore, samples were homogenized in 1 ml TRIzol® Reagent with a 2 ml glass homogenizer or with a sonifier (15 seconds) on ice. Due to its high amount of fat, samples from mammary gland were centrifuged to separate the fat from the sample. Chloroform addition allowed phase separation where the RNA was located in the upper aqueous phase, while proteins were solved in the phenol-chloroform phase, and the DNA was found in the intermediate phase. RNA precipitated using isopropanol, washed with ethanol, dried, and was finally re-suspended with 20 µl RNase-free water.

Following RNA extraction cDNA was synthesized using Maxima reverse transcriptase (Table 2-5). Total RNA from cultured cells or tissue was reverse transcribed in a 20 µl reaction volume, following the manufacturer's instructions:

1 µg RNA
4 µl 5x reaction mix
2 µl Maxima RT enzyme
to 20 µl RNase-free H₂O

The reaction mix was vortexed and spun down. Reverse transcription was executed in a PCR cycler starting with an incubation for 10 minutes at 25°C, followed by 20 minutes at 50°C, and finally 5 minutes at 85°C. Samples were stored at -20°C or -80°C for long-term storage.

2.2.5 DNA and RNA concentration measurement

DNA and RNA were diluted in ddH₂O and RNase-free H₂O, respectively. Concentration of nucleic acids (dsDNA or RNA) was measured with the appropriate reference using a nano spectrophotometer (Implen). Concentration was measured at A₂₆₀ nm, while purity was estimated with the A₂₆₀/A₂₈₀ ratio, which should range from 1.8 to 2.0. Further, an A₂₆₀/A₂₃₀ ratio indicated contamination with chaotropic salts, phenol or protein when values are below 1.0.

2.2.6 Agarose gel electrophoresis

Due to its negative charge at neutral pH DNA can be separated by its length on polymerized agarose gels. In this work, usually 1% agarose gels were prepared heating agarose in 1x TAE in a microwave oven. Roti®Gel-stain (Carl Roth) was added 1:20,000 to the solution and then poured into a tray with a comb placed in it. After solidification, the comb was removed from the gel and the electrophoresis chamber was filled with 1x TAE. The DNA samples were mixed with 5x loading buffer, and were loaded onto the gel. A current of 100 V was applied until the desired separation was reached. The stained DNA in the gel was analyzed with UV-light. Eventually, DNA bands were excised from the gel and purified using the NucleoSpin Gel and PCR clean-up kit (Table 2-5) for further downstream applications.

2.2.7 Quantitative real-time reverse transcription polymerase chain reaction (qPCR)

Probe-based quantitative real-time PCR was carried out using Taqman Universal PCR Master Mix and Taqman assay probes (see Table 2-5). cDNA was diluted 1:4 with RNase-free water. Data was acquired with the CFX-96 detection system (Table 2-3). Experiments were run in triplicates.

2.2.8 Protein isolation

In this work, proteins were extracted from cultured cells and tissues. Protein extracts from cultured cells were generated using radioimmunoprecipitation assay (RIPA) buffer enabling efficient cell and tissue lysis. The addition of protease and phosphatase inhibitors prevents protein degradation and preserves the phosphorylation status of proteins.

For whole cell protein isolation, adherent cells were washed once with ice-cold PBS followed by the addition of 50 µl (volume for 12-well culture dishes) RIPA buffer plus protease (1:1,000) and phosphatase (1:100) inhibitors. The cells were incubated for 20 minutes at 4°C and harvested with a rubber policeman. When protein extracts were made from spheroids, spheroids from three 96-well plates were harvested with a glass capillary in micro centrifugation tubes and collected at the bottom of the tube by centrifugation. Then, 20 µl RIPA buffer was added and spheroids were incubated for 20 minutes on ice. Subsequently, lysates from adherent cells and spheroids were homogenized by sonification for 15 seconds. The lysates were centrifuged at 10,000 g for 15 minutes and the cleared supernatants were stored at -20°C until further use.

2.2.9 Protein concentration measurement

In this work, protein concentration was examined according to the Bradford method. Here, the binding of Coomassie Blue G-250 to proteins causes a shift in the absorption maximum of the dye from 465 to 595 nm (Bradford, 1976). In a cuvette, 1 µl of the protein lysate was mixed with 200 µl Bradford Reagent (Table 2-5) and 800 µl ddH₂O and incubated for 10 minutes at room temperature

in a dark box. The absorption at 595 nm was measured with a photometer and compared to the reference (1 μ l of lysis buffer, 200 μ l Bradford reagent, and 800 μ l ddH₂O). Comparing the absorption to a protein calibration curve (Supplemental Figure 7-4), the protein concentration of the sample was estimated.

2.2.10 Sodium dodecyl sulfate polyacrylamide gel electrophoresis (SDS-PAGE)

A tool commonly used for protein analysis is the denaturing SDS-PAGE according to Laemmli (Laemmli, 1970). Proteins travel along the electric field through a gel composed of polymerized acrylamide. Separation by molecular weight is achieved by SDS and 2-mercaptoethanol, which disrupt hydrogen, hydrophobic, and disulphide bonds and results in a negative charge of proteins (Shapiro et al., 1967). Consequently, the SDS-protein complexes move towards the positive pole, which results in separation by the molecular weight. The detailed composition of the polyacrylamide gels is listed in Table 2-13.

Table 2-13: Polyacrylamide gel composition and pipetting scheme.

separation gel				stacking gel	
acrylamide concentration	8%	10%	16%	5%	
30% acrylamide	1.60 ml	2.00 ml	3.20 ml	30% acrylamide	0.67 ml
1.88 M Tris-HCl pH 8.8	1.20 ml	1.20 ml	1.20 ml	0.62 M Tris-HCl pH 6.9	0.80 ml
ddH ₂ O	2.90 ml	2.50 ml	1.30 ml	ddH ₂ O	2.35 ml
2.5% [w/v] SDS	0.25 ml	0.25 ml	0.25 ml	2.5% [w/v] SDS	0.16 ml
10% [w/v] APS	30 μ l	31 μ l	34 μ l	10% [w/v] APS	20 μ l
TEMED	5 μ l	6 μ l	9 μ l	TEMED	4 μ l

Discontinuous gels were assembled in a running chamber (Bio Rad) and 1x SDS running buffer was added. Protein samples (10 – 30 μ g) were mixed with protein loading buffer (Roti Load 1, Carl Roth) and denatured at 90°C for 5 minutes. Samples and a pre-stained molecular weight marker (PageRuler, Thermo Scientific) were loaded onto the gel and a constant voltage of 100 V was applied until the sample buffer dye reached the bottom of the gel.

2.2.11 Western (immuno-) blot analysis

Western blot is the electrophoretic transfer of proteins from a SDS gel onto a membrane to make proteins accessible for downstream applications such as immunodetection. In this work, the semi-dry procedure was performed. Nitrocellulose membrane and filter paper were soaked with Western transfer buffer.

From the anode to the cathode of the blotting chamber (Bio Rad), the order was to add three filter paper, the membrane, then the SDS gel, and finally another three layers of filter paper. For the transfer, a constant current of 1.5 mA per cm² blotting area was applied for 1 hour.

Following blotting, the membrane was washed for at least 1 minute with TBS-T, and then blocked with 5% BSA (for anti- β -casein antibody detection) or 5% milk in TBS-Tween (0.1%) buffer for

1 hour at room temperature on a rocking shaker. After blocking, the membrane was washed with TBS-T (3x 5 minutes) and then incubated with the primary antibody (diluted in TBS-T with 2.5% BSA) overnight shaking at 4°C. Afterwards, the membrane was washed with TBS-T three times for 5 minutes each, followed by incubation with the HRP-conjugated secondary antibody (diluted in TBS-T with 2.5% BSA) for 1.5 hours at room temperature followed by another three washes for 5 minutes each. In this work, horseradish peroxidase (HRP)-conjugated secondary antibodies were used. This enzyme fulfils a chemiluminescent reaction after addition of substrate (ECL solution), which leads to light emission at sites where the secondary antibody bound. The luminescence was detected with the Chemostar luminescence detection system from Intas.

2.2.12 Immunofluorescence staining

Immunofluorescence staining was carried out on cells grown as monolayer as well as on whole mount spheroids.

Immunofluorescence on monolayer cultures

Cells grown on coverslips were washed once with ice-cold PBS and fixed with 4% PFA for 10 minutes at room temperature. This was followed by three washes with PBS, each for 1 minute. Cells were permeabilized for 10 minutes at room temperature using 0.1% Triton X-100 in PBS. Free antibody binding sites were blocked for 20 minutes with 10% goat serum diluted in PBS. Coverslips were then placed in a humidified chamber and antibodies diluted in blocking solution were added. Primary antibodies were incubated overnight at 4°C, secondary antibodies for 1 hour at room temperature. In between, and after antibody incubation, three washes for 1 minute and three washes for 5 minutes were performed with PBS. Cell nuclei were counterstained for 5 minutes with 1 µg/ml DAPI. Finally, coverslips were washed three times with PBS for 5 minutes each and then mounted onto glass slides using Mowiol.

Immunofluorescence on spheroid cultures

For an efficient *in toto* immunostaining of spheroids, different protocols were tested (section 3.2.1). Here, the final optimized immunostaining procedure for whole mount spheroids is described.

Spheroids were fixed with 4% paraformaldehyde (PFA) for 15 minutes. Then, spheroids were washed two times with PBS before they were subjected to permeabilization with 0.3% Triton X-100 in PBS for 15 minutes. Subsequently, free antibody binding sites were blocked by incubating spheroids for 1 hour at room temperature in blocking solution according to Debnath *et al.* (Debnath *et al.*, 2003). Primary antibodies were diluted in blocking solution and spheroids were incubated for 18-24 hours at 37°C on a thermoshaker at 600 *r.p.m.*. This was followed by three washes with PBS for 20 minutes each and an incubation with secondary antibodies and nuclear staining dye diluted

in blocking solution for 4 hours shaking at 37°C. Finally, spheroids were washed three times with PBS for 20 minutes each and stored in dark at 4°C until further use.

2.2.13 Immunohistochemistry

PFA-fixed spheroids or mammary gland tissue were embedded in paraffin after dehydration with ascending ethanol concentrations and incubation in xylol. The dehydration was carried out using an automated embedding station (see section 2.1.3) with the following program: 70%, 80%, 95% and 2x 100% ethanol, followed by incubation in xylol and twice in paraffin. Each step was conducted for 1.5 hours. Sections with a thickness of 4 µm were prepared with a Leica microtome and mounted onto SuperfrostPlus object glasses. Next, sections were dewaxed by incubation in xylol (2x 5 minutes) and rehydrated with a series of descending ethanol concentrations (100% 2x 5 minutes, 95% 1x 3 minutes, 70% 1x 3 minutes, and 50% 1x 3 minutes) followed by rinse with water for at least 3 minutes. Antigen retrieval was performed by heating the slides for 3 minutes in 10 mM citrate buffer pH 6 in a pressure cooker followed by washing with tap water. Next, sections were circled with a wax pen and rinsed with 1x TBS (2x 5 minutes) followed by incubation with blocking solution (0.5% Triton X-100, 10% FBS in PBS) for 1 hour at room temperature. Primary antibody was diluted in block solution and incubated on the sections in a humidified chamber overnight at 4°C. Following that, slides were washed three times for 5 minutes with TBS and incubated with secondary antibody diluted in block solution for 1.5 hours at room temperature. In addition, cell nuclei were counterstained with 1 µg/ml DAPI (Life Technologies) for 15 minutes. After two final washes in TBS, slides were mounted with Mowiol.

2.3 Lentivirus production

Lentiviral vectors introduce genes stably and efficiently into the genome of non-dividing cells. The expression system is based on HIV-1-derived particles (Naldini et al., 1996). Third generation lentivirus vectors are replication defective and the viral genes, which are necessary for virus production, are expressed in *trans* by packaging vectors. Further, the viral particles are pseudotyped with the G protein from vesicular stomatitis virus (VSV G), which targets the vector to the endocytic pathway. The resulting viral particles cannot replicate, thus only one round of infection can be accomplished (Dull et al., 1998).

On the lentiviral vector, a deletion of the viral enhancer and promoter sequences in the 3' long terminal repeat (LTR) leads to self-inactivation (SIN) of the system. This prevents insertional activation of cellular proto-oncogenes by random integration of the vector and further enables regulated expression of genes by elimination of *cis*-actin effects of the LTR (Miyoshi et al., 1998).

The Lentiviral Gene Ontology (LeGO) vectors allow expression of a transgene of interest and, if required, shRNA and simultaneous expression of a fluorescent marker (Weber et al., 2008).

The HEK 293T/17 cell line is commonly used for virus production. These cells are highly transfectable and derive from the 293 cell line, which was modified to contain the SV40 T-antigen. For production of virus particles, a one-day-old culture from 1×10^6 seeded cells (in a T75-flask) was transfected with 10 μg pLeGO, 6.5 μg pCMV Δ R8.91 and 3.5 μg pMD2.G. Plasmids were diluted in 450 μl water and 50 μl 2.5 M CaCl_2 solution was added. 2x HBS was drop-wise added to the DNA/ CaCl_2 -solution while blowing air with a pipette through the DNA/ CaCl_2 -solution. The mixture was incubated at room temperature for 20 minutes. Meanwhile, old medium was removed from the cultured cells and 10 ml medium including 25 μM chloroquine was added. The DNA-mixture was added drop-wise to the cells and incubated for 12 hours in the incubator. Cells were washed once with PBS and 8 ml fresh medium was added. Virus particles were collected by harvesting the supernatant at 24, 48, and 72 hours after transfection and stored at 4°C. Pooled supernatants were filtered through a 0.45 μm pore nitrocellulose membrane to remove cellular debris. Aliquots were stored at -80°C.

2.4 Cell culture methods

2.4.1 Cell culture

All cell lines were incubated at 37°C in an atmosphere of 5% CO_2 , 21% O_2 , and 95% humidity. Cells were propagated when they reached 80 - 90% confluence. They were washed with warm PBS and incubated with accutase for 5 – 10 minutes to detach cells from the growth surface. Cells were diluted with their appropriate growth medium harvested in a conical tube and resuspended by pipetting. The suspension-containing tube was centrifuged for 4 minutes at 400 g. The supernatant was removed and the remaining cell pellet was resuspended with 5 ml growth medium. One portion of suspended cells was recultured (1:12 for HC11, 1:8 for 4T1, 1:5 for T47D, and 1:10 for HEK 293T cells), while the remaining cells were eventually used for experiments.

2.4.2 HC11 lactogenesis assay

The non-tumorigenic mouse mammary epithelial cell line HC11 is a prolactin-responsive clone of the COMMA-1D cell line (Danielson et al., 1984), which was isolated from mid-pregnant BALB/c mice capable to perform lactogenesis without coating the dish with extracellular matrix. Upon hormonal induction, cells differentiate and produce milk proteins (Ball et al., 1988).

For *in vitro* differentiation, confluent cultures were incubated for 3 days in starvation medium. Then, cells were washed twice with PBS to remove residual growth factors and incubated in differentiation medium (Table 2-12).

2.4.3 Spheroid formation

For spheroid formation, the liquid-overlay technique was used (Carlsson and Yuhas, 1984). In brief, 96-well culture dishes were coated with 50 μ l 1% low-melt agarose to form concave non-adhesive wells. Following cell separation, a favored number of cells was seeded into the wells and plates were centrifuged at 400 *g* for 4 minutes to collect the cells at the bottom of the wells.

2.4.4 Spheroid compression

Agarose capillaries were produced by pipetting liquid 2% low-melt agarose into a capillary. Before the agarose solidified, a glass rod of either 200 μ m or 300 μ m diameter was inserted into the center of the agarose column. The agarose solidified for approximately 5 minutes at 4°C. The glass rod was removed carefully and agarose-glass columns were stored in PBS until further use. For the experiment, the agarose column was removed from the glass capillary and cut into fragments with length of approximately 1 cm. Spheroids were seeded from 5,000 HC11 cells in presence of 7 μ g/ml bovine type I collagen to promote spheroid formation. After 10 days of growth, spheroids were inserted into the capillaries by means of capillary forces. The mounted spheroids were then placed into 6-well plates containing 2 ml assay medium (RPMI supplemented with 10% FBS and 2 mM L-glutamine). For autophagy induced by nutrition deprivation, the spheroids were incubated in EBSS medium. After indicated time points, spheroids were subjected to further analyses.

2.4.5 Lentivirus transduction

Viral particles were produced as described in section 2.3. Recipient cells were seeded at 4×10^5 cells per well in a 6-well plate and were transduced after 8-14 hours. Therefore, 2 ml of viral supernatant and 1 ml of growth medium were loaded onto the cells. Polybrene was added to a final concentration of 8 μ g/ml. Subsequently, the plate was centrifuged at 1.000 *g* for 1 hour at room temperature. The medium was refreshed after 8-14 hours and the expression of the transgene was monitored with the fluorescence microscope. When the CRISPR/Cas9 technology was used, cells were propagated the day after transduction. At day 3 following transduction, puromycin was added at a concentration of 5 μ g/ml. After 4 days of puromycin treatment, cells were incubated in normal growth medium.

2.4.6 Generation of knockout clones

Cells were treated as described in section 2.4.5. After 4 days of puromycin treatment, cells were seeded sparsely in growth medium into a 6-well dish to let single colonies form. Then, they were

incubated for 1 minute with accutase to allow the beginning of cell detachment. Single colonies were picked with a 10- μ l pipette tip and transferred into the wells of a 96-well plate. After several steps of propagation, one part of the cells was used to prepare protein lysates (sections 2.2.8, 2.2.9 and 2.2.10) to check for a successful knockdown. Clones, which showed a band deletion, were further propagated. In a next step, genomic DNA was extracted (section 2.2.3) and analyzed for a monoallelic or biallelic deletion of the gene of interest.

2.4.7 Live-dead assay (LDA)

LDA in two-dimensional cell cultures

To analyze the amount of dead cells in monolayer cultures, 40,000 cells were seeded into wells of a 96-well plate and grown for 24 hours. Cells were either genetically modified or treated with specific compounds for the indicated time. Then, dead cells were stained with SytoxGreen or SytoxOrange (Life Technologies) while the total amount of cells (also live cells) was stained with 1 μ g/ml Hoechst 33342 (Life Technologies). As positive control, cells were permeabilized with 1% Triton X-100 just before the staining. After an incubation of 30 minutes, fluorescence intensity was captured with a microplate reader (Tecan). Hoechst 33342 excitation was at 350 nm and emission at 461 nm. For SytoxGreen, excitation and emission were set to 504 nm and 523 nm. SytoxOrange has absorption and emission maxima of 547 nm and 570 nm.

LDA in three-dimensional cell cultures

Dead cells were either stained with 2.5 μ M SytoxBlue or SytoxGreen (Life Technologies) for 30 minutes, while live cells expressed EGFP-H2B or were labeled with Hoechst 33342 (Life Technologies) at a final concentration of 1 μ g/ml. As positive control, spheroids were permeabilized with 1% Triton X-100 (Roth) for 5 minutes prior to the staining. Fluorescence microscopy was performed with a laser scanning confocal microscope (LSM 780, Carl Zeiss) equipped with a Plan-Apochromat 10x/NA 0.3 objective. Images were acquired using a 488 nm and a 458 nm (or a 405 nm laser for Hoechst) laser. The spacing between the planes was set to 13.30 μ m.

The images were processed for further analyses by Biena Mathew. First, the average projection of a stack of fluorescence images along the z-axis was computed with *ImageJ*. Subsequent steps were performed with *Mathematica*. The area covered by the live cells was determined using the approach described in section 2.7 for fluorescence images. The resulting binary image was used as a mask for the channel showing dead cells. The mean intensity was calculated in the area of both, the live and the dead channel and a ratio was formed.

2.4.8 Cell adhesion assay

Wells of a 96-well plate were coated for 1 hour at room temperature with $6 \mu\text{g}/\text{cm}^2$ bovine fibronectin (Sigma Aldrich), $15 \mu\text{g}/\text{cm}^2$ bovine type I collagen (Gibco), or were left uncoated. Then, the remaining medium was removed and free binding sites were blocked with 2.5 mg/ml BSA for 1 hour at 37°C . Cells were stained with $0.5 \mu\text{g}/\text{ml}$ Hoechst 33342 (Life Technologies) for 15 minutes on a rotating wheel. Cells were washed once with medium. Finally, cells were seeded at 1×10^5 cells per well, centrifuged for 1 minute at 100 g, and incubated for 1 hour at culture conditions. Non-adherent cells were washed off twice and fluorescence intensity of the attached cells was measured with the microplate reader Infinite M200 (Tecan).

2.4.9 Cell proliferation assay

A colorimetric assay was used to determine cell viability. Therefore, 7,500 cells were seeded into a 96-well plate. After a growth period of 18 hours, cells were treated with drugs at indicated concentrations for 2 hours and 24 hours. Subsequently, 20 μl MTS solution (AQueous One Solution, Promega) was added and cells were incubated for further 2 hours to 4 hours. The solution contains a tetrazolium compound [3-(4,5-dimethylthiazol-2-yl)-5-(3-carboxymethoxyphenyl)-2-(4-sulfophenyl)-2H-tetrazolium, inner salt; MTS] and an electron coupling reagent (phenazine ethosulfate; PES). PES provides stability of the solution. The tetrazolium compound MTS is reduced by metabolically active cells into a soluble formazan product, which absorbs light at 490 nm. Absorbance and background at 700 nm were measured with the microplate reader Infinite M200 (Tecan) (Barltrop et al., 1991).

2.4.10 Cell migration assay

Biocompatible silicone culture inserts (ibidi, 80209) were inserted into wells of a 24-well plate. The silicone insert prevented cells to grow on a gap with a width of approximately $500 \mu\text{m}$ ($\pm 50 \mu\text{m}$). In each chamber, 30,000 cells in 70 μl assay medium were seeded. After 24 hours, medium was removed and cells were washed twice with PBS. Starvation medium (1% FBS in RPMI 1640 supplemented with L-glutamine) was added for 18 hours. The silicone insert was removed carefully and cells were washed twice with PBS to remove debris. Fresh starvation medium was added to the cells and wound closure was analyzed with the Zeiss Axio Observer.Z1 for 48 hours with intervals of 4 hours.

Data analysis was performed using *ImageJ*. Background was subtracted with a rolling ball radius of 15 pixels. The images were filtered using a Gaussian kernel (radius = 6). Then, images were binarized setting the minimum threshold to 18. Following inversion of the images, particles were analyzed that were larger than 20,000 pixels. With it, the area of the gap was measured.

2.5 Optical clearing

Optical clearing is a method to render whole specimens transparent to make them accessible for light microscopy. Myriad techniques exist to accomplish specimen transparency. Here, specimens were cleared with Murray's clear (Dent et al., 1989). Samples were dehydrated using ethanol at increasing concentrations (30%, 50%, 70%, 90%, 96%, 2x 100%, 2 minutes each) at room temperature. Specimens were then transferred into a solution composed of one part benzyl alcohol and two parts benzyl benzoate (BABB) with a refractive index of 1.5598. Samples were incubated until transparency.

2.6 Microscopy

2.6.1 Wide-field fluorescence microscopy

Time-lapse images were recorded with the Axio Observer.Z1 (Carl Zeiss) for a duration of 48 hours with 30 minutes intervals. Incubation conditions of 37°C and 5% CO₂ were maintained during the whole acquisition period. A 10x/NA 0.5 objective (Zeiss) was used. Fluorescence images (488 nm laser) and transmission images were acquired. Controls were only imaged at the beginning and the end of the time-lapse to control effects caused by the laser exposure.

2.6.2 Confocal laser scanning microscopy

Confocal laser scanning microscopy was performed with the Zeiss LSM780 (Carl Zeiss) microscope. Information about the imaging parameter are indicated wherever necessary.

2.6.3 Light sheet-based fluorescence microscopy

Fixed or live samples were mounted onto the pinhole sample holder (Strobl et al., 2017). First, a 5 µl drop of 1% low-melt agarose was pipetted onto the pinhole. Then, the sample was placed inside the agarose drop (Figure 2-1a). After solidification of the agarose, the sample holder was placed inside the microscope chamber, which was filled with PBS. The holder was rotated 45° with respect to the light sheet to prevent excitation and emitting light from hitting the steel holder. For multi-view imaging, the holder was further rotated by another 90°, 180°, and 270° to obtain datasets from four view angles (Figure 2-1b).

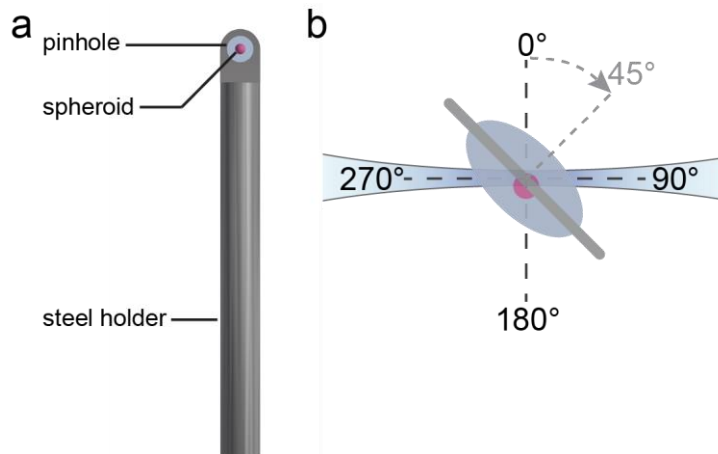


Figure 2-1 Spheroid mounting onto a pinhole sample holder. (a) Illustration of the pinhole sample holder for not cleared specimens developed by Frederic Strobl. A spheroid is placed in the center of an agarose drop in the pinhole. (b) Top view of the pinhole sample holder. The holder is rotated by 45° with respect to the light sheet. The blue bar depicts the light sheet. For multi-view image fusion, additional view angles are recorded.

Optically cleared samples were mounted into a rectangular glass capillary (Hilgenberg; dimensions were $1.35 \text{ mm} \pm 0.05 \text{ mm} \times 1.35 \text{ mm} \pm 0.05 \text{ mm}$ with a wall thickness of 0.25 mm). Glass capillaries were previously cleaned by incubation for 2 hours at 80°C in 1% Hellmanex®. Following that, capillaries were rinsed with deionized water and air dried at 60°C for 1 hour. Dried glass capillaries were mounted onto the stainless steel holder and sealed with Parafilm®. Then, the specimen-containing BABB solution was pipetted dropwise into the capillary (Figure 2-2a). The sample holder was then placed into the microscope chamber, which was previously filled with 2,2'-thiodiethanol (TDE).

Since the excitation and emitted light penetrate layers of diverging refractive indices (Figure 2-2b), the light rays are deflected, which results in a shift of the focus when the sample together with the stage is moved. To correct for this, the position of the detection lens was re-adjusted during image acquisition to keep the focal planes of the illumination and detection lens overlapping (Supplemental Figure 7-7).

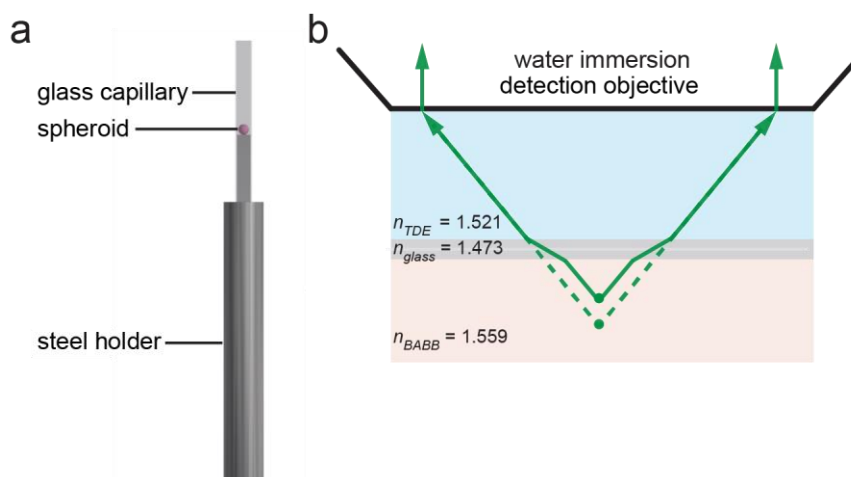


Figure 2-2 Mounting of optically cleared spheroids. (a) A rectangular glass capillary is mounted onto a steel holder. The cleared specimen is located inside the capillary immersed in clearing medium. (b) The actual working distance of a water immersion detection lens is shifted in a

microscope setup for optical clearing. The emission light penetrates layers of different refractive indices resulting in aberration of the light rays.

2.7 Analysis of the projected area

The projected area is the simplified estimation of properties three-dimensional specimens. When a three-dimensional specimen is imaged with a wide-field microscopy approach, the covered area is the projected area. Two methods were developed by Biena Mathew to automatically segment the projected area in transmission and fluorescence images.

First, the intensity values in a fluorescence image were scaled to values between 0 and 1. Contrast and brightness were adjusted by an amount of 0. A gamma correction was performed by raising values to the power 1. The background was subtracted (mean intensity of the upper 200 rows in an image). Then, the images were filtered using a large Gaussian kernel (radius = 36 to 60) to blur the cell nuclei. The subsequently detected foreground (i.e. aggregate) was separated from the background by applying the Otsu's cluster variance maximization (Otsu, 1979). Holes in the foreground were filled and the largest object was selected (the remaining foreground objects were removed).

For transmission images, binarization thresholds were determined locally. For each pixel within a radius r the local threshold t_{local} was calculated as following:

$$t_{local} = \alpha\mu + \beta\sigma + \gamma,$$

where μ and σ were the local mean and standard deviation, respectively. Finally, holes in the object were filled. Parameter values for spheroids imaged with a wide-field microscope (Axio Observer.Z1) were set to $r = 15$, $\alpha = 0.3$, $\beta = 10$ and $\gamma = 0$.

2.8 Statistical analyses

Statistical analyses were performed with *OriginPro 2016G* or *Mathematica*. For normal distributed data, the Student's t-test was used and combined with a Bonferroni correction for multiple testing. For non-parametric data, the Mann-Whitney test was used and combined with a Bonferroni or a Holm correction. Statistical significance was defined as $p < 0.05$ (*). Two additional thresholds were $p < 0.01$ (**) and $p < 0.001$ (***)).

2.9 Agent-based computational model

The computational model provided additional analyses of the spheroid formation dynamics. Dr. Sabine Fischer developed the model (Garg et al., 2015). In brief, the model assumes that cells are spherical, move in a convex well and aggregate to form clusters. The movement is random within the boundaries of the well. Cell sinking is defined by a buoyancy parameter. A sufficient proximity allows cells to form contacts with each other. The capability to form a contact is given by the

binding probability p_{bind} , and the contact break-up by the unbinding probability p_{unbind} . To avoid cells from accumulating and squashing at the bottom of the well, an upward movement was implemented. *Mathematica* (version 10) was used to simulate the accumulation of 50 cells as previously described (Garg et al., 2015). The normalized area is the area of the convex hull of the cell coordinates projected to the x,y-plane. The parameter values for the model for different experimental conditions were determined by fitting the normalized area of the simulations to the normalized area of the experimental data. First, the buoyancy parameter value was determined. It was $1 \text{ mg}\cdot\text{ml}^{-1}$ for T47D cells, $2 \text{ mg}\cdot\text{ml}^{-1}$ for HC11 cells, and $4 \text{ mg}\cdot\text{ml}^{-1}$ for 4T1 cells. For each buoyancy parameter, a parameter scan for the binding and unbinding probabilities was performed. Thereby, the binding probability was varied between 0.05 and 1.0, and the unbinding probability between 0.01 and 0.2. 25 simulations per parameter combination were performed. With these, the 25 simulations that fitted best to each experimental condition were selected and descriptive statistics (mean and standard error of the mean) were calculated. The goodness of fit was obtained by the Akaike information criterion (AIC).

3 Results

The results of this work are divided into four parts. The following sections focus on the cell biological aspects of factors that influence tissue integrity in mammary epithelia. In the first part (section 3.1), the expression of the pro-survival factor BAG3 is assessed in the developing mammary gland and its influence on cell viability and cell migration in monolayer cultures is shown. For the work with three-dimensional cell cultures, part two (section 3.2) focuses on methodical aspects and the evaluation of immunofluorescence staining and imaging of large spheroids *in toto*. The third part (section 3.3) highlights spheroids as model systems that display many characteristics of epithelia, such as the synthesis and distribution of ECM, polarization and differentiation. The fourth part (section 3.4) elucidates the impact of mechanical stress on the integrity of cellular spheroids from a morphological and cell survival point of view. It reveals new insights into the morphological adaption of cellular cluster to external forces. The last part (section 3.5) investigates other aspects of tissue integrity. A spheroid formation assay shows the involvement of E-cadherin, actin, microtubules, FAK and BAG3 in the aggregation process that is mainly driven by cell adhesion and active rearrangement of cells to ensure the integrity of the spheroid.

3.1 BAG3 is associated with cell survival and differently expressed during mammary gland development

It has been suggested that autophagy predominantly acts as a pro-survival signal to facilitate the halt of involution and the resumption of lactation (Pensa et al., 2014). However, apart from the early local factor LIF, it is not well understood what the initial trigger for the induction of the first phase of involution is. Two existing hypotheses suggest an involvement of mechanical stress and/or the action of death signals accumulating in the milk, which are both induced upon milk stasis (Kritikou et al., 2003).

The co-chaperone BAG3 is known as a pro-survival factor and has been shown to be heavily involved in processes that are induced upon mechanical stress. In muscle cells, its expression increases when cells underlie heavy mechanical challenges. There, it modulates CASA, a specialized adaptation of autophagy to recycle cytoskeletal proteins that have been damaged upon mechanical stress (Ulbricht et al., 2013b). BAG3 has further been shown to play a role in the development of diseases. The major cause upon BAG3 mutation is muscle dystrophy. However, also breast cancer has been shown to be mutant for BAG3. Thus, it is of interest whether BAG3 is

involved in developmental processes of the mammary gland, especially in the induction of post-lactational regression.

3.1.1 The expression of BAG3 mRNA changes during mouse mammary gland development

We investigated the potential physiological role of BAG3 in the developing mammary gland. In histological sections from murine mammary glands at different developmental stages, BAG3 showed a cytoplasmic distribution, which was unaltered in lactating compared to regressing mammary glands (Supplemental Figure 7-1). To analyze the expression of BAG3, mammary glands were excised from approximately eight weeks old female virgin BALB/c mice, from pregnant mice at day 11.5, 13.5 and 16.5, from 2 days and 8 days lactating mice. Forced involution was induced in mice at the peak of lactation, 8 days after parturition. These mice underwent forced involution for 12 hours and 24 hours, 3 days, 7 days and 14 days. From these glands, RNA was extracted to analyze the expression of BAG3. As a reference gene, Rpl13a was chosen, which has been shown best suitable for mouse mammary gland data normalization (Han et al., 2010). As positive control, c-Fos was chosen (Supplemental Figure 7-2), which is known to be upregulated during mammary gland involution (Marti et al., 1999). For the use of the $\Delta\Delta C_T$ method, an efficiency (E) between 95% - 105% is a prerequisite, which the experimental conditions reached (Supplemental Figure 7-3). However, since multiple data from animals at different developmental stages were used, a control group was not existent, which is necessary for the $\Delta\Delta C_T$ method. Therefore, the relative expression was chosen as a measure. The expression of BAG3 differed between the developmental stages of mammary gland development. In virgin mice, BAG3 had a median relative expression of about 0.14 ± 0.03 (median \pm SEM). This value decreased to 0.04 ± 0.009 at mid-pregnancy (P11.5) and to 0.02 ± 0.006 in late pregnancy (P16.5). Following parturition, the relative expression of BAG3 rose from 0.05 ± 0.003 at day 2 to 0.08 ± 0.03 at day 8 of lactation. Interestingly, when pups were removed, and therewith forced involution was induced, the relative BAG3 expression constantly increased and was about 2.3-fold stronger at day 3 of involution compared to the virgin gland. Compared to day 8 of lactation, involution at day 3 showed a 5.3-fold stronger expression of BAG3. In the further course of involution, BAG3 expression decreased and was found to be similar to the virgin gland 14 days after pup removal (Figure 3-1a). Next, the time points of investigation were assigned to their developmental stages of virginity, pregnancy, lactation and involution. Statistical analysis was performed among these stages. BAG3 expression was found to be similar in virgin compared to regressing glands. The expression was statistically different between regressing glands and both, mammary glands during pregnancy ($p < 0.001$) and lactation ($p < 0.01$, Figure 3-1b). However, involution separates into two distinct phases according to different cellular mechanisms. The switch between the first and the second phase occurs approximately 48 hours after pup removal. Thus, the data from involution time points were sorted according to the two phases. Time points 12

hours and 24 hours were assigned to the first phase, and time points 3 days and 7 days were assigned to the second phase. Involution after 14 days was excluded from this data presentation, since this late time point already reflects the status after remodeling, which is comparable to the virgin gland. The median BAG3 expression in the first phase was 0.14 ± 0.07 compared to 0.27 ± 0.05 in the second phase. Despite the increase, the expression was not statistically different (Figure 3-1c).

These results showed that the expression of BAG3 was differently regulated in the developing mammary gland. It was very low during pregnancy and reached a strong expression at about 3 days of involution, which decreased with proceeding mammary gland regression to reach an expression level comparable to the virgin gland.

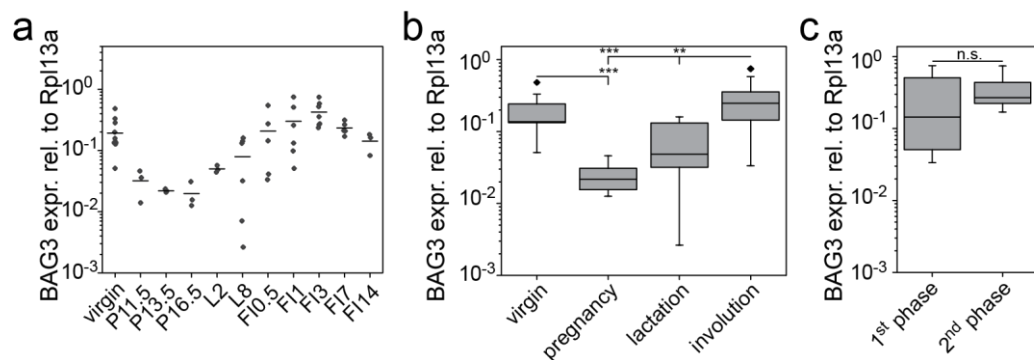


Figure 3-1 Gene expression analysis of BAG3 in the developing mammary gland. RNA was extracted from mammary gland #4 of mice in different developmental stages. RNA was transcribed into cDNA and then used for qPCR with Taqman primer to detect BAG3. (a) The dots represent data from individual mice, and the lines show the mean values. (b) BAG3 expression in four phases of mammary gland development. Data were pooled from the time points that contribute to a developmental phase. (c) BAG3 expression in the first and second phase of involution. FI0.5 and FI1 were pooled to represent the first phase, and FI2 and FI7 were pooled to obtain the second phase of forced involution. Boxplot parameters: the box contains 50% of the data points, the middle line is the median, whiskers and outliers represent the upper and lower 25% of the data. Outliers are outside the 1.5x interquartile range. ♦, outliers. Statistics: Mann-Whitney test with Bonferroni correction for multiple comparison (** $p < 0.01$, *** $p < 0.001$). P: pregnancy, L: lactation, FI: forced involution.

3.1.2 The CRISPR/Cas9 technology introduces a stable BAG3 knockout in mammary epithelial cells

Yet, it is not known in which cellular processes BAG3 is involved under physiological conditions in mammary epithelial cells. BAG3 reportedly influences cell survival and cell migration (Iwasaki et al., 2007), of which both processes are important in the developing mammary gland (Ewald et al., 2008; Hennighausen and Robinson, 2005). An *in vitro* assay was chosen to study the role of BAG3 in non-malignant mammary epithelial cells. The cell line HC11 was used, which drives prolactin-dependent *in vitro* induction of β -casein expression without the need of exogenously added ECM or co-cultivation with other cell types (Ball et al., 1988).

To determine the role of BAG3 in mammary gland development, we used clustered regularly interspaced short palindromic repeats (CRISPR) RNA-guided Cas9 nucleases to knock out BAG3

in mammary epithelial cells. Three single guide RNAs (sgRNAs) were used. sgRNA-T1 bound a region in exon 1, sgRNA-T2 targeted an intron between exon 1 and exon 2, and sgRNA-T3 targeted a region within exon 2 in the murine BAG3 gene. All three sgRNAs were in separate lentiviral vectors. HC11 cells were transduced with viral particles that were produced using the helper cell line HEK 293T/17. Following selection with puromycin, individual colonies were picked and grown under standard conditions. Protein extractions and Western analysis revealed promising clones that showed no synthesis of BAG3 protein (Figure 3-2a). Potential clones were T3B9, T3G9 and T1B8 (Figure 3-2a, red asterisks). These, and the negative controls, which were transduced with nonsense-scrambled sgRNA (sgscr), were further cultivated and analyzed. At single cell morphology, HC11 wildtype cells had filopodial cell protrusions and only few lamellipodia (Figure 3-2b, arrowheads). The cell clones sgscrE11, T1B8, T3B9 and T3G9 showed a similar morphology compared to the wildtype cells. Cell clone sgscrF11 showed many cells with extended cytoplasm and abundant filopodia (Figure 3-2b, arrows).

3.1.3 BAG3 is dispensable for lactogenic differentiation of mammary epithelial cells

Next, a lactogenesis assay with the potential BAG3 knockout cell lines was performed to investigate whether a knockout might influence the differentiation capability of the cells. Therefore, BAG3 was either re-expressed as a fluorescent fusion protein with EGFP or EGFP was expressed alone as a control. The lactogenesis assay was conducted and proteins were extracted 5 days after prolactin treatment. The detection of the milk protein β -casein was regarded as a successful lactogenic differentiation of the cells. We found that wildtype cells, regardless of BAG3-EGFP or EGFP expression only, underwent lactogenic differentiation. Interestingly, different results were obtained for the tested cell clones. The BAG3 knockout clone T3G9 expressed β -casein. In addition, the control clone sgscrE11 contained milk protein. However, β -casein was not detected in the BAG3 knockout clones T1B8 and T3B9. Interestingly, the control clone sgscrF11 did not differentiate successfully. The restored expression of BAG3-EGFP in the BAG3 knockout clones T1B8 and T3B9 as well as in the control cell line sgscrF11 failed to induce lactogenic differentiation (Figure 3-2c). This suggested that these cell clones lost their differentiation capabilities during the selection process. We concluded from this that BAG3 was not necessary in mammary epithelial cells to successfully undergo lactogenic differentiation, thereby leaving only one potential BAG3 knockout clone: T3G9.

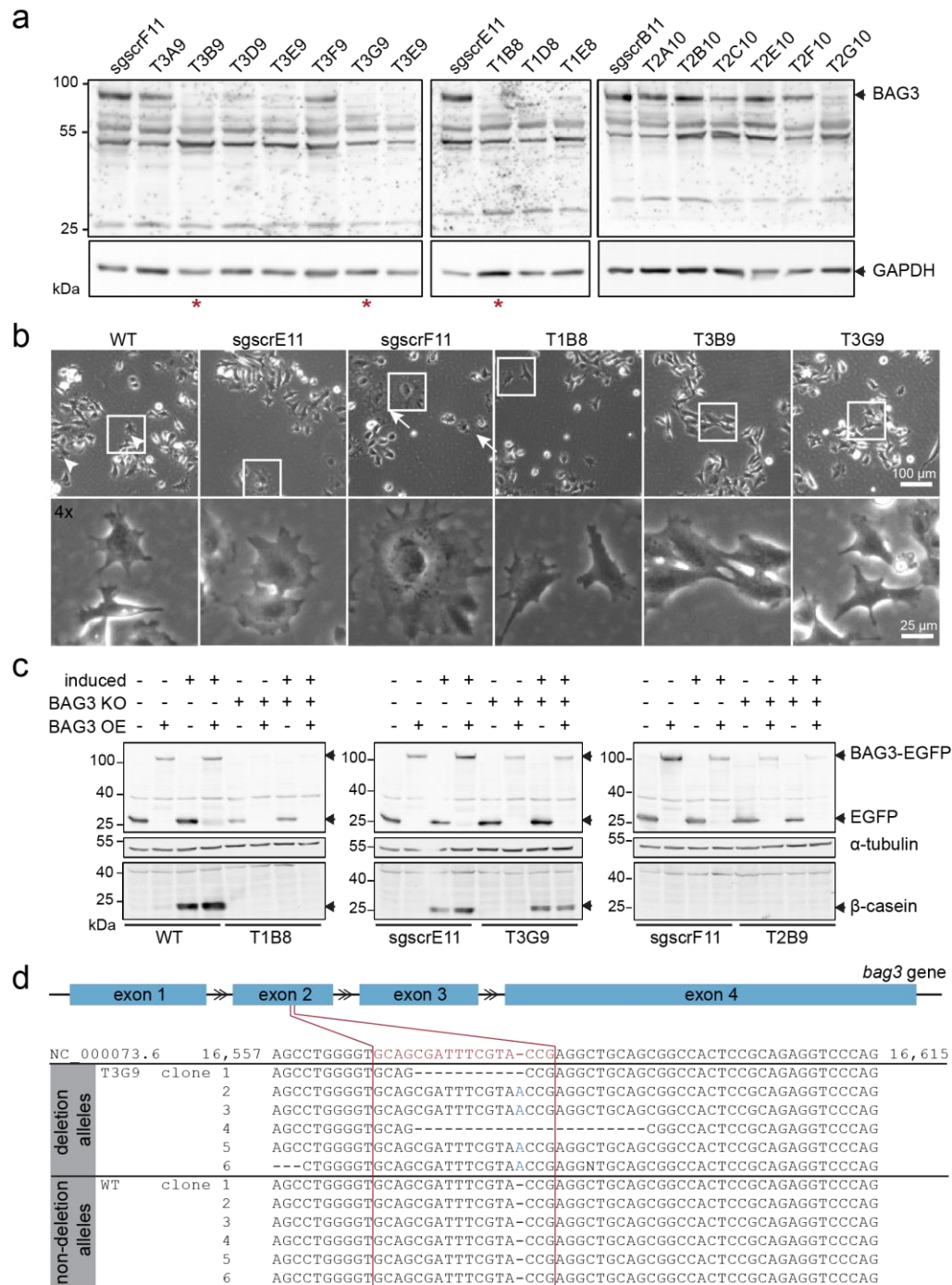


Figure 3-2 Generation and analysis of BAG3 knockout (KO) clones in HC11 cells. (a) Three sgRNAs targeting different regions in the murine BAG3 gene were transduced into HC11 cells. 16 clones were selected and BAG3 protein synthesis was analyzed. As a control, cells were transduced with viral particles containing a scrambled (sgscr) sgRNA sequence. BAG3 is expected to run between 70 kDa and 100 kDa (highlighted with an arrow). GAPDH was used as a loading control. Promising clones are highlighted with red asterisk. (b) Single cell morphology of potential knockout clones. Microscope: Zeiss Axiovert, objective lens: A-Plan 10x/NA 0.25. (c). WT, sgscr and potential BAG3 knockout clones were transduced with viral particles to express BAG3-EGFP or EGFP. Lactogenic differentiation was only present in clone T3G9. The expression of β -casein was analyzed in cell lysates. (d) Sequence alignment of bases 16,557-16,615 of the RefSeqGene murine BAG3 sequence (NC_000073.6). Genomic DNA was extracted and a region including the deletion site was amplified in multiple PCR reactions to capture both alleles. Following subcloning, Sanger sequencing revealed that one allele contained an insertion, while the other allele had a deletion of multiple nucleotides.

To characterize the gene editing further, genomic DNA was extracted from HC11 wildtype and the knockout cell line T3G9 and fragments were amplified with a primer pair flanking the region where the sgRNA-T3 bound complementary. PCR is a stochastic process, which will amplify both alleles of genomic target DNA when a certain amount of reactions is performed. Thus, several reactions were prepared to amplify the two alleles of the BAG3 gene. Following amplification, six fragments of the HC11 wildtype cells and the BAG3 knockout clone were TA cloned and sequenced. The sequencing data revealed that one allele contained a single nucleotide insertion, consequently resulting in a frame shift (Figure 3-2d, T3G9 clones 2, 3, 5, 6). The other allele had a deletion of at least ten nucleotides (Figure 3-2d, T3G9 clone 1). However, one sequenced clone had a deletion of 22 nucleotides (Figure 3-2d, T3G9 clone 4). This rose the question whether gene duplication, and thus multiple alleles of BAG3 were present in HC11 cells, or whether this result was due to inaccuracies in the sequencing analysis. Although we could not solve this question, we found that a biallelic mutation of the BAG3 gene was introduced in the T3G9 cell clone.

Taken together, these findings confirm the generation of a BAG3 knockout HC11 cell line using the CRISPR/Cas9 system.

3.1.4 Short hairpin RNA (shRNA) introduces a stable BAG3 knockdown in mammary epithelial cells

Studies have shown that a knockout via genetic inactivation compared to a knockdown via antisense mechanisms can lead to different phenotypes. Reasons for this are for example off-target effects of the antisense RNA or compensatory mechanisms upon complete loss of a protein (Rossi et al., 2015). This may also apply for the BAG3 knockout introduced by CRISPR/Cas9 gene editing. Thus, we decided to complement all phenotypic analyses with a stable BAG3 knockdown cell line.

Lotta Hof, who prepared her Master's thesis under my supervision, cloned the shRNA sequences, transduced the HC11 cells and evaluated the knockdown. Three short-hairpin RNAs were designed to target different regions on the BAG3 mRNA. shBAG3-1 and shBAG3-3, which target exon 2 and exon 4, respectively, have been successfully used as reported by previous studies (Meng et al., 2014; Homma et al., 2006). An alternative region on exon 4 was targeted by shBAG3-2 (Figure 3-3a). The shRNAs targeting BAG3 and the control (scrambled) were composed of a 20- or 21-nucleotide long sense strand, a loop region, a 20- or 21-nucleotide anti-sense strand and a transcriptional terminator sequence. A XhoI restriction site was added to the 3'-end (Figure 3-3b) to facilitate a 5' blunt and 3' cohesive end insertion into the pLeGO-iG2 vector (Figure 3-3c). Lentiviral particles were produced in the HEK 293T/17 helper cell line. The viral particle containing supernatant was used to transduce HC11 cells. Successfully transduced cells showed the expression of EGFP. The knockdown was evaluated by Western blotting analysis. It revealed that

only the shBAG3-3 construct sufficiently downregulated BAG3 expression in HC11 cells (Figure 3-3d).

FACS was used to enrich EGFP⁺ cells from the newly generated HC11 shBAG3 and HC11 shscr cell lines (Supplemental Figure 7-5a, b). In subsequent experiments, cells were used for a maximum of eleven passages (approximately four weeks of culture).

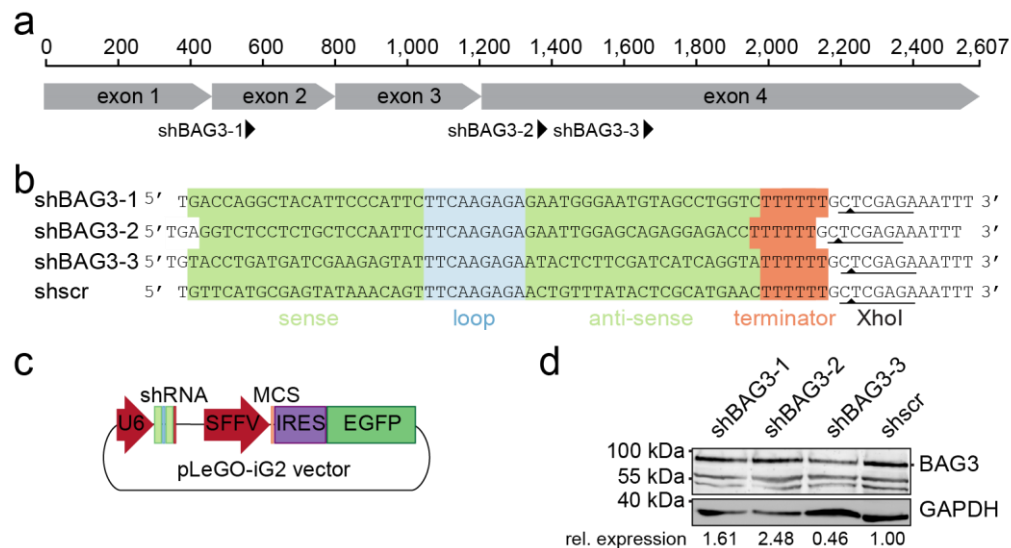


Figure 3-3 Generation of a BAG3 knockdown cell line. (a) Three regions on BAG3 mRNA (black triangles) served as targets for shRNA-mediated knockdown. (b) Sequence of shRNAs. From 5' to 3', all shRNAs contain a sense sequence, a loop region, an anti-sense sequence, which is followed by a terminator sequence. At their 5'-ends shRNAs were blunt-end inserted into the pLeGO vector, while their 3'-ends were enzymatically digested with XhoI before insertion. (c) An U6 promoter drives the expression of the shRNA inserted in the pLeGO-iG2 vector. An SFFV promoter drives the expression of EGFP. A multiple cloning site (MCS) facilitates additional insertion of an open reading frame (ORF). ORF and EGFP are expressed simultaneously. The internal ribosomal entry site (IRES) allows the ribosomes to translate both transcripts individually. This feature was not used in this setup. (d) Following transduction into HC11 cells, the expression of BAG3 was analyzed via SDS-PAGE and Western blot. 40 μ g protein lysate were loaded onto the gel. The relative expression of BAG3 against GAPDH is shown.

3.1.5 BAG3 knockout and knockdown cells develop different phenotypes

The major function associated with BAG3 is cell survival. By interaction with different molecules, BAG3 is involved several pathways (Rosati et al., 2011). Thus, the cell viability of HC11 was investigated in both, BAG3 knockdown and knockout cells. The cell viability was measured with a MTS assay. When the cells carried a knockdown for BAG3, cells were as viable as the controls (Figure 3-4a). However, the cell viability in BAG3 knockout cells was reduced by more than 20% ($p < 0.01$, Figure 3-4b). This suggests that only a complete lack of BAG3 makes cells more sensitive to cell death and that a low BAG3 expression is sufficient to circumvent cell death pathways.

Besides its pro-survival function, BAG3 has been reported to be associated with the regulation of cell adhesion, migration and invasion, thereby contributing to tumorigenesis and metastasis (Kassis et al., 2006; Iwasaki et al., 2007; Suzuki et al., 2011). To investigate whether BAG3 influences cell

migration in non-tumorigenic cells, a wound-healing assay was conducted with HC11 cells. The migration of cells into a gap was analyzed in both, the BAG3 knockdown and the knockout cell lines. This was recorded with a wide-field microscope. Images were acquired for 48 hours with intervals of 4 hours. A semi-automatic image analysis pipeline was established to analyze the dynamics of the closing gap over time (Supplemental Figure 7-6).

When BAG3 was downregulated (shBAG3), the gap closed significantly faster compared to the control (shscr). However, within the first 24 hours, shBAG3 cells moved equally fast into the gap compared to the control. From this time point on, shBAG3 cells moved faster into the gap. The differences became significant at time points 44 hours and 48 hours (Figure 3-4c). After 44 hours, the remaining gap sizes were 0.17 ± 0.03 (average \pm SEM) for the control and 0.08 ± 0.02 for BAG3 knockdown cells ($p < 0.05$). At time point 48 hours, the gap sizes were 0.13 ± 0.03 for the control and 0.05 ± 0.01 for knockdown cells ($p < 0.05$).

For the BAG3 knockout cells, a similar effect was observed. Within the first 16 hours after setting the gap, the BAG3 knockout cells and control cells occupied a similar area in the gap. From 20 hours on, BAG3 knockout cells moved faster into the gap. Between 24 hours and 48 hours, BAG3 knockout cells moved significantly faster into the gap (Figure 3-4d). For example, the remaining gap size after 32 hours for the knockout cells was 0.21 ± 0.04 compared to 0.36 ± 0.03 for the control ($p < 0.01$).

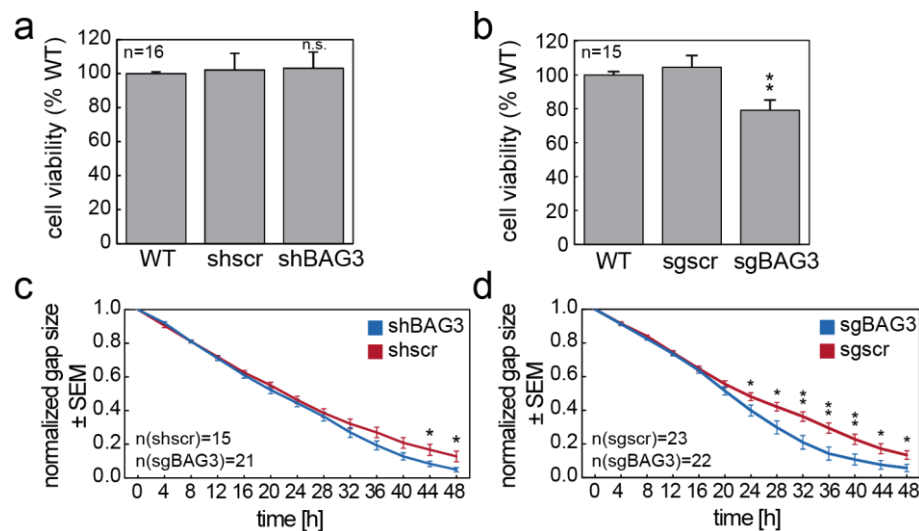


Figure 3-4 BAG3 affects cell viability and cell migration in mammary epithelial cells. (a, b) Cell viability was measured in HC11 cells with a stable BAG3 knockdown (shBAG3) and a BAG3 knockout (sgBAG3). Knockdown cells did not show a significant difference, but knockout cells showed a reduced viability of about 20%. Statistics: Kruskal-Wallis test. Five independent experiments were performed for shBAG3 cells and four independent experiments for sgBAG3 cells. (c, d) Cell migration of shBAG3 and sgBAG3 cells was analyzed over a period of 48 hours. shBAG3 cells migrated faster than the control, which was significant after 44 hours and 48 hours. sgBAG3 cells migrated faster than control cells, which was significantly different from 24 hours until 48 hours after the wound was set. Data for shBAG3 cells was obtained from four independent experiments, and for sgBAG3 from three independent experiments. Data analysis: Mann-Whitney test, for each condition, the highest and lowest outlier were not included into the statistical test (*: $p < 0.05$, **: $p < 0.01$).

In summary, these results showed that BAG3 enhanced cell survival in non-malignant mammary epithelial cells. In addition, a reduced BAG3 expression did not affect cell viability, which indicated that the amount of expressed BAG3 does not contribute to cell survival, but rather by its presence. In cell migration, both cell lines with BAG3 knockdown and knockout closed the wound area significantly faster than the controls. This indicated that the expression of BAG3 had a reducing impact on cell migration in non-tumorigenic mammary epithelial cells and that the migration capacity of the cells depended on the amount of BAG3 protein.

3.2 Fluorescence microscopy of large spheroids *in toto*

3.2.1 *In toto* immunostaining of large spheroids

To maintain the three-dimensional architecture of specimens, it is favorable to label and image them *in toto*. Small molecular dyes penetrate large three-dimensional specimens well. However, antibodies, which are frequently used in immunofluorescence staining, penetrate these specimens only poorly. This causes a concentration gradient from the surface to the inner regions and results in an inhomogeneous stain.

The following section describes the development of an evaluation for immunostaining protocols in three-dimensional spheroids. Julia Tarnick, a former Master student, performed experiments related to this project and helped with the analysis. The results of this project have been published 2017 in the journal *Biomedical Optics Express* (Smyrek and Stelzer, 2017). The contents of section 3.2.1 were adapted and modified from this publication.

Introduction of the evaluation criteria

The criteria, which are necessary to rate an immunostaining being successful are summarized in Figure 3-5a. First, a highly specific stain is indispensable in an immunofluorescence staining approach. Antibodies detect epitopes on proteins to give information about the gene expression, distribution and appearance of certain proteins or structures within cells. According to the treatment of the specimen, the stain is sensitive towards a destruction of the epitopes and the production of artifacts such as speckles, which make the data not interpretable (Schnell et al., 2012). Second, the fluorescence signal obtained from the stain has to be brighter than the background noise. High signal intensities affect the contrast positively, which is necessary to clearly identify specific structures and to eventually exert downstream applications such as object segmentation (Mathew et al., 2015). Third, the homogeneous distribution of the fluorophores is necessary to conclude about the strength of gene expression of the protein of interest in different regions of the specimen. It becomes especially important in thick three-dimensional specimens. Antibodies are large molecules and, due to their size and charge, poorly diffuse into regions inside three-dimensional specimens.

However, the density of the specimens does not facilitate a homogeneous stain. Dense specimens exhibit a certain spatial hindrance for antibodies to diffuse without restriction. While the researcher rates the first aspect of specificity, the other two aspects (i.e. intensity and homogeneity) are measurable quantities.

Introduction of the evaluation procedure

Following immunostaining, spheroids were optically cleared using Murray's clear (Dent et al., 1989) to render the inner spheroid region accessible for fluorescence microscopy. LSFM facilitated a rapid acquisition of the entire spheroid. The image data was analyzed by computing average projections, in which an intensity profile through the center of the spheroid was measured. The ratio between the mean signal and the standard deviation of the background signal provided information about the signal intensity (Figure 3-5b). To assess the homogeneity of the stain, the radial dispersion of the fluorophores was measured. Therefore, the intensity profiles of the antibody staining was plotted against the intensity of the DAPI stain (Figure 3-5b). DAPI, a small organic molecule of only a few hundred Dalton diffuses easily even through large amount of biomaterials, thus providing a gold standard for a homogeneous fluorophore distribution in spheroids. Next, we computed the Pearson's R correlation coefficient, which is a measure for the linear dependence between (at least) two variables. With it, values close to one represent a linear relationship between the antibody and the DAPI stain, while values close to zero do not.

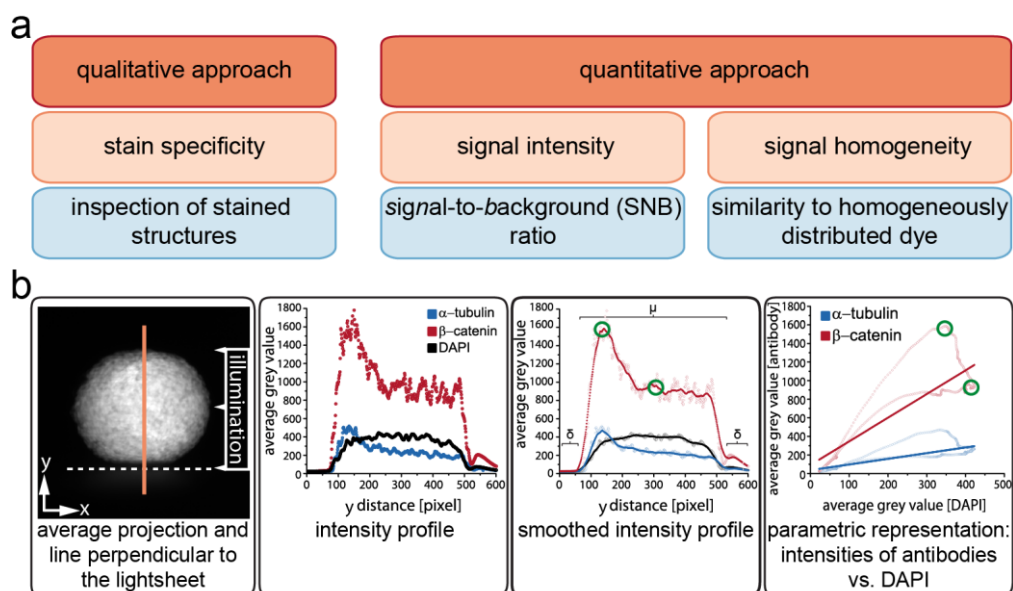


Figure 3-5 Schematic of the evaluation procedure. (a) For a successful evaluation, three main properties of the immunostaining have to be considered, the stain specificity, the signal intensity and the signal homogeneity. The first one is a qualitative approach, while the other two are quantitative measures of the SNB ratio and the homogeneity of the signal. (b) The optically cleared spheroid is mounted onto the sample holder (the edge of the sample holder is indicated with the white dashed line). The illuminating laser beam hits the spheroid from the right side. The first post-processing step is the computation of an average projection of the image z-stack. At the center of the spheroid, the intensity profile along a line orthogonal to the direction of the light sheet (orange line) is measured in each fluorescence channel (i.e.: α -tubulin, β -catenin and DAPI).

The intensity profiles are smoothed to reduce morphological variations. To obtain the SNB ratio, the average signal (μ) is compared to the standard deviation of the background signal (δ). To assess the signal homogeneity, the DAPI signal is regarded as the ideal dispersion of the fluorophores in the spheroid. Thus, the smoothed grey values of the antibodies are plotted against the smoothed DAPI values and the correlation is computed. The output is the Pearson's R, where one and zero indicate a match and a difference of antibody and the DAPI profile, respectively. The red circles show the location of the highlighted values in the different representations. (modified from Smyrek and Stelzer, 2017).

Summing it up, an evaluation of the three parameter, (1) the stain specificity, (2) the signal intensity, and (3) the signal homogeneity, give valuable information about the success of an immunostaining approach in spheroids.

Overview of the immunostaining protocols

All immunofluorescence staining approaches share common existing protocols and common steps, which are (1) the fixation, (2) the permeabilization, (3) the blocking, (4a) the primary antibody incubation, and eventually (4b) the secondary antibody incubation. All of these steps are to a certain extent variable to improve the staining quality. Thus, all steps were varied except for the blocking, which was performed according to Debnath *et al.* with BSA, goat serum, Triton X-100 and Tween-20 (Debnath et al., 2003). Various fixation conditions were tested systematically using either PFA, ethanol or methanol-acetone (Figure 3-6). A fixation with organic solvents such as alcohols already permeates or even dissolves biological membranes, and therefore did not require a subsequent permeabilization. Differently, specimens fixed with the crosslinker PFA were subjected either to a detergent-based permeabilization with Triton X-100, or they were permeabilized using the organic solvents ethanol or methanol (Figure 3-6). Not least, we examined several antibody incubation conditions. The antibody concentration remained constant, but the incubation temperature from the usual 4°C for long-term incubation was elevated to 37°C. Further, we compared a four-hour long incubation for the secondary antibodies to an overnight incubation. The detailed protocols are listed in Supplemental Table 7-2.

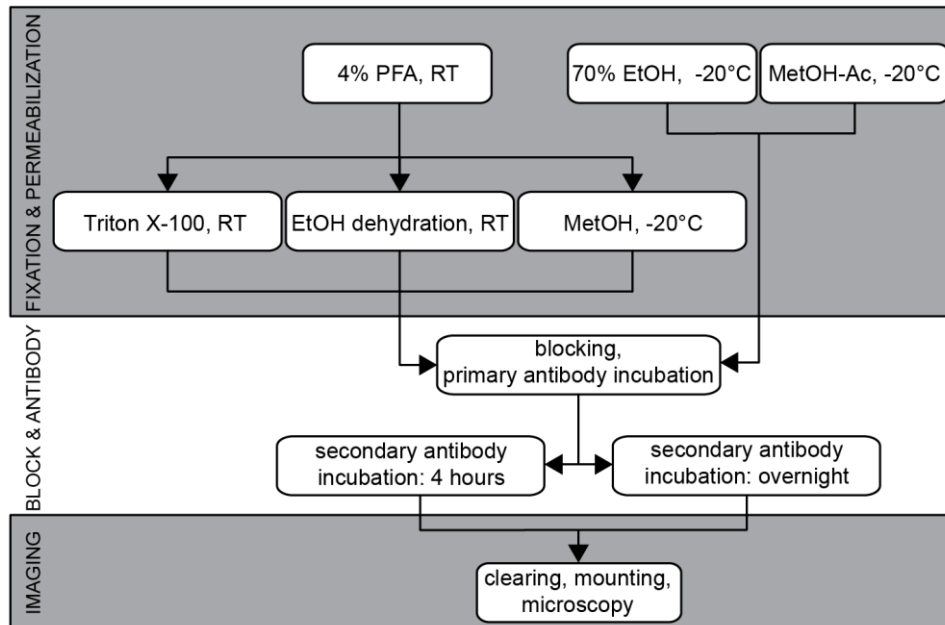


Figure 3-6 Schematic of the tested immunostaining protocols. The main steps are fixation, permeabilization, blocking, antibody incubation and optical clearing. RT: room temperature. (modified from Smyrek and Stelzer, 2017).

Paraformaldehyde fixation maintains the staining specificity

In this project, we decided to work with the human oligodendrogloma cell line U343, which quickly forms round spheroids and thereby ensures a high degree of reproducibility. To obtain spheroids with an average diameter of approximately 600 μm , 10,000 U343 cells were seeded and spheroids were formed for 6 days (Figure 3-7a). The detection of two well-known proteins that display characteristic structural detail was chosen: β -catenin and α -tubulin. β -catenin is a protein involved in adherens junction formation, and is therefore mainly located at the plasma membrane of cells. α -tubulin is a subunit of the microtubule cytoskeleton. In a three-dimensional context, the microtubules rather accumulate in the cell periphery, whereas the spindle apparatus is a characteristic of mitotic cells. Cell nuclei were stained with the small organic dye DAPI.

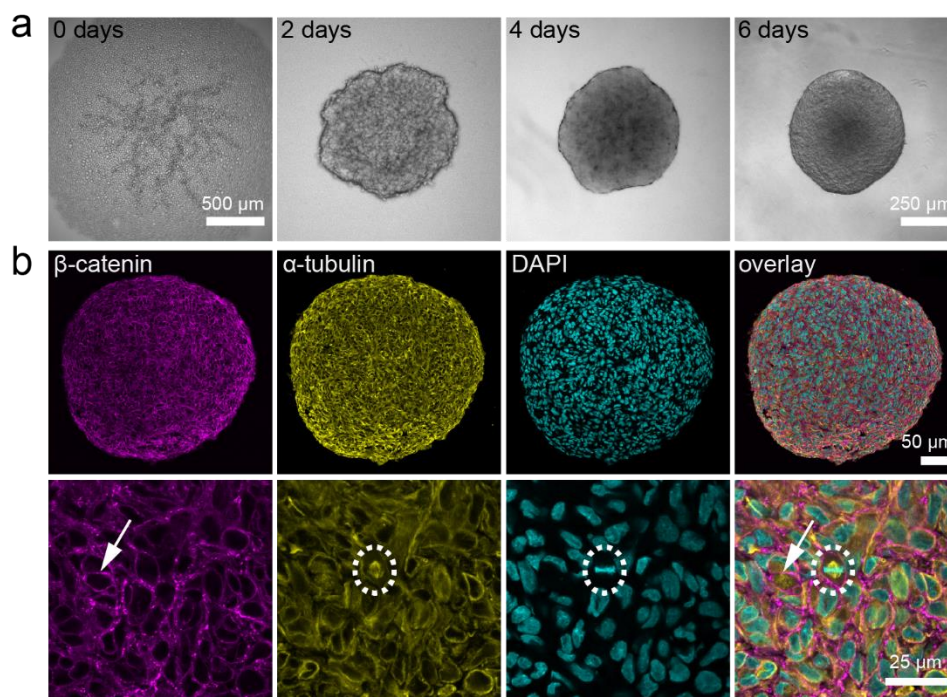


Figure 3-7 Immunohistochemistry analysis of U343 spheroid center sections shows a nearly homogeneous stain for α -tubulin and β -catenin. (a) U343 spheroids were formed for 6 days from 10,000 seeded cells and had an approximate diameter of at least 500 μm (b) Paraffin-embedded spheroids were cut into 4 μm thick sections and stained against α -tubulin and β -catenin. A section from a spheroid shows the dispersion of the signal for α -tubulin as well as β -catenin. Cell nuclei were stained with DAPI. β -catenin localizes at the plasma membranes of cells (arrow). A specific stain for α -tubulin, a component of the microtubules, is well recognizable in the mitotic spindle (dashed circle). Microscope: Zeiss LSM780; objective lens (upper panel): Plan-Apochromat 20x/numerical aperture (NA) 0.8; objective lens (lower panel): Plan-Neofluar 40x/NA 1.3. (modified from Smyrek and Stelzer, 2017).

In histological sections from U343 spheroids, the signals for α -tubulin and β -catenin were almost evenly distributed in the spheroid, suggesting an uniform expression throughout the spheroid. Only the intensity of the β -catenin signal was slightly stronger at the spheroid rim. Here, cells often adapted a shape that suggested compression compared to the cells in the in the spheroid interior. This indicated that the increased signal at the rim was due to increased cell compaction at the spheroid surface (Figure 3-7b, upper panel). At cellular detail, the β -catenin stain in U343 spheroids, it clearly highlighted the cell circumference (Figure 3-7b, lower panel, white arrow). A specific α -tubulin antibody staining was best observable during mitosis when the microtubules organize to form the mitotic spindle (Figure 3-7b, lower panel, dashed circle).

When we investigated the *in toto* stained U343 spheroids, we found that in about 50% of the tested conditions, the spindle apparatus was not detectable. This was most evident for staining protocols that used organic solvents at any point of the protocol. The loss of stain specificity resulted in a punctate pattern (Figure 3-8, left column). In comparison, in all tested protocols, the β -catenin antibody stained the cell circumference indicating a high specificity of this stain (Figure 3-8, middle column).

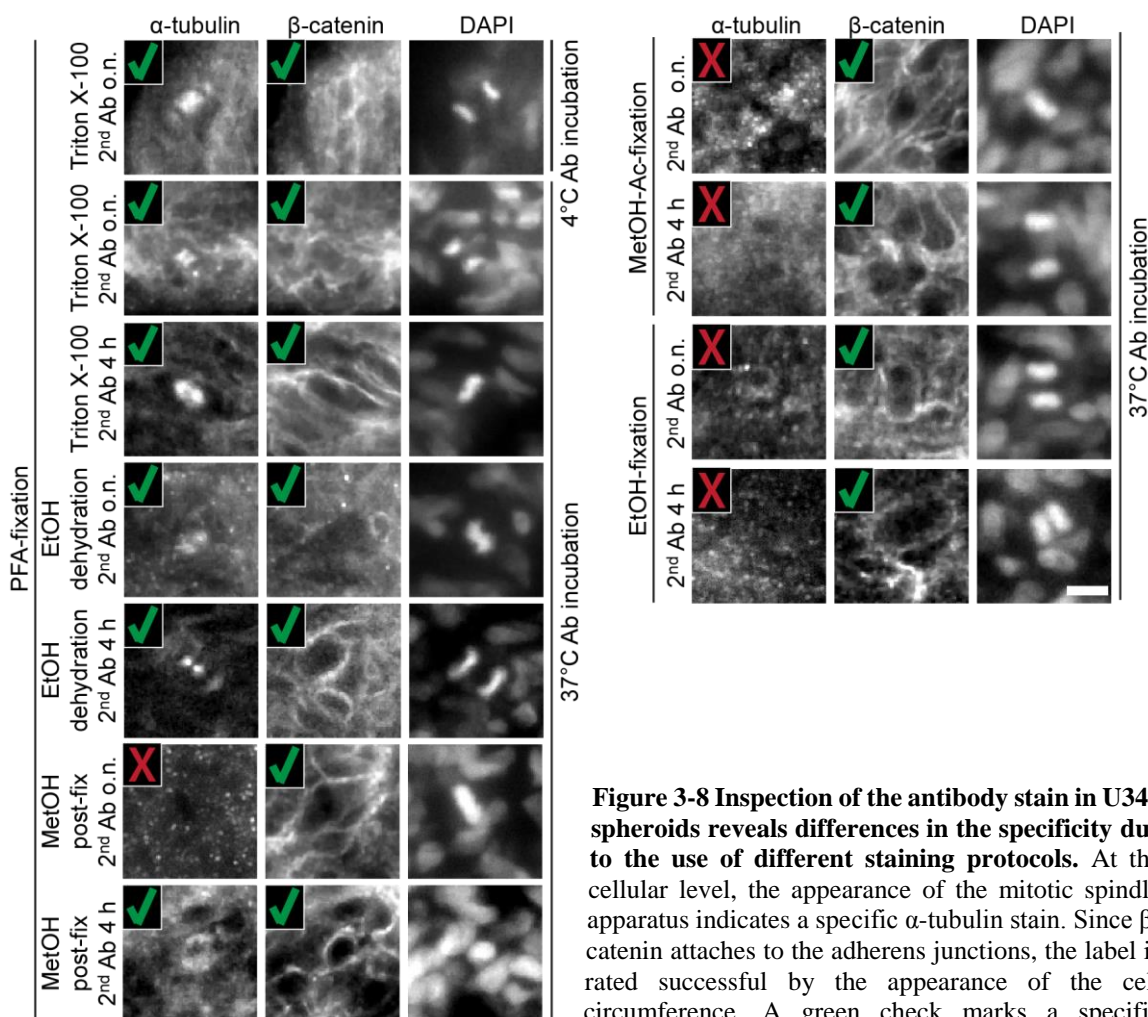


Figure 3-8 Inspection of the antibody stain in U343 spheroids reveals differences in the specificity due to the use of different staining protocols. At the cellular level, the appearance of the mitotic spindle apparatus indicates a specific α -tubulin stain. Since β -catenin attaches to the adherens junctions, the label is rated successful by the appearance of the cell circumference. A green check marks a specific

antibody stain and a red cross marks an unspecific stain. Microscope: mDSLMS; illumination lens: Epiplan-Neofluar 2.5x/NA 0.06; detection lens: N-Achroplan 20x/NA 0.5; α -tubulin: 561 nm, 0.09 mW, bandpass filter 607/70; β -catenin: 488 nm, 0.15 mW, bandpass filter 525/50; DAPI: 405 nm, 0.01 mW, bandpass filter 447/55; scale bar: 10 μ m. Ab: antibody; o.n.: overnight; h: hours. (modified from Smyrek and Stelzer, 2017).

In summary, *a priori* knowledge about the localization and expression pattern of the antigen of interest is necessary to assess the stain specificity. The antibodies against α -tubulin and β -catenin performed differently regarding the stain specificity, indicating that certain chemicals, i.e. organic solvents, can harm the epitope recognition sites of certain antigens, i.e. α -tubulin.

The antibody incubation time and temperature influence the fluorescence intensity

Next, quantitative approach evaluated the staining quality. First, the measured signal intensities of all conditions and all samples were plotted (Figure 3-9a). These plots showed that the fluorescence intensity varied strongly between the different conditions and that in some conditions, the signal intensities differed along the y distance. The next step achieved a comprehensive comparison between the different staining protocols by calculating the SNB ratio (Figure 3-5 and Figure 3-9b). The median values of the SNB ratio are summarized in Table 3-1.

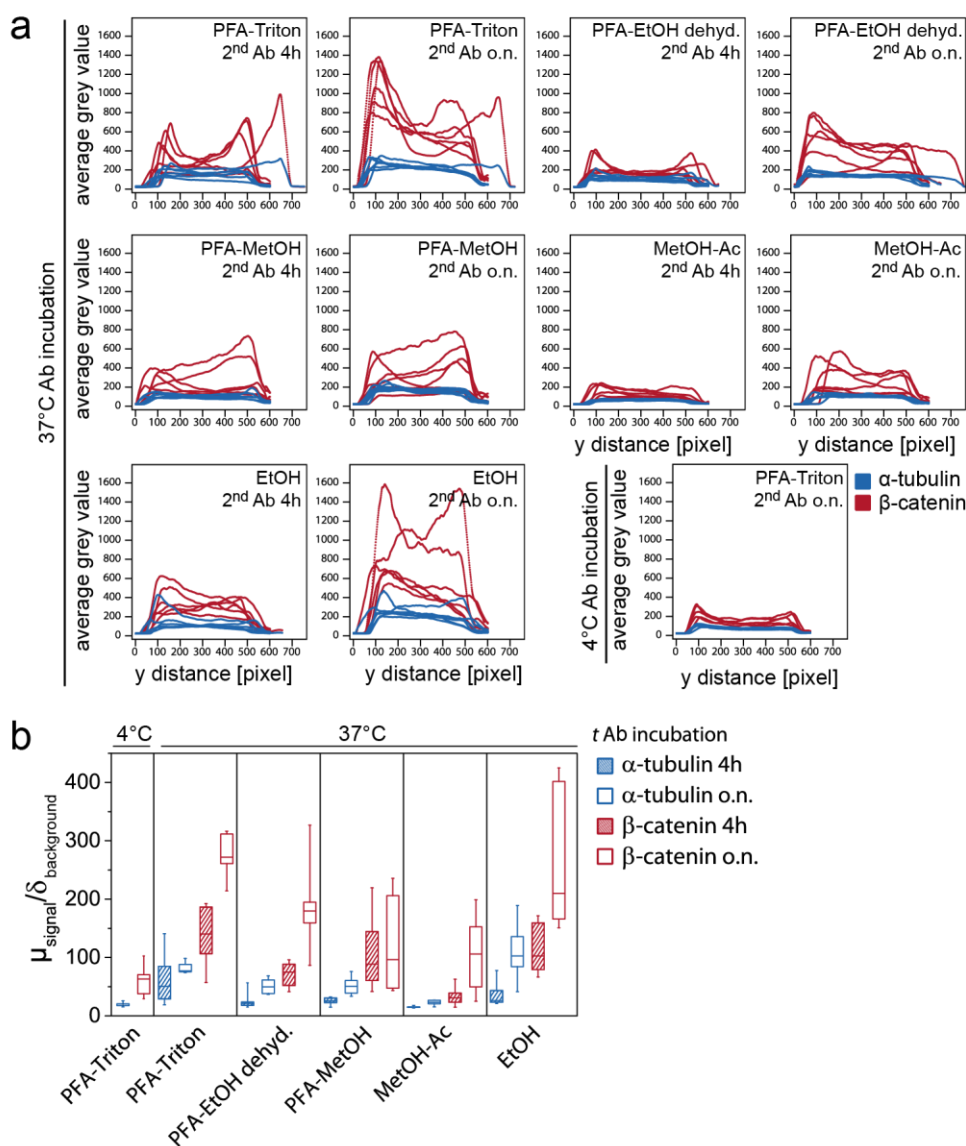


Figure 3-9 Overview of the signal intensities in spheroids obtained from different immunostaining conditions. (a) Smoothed average signal intensity plots. For all conditions and samples, α -tubulin and β -catenin intensity values are plotted against the pixel distance along a line through the center of the spheroid. An incubation temperature of 37°C improves the signal intensity compared to the conventional incubation at 4°C. The short incubation time of the secondary antibody for 4 hours results in lower signal intensities. (b) The ratio between the mean intensity of the spheroid and the background intensity is a measure of the intensity yield. Ratios with values above 60 and low variance are desirable whereas values below 30 are considered insufficient. Boxplot parameters: the box contains 50% of the data points, the whiskers and outliers show the upper and lower 25% of the data. The line in the box is the median. $N(\text{PFA-Triton-4}^\circ\text{C}) = 5$, $n(\text{PFA-MetOH o.n.}) = 7$, $n(\text{rest}) = 6$. Ab: antibody, Ac: acetone, dehyd.: dehydration, EtOH: ethanol, h: hours, MetOH: methanol, o.n.: overnight. (modified from Smyrek and Stelzer, 2017).

An antibody incubation at the conventional incubation temperature of 4°C obtained signal intensities for α -tubulin and β -catenin stain of 19.40 and 60.63, respectively. However, an increase of the antibody incubation temperature to 37°C resulted in an increase of the signal intensities in most cases. The only exception was when spheroids were fixed with methanol-acetone and the secondary antibodies were incubated for only 4 hours. Here, the SNB ratios were 15.13 for α -

tubulin and 33.52 for β -catenin. Interestingly, a prolonged secondary antibody incubation time increased the SNB ratio to 22.69 and 106.41 for α -tubulin and β -catenin, respectively. The organic solvent-based fixation with ethanol resulted in ratios of 36.30 for α -tubulin and 113.56 for β -catenin for a four-hour secondary antibody incubation period, and 109.37 and 260.54 for an overnight incubation. When ethanol or methanol were used following a PFA fixation, similar values were obtained for the signal intensity. PFA fixation followed by a detergent-based permeabilization also increased the SNB ratios (for α -tubulin for 4 hours and overnight incubation 62.41 and 81.75, and for β -catenin 137.10 and 274.58) (Table 3-1).

Table 3-1 Overview of the immunofluorescence quality evaluation from different staining protocols. Evaluation parameter describe (1) the specificity of the stain estimated by the appearance of expected structures, (2) the signal intensity described by the SNB ratio and (3) the homogeneity of the antibody stain described by the R-value of the similarity of the intensity profiles to the DAPI stain. Stain specificity: green indicates that the stain for α -tubulin shows the spindle apparatus during mitosis and that β -catenin is located at the cell periphery. Signal intensity: green indicates a ratio above 60, orange indicates ratios between 30 and 60, and white shows ratios below 30. Signal homogeneity: green indicates values above 0.75, orange values between 0.55 and 0.74 and, white is used for values below 0.54 (adapted from Smyrek and Stelzer, 2017).

protocol (short description)	<i>t</i> sec. AB incubation	epitope	stain specificity	signal intensity	signal homogeneity
PFA-Triton-4°C	o.n.	α -tubulin	yes	19.40	0.568
PFA-Triton-4°C	o.n.	β -catenin	yes	60.63	0.501
PFA-Triton-37°C	4 hours	α -tubulin	yes	62.41	0.823
PFA-Triton-37°C	o.n.	α -tubulin	yes	81.75	0.797
PFA-Triton-37°C	4 hours	β -catenin	yes	137.10	0.633
PFA-Triton-37°C	o.n.	β -catenin	yes	274.58	0.433
PFA-EtOH-37°C	4 hours	α -tubulin	yes	25.86	0.706
PFA-EtOH-37°C	o.n.	α -tubulin	yes	50.71	0.589
PFA-EtOH-37°C	4 hours	β -catenin	yes	71.23	0.559
PFA-EtOH-37°C	o.n.	β -catenin	yes	187.75	0.488
PFA-MetOH-37°C	4 hours	α -tubulin	yes	25.22	0.762
PFA-MetOH-37°C	o.n.	α -tubulin	no	50.92	0.857
PFA-MetOH-37°C	4 hours	β -catenin	yes	107.27	0.435
PFA-MetOH-37°C	o.n.	β -catenin	yes	119.76	0.713
MetOH-Ac-37°C	4 hours	α -tubulin	no	15.13	0.956
MetOH-Ac-37°C	o.n.	α -tubulin	no	22.69	0.876
MetOH-Ac-37°C	4 hours	β -catenin	yes	33.52	0.870
MetOH-Ac-37°C	o.n.	β -catenin	yes	106.41	0.709
EtOH-37°C	4 hours	α -tubulin	no	36.30	0.947
EtOH-37°C	o.n.	α -tubulin	no	109.37	0.884
EtOH-37°C	4 hours	β -catenin	yes	113.56	0.875
EtOH-37°C	o.n.	β -catenin	yes	260.54	0.846

AB: antibody, Ac: acetone, EtOH: ethanol, MetOH: methanol, o.n.: overnight.

Alcohol-based fixation improves antibody penetration in large spheroids

Optical sections of the central spheroid regions showed that the penetration of the fluorophores differs strongly between the different immunofluorescence staining protocols (Figure 3-10a).

Thus, we analyzed the radial dispersion of the fluorophores from the spheroid surface into the inner spheroid region. This was achieved by correlating (Pearson's R) the antibody signal intensity with the intensity of the homogeneously dispersed dye DAPI.

When the antibody incubation was carried out at 4°C, the median Pearson's R-values were 0.568 for the α -tubulin and 0.501 for the β -catenin stain. Interestingly, when the antibody incubation temperature was 37°C, the Pearson's R increased in all tested conditions for the α -tubulin stain, and for most conditions when β -catenin was stained. The exceptions were a PFA fixation, which was followed either by a Triton X-100 permeabilization (Pearson's R 0.433) or by an ethanol de- and rehydration (Pearson's R 0.488) in combination with an overnight secondary antibody incubation. When an ethanol de- and rehydration for permeabilization followed a PFA fixation, the antibodies poorly diffused into the spheroids. The R-value for α -tubulin and β -catenin were 0.706 and 0.559, respectively, when the secondary antibodies were incubated for 4 hours, and 0.589 and 0.488 when the antibody incubation was prolonged to overnight. When methanol was used to permeabilize following a PFA fixation, we obtained R-values for α -tubulin with 0.762 and 0.857 and β -catenin with 0.435 and 0.713 for a secondary antibody incubation for 4 hours and overnight, respectively. Interestingly, the most homogenous dispersion of the antibodies was achieved when spheroids were fixed with organic solvents such as ethanol or methanol-acetone. Here, R-values for both antibody labels were between 0.846 and 0.947 for ethanol-fixed samples, and 0.709 and 0.956 for methanol-acetone-fixed samples (Figure 3-10b and Table 3-1).

As reported by the Pearson's R correlation coefficient, it occurred that the α -tubulin antibody penetrated well into the deep parts of the spheroids whereas the antibody against β -catenin labeled the outer rim of the spheroid but in most cases failed to reach the interior region (Figure 3-10a). Interestingly, the dispersion of the fluorophores was often more consistent when the short incubation time of 4 hours was used for the secondary antibody.

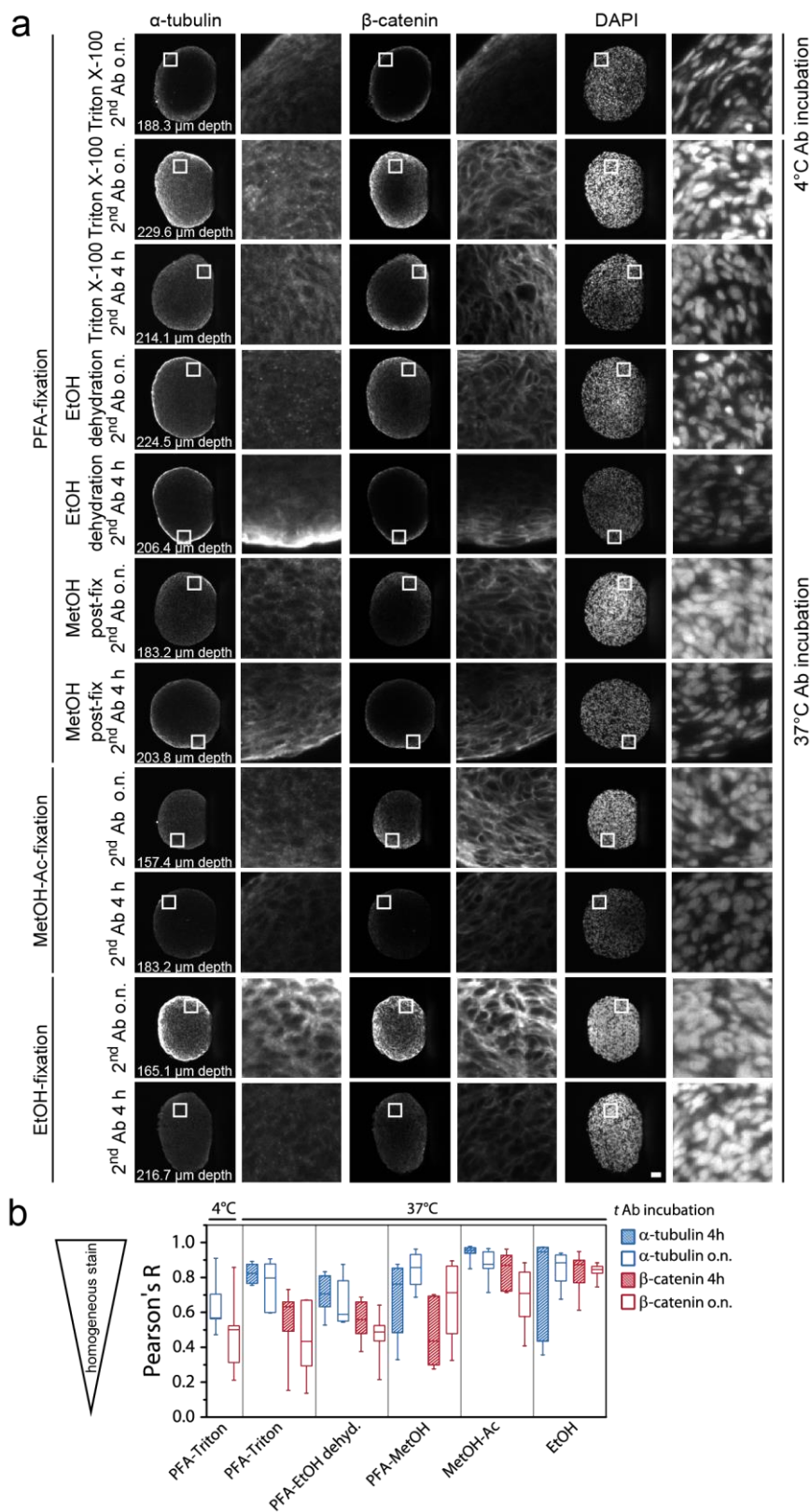


Figure 3-10 Antibody diffusion into spheroids varies between the different immunostaining protocols.

(a) Single planes from the central region (z-depth is indicated) from U343 spheroids show the dispersion of the antibody as well as the quality of the stain. White squares show the magnified areas (8x) in each spheroid. Microscope: mDSLMS; illumination lens: Epiplan-Neofluar 2.5x/NA 0.06; detection lens: N-Achroplan 10x/NA 0.3; α -tubulin: 561 nm, 0.09 mW, bandpass filter 607/70; β -catenin: 488 nm, 0.134 mW, bandpass filter 525/50; DAPI: 405 nm, 0.01 mW, bandpass filter 447/55; scale bar: 50 μ m. (b) The Pearson's R

describes the degree of similarity between the antibody and the DAPI intensity profiles. DAPI represents a homogeneous dispersion of a fluorophore within a spheroid. Boxplot parameters: the box contains 50% of the data points, the whiskers and outliers show the upper and lower 25% of the data. The line in the box is the median. Ab: antibody; Ac: acetone, dehyd.: dehydration, EtOH: ethanol, h: hours, MetOH: methanol, o.n.: overnight. (modified from Smyrek and Stelzer, 2017).

To summarize this section, we introduced an objective evaluation procedure to analyze the quality and success of immunofluorescence staining the three-dimensional specimens such as cellular spheroids. This procedure includes the examination of the stain specificity, and the measurement of the signal intensity and the signal homogeneity. Based on this, we tested various existing immunofluorescence staining protocols and modified them. We concluded that a fixation using a cross linker such as PFA was most suitable to obtain a specific antibody label. In combination with this, a detergent-based permeabilization and an increase of the antibody incubation temperature to 37°C positively affected the signal intensity as well as the dispersion of the fluorophores compared to an alcohol-based permeabilization or an antibody incubation temperature at 4°C. In addition, a shorter incubation period for the secondary antibody provided more stain homogeneity than a prolonged incubation. The outcome is a timesaving, straightforward and inexpensive immunofluorescence staining protocol for large three-dimensional spheroids *in toto* (Figure 3-11).

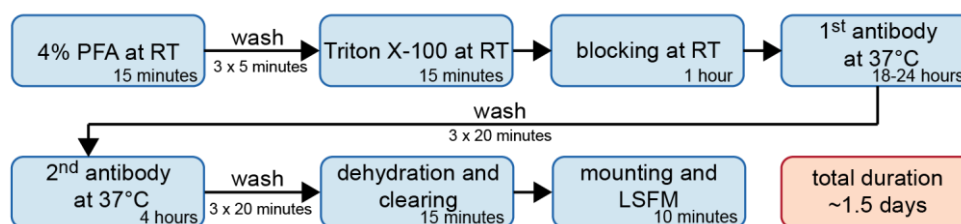


Figure 3-11 Illustration of the suggested immunofluorescence protocol for large spheroids. The duration from sample fixation to image acquisition consumes approximately 1.5 days. This timesaving protocol comprises a sample fixation with PFA followed by a detergent-based permeabilization and block of unspecific binding sites. To facilitate a homogeneous dispersion of the antibody, the incubation temperature is set to 37°C, while all other steps are performed at room temperature. Optical clearing achieves transparency of the stained specimens. The cleared samples are investigated with LSFM. RT: room temperature. (modified from Smyrek and Stelzer, 2017).

3.2.2 A comparison between multi-view image fusion and optical clearing

In this work, two approaches to improve image quality of spheroids imaged *in toto* with LSFM have been compared. The multi-view image fusion approach addresses the problem by combining images acquired from different views into a single image. The acquisition of multi-view image datasets can be achieved by rotating the specimen around its y-axis in the microscope, which are later fused to obtain a single high-quality image (Figure 3-12a). Multi-view image fusion has been implemented as a plugin for *ImageJ* (Preibisch et al., 2010). The second approach is optical clearing of the specimen. When optically cleared specimens are used, the light scattering effect is negligible and cellular detail is obtained from all regions of the specimen without the need for acquiring multiple views (Figure 3-12b).

Elena Gosau wrote her Bachelor thesis on this topic. Alexander Schmitz and I supervised her thesis. Thus, Elena acquired all experimental data, which she analyzed either by herself or together with Alexander. I contributed to this work by developing and guiding the project, giving practical advice and interpreting the results.

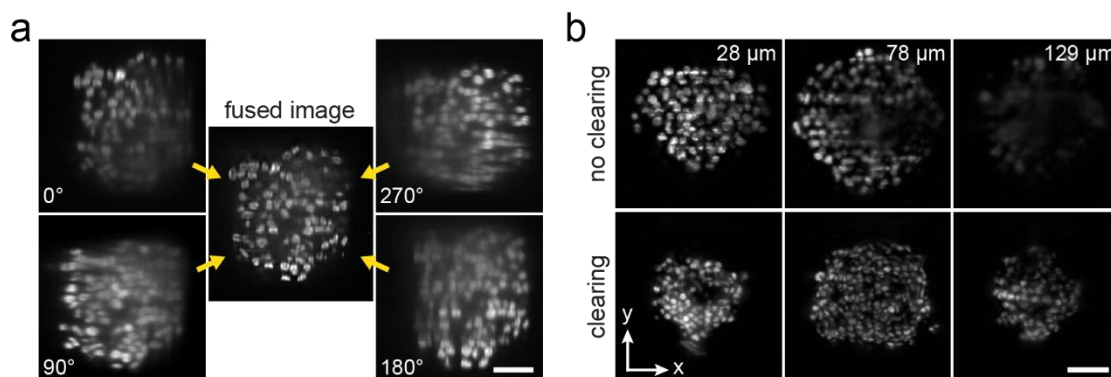


Figure 3-12 Approaches to obtain insight into biological specimens with LSFM. (a) Single planes along z-y-direction from four different view angles. Image fusion combines the information of the four view angles in one three-dimensional image (see image in the center). (b) Optical sections of different depths along the x,y-direction of a non-cleared and a cleared spheroid. Clearing improves the obtained image quality by reducing light scattering. Regions deep within the specimens are not blurred. Microscope: mDSLm, illumination lensMVF: 2.5x/NA 0.06, illumination lensOC: 5x/NA 0.16, detection lens: 20x/NA 0.5, fluorophore/laser: DAPI/405 nm, scale bar: 50 μm . MVF: multi-view image fusion, OC: optical clearing.

Spheroids were generated from human (T47D) and mouse (4T1) mammary breast tumor cell lines. Cell nuclei and β -catenin were labeled in these spheroids. LSFM was used to acquire images of spheroids from four view angles (0° , 90° , 180° , 270°). For multi-view imaging, spheroids were mounted onto a pinhole sample holder in a drop of agarose. This drop contained fluorescent beads, which later served as landmarks for the image reconstruction with the *ImageJ* plugin *Multiview Reconstruction* (Preibisch et al., 2010). The appropriate bead concentration required for the registration of the images was found to be 1.8×10^6 beads per μl (Supplemental Figure 7-8).

Next, visualizations of the data sets were investigated from three view directions (x,y; x,z and y,z), which showed that the fused images reached a virtually isotropic resolution (Figure 3-13a). In the fused images, all cell nuclei in T47D spheroids were resolved (Figure 3-13a, upper panel). Contrary, fused images of 4T1 spheroids showed a blurred region, which immediately started below the first few cell layers below the spheroid surface. Cell nuclei in this central region of 4T1 spheroids were not resolved (Figure 3-13a, lower panel).

In the second approach, Murray's clear (Dent et al., 1989) was used to render spheroids transparent. The clearing solution BABB disintegrates polystyrenes and thus has to be kept separate from the detection objective and the plastic-ware inside the microscope chamber. Therefore, the cleared spheroids were transferred into a rectangular glass capillary, which was mounted on a stainless steel holder into the microscope. For these experiments, a 5x illumination lens was used to produce a

light sheet with a thinner waist. This improved the axial resolution (Supplemental Figure 7-9), which provided images with similar quality observed from either direction, x,y; x,z or y,z (Figure 3-13b). The data sets were investigated along different directions, which showed that this approach resolved all cell nuclei in the spheroids of both cell lines, even those in the center of the spheroids (Figure 3-13b).

The optical clearing technique is a harsh treatment that uses alcohols to dehydrate the sample. Thus, we hypothesized that the cell and cell nuclei morphology is altered upon optical clearing. The cell nuclei staining showed that the shape of the cell nuclei was not altered when spheroids were optically cleared. Apparently, the cell nuclei volume was reduced (Figure 3-13a, b). To investigate the morphology of the cells, the membrane-associated protein β -catenin was stained in the spheroids to outline the cell circumference. The cells decreased in size upon optical clearing. However, the outlining of the cells (i.e. β -catenin stain) remained intact and no membrane ruffling, which indicates improper dehydration, was observed (Figure 3-13c).

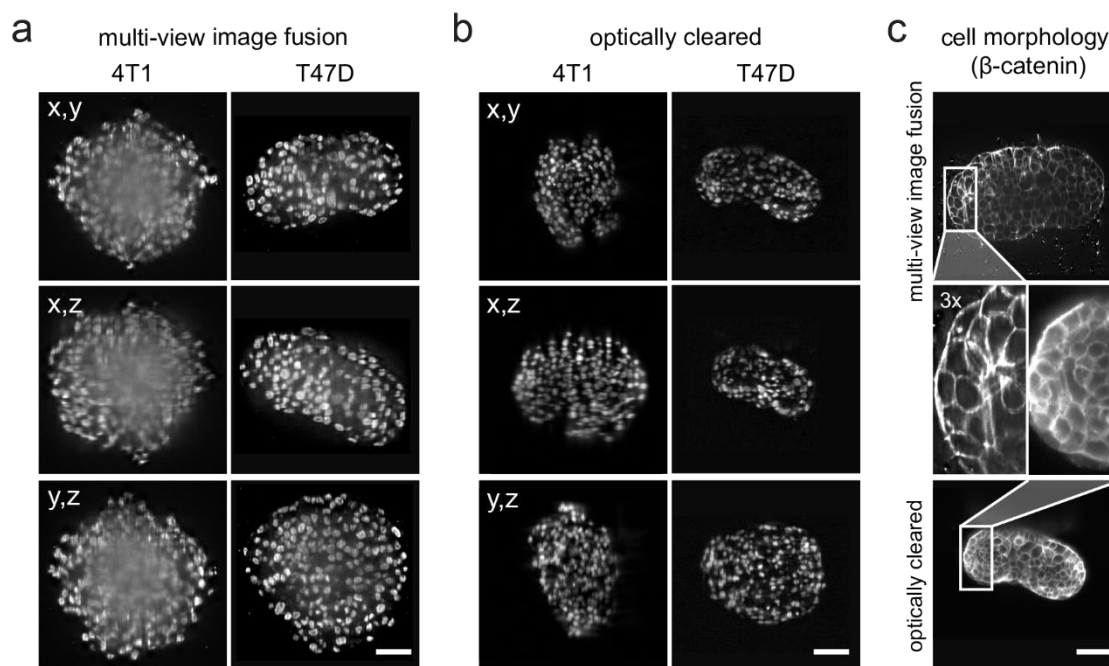


Figure 3-13 Comparison of image quality and of spheroid morphology using different LSFM imaging techniques. (a) Multi-view image fusion was performed with T47D and 4T1 spheroids by recording data from four view angles. The reconstructed images of 4T1 spheroids have low contrast in the central region of the spheroid. (b) T47D and 4T1 spheroids were optically cleared and then recorded along one direction. Clearing reduced the spheroid volume but provided information from all regions of the spheroid. (c) Cell morphology was investigated by staining membrane-associated β -catenin. Cells shrink upon optical clearing. The appearance of the membrane is comparable to not cleared specimens. Microscope: mDSLML, illumination lensMVF: Epiplan-Neofluar 2.5x/NA 0.06, illumination lensOC: Plan-Neofluar 5x/NA 0.16, detection lens: 20x/NA 0.5, scale bar: 100 μ m. MVF: multi-view image fusion, OC: optical clearing.

Next, the data sets generated with both approaches were subjected to our segmentation pipeline to obtain quantitative information about the spheroid volume and the cell nuclei volume. This pipeline

has been developed and implemented by Alexander Schmitz and Dr. Sabine Fischer (Schmitz et al., 2017). The segmentation performance was analyzed and compared. Generally, the cell nuclei segmentation performance was better for images with higher contrast. Images from T47D spheroids showed high contrast independent of the approach. In 4T1 spheroids, the cell nuclei segmentation performance was higher for optically cleared spheroids. For 4T1 spheroids, the central part of the spheroid in fused data sets was not resolved and thus did not allow a segmentation of cell nuclei (Supplemental Figure 7-10).

Most optical clearing reagents are harmful and probably affect the morphology of the specimen. We characterized the impact of optical clearing based on the spheroid volume. Upon optical clearing, the spheroid volumes were reduced by 70% in both, T47D and 4T1 spheroids (Figure 3-14a, b).

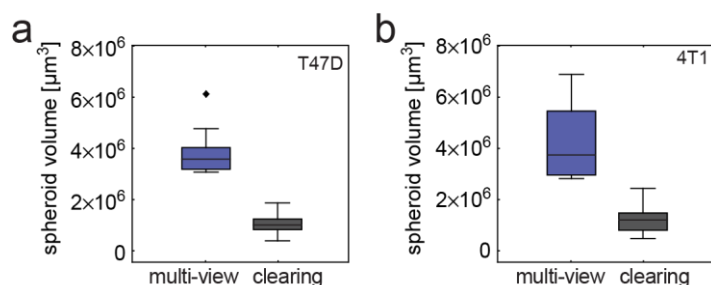


Figure 3-14 Optical clearing reduces the spheroid volume. (a, b) Spheroid volume of multi-view image fusion and optically cleared data of T47D and 4T1 spheroids.

In summary, both approaches are suitable for imaging spheroids. Optical clearing provides a better insight into a spheroid compared to multi-view reconstruction. However, using optical clearing, it has to be considered that the harsh treatment alters the specimen morphology. In our experiments, optical clearing caused a massive shrinkage but maintained the cellular structures, i.e. cell nuclei shape and cell membrane shape.

The establishment of an immunofluorescence staining protocol for spheroids and the appropriate imaging conditions using LSFM served as a fundamental methodical basis for subsequent analyses of mammary epithelial cell spheroids.

3.3 Mammary epithelial cell spheroids display morphological and functional characteristics of epithelial tissue

The mammary gland is an organ that undergoes multiple rounds of cell division, differentiation and cell death. A morphological hallmark is the formation of epithelial tubes (Hennighausen and Robinson, 2005). These features account for the complexity of this organ. However, modern cell culture aims at investigating the morphology and physiological as well as pathological processes in model systems that resemble the Physiology of the organ *in vivo* (Pampaloni et al., 2007).

Cellular spheroids are three-dimensional cell clusters that can be formed from cells of different origin, including tumorigenic or non-tumorigenic cell lines and primary cells. However, each cell type has characteristic morphological features. The objective of this project was, to characterize mammary epithelial cell spheroids. Therefore, epithelial characteristics including the synthesis of a BM-like ECM, polarization and differentiation were investigated.

Three mammary epithelial cell lines with different phenotypes were used: HC11, 4T1 and T47D cells (Figure 3-15a). HC11 cells have been isolated from a prolactin-responsive cell clone from the luminal COMMA-1D mouse mammary epithelial cell line with BALB/c origin (Danielson et al., 1984). This cell line is non-tumorigenic and induces prolactin-dependent milk protein gene expression without the need for co-cultivation with other cell types or the requirement for exogenously added ECM (Ball et al., 1988). Contrary to this line is the 4T1 cell line, which derived from an invasive and metastatic mouse mammary epithelial cancer from BALB/c mice and resembles late-stage human breast cancer. These cells metastasize to the lung, liver, bone and brain primarily via the blood system (Heppner et al., 2000; Aslakson and Miller, 1992). The third cell line was a human mammary epithelial cancer cell line (T47D), which is derived from a pleural metastasis and is classified as luminal A (ER⁺, PR⁺, Her2⁻) (Holliday and Speirs, 2011; Keydar et al., 1979).

3.3.1 Morphological features of spheroids formed from different mammary epithelial cell lines

Spheroids were formed for 24 hours, 48 hours or 7 days, fixed and investigated by confocal fluorescence microscopy. The nuclear marker DAPI was used to label individual cells.

HC11 and 4T1 spheroids had an oblate shape after 24 hours of formation and appeared spherical after 48 hours of culture. 24 hours after cell seeding, T47D cells assembled and formed thin aggregates of only a few cell layers. These thin aggregates became thicker with the course of time, and after 7 days, the T47D spheroids had an oblate shape (Figure 3-15b).

According to the cell nuclei stain, the number of HC11 cells in the spheroid decreased over the time course, while in spheroids formed from 4T1 cells it strongly increased. For T47D spheroids, the number of cells did not obviously change with the course of time (Figure 3-15b).

The spheroids showed large areas devoid of cells (Figure 3-15b, arrowheads). It is known that epithelial cells synthesize and secrete ECM proteins such as laminins to support the BM (Pollard et al., 2017). In addition, it has been shown that ECM is produced by cells under two-dimensional and three-dimensional culture conditions (Paulus et al., 1994). This proves that ECM proteins, which are secreted by the cells, occupy the cell-free areas in HC11, 4T1 and T47D spheroids. However, it not well documented, which ECM proteins are synthesized and how they are distributed in the spheroids.

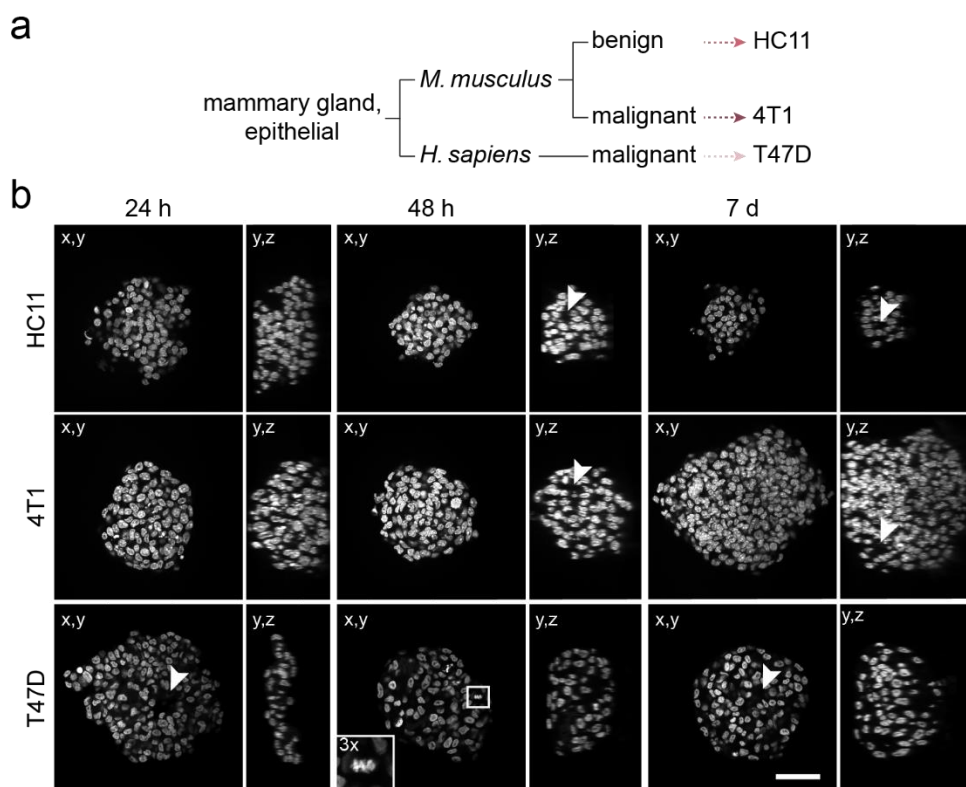


Figure 3-15 Spheroids formed from mammary epithelial cells show morphological differences. (a) Relationship between the cell lines HC11, 4T1 and T47D. (b) Different view directions show spheroid dimensions at 24 hours, 48 hours and 7 days of formation. Arrowheads point at cell-free areas within the spheroids. The image detail shows a dividing cell. Microscope: Zeiss LSM780, objective lens: Plan-Neofluar 40x/NA 1.3 oil, z-spacing: 2 μ m, scale bar: 50 μ m. (modified from Smyrek & Mathew *et al.* 2017).

3.3.2 Type I collagen and fibronectin mRNA are expressed in mammary epithelial cell spheroids

To address these questions, we first investigated whether the cells expressed ECM at all. RNA was extracted from HC11, 4T1 and T47D cells to detect type I collagen and fibronectin mRNA expression. Type I collagen is a stromal ECM protein, whereas fibronectin is predominantly localized within the BM. Murine mammary gland RNA extracts and RNA extracts from the human mammary tumor cell line MCF10A as well as from the human endometriotic cell line 22B were used as positive controls (kindly provided by the Starzinski-Powitz lab). Cells grown in a two-dimensional monolayer culture expressed both, type I collagen and fibronectin (Figure 3-16a).

Next, the adhesion capability of the cells to the ECM proteins was investigated. Cell suspensions were incubated for 1 hour on surfaces coated with either type I collagen, fibronectin or without any coating (BSA only). The amount of attached cells from the entire population was measured after washing away the non-adherent cells. Cells from the three cell lines attached to both, type I collagen and fibronectin-coated surfaces. The number of attached cells differed among the two ECM proteins. A small number of the seeded HC11 cell population (mean 14% \pm SEM 1%) bound to the type I collagen-coated surfaces. Compared to that, a higher number of HC11 cells bound to

fibronectin (mean $44\% \pm \text{SEM } 2\%$). Both, 4T1 and T47D cells, bound equally well to type I collagen and fibronectin, respectively. The mean number of attached 4T1 cells to type I collagen was $46\% \pm 2\%$ and to fibronectin $44\% \pm 3\%$. However, compared to 4T1 cells, T47D cells showed a reduced affinity to type I collagen ($23\% \pm \text{SEM } 2\%$) and fibronectin ($25\% \pm \text{SEM } 2\%$) (Figure 3-16b).

To investigate whether these results were transferable to the three-dimensional spheroid cultures, the mRNA abundance of ECM proteins was analyzed in cellular spheroids. Spheroids from HC11, 4T1 and T47D cells were formed for either 2 day or 7 days and the mRNA abundance of type I collagen and fibronectin was measured. Cells from the three cell lines contained ECM mRNA when grown as spheroids. 4T1 and T47D cells contained mRNA of both ECM proteins, type I collagen and fibronectin, at the two investigated time points. HC11 cells contained fibronectin mRNA at both time points but type I collagen mRNA only in spheroids that were formed for 2 days. Type I collagen mRNA was absent in spheroids that grew for 7 days (Figure 3-16c).

In summary, these results showed that cells produced ECM mRNAs and that the transcription differed between two-dimensional monolayer and three-dimensional spheroid cultures. Further, the three cell types showed differences in the ECM adhesion capabilities.

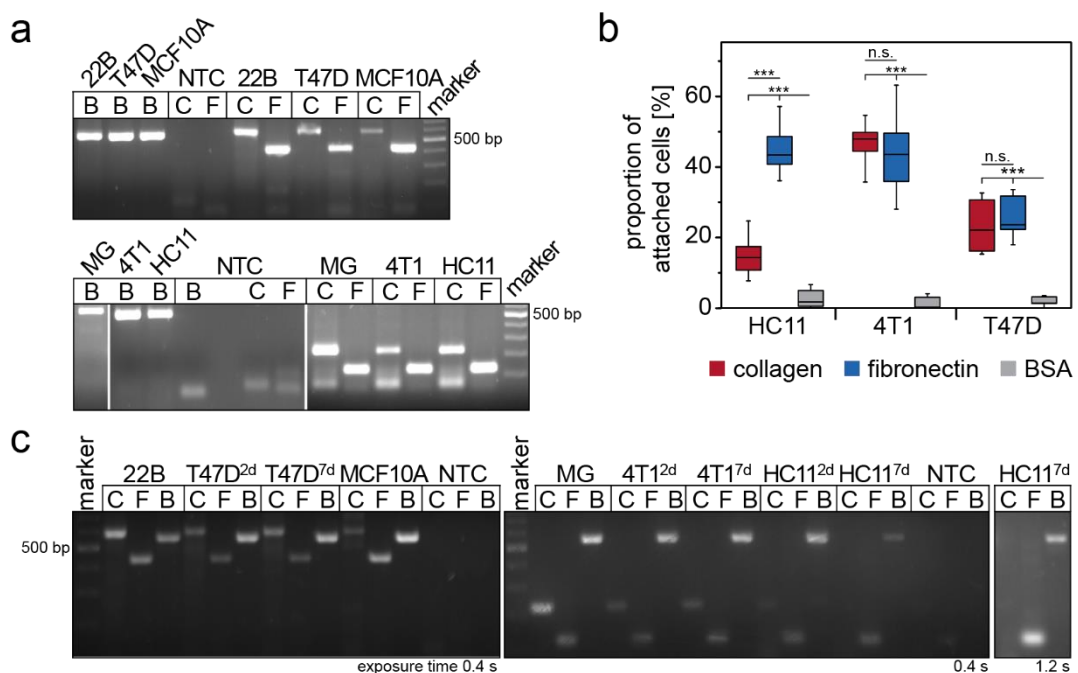


Figure 3-16 Type I collagen and fibronectin are present in cellular spheroids. (a,c) Amplification of human and murine type I collagen and fibronectin mRNA. Amplicon length of human and mouse collagen 1a1 is 600 bp and 223 bp, respectively. Amplicon length of human and mouse fibronectin 1 is 438 bp and 124 bp, respectively. BiP amplification was used as a control and had a fragment size of 560 bp. As positive control, RNA from murine mammary glands (MG), MCF10A epithelial breast cells and 22B endometriotic stromal cells were used. For T47D, 4T1 and HC11 cells, RNA was extracted either from (a) monolayer culture or from (c) spheroids cultured for 2 or 7 days. Bands below 100 bp show remaining primer. (b) The three cell lines showed different affinity to surfaces coated with ECM proteins. Statistical analysis: Wilcoxon rank sum test with Holm correction for multiple testing. Asterisks indicate significant differences (** $p < 0.001$). BSA:

bovine serum albumin, B: binding immunoglobulin protein (BiP), C: collagen, F: fibronectin, n.s.: no significance, NTC: no template control. (modified from Smyrek & Mathew *et al.* 2017).

3.3.3 HC11 spheroids synthesize type IV collagen, fibronectin and laminin but low amounts of collagen I

After investigating the mRNA of ECM proteins, we asked whether the proteins were successfully synthesized and secreted by the cells. Thus, we analyzed the protein appearance and distribution in spheroids 24 hours, 48 hours and 7 days after cell seeding with immunofluorescence staining against type I collagen and IV, fibronectin and laminin. Type IV collagen, laminin and fibronectin represent proteins of the BM, while type I collagen is a protein of the stromal ECM.

Spheroids formed from HC11 cells synthesized a small amount of type I collagen, which appeared as puncta throughout the entire spheroid. The detected signal was low at all investigated time points (Figure 3-17, first column). The fluorescence signal of type IV collagen was stronger and distributed differently compared to type I collagen. Type IV collagen accumulated in extracellular spaces within the spheroids. These patches and large areas were prominent in spheroids that were 24 hours old. After 7 days of culture, type IV collagen was mainly present at the spheroid surface lining the outer cell layer (Figure 3-17, second column). Fibronectin showed a similar extracellular accumulation as type IV collagen in HC11 spheroids. However, the detected signal of fibronectin was stronger compared to type IV collagen and after 7 days of culture, it accumulated in large extracellular spaces within the spheroids (Figure 3-17, third column). Laminin was predominantly distributed at the spheroid surface. In the first 24 hours, cells that loosely attached to the spheroid surface showed a clear cytoplasmic distribution of laminin. After 48 hours, these were integrated into the spheroid. An outer rim of laminin was detectable at the spheroid surface indicating a secretion of laminin by the surface cells. HC11 spheroids additionally assembled laminin in speckles 7 days after spheroid formation, which appeared randomly in the entire spheroid (Figure 3-17, fourth column).

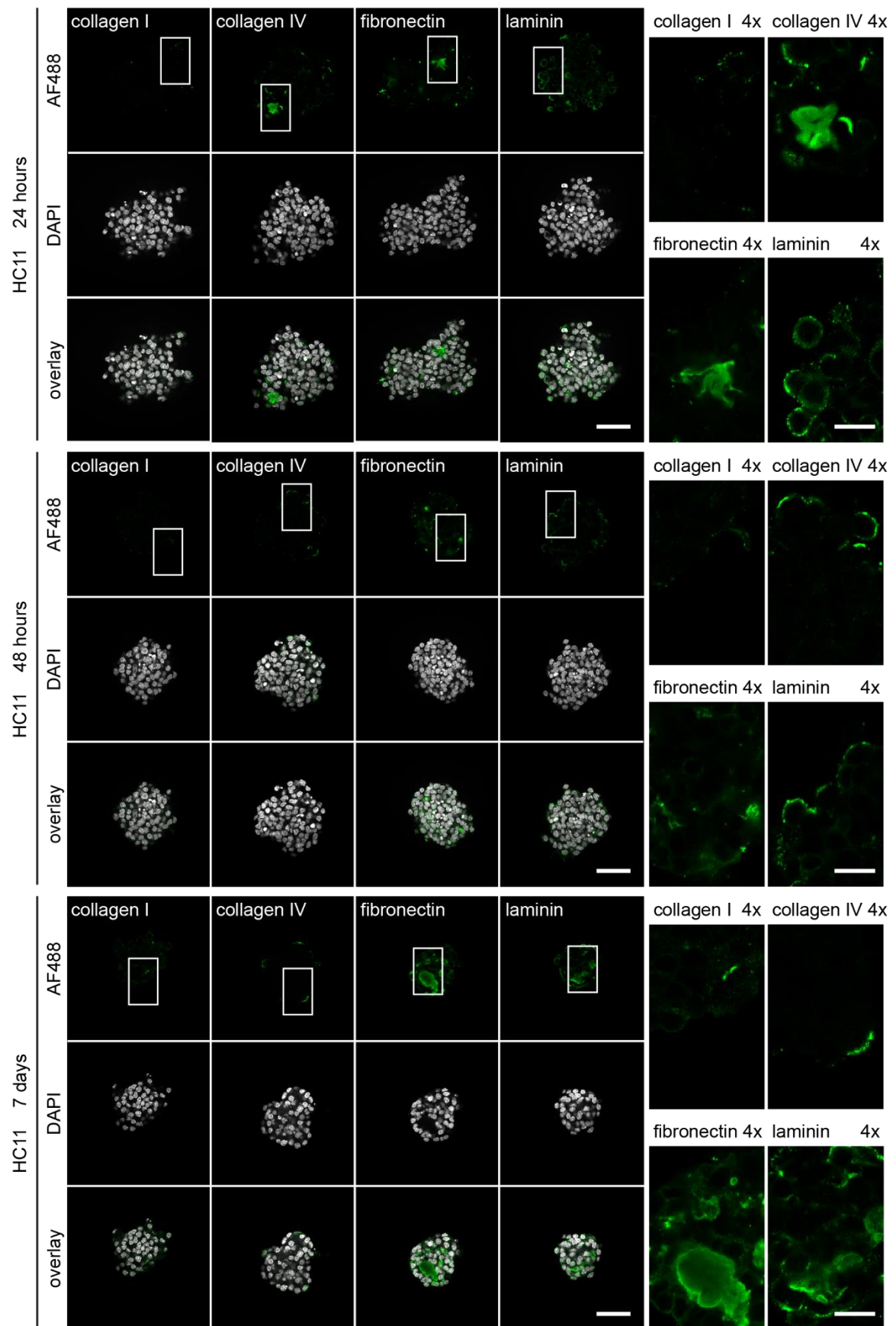


Figure 3-17 Cellular spheroids from HC11 cells synthesize ECM proteins. Type I collagen and IV, fibronectin and laminin were immunolabeled (green) in spheroids at different time points after seeding:

24 hours, 48 hours and 7 days. Cell nuclei were stained with DAPI (grey). Images show optical sections of the spheroid central region. Image details on the right show a 4x magnification of the region indicated with a white box. Microscope: Zeiss LSM780, objective lens: Plan-Neofluar 40x/NA 1.3 oil, scale bar: 50 μm (15 μm image detail).

3.3.4 4T1 spheroids accumulate high amounts of ECM proteins and rearrange ECM

In 4T1 spheroids formed for 24 hours, randomly distributed patches of type I collagen were detected. With increasing spheroid age, type I collagen formed a meshwork to connect multiple cells and was rather detected in the interior spheroid region than at the spheroid surface (Figure 3-18, first column). Type IV collagen speckles appeared as patches, which were homogeneously dispersed in 24 hours old spheroids. In spheroids that were 7 days old, type IV collagen was completely absent in the interior regions. A layer of two to three cells from the spheroid surface was surrounded by patches of type IV collagen (Figure 3-18, second column). Fibronectin was detected in 4T1 spheroids after 24 hours of spheroid formation. At this time point, the stain appeared in numerous small speckles forming a meshwork at the interfaces between cells. The fibronectin fluorescence signal was homogeneous in the entire spheroid. In spheroids that were 48 hours old, fibronectin was still detectable in the entire spheroid but a patchy accumulation in extracellular areas was observed. Interestingly, after 7 days in culture, fibronectin was primarily found in a layer that was several cells thick (Figure 3-18, third column). This layer was localized $25.8 \mu\text{m} \pm 2.43 \mu\text{m}$ (median distance to surface \pm SEM) below the spheroid surface (Figure 3-19).

In 4T1 spheroids laminin localized two to three cell layers from the spheroid surface. In all time points, laminin accumulated in the cytoplasm of the cells, indicating that the cells failed to secrete this ECM protein. Laminin was rarely found in the interior of the spheroid, but appeared there at the interfaces between cells (Figure 3-18, fourth column).

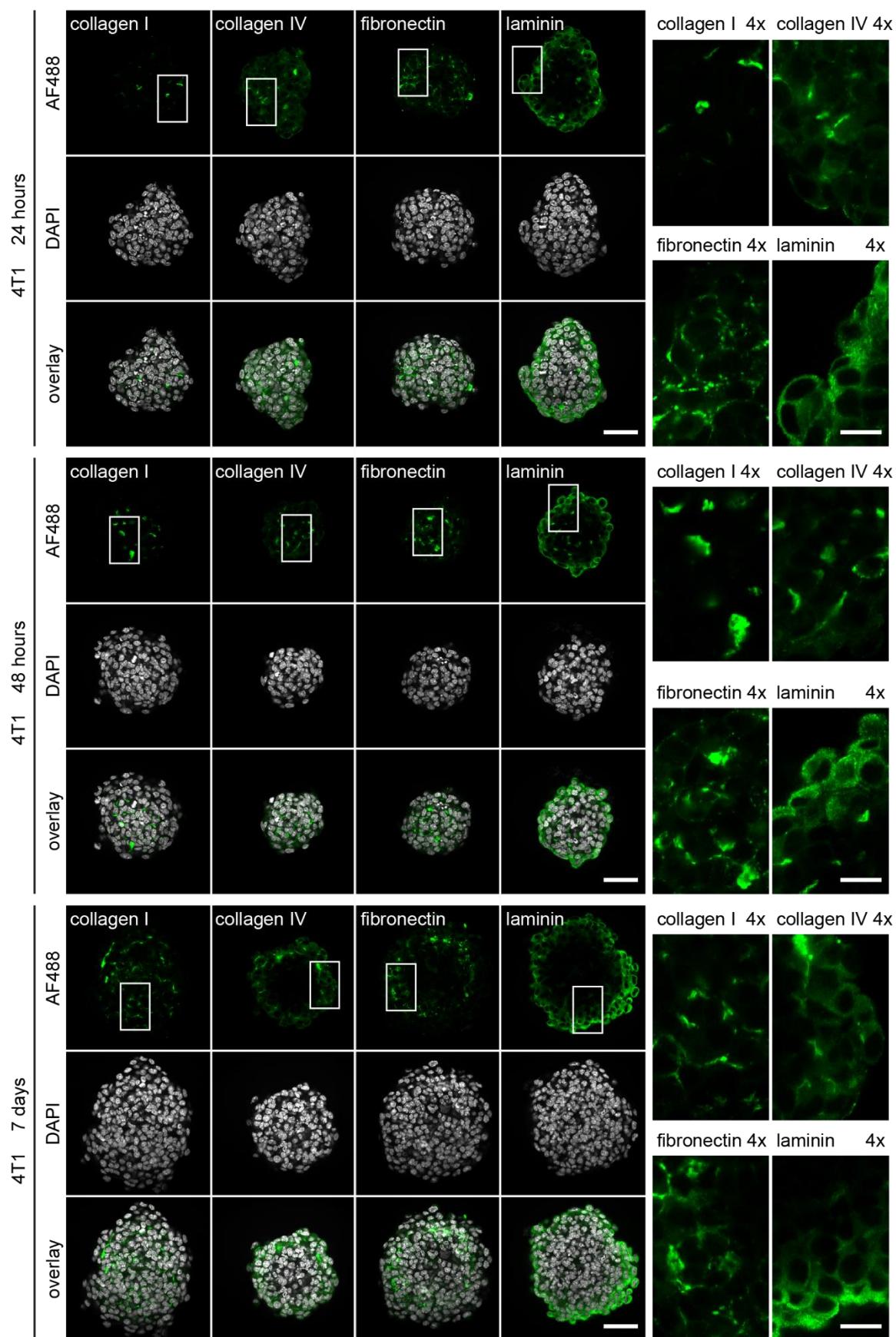


Figure 3-18 Cellular spheroids from 4T1 cells synthesize ECM proteins. Type I collagen and IV, fibronectin and laminin were immunolabeled (green) in spheroids at different time points after seeding:

24 hours, 48 hours and 7 days. Cell nuclei were stained with DAPI (grey). Images show optical sections of the spheroid central region. Image details on the right show a 4x magnification of the region indicated with a white box. Microscope: Zeiss LSM780, objective lens: Plan-Neofluar 40x/NA 1.3 oil, scale bar: 50 μm (15 μm image detail).

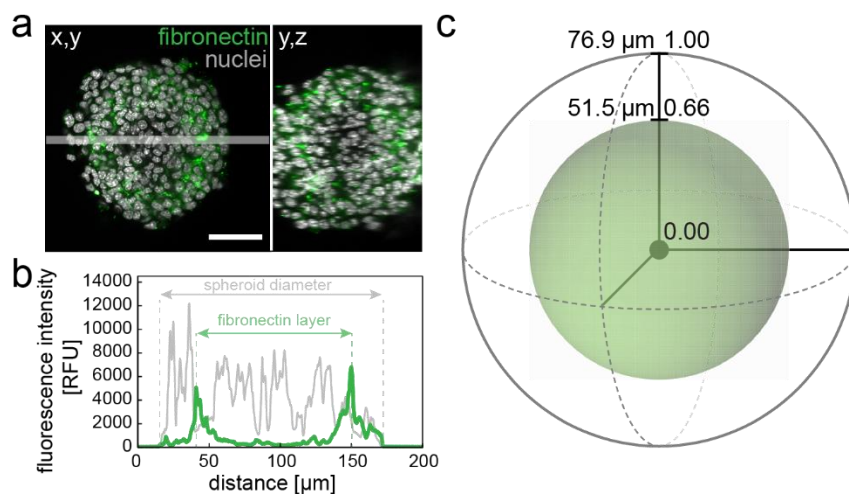


Figure 3-19 Spheroids from highly invasive cancer cells rearrange fibronectin into a pattern. (a) 4T1 spheroids formed from 600 cells grew for 7 days. Orthogonal views of the fibronectin staining pattern. (b) Fluorescence intensity profiles of fibronectin and cell nuclei (DAPI) were measured along an 8 μm

thick line (grey bar in (a)) and plotted as a function of the distance. Spheroid diameter was estimated from DAPI fluorescence intensity. Fibronectin localization was measured from fibronectin intensity peaks. (c) Schematic of the fibronectin distribution characteristics. Values obtained from measurements from seven spheroids from two independent experiments. Shown are the median radius of the spheroid and the fibronectin location. Microscope: Zeiss LSM780, objective lens: Plan-Neofluar 40x/NA 1.3 oil, scale bar: 50 μm .

3.3.5 T47D spheroids synthesize laminin, fibronectin and type IV collagen but low amounts of type I collagen

The human mammary epithelial tumor cell line T47D produces only low amounts of type I collagen. In spheroids of all ages (24 hours, 48 hours and 7 days), only few homogeneously distributed puncta of type I collagen were detected (Figure 3-20, first column). A discontinuous layer of type IV collagen surrounded the outer cell layer at the spheroid surface. This was found in spheroids at all investigated time points. Additionally, type IV collagen covered large extracellular areas within the spheroid inner region (Figure 3-20, second column). T47D spheroids contain fibronectin, which was found in large and few extracellular areas homogeneously distributed throughout the spheroids (Figure 3-20, third column). Laminin was detected in T47D spheroids primarily next to cells at the spheroid surface. T47D spheroids showed a rather thin outer rim of laminin, suggesting that the outer cell layer secreted this ECM protein (Figure 3-20, fourth column).

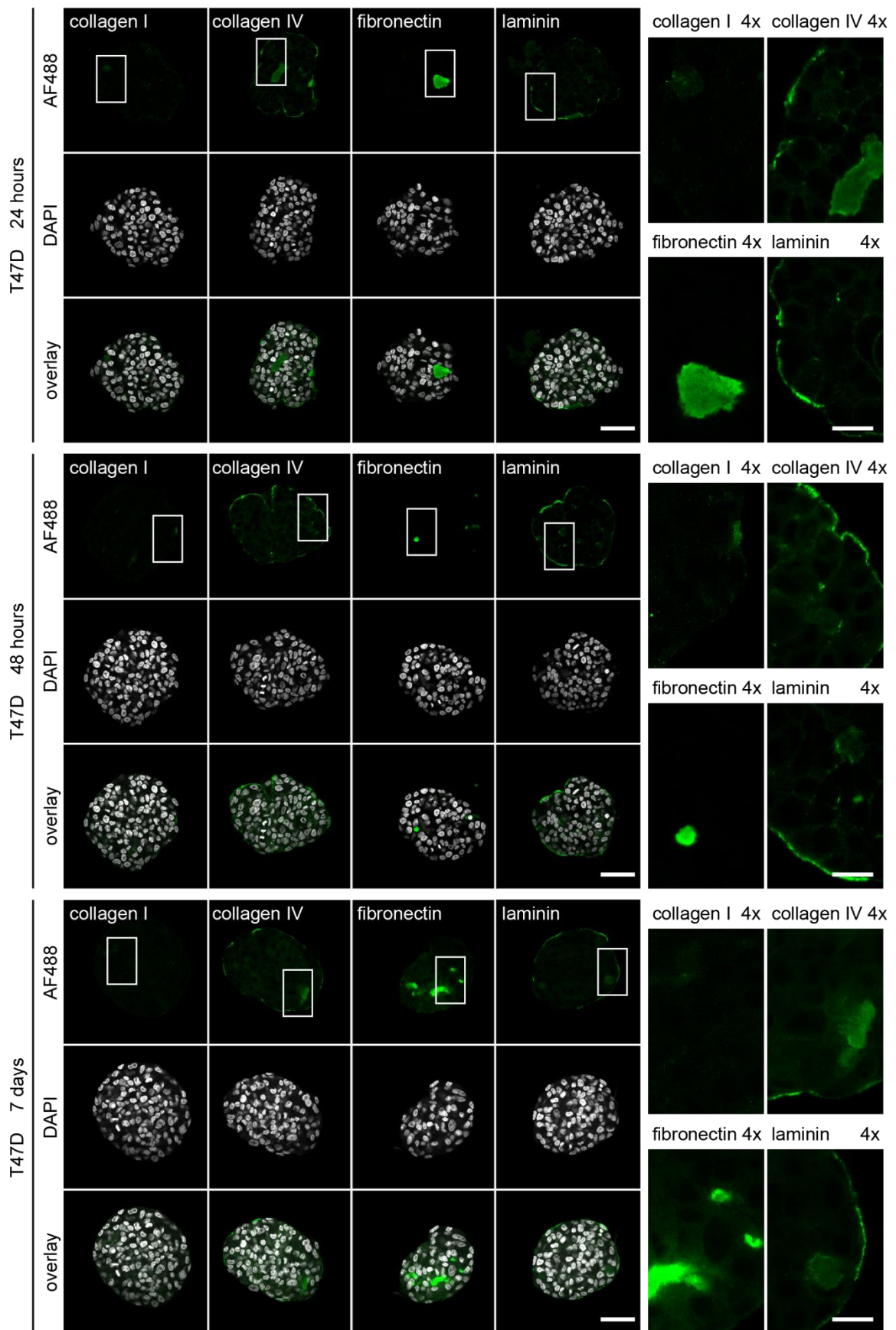


Figure 3-20 Cellular spheroids from T47D cells synthesize ECM proteins. Type I collagen and IV, fibronectin and laminin were immunolabeled (green) in spheroids at different time points after seeding:

24 hours, 48 hours and 7 days. Cell nuclei were stained with DAPI (grey). Images show optical sections of the spheroid central region. Image details on the right show a 4x magnification of the region indicated with a white box. Microscope: Zeiss LSM780, objective lens: Plan-Neofluar 40x/NA 1.3 oil, scale bar: 50 μm (15 μm image detail).

Table 3-2 Comparison of ECM distribution patterns in cellular spheroids of different cell types.

cell line	ECM protein	time point	main localization	structure	appearance	
HC11	type I collagen	24 h	homogeneous	puncta	extracellular	
		48 h	homogeneous	puncta	extracellular	
		7 d	homogeneous	puncta	extracellular	
	type IV collagen	24 h	homogeneous	patches & large areas	patches & large areas	extracellular
		48 h	homogeneous	patches	patches	extracellular
		7 d	surface	stripe	stripe	extracellular
	fibronectin	24 h	homogeneous	patches & large areas	patches & large areas	extracellular
		48 h	homogeneous	patches & large areas	patches & large areas	extracellular
		7 d	homogeneous	patches & large areas	patches & large areas	extracellular
	laminin	24 h	surface	surface	puncta	intracellular
		48 h	surface	surface	stripe	extracellular
		7 d	surface & inner region	surface & inner region	stripe & patches	extracellular
4T1	type I collagen	24 h	homogeneous	patches	extracellular	
		48 h	homogeneous	patches	extracellular	
		7 d	inner region	meshwork	extracellular	
	type IV collagen	24 h	homogeneous	patches	patches	extracellular
		48 h	homogeneous	patches	patches	extracellular
		7 d	outermost cell layers	patches	patches	extracellular
	fibronectin	24 h	homogeneous	homogeneous	meshwork	extracellular
		48 h	homogeneous	homogeneous	meshwork & patches	extracellular
		7 d	beneath surface cell layers	beneath surface cell layers	meshwork	extracellular
	laminin	24 h	outermost cell layers	outermost cell layers	puncta	intracellular
		48 h	outermost cell layers	outermost cell layers	puncta	intracellular
		7 d	outermost cell layers	outermost cell layers	puncta	intracellular
T47D	type I collagen	24 h	homogeneous	puncta	extracellular	
		48 h	homogeneous	puncta	extracellular	
		7 d	homogeneous	puncta	extracellular	
	Type IV collagen	24 h	surface & inner region	surface & inner region	stripe & large areas	extracellular
		48 h	surface & inner region	surface & inner region	stripe & large areas	extracellular
		7 d	surface & inner region	surface & inner region	stripe & large areas	extracellular
	fibronectin	24 h	homogeneous	homogeneous	large areas	extracellular
		48 h	homogeneous	homogeneous	large areas	extracellular
		7 d	homogeneous	homogeneous	large areas	extracellular
	laminin	24 h	surface	surface	stripe	extracellular
		48 h	surface	surface	stripe	extracellular
		7 d	surface	surface	stripe	extracellular

In summary, the non-tumorigenic HC11 cells as well as the T47D tumor cells showed only sparse type I collagen protein synthesis. The highly invasive 4T1 cells synthesized high amounts of type I collagen. Type IV collagen was synthesized in spheroids of all three cell lines but showed different structures. HC11 cells arranged type IV collagen in extracellular patches found in the spheroid interior. These patches disappeared in 7 days old spheroids and type IV collagen was lining the

spheroid surface. In 7 days old 4T1 spheroids, a few cell layers at the spheroid surface synthesized type IV collagen. In T47D spheroids, type IV collagen was found mainly at the outer rim of the spheroid. Fibronectin was detected in the three cell lines. In HC11 and T47D spheroids, fibronectin appeared in large extracellular spaces. The amount of fibronectin in 7 days old HC11 spheroids was high, while it was low in T47D spheroids. After 7 days in culture, 4T1 spheroids showed a fibronectin layer that was a few cell layers thick. This layer was located a few cell layers below the spheroid surface. Laminin was found in spheroids from all cell lines at the outer rim. In HC11 and T47D spheroids, a thin layer of laminin was lining the spheroid surface. However, 4T1 cells showed cytoplasmic laminin, indicating that it was not secreted into the extracellular space.

3.3.6 Non-malignant mammary epithelial cell spheroids form polarized structures and express lactation-associated genes upon cell differentiation

The structure of ECM in the mammary epithelial spheroids is an indication of epithelial morphogenesis in these spheroids (O'Brien et al., 2001). One hallmark of epithelial morphogenesis is polarization (Gumbiner, 1992). Polarized epithelia show an asymmetric distribution of their membrane-associated proteins (i.e. β -catenin, actin, ezrin) and of their trafficking machinery that is composed of the endoplasmic reticulum, the Golgi complex and endosomal components (Rodriguez-Boulan and Macara, 2014). To investigate whether spheroids develop polarized structures, we stained β -catenin, F-actin, ezrin and the Golgi apparatus in spheroids formed from HC11 cells. These cells are non-tumorigenic and thus, should exhibit functional polarization and furthermore differentiation in a three-dimensional cell culture context (Xian et al., 2005). After 10 days in culture, HC11 spheroids developed morphological characteristics resembling acinar or duct-like structures. In most cases, the cells surrounding a lumen adapted a columnar shape with strong β -catenin distribution at their lateral membranes (Figure 3-21a). The actin cytoskeleton accumulated predominantly at the luminal side of the cells. Ezrin was detected exclusively in cells that formed a lumen and in cells at the surface of the spheroid. In these surface cells ezrin localized at the membranes facing the lumen or medium, respectively (Figure 3-21b). The Golgi apparatus was stained using the cis-Golgi marker GM130. The Golgi did not become oriented to the luminal surface. Its position was rather at the basal than on the apical site of the cells (Figure 3-21a, white arrow), indicating that the trafficking machinery was not polarized.

The HC11 cell line has been developed to express casein and other milk-related genes upon prolactin stimulation. To evaluate whether HC11 cells retain their differentiation capability, spheroids were grown for 7 days. Then, spheroids were conditioned for 3 days with EGF-containing medium followed by induction of lactogenic differentiation with the prolactin-containing induction medium. After 5 days of lactogenic induction, β -casein was detected on the immunoblot (Figure 3-21c). The synthesis of β -casein was independent of supplemented collagen to support growth of

the culture (Supplemental Figure 7-11c). Thus, the differentiation capability of HC11 cells was retained under three-dimensional spheroid culture conditions.

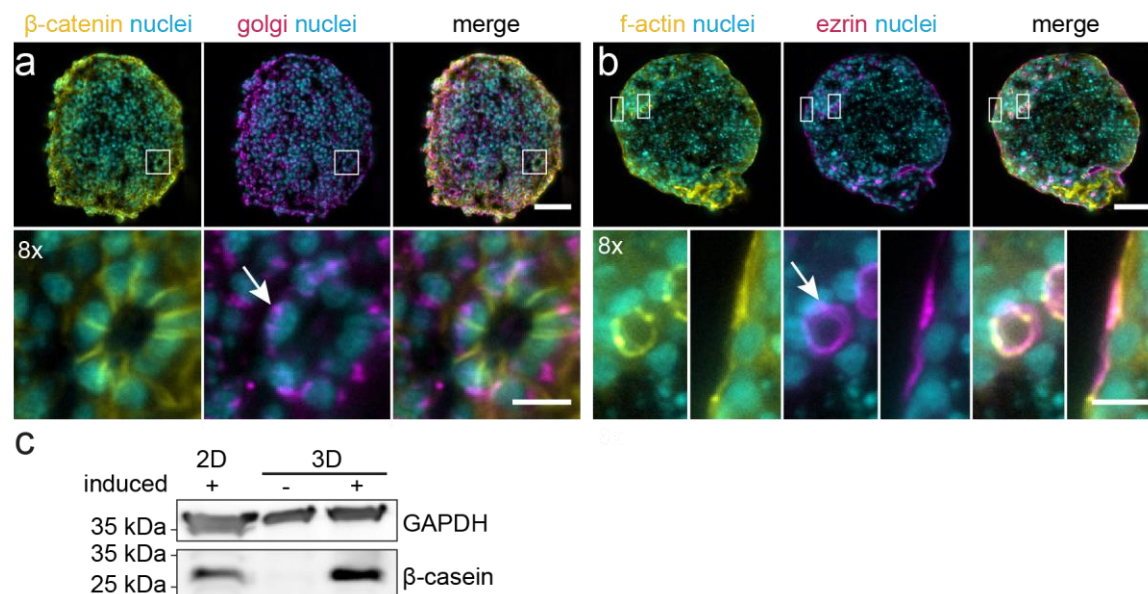


Figure 3-21 Spheroids formed from HC11 cells develop mammary epithelial-specific characteristics.

(a) HC11 spheroids were stained for β -catenin, the Golgi complex (GM130) and the cell nuclei (DAPI). Spheroids form acinar structures with polarized cells that surround a lumen. The localization of the Golgi apparatus did not indicate a polarization (arrow). Single planes and highlighted regions show characteristics of the respective stain. (b) Spheroids formed from HC11 cells were stained for F-actin (phalloidin), ezrin and cell nuclei (DAPI). Ezrin as a polarization marker as well as an accumulation of F-actin showed that the cells had a polarized membrane. (c) HC11 spheroids underwent lactogenic differentiation. After 7 days of formation, spheroids were starved for 3 days before the gene expression of β -casein was induced for 5 days with a prolactin-containing medium. Microscope: mDSLMM; illumination lens: Plan-Neofluar 5x/NA 0.16; detection lens: N-Achroplan 20x/NA 0.5; spacing: 1.29 μ m; camera: Andor Clara; laser - filter (phalloidin AF546, β -catenin): 561 nm – bandpass 607/70; laser – filter (GM130, ezrin): 488 nm – bandpass 525/50; laser - filter (DAPI): 405 nm – bandpass 447/55; scale bar: 50 μ m, 10 μ m (image detail).

In summary, spheroids formed from HC11 cells developed epithelial-like morphological characteristics. Duct-like or acinar structures showed a membrane polarization but no polarization of the secretory trafficking machinery. HC11 spheroids retained the capability of lactogenic differentiation.

3.4 Mechanical stress modulates tissue integrity

Developmental processes are often accompanied by the appearance of physical forces such as mechanical stress. However, mechanical stress plays also an important role in pathogenesis. Tissues of the body show different degrees of stiffness, which often correlate with their function, i.e. bone has stabilizing function. Apart from periodic differences due to the estrous cycle, the healthy breast tissue is usually very soft. The stiffness can dramatically increase in pathological conditions such as breast cancer (Figure 3-22a). The increasing stiffness of the ECM accompanies breast cancer as activated mechanotransduction leads to increased cell proliferation and invasion (Schedin and

Keely, 2011). In mammary gland development, mechanical stress is likely to be an inducer of the post-lactational regression (Quaglino et al., 2009). In the following section, we investigated to which extent the application of physical forces changes the morphology of cells and whether cellular processes are initiated as a response to the applied force.

3.4.1 Strain in two-dimensional cell cultures

In monolayer cultures, two approaches to apply mechanical stress onto cells were tested. First, we generated hydrostatic pressure and second, we applied radial strain.

In our first approach, hydrostatic pressure of approximately 3,000 Pa was applied on non-tumorigenic mammary epithelial cells (Figure 3-22b), which is more than three times larger than what cells in the healthy breast experience. Hydrostatic pressure was applied by the liquid medium, which was pressed onto the confluent grown cell layer by centrifugation. Preceding centrifugation, cells were either induced to undergo lactogenic differentiation or not. The successful lactogenic differentiation was monitored by the detection of the milk protein β -casein (Figure 3-22c). In addition, it was assessed whether a previous induction of autophagy with the mTOR inhibitor rapamycin was further affected by the applied pressure. Autophagy was assessed by comparing the non-lipidated LC3B-I to the lipidated, autophagosome-bound LC3B-II variant. Densitometry of these two detected bands showed that with increasing complexity (lactogenic induction, rapamycin treatment and hydrostatic pressure) the lipidated LC3B-II was more abundant than LC3B-I. However, no factor alone was able to significantly increase LC3B lipidation (Figure 3-22d).

Since BAG3 was found upregulated in the first phase of mammary gland involution, its expression upon hydrostatic pressure was assessed. Due to the lack of appropriate culturing conditions in the centrifuge, the hydrostatic pressure was applied only for 1 hour. During this time span, effects on gene expression alterations cannot be assessed. However, phosphorylation events or protein degradation can occur in such a short time span. Therefore, BAG3 protein appearance was investigated. Despite lactogenic induction, rapamycin treatment or applied hydrostatic pressure, the BAG3 protein level did not change (Figure 3-22c). The molecular weight of BAG3 protein is 75 kDa (Behl, 2016). Interestingly, the BAG3 antibody detected two bands with a molecular band of approximately 55 kDa and under lactogenic differentiation, the lower band disappeared. We could not detect alternative transcript variants of BAG3 with primer that flanked the BAG3 coding sequence (Supplemental Figure 7-12). Thus, we suggested that these lower molecular weight bands could descend from cleaved or partially decomposed BAG3.

In conclusion, hydrostatic pressure alone was not sufficient to induce LC3B lipidation and it did not affect the BAG3 protein level. This indicated that the applied pressure might not reflect the deformation that cells undergo upon milks stasis in the mammary gland.

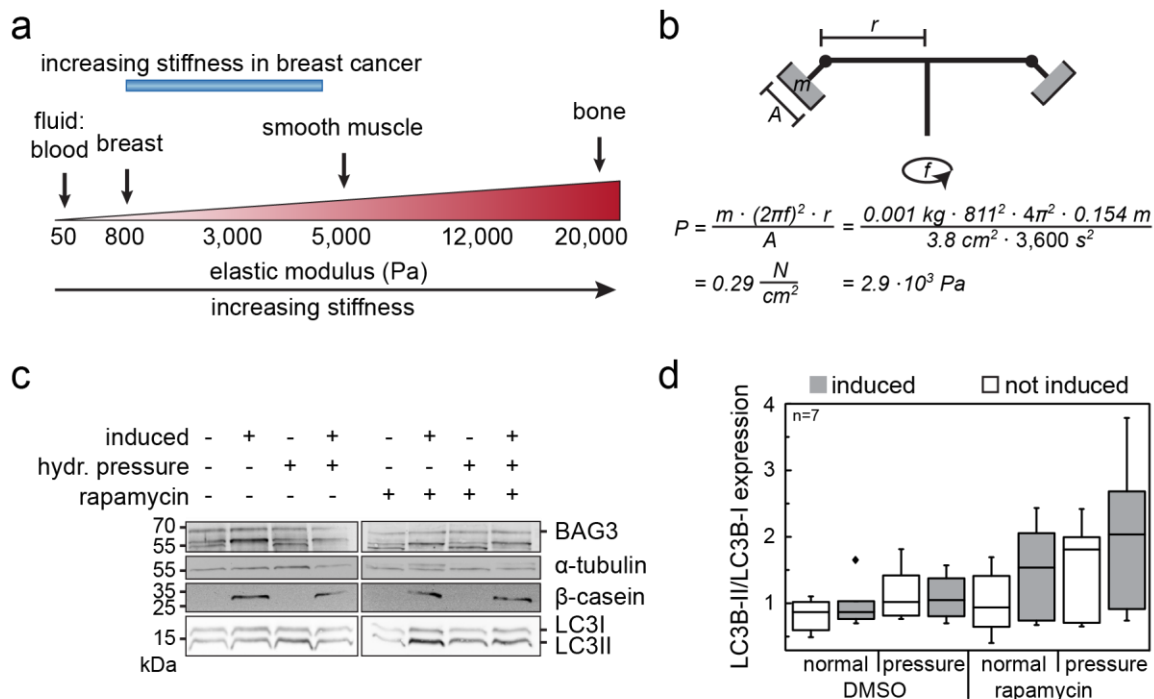


Figure 3-22 Hydrostatic pressure on mammary epithelial cells increases autophagy when cells are additionally treated with the autophagy stimulating agent rapamycin. (a) Cells in tissues are exposed to different stresses that are, on a nanoscale, generated by cell-cell and cell-ECM interactions. Compared to bone, breast tissue is relatively soft. However, in cancer progression, the stiffness in the tissue increases (based on Butcher et al. 2009). (b) Hydrostatic pressure applied by centrifugation. Growth area, volume of the overlying medium, rotor radius and the amount of rotations per minute account for the applied pressure (Redlich et al., 2004). (c) Protein analysis of differentiated or undifferentiated HC11 cells under hydrostatic pressure. Cells were treated with Rapamycin 16 hours prior stress application. Stress was applied for 60 minutes. (d) Densitometry analysis of LC3-I and LC3-II protein level from seven independent experiments. Increasing LC3-II/LC3-I ratios indicate increased assembly of autophagosomes. Boxplot parameters: the box contains 50% of the data points, the whiskers and outliers show the upper and lower 25% of the data. The line in the box is the median. Outliers are outside the 1.5x interquartile range. ♦, outliers.

To execute a controlled deformation of the cells, another promising approach was used. This approach was adapted from Quaglino *et al.*, who reported that radial strain induces gene expression and phosphorylation of proteins that are associated with mammary gland involution (Quaglino et al., 2009). The strain is executed by insertion of a flexible membrane with attached cells into a stretching device, which brings the membrane into a stretched conformation (Figure 3-23a). It has been reported that the device delivers up to 30% of two-dimensional homogeneous strain to the silicone membranes (Quaglino et al., 2009). Cells grew on a flexible membrane coated with collagen. When the silicone membrane was inserted into the device, only a small area around the center was actually stretched. The indenter ring that was pressed onto the membrane to apply the strain occupied the remaining area (Figure 3-23b). To investigate whether the applied strain within the small central area was homogeneous, fluorescent beads were mounted into the silicone membrane, which was stretched. The changing distance of fluorescence beads was measured on a relaxed (0 turns), medium stretched (4 turns) and fully stretched membrane (8 turns). Within the

central area, the distances between beads within the core region and the border region were compared (Figure 3-23c). Stretching of the membrane increased the distances of beads that were located in the core region. However, the beads that were located in the border region did not increase the distance to another (Figure 3-23d). This indicates that the applied strain was not homogeneously distributed on the membrane, which results in uncontrollable and inhomogeneous deformation of the cells and thus, inconclusive results. Nevertheless, we grew cells on silicone membranes that were coated with collagen and subjected them to radial strain. Since we were interested to investigate the effects that are present during early involution of the mammary gland, cells had to grow fully confluent to undergo differentiation. Both, stretched cells and the controls were treated for 5 days with prolactin-containing medium to induce lactogenic differentiation. When those confluent cell layers were subjected to experience mechanical strain, they partially detached from the silicone membrane (Figure 3-23e, white arrow). No obvious morphological change was detected after 45 minutes and 240 minutes of applied strain by an F-actin label of the cell circumference (Figure 3-23e). RNA was extracted from cells that were continuously stretched for 18 hours and controls. When strain was applied, c-Fos, which served as an indicator for active mechanosignaling, was on average two-fold upregulated compared to the control. The detection of BAG3 mRNA showed strong variations between the experiments (Figure 3-23f), so that no conclusion could be determined.

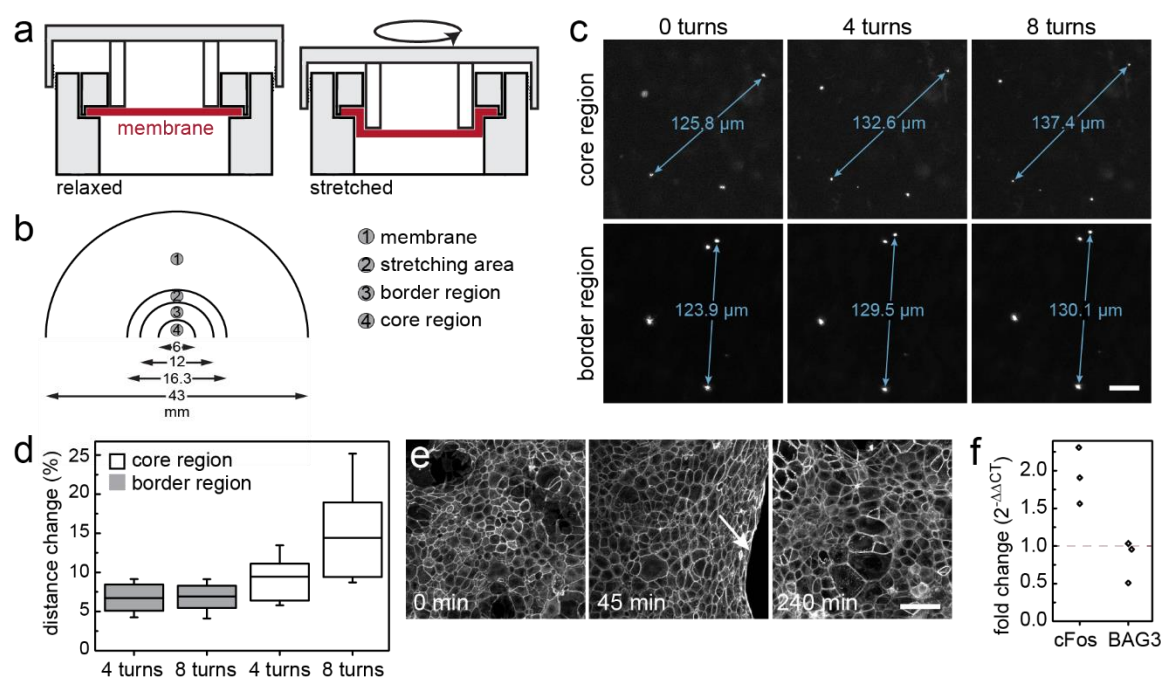


Figure 3-23 Application of radial strain on cells cultured on flexible membranes. (a) Schematic of the radial stretching device. The silicone membrane is stretched when a Teflon ring indents the fixed membrane. The Teflon ring indents the membrane when the aluminum screw-top is fastened. (b) Depicted is half of a (1) silicone membrane. The localization of the Teflon indenter ring defines the (2) stretching area. The (3, 4) area where cells grow and are exposed to the stretch is subdivided into an (3) outer border region and an (4) inner core region. (c) Beads were embedded into the silicone membrane and the changing distance between beads in the core and the border region was measured. Microscope: Zeiss Axiovert, objective lens: 20x, scale bar:

25 μm . (d) Twelve bead distances per region (core and border region) were measured and plotted as the change in distance. (e) HC11 cells were grown on a collagen-coated silicone membrane until confluence. The silicone membrane was stretched (8 turns). After fixation, F-actin was labeled with phalloidin AF488. The arrow points at a sheet of cells that detached from the membrane. Microscope: Zeiss LSM780, objective lens: 20x, scale bar: 50 μm . (f) qPCR HC11 DIP induced cells. 18 hours stretch. Boxplot parameters: the box contains 50% of the data points, the whiskers and outliers show the upper and lower 25% of the data. The line in the box is the median. Outliers are outside the 1.5x interquartile range.

In summary, the second approach of applying mechanical stress onto two-dimensionally grown cells did not work as proposed by Quaglino and colleagues. The area of applied strain was small and within this area, the strain was not applied homogeneously. The detachment of cells from the silicone membrane may result in the induction of cellular events other than the ones induced by strain, i.e. detachment induced apoptosis (Frisch and Francis, 1994). In addition, no morphological alterations were detected upon applied stretch. Although c-Fos mRNA increased upon stretch, it was not comparable with the amount found in the mammary gland, where a 13.5-fold induction was measured 12 hours after pup removal. The abundance of BAG3 mRNA varied strongly among the experiments. All in one, both approaches, the application of hydrostatic pressure and the application of radial strain did not provide conclusive results and showed a high degree of experimental uncertainty.

3.4.2 Spheroids adapt to compression by morphological and functional alterations of cells

Almost all cells form three-dimensional cell aggregates in a non-adhesive environment. Spheroids resemble the three-dimensionality of cell-neighborhood relations well. Thus, they serve as a model to study the influences of mechanical stress on the architectural changes of cell aggregates.

In this project, I designed the study and performed all experimental work. Alexander Schmitz performed the image analysis of optically cleared spheroids to conclude about the morphological characteristics and the caspase activation under spheroid confinement.

To augment tissue tension, and thereby induce mechanical stress, spheroids were deformed to a cylindrical shape. This method was adapted from Campinho *et al.*, who applied this method to deform zebrafish embryos (Campinho *et al.*, 2013).

Agarose capillaries with a defined diameter were prepared. Agarose allows gas and medium exchange and provides a certain stability to induce the deformation of spheroids. The inner agarose capillary lumen was generated using glass rods with the diameter of either $200\ \mu\text{m} \pm 20\ \mu\text{m}$ or $300\ \mu\text{m} \pm 20\ \mu\text{m}$. These were inserted into the liquid agarose column inside a glass capillary (Figure 3-24a). Spheroids were formed from HC11 cells for 10 days. The spheroids were mounted inside the agarose capillaries by placing them onto the opening of the capillary lumen. Capillary forces pulled spheroids into the capillary lumen (Figure 3-24b). The diameters of the spheroids were about

250 μm . When spheroids were inserted into agarose capillaries with an inner diameter of 200 μm , spheroids were compressed, whereas they retained their shape when they were inserted into the agarose capillaries with an inner diameter of 300 μm . The mounted spheroids were incubated for up to 96 hours (Figure 3-24c). Spheroids were fixed inside the agarose capillaries, removed from the capillaries, stained and then subjected to optical clearing and LSMF (Figure 3-24d). The high quality of the image data allowed for subsequent quantitative analysis.

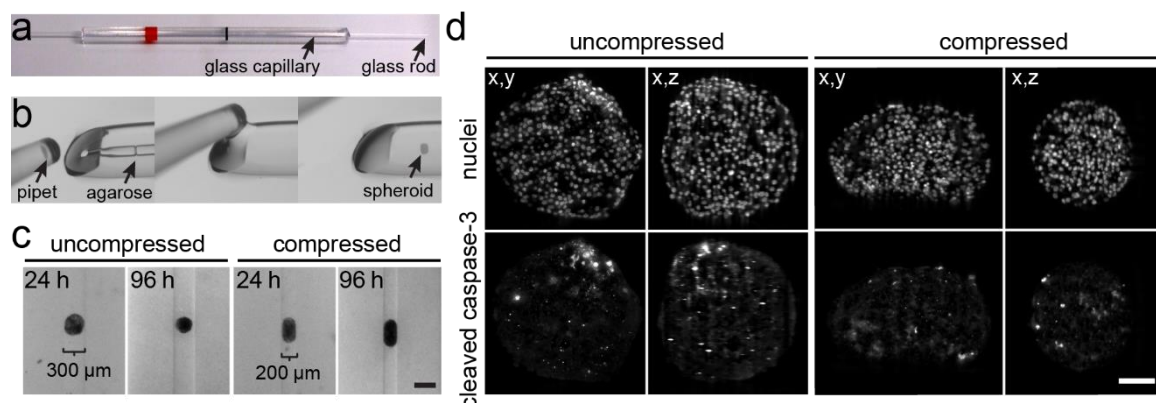


Figure 3-24 Spheroid integrity is preserved under confinement in the long-term. (a) Agarose capillaries were produced by pipetting liquid 2% low-melt agarose into a glass capillary. Subsequently, a glass rod with a diameter of either 200 μm or 300 μm was inserted into the liquid agarose. The capillary-agarose-glass rod construction was incubated at 4°C for approximately 5 minutes until the agarose solidified. (b) After removal of the glass rod and the glass capillary, the agarose capillary was cut into approximately 1 cm fragments. A spheroid was placed at the opening of the agarose capillary and pulled inside by capillary forces. (c) Spheroids mounted inside the agarose capillaries were incubated in growth medium for the indicated time. Agarose capillaries with a diameter of 200 μm deformed spheroids, while spheroids in a 300 μm capillary retained their shape. Microscope: Zeiss Discovery V.8 SteReo, scale bar: 300 μm . (d) Compressed spheroids retained their shape following fixation. This allowed staining and analysis. Following staining, spheroids were optically cleared and subjected to LSMF. Single slides show cleaved caspase-3 and DAPI in compressed and uncompressed spheroids after 24 hours. Microscope: mDSLM, illumination lens: Plan-Neofluar 5x/NA 0.16, detection lens: N-Achroplan 20x/NA 0.5, camera: Andor Clara, laser – filter (cleaved caspase 3): 488 nm – bandpass 525/50, laser – filter (DAPI): 405 nm – bandpass 447/55, scale bar: 50 μm .

Spheroid compression activates caspases at the short term and alters cell nuclei volume

Alexander Schmitz performed a detailed quantitative analysis of the spheroid morphology. A pre-selection of the data was executed to exclude spheroids that were not sufficiently deformed or had an oblate shape due to mishandling. Principal component analysis (PCA) on the cell nuclei positions was performed. It obtained the absolute extension along the principal direction $p1$, $p2$ and $p3$. Pairwise ratios between these directions provided the relative ratios. A threshold was set to select spheroids that were not deformed by incubation inside the 300 μm agarose capillaries. This threshold was empirically set to select spheroids that showed an elongation of at most 15% (i.e. the ratio between $|p1|$ and $|p2|$ was less or equal to 1.15). For the compressed spheroids, which were incubated in the 200 μm agarose capillaries, the selection contained spheroids that showed an elongation of at least 25% (i.e. the ratio between $|p1|$ and $|p2|$ was equal or greater than 1.25). Thus, compressed spheroids had a prolate shape and the control spheroids had a spherical shape (Figure

3-25a). The applied lateral strain was 12.2%, 12.6% and 18.2% when spheroids were compressed for 1 h, 24 h and 96 h, respectively. All subsequent analyses were performed with the spheroids that passed the selection criteria (Supplemental Figure 7-13). The dataset contained data that originated from different experiments. Due to experiment-to-experiment variations, i.e. in the seeded cell number, the cell count as well as the spheroid volume were normalized to the control spheroids within the individual experiment.

The spheroid volumes did not remarkably deviate from the controls when spheroids were compressed. After 1 hour of compression, the median volume of spheroids rose about 23% ($p < 0.05$), but the variance within this condition was high. After 24 hours and 96 hours of compression, the median spheroid volume decreased not significantly by 5% (Figure 3-25b). The number of cells was increased by 24% in spheroids that were compressed for 1 hour compared to the uncompressed spheroids ($p < 0.001$). After 24 hours of compression, the number of cells per spheroid was 12% higher compared to the control and after 96 hours, it was increased by 9% (Figure 3-25c). Next, we investigated the volume of the cell nuclei. It did not change when spheroids were compressed for 1 hour. The median cell nuclei volumes were $68.8 \mu\text{m}^3$ when spheroids were compressed and $69.5 \mu\text{m}^3$ in the controls. Interestingly, when spheroid compression lasted for 24 hours, the volumes were significantly decreased by 20.3% compared to the uncompressed controls (volume compressed spheroids: $72.3 \mu\text{m}^3$; volume uncompressed spheroids: $92.6 \mu\text{m}^3$). After 96 hours, this effect declined and the median volume of cell nuclei in compressed spheroids was 7.5% smaller compared the cell nuclei in uncompressed spheroids (volume compressed spheroids: $64.6 \mu\text{m}^3$, volume uncompressed spheroids: $72.1 \mu\text{m}^3$) (Figure 3-25d).

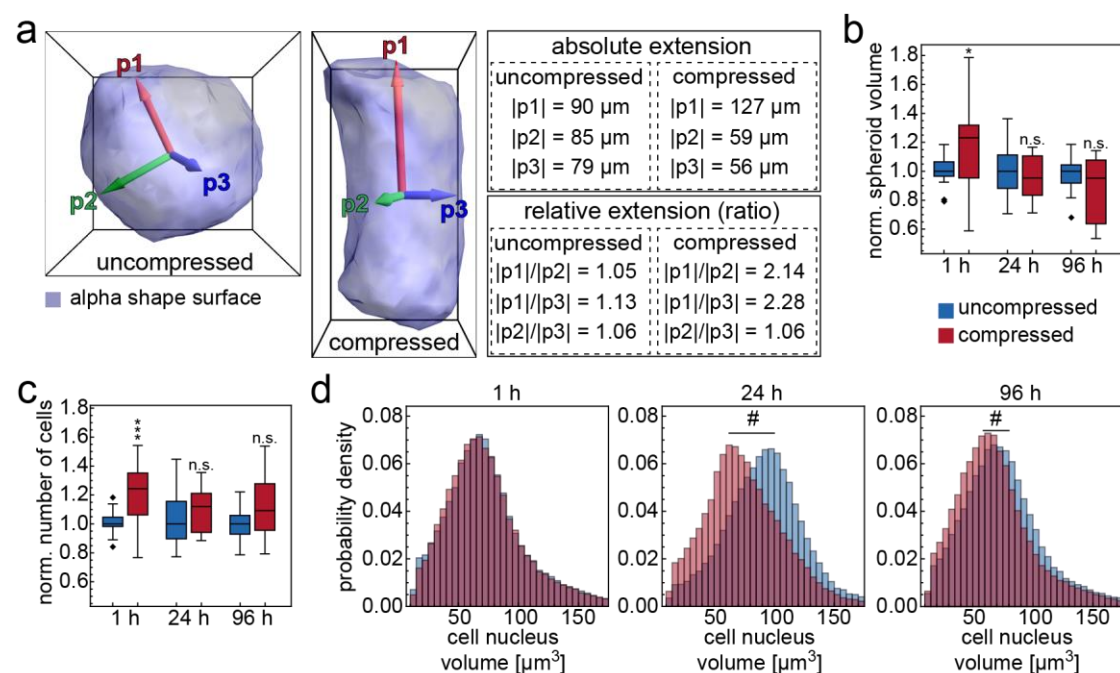


Figure 3-25 Compression of mammary epithelial cell spheroids alters the cell nuclei volume. (a) Shape analysis with principal component analysis (PCA) exemplified on one spheroid. PCA gives the principal

directions p1, p2 and p3 of the spheroids and measures the absolute extension in μm . The pairwise ratios between the principal directions provides a relative extension in a certain direction. (b) Boxplots of the normalized spheroids volume at the three indicated time points. Normalization was performed to the median value of the uncompressed spheroids at each time point (c) Boxplots of the normalized number of cells measured for the indicated time points. (d) Distribution histogram of the cell nuclei volume pooled for each condition. Boxplot parameters: the box contains 50% of the data points, the whiskers and outliers show the upper and lower 25% of the data. The line in the box is the median. Sample numbers are listed in Supplemental Table 7-4. Outliers are outside the 1.5x interquartile range. Statistical analysis: Mann-Whitney test. Asterisks indicate statistical significance (* $p < 0.05$, *** $p < 0.001$). The hash (#) indicates biological significance. ♦, outliers. h: hours, n.s.: no significance.

It has been shown previously, that compression of spheroids by increased pressure reduces cell division and increases cell death via apoptosis (Montel et al., 2011, 2012; Delarue et al., 2014; Desmaison et al., 2013). Thus, cleaved caspase-3, which is the active protein form, was stained to assess caspase-dependent programmed cell death in compressed and in control spheroids. Regardless of compression or not, cleaved caspase-3 positive regions were more abundant in the core of the spheroids. The outermost cell layers of the spheroids were vital and rarely showed a positive signal for active caspase-3 (Figure 3-26a). After 1 hour of compression, the amount of cleaved caspase-3 regions was higher compared to uncompressed spheroids (compressed: 7.9%, uncompressed: 2.1%; $p < 0.001$). This difference was balanced when spheroids were compressed for 24 hours. The amount of cleaved caspase-3 positive regions in compressed spheroids did not differ from the controls. Prolonged compression for 96 hours resulted in a decrease of apoptotic areas within the spheroids. In compressed spheroids, 6.2% of the total spheroid volume was positive for cleaved caspase-3, whereas the amount of cleaved caspase-3 in control spheroids was 11.5% ($p < 0.05$) (Figure 3-26b).

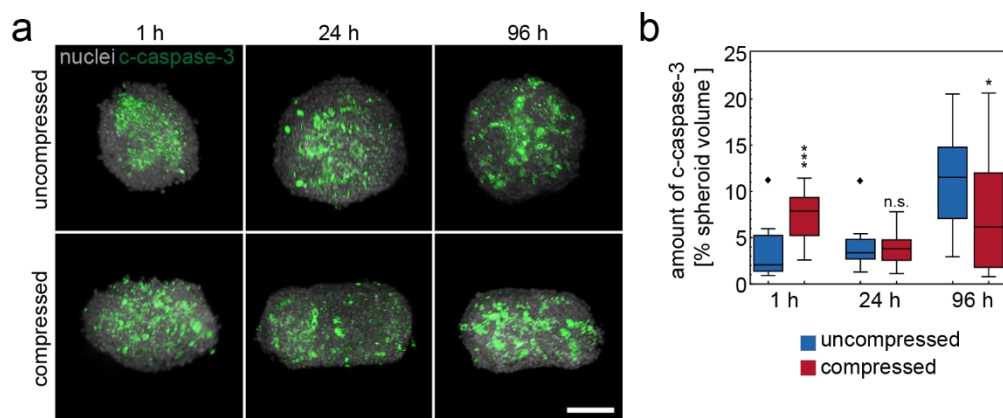


Figure 3-26 The amount of apoptotic cells differs in compressed spheroids. (a) HC11 spheroids were compressed after 10 days of growth. After the indicated time points, spheroids were fixed and cleaved caspase-3 (c-caspase-3) and cell nuclei (DAPI) were labeled. Three-dimensional maximum intensity rendering using Arivis. Microscope: mDSLM, illumination lens: 20x/NA 0.5, detection lens: 5x/NA 0.16, scale bar: 60 μm . (b) Cleaved caspase-positive areas were segmented. The proportion of cleaved caspase-3 positive areas within the spheroid volume was computed. Boxplot parameter: the box contains 50% of the data points, the whiskers and outliers show the upper and lower 25% of the data. The line in the box is the median. Outliers are outside the 1.5x interquartile range. Sample numbers are listed in Supplemental Table 7-4. Statistical analysis: Mann-Whitney test. Statistical significance is indicated with asterisks (* $p < 0.05$, *** $p < 0.001$). ♦, outliers. h: hours, n.s.: no significance.

In summary, short-term compression slightly increased the spheroid volume and the number of cells compared to the controls. Prolonged compression affected neither spheroid volume nor the number of cells. Interestingly, when spheroids were compressed for 24 hours, the cell nuclei volume was strongly decreased compared to the controls. This effect attenuated after prolonged compression for 96 hours. This result indicated that upon compression, cells actively change their cell nuclei volume. The investigation of the amounts of cleaved caspase-3 in the spheroids revealed that a short-term compression increased its activation, whereas a prolonged compression rather decreased caspase-3 activity in spheroids. These results indicated a time-dependent regulation of caspase-induced programmed cell death upon compression of spheroids. This however, not significantly altered the number of cells, indicating that cell proliferation might be altered.

Compression of spheroids does not induce the autophagy flux

Autophagy has been reported to be induced upon mechanical stress in muscle cells (Ulbricht et al., 2013b), cells from the trabecular meshwork (Porter et al., 2014) and human breast adenocarcinoma (King et al., 2011). Chaperone-assisted selective autophagy (CASA) has been reported as a specialized tension-induced autophagy pathway essential for mechanotransduction in mammalian cells (Ulbricht et al., 2013b). We investigated whether CASA was induced in compressed spheroids.

Filamin is damaged upon mechanical forces and needs to be replaced. It has been shown in muscle cells, that the CASA machinery recycled damaged filamin and induces its expression (Ulbricht et al., 2013a). Thus, the mRNA level of filamin was analyzed in spheroids that were compressed and compared to the controls. Therefore, RNA was extracted from spheroids that were incubated in agarose capillaries for 24 hours. The filamin mRNA levels of compressed spheroids compared to the controls did not remarkably change (Figure 3-27a). To further confirm these results, the mRNA level of the co-chaperone BAG3 was analyzed in the compressed spheroids and compared to the controls. BAG3 is an essential protein in the CASA machinery. Upon mechanical stress, unfolded proteins are degraded by the CASA machinery, which in turn reduced the pool of available CASA proteins, thereby activating their expression (Ulbricht et al., 2013a). Interestingly, spheroids that were compressed for 24 hours exhibited a reduced amount of BAG3 mRNA by approximately 20% (Figure 3-27a). This further indicates that CASA was not induced when spheroids were compressed.

Even though CASA was not induced in the compressed spheroids, we investigated whether autophagy was induced in general, as it has been reported that strain-induced autophagy not necessarily has to activate the CASA machinery (Porter et al., 2014).

In 2007, Kimura *et al.* presented a reporter to monitor the autophagic flux in cells via fluorescence microscopy. The fluorescence proteins mRFP and GFP are fused to the microtubule-associated protein 1 (MAP1) light chain 3 (LC3), which is then named tandem-fluorescent LC3 (tfLC3).

Following lipidation, LC3 is bound to the autophagosome membrane. Upon fusion with a lysosomal compartment, the pH in the vesicle drops, which quenches the GFP ($pK_a = 6.0$), whereas the mRFP ($pK_a = 4.5$) remains stable. Thus, a loss of green fluorescent signal over the remaining red fluorescent signal is interpreted as an increase of the autophagic flux (Kimura et al., 2007).

To assess the autophagic flux in compressed spheroids, tfLC3 was stably introduced into HC11 cells. Therefore, the coding sequence of tfLC3 was amplified by PCR from the RCAS-CMV-RFP-GFP-LC3 vector. Restriction sites for BamHI and EcoRI were added to the 5' and the 3' end, respectively. Following enzymatic restriction, the sequence was inserted into the pLeGO- Δ iC2 vector, which is devoid of the fluorescent reporter by excision with PciI. In the resulting vector, a SFFV promoter drives the expression of tfLC3. Lentiviral particles were produced to transduce HC11 cells. GFP⁺ and mRFP⁺ cells were enriched with FACS (Supplemental Figure 7-14). These cells were used at a maximum of 12 passages (approximately four weeks).

To analyze the autophagic flux upon compression, spheroids were formed for 10 days. Then, the spheroids were inserted into either agarose capillaries with a diameter of 200 μ m to induce a deformation of the spheroids, or 300 μ m agarose capillaries as controls. After insertion, the mounted spheroids were cultured for 24 hours in assay medium. For a positive control, spheroids mounted in 300 μ m thick agarose capillaries were incubated in starvation (EBSS) medium to induce autophagy.

Following the incubation period, the signal intensities of GFP and mRFP were analyzed with a wide-field fluorescence microscope. The positive control clearly showed an induction of autophagy, since the mRFP signal exceeded the GFP signal (Figure 3-27b). Qualitatively, a difference between compressed and uncompressed spheroids was not distinct. Therefore, a quantitative analysis of the image data was performed (Pampaloni et al., 2017). The mRFP and the GFP signals were measured and the ratio between them indicated the strength of the autophagic flux. This analysis showed that the mechanical compression for 24 hours spheroids had no impact on the induction of autophagy in spheroids (Figure 3-27c). However, the autophagic flux showed a large variance, thus mild changes of autophagy induction are likely to be missed by this analysis.

In summary, the BAG3 mRNA was reduced upon compression of spheroids, while the filamin mRNA level was unaltered in compressed spheroids. This, in conjunction with the unchanged autophagic flux, indicate that neither autophagy in general nor CASA were not induced upon compression of spheroids.

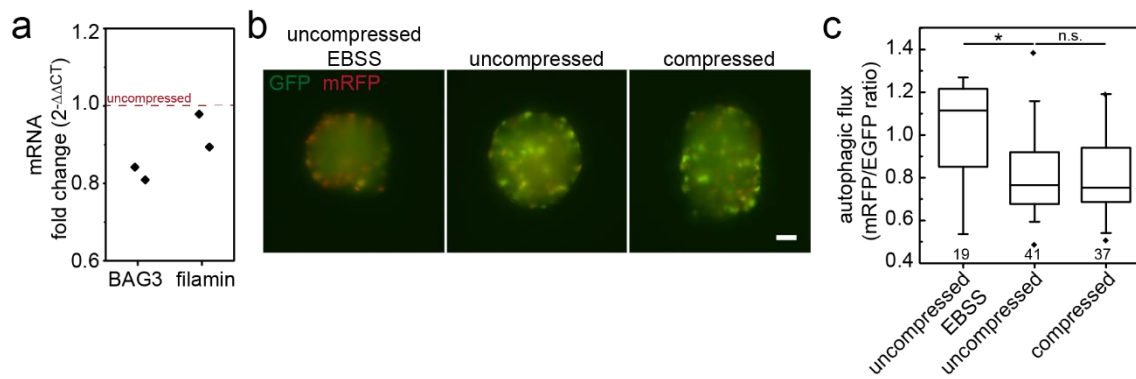


Figure 3-27 Autophagic flux does not increase upon compression of mammary epithelial cell spheroids.

(a) Amount of BAG3 mRNA in spheroids compressed for 24 hours compared to the control (red dashed line). About 25 spheroids per condition were pooled prior RNA extraction. The experiment was conducted twice. (b) HC11 spheroids expressing tFLC3 were seeded from 5,000 cells and incubated in agarose capillaries after 10 days of growth. Control spheroids were incubated in starvation medium (EBSS) during the period of compression. After 24 hours of compression, spheroids were subjected to fluorescence microscopy. Microscope: Zeiss Axio Observer.Z1, objective lens: Fluor 10x/NA 0.5, scale bar: 50 μ m. (c) Ratio between mRFP and EGFP signal was measured in the spheroids. Higher ratios indicate an increased autophagic flux. ♦, outliers. Statistical analysis: Mann-Whitney test with Bonferroni correction for multiple testing (n.s.: not significant, * $p < 0.05$).

3.5 A spheroid formation assay reproduces modalities of tissue integrity

In addition to physical forces, cellular processes like cell adhesion and growth are involved in modulating tissue integrity. These processes were investigated in a three-dimensional context using a spheroid formation assay. This assay allows studying various processes in an adhesion-free environment. Cell adhesion to other cells and to the ECM as well as cell growth are abundant during spheroid formation. The contribution of proteins that are prominent in these processes, such as E-cadherin, the actin and the microtubule cytoskeleton, FAK and BAG3, was investigated in the formation of three-dimensional cell clusters.

Several people contributed to the spheroid formation project. Biena Mathew and I did the conceptual work. Further, I generated the transgenic HC11 and 4T1 cells and performed the experiments with the help of several people. Susanna Lissek performed the spheroid formation assay for T47D cells and helped with other laboratory work. Sigrun Becker analyzed the mRNA abundance of ECM proteins and performed the attachment assay. Melisa Merdan-Desik, Sanam Saeifar and Carolin Fix worked with HC11, 4T1 and T47D cells, respectively, to determine the appropriate working concentrations of the drugs. Biena Mathew did all image and statistical analysis and Dr. Sabine Fischer worked on the agent-based computational model. Biena Mathew and I interpreted the results and wrote a manuscript. Contents of the sections 3.5.1 - 3.5.5 were submitted for publication to a peer-reviewed scientific journal.

3.5.1 Aggregation, compaction and growth are phases in spheroid formation

Spheroid formation is a highly dynamic process and time-lapse microscopy obtains temporal resolution for its detailed investigation. To monitor spheroid formation, the three cell lines were transformed by retroviral transduction with a fluorescent nuclear marker (EGFP-H2B) and an F-actin marker (LifeAct-tagRFP). Fluorescent cells were enriched with FACS. The image acquisition of the nuclear marker allowed to monitor the accumulation of living, fluorescent cells and to discriminate them from dead, non-fluorescent cells. An analysis of the transmission channel would not have allowed this, because it provides a non-specific contrast.

Spheroids were formed according to the liquid overlay method (Carlsson and Yuhás, 1984) and imaged over a period of 48 hours with intervals of 30 minutes with a wide-field fluorescence microscope. A transmission channel as well as a fluorescence channel, showing the nuclear marker EGFP-H2B, were acquired (Figure 3-28a). To exclude phototoxic effects by increased light exposure, controls were imaged at the first (0 hours) and the last (48 hours) time point of the experiment (Supplemental Table 7-5). In addition to the highly temporally resolved first 48 hours of spheroid formation, the spheroids were imaged 7 days after formation to study effects in the long term. Biena Mathew analyzed the image data. She segmented the projected area of the spheroids in the fluorescence images, if not stated otherwise (Supplemental Figure 7-15a), plotted the normalized projected area as a function of the time and performed the statistical analyses.

In these experiments, the volume occupied by the cells was projected to the x,y-plane. The projected area is large when cells are not connected with each other or when cells proliferate. When cells accumulate and form cell contacts, the projected area decreases. Spheroid formation has been reported to consist of three phases: aggregation, compaction and growth (Enmon et al., 2001; Lin et al., 2006). According to the area-time plots, the phases were partially distinguished. A fast decay of the projected area at the beginning of spheroid formation indicated the aggregation phase. Then, the curve underwent an inflection point to reach a course with a rather invariable projected area. The point of inflection indicated the commencing compaction of cells. When the progression of the curve showed a steadily increasing projected area, spheroid growth was initiated. To determine the phases of spheroid formation precisely, Biena Mathew computed the shrinkage rate. The shrinkage of the projected area was linearly approximated by $\Delta NA/\Delta t$, where ΔNA is the difference of the normalized area between two time points and Δt is the according time step (Figure 3-28c). The transition between the phases was empirically determined based on the shrinkage rate of 4T1 spheroids, which showed the three phases within the time course of 48 hours. It revealed the transition from the aggregation to the compaction phase as drop of the shrinkage rate that lasted more than 1.5 hours. The obtained threshold value was approximated at a shrinkage rate of 0.008. The growth phase was initiated when the shrinkage rate that dropped below zero for at least 1.5 hours. According to these rules, the spheroid formation phases were assigned accurately. The

assigned phases fitted well the previous assumptions made from the area-time plots. The analyses revealed different spheroid formation dynamics among the three cell lines (Figure 3-28b). HC11 cells aggregated within the first 18.5 hours and compacted until at least 48 hours of spheroid formation. 4T1 cells exhibited a shorter aggregation phase of only 12 hours. After 24 hours, growth overcame compaction and spheroids gained size. The slowly accumulating T47D cells showed a transition from the aggregation to the compaction phase after 29.5 hours (Figure 3-28c).

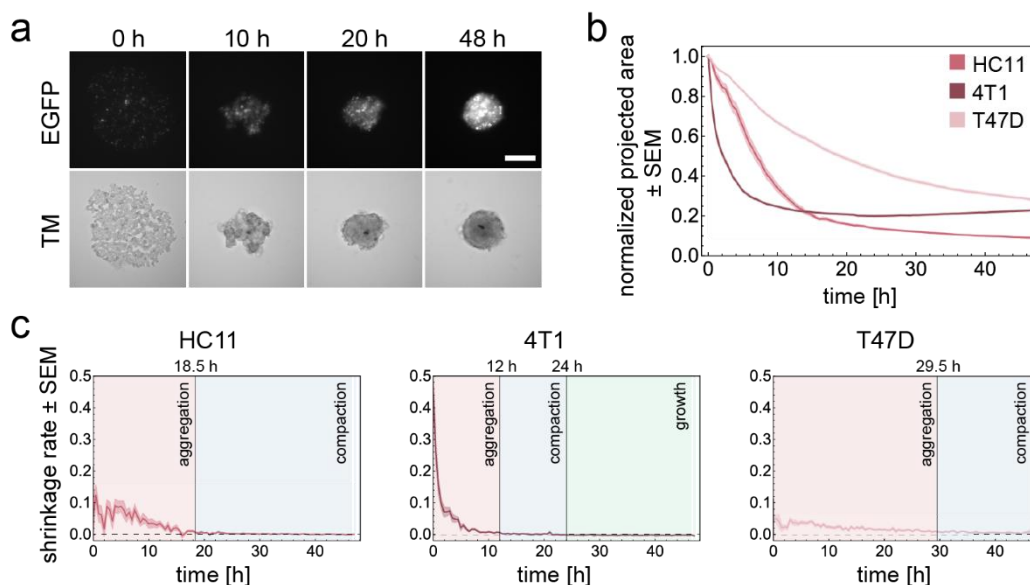


Figure 3-28 Cell lines have different spheroid formation dynamics. (a) Spheroid formation exemplified with mouse mammary epithelial cells (HC11) over 48 hours. Images show the transmission and fluorescence channel, where EGFP-H2B was captured. (b) Formation dynamics were expressed as the projected area occupied by the cells. Data was normalized to the first time point. Shaded regions show the SEM. Spheroids were formed in presence of DMSO. (c) The shrinkage rate of forming spheroids was approximated by $\Delta NA/\Delta t$, where ΔNA is the difference of the normalized area between two time points and Δt the time step. The compaction phase begins when the shrinkage rate drops below 0.008. The growth phase is initiated when the shrinkage rate is below zero. Microscope: Zeiss Axio Observer.Z1, objective lens: Fluor 10x/NA 0.5, scale bar: 50 μm (modified from Smyrek & Mathew *et al.* 2017).

The analysis of the aggregation dynamics revealed the spheroid formation characteristics of the individual cell lines. However, according to their metastatic potential (HC11<T47D<4T1), these results did not allow a conclusive interpretation. Therefore, further experiments were performed.

3.5.2 E-cadherin is required for tight aggregation of mammary epithelial cells

To investigate the role of E-cadherin in spheroid formation in the three cell lines, an E-cadherin function-blocking antibody, DECMA-1 was used (Vestweber and Kemler, 1985). DECMA-1 disrupted cell adhesion sites at a concentration of 10 $\mu\text{g}/\text{ml}$ (Supplemental Figure 7-16b). The spheroid formation assay showed that DECMA-1 inhibited the adhesion capabilities of the cells. HC11 and 4T1 cells did not form spheroids but rather lose cell aggregates. During the entire process, the cell cluster showed a strong agility, which was reflected by the strong variations of the projected

area in subsequent time steps (Figure 3-29a). The projected area of DECMA-1- treated T47D cells decreased steadily but did not reach the size of the controls. The strong fluctuations in the projected area found in HC11 and 4T1 cells were absent in T47D cells (Figure 3-29a). The projected area of DECMA-1-treated cells compared to the controls was significantly increased in all cell lines at nearly all time points. An exception were T47D cells, which after 6 hours of formation showed no difference between DECMA-1 and the control (Figure 3-29b). After 7 days in culture, cells treated with DECMA-1 did not form spheroids, but rather loose cell aggregates (Supplemental Figure 7-17).

An agent-based computational approach (by Dr. Sabine Fischer) has been established to characterize the binding and unbinding probability of the cells during the spheroid formation process (Garg et al., 2015). Fitting the data from the computational model to the experimental data revealed that in neither case the binding probability was different from the control but rather the unbinding probability. Spheroids formed from HC11 cells showed an increased unbinding probability by more than three times when E-cadherin was blocked with antibodies ($p_{\text{unbindIgG1}} = 0.02 \pm 0.003$, $p_{\text{unbindDECMA-1}} = 0.07 \pm 0.006$). In 4T1 cells, the unbinding probability was increased upon DECMA-1 treatment compared to the control ($p_{\text{unbindIgG1}} = 0.06 \pm 0.008$, $p_{\text{unbindDECMA-1}} = 0.09 \pm 0.007$). Interestingly, T47D spheroids showed no difference between the unbinding probability of DECMA-1-treated cells compared to the control ($p_{\text{unbindIgG1}} = 0.01 \pm 0.0$, $p_{\text{unbindDECMA-1}} = 0.01 \pm 0.002$) (Figure 3-29c, Supplemental Figure 7-18).

The involvement of E-cadherin in the spheroid formation process is believed to primarily, but not exclusively, accomplish spheroid formation (Saias et al., 2015; Ivascu and Kubbies, 2007; Lin et al., 2006). However, little is known about the time-dependent contribution of intracellular molecules in this contact formation process. Thus, the actin cytoskeleton, myosin II, microtubules and the focal adhesion kinase (FAK), which are well-known contributors to the adhesion machineries, were chosen for further investigation. Therefore, pharmacological inhibitors were used: cytochalasin D to inhibit actin polymerization (Fox and Phillips, 1981), para-nitroblebbistatin to inhibit myosin II activity (Képiró et al., 2014), nocodazole to block microtubule polymerization (Samson et al., 1979), thereby leading to microtubule catastrophe, and PF-573228 to inhibit phosphorylation of FAK at position Y397, and thereby inactivating it (Slack-Davis et al., 2007).

The appropriate concentrations of the drugs were determined in cells grown in two-dimensional cell culture. For the drugs cytochalasin D, para-nitroblebbistatin and nocodazole, F-actin and microtubules were labeled. Cells were treated with different drug concentrations for different periods of time. The integrity of these two cytoskeletal proteins indicated the efficacy of the drugs. The efficacy of PF-573228 was investigated with an immunoblot.

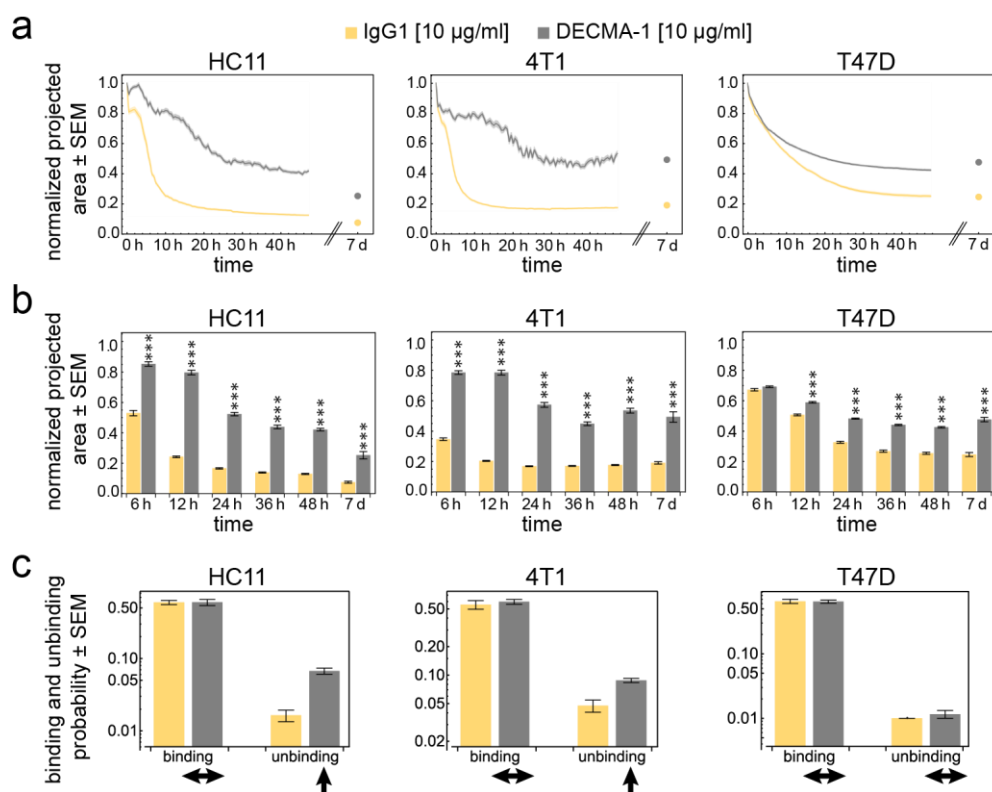


Figure 3-29 Mammary epithelial cells require E-cadherin to form spheroids. (a) Spheroid formation dynamics of HC11, 4T1 and T47D cells. Cells were treated with DECMA-1 antibody to block E-cadherin function or with IgG1 antibody as control. The projected area was measured and normalized to the first time point. Spheroid formation was investigated for 48 hours and the final size of spheroids was measured after 7 days (dot). The shaded regions show the SEM. (b) Bars show the normalized projected area at specific time points: 6, 12, 24, 36, 48 hours and 7 days. (c) Binding and unbinding probabilities obtained from fitting the agent-based computational model to the experimental data. The arrows show the difference of the binding and unbinding probability compared to the control. The Wilcoxon rank sum test with Holm correction for multiple testing was used for hypothesis testing. Asterisks show significant differences (* $p < 0.05$, ** $p < 0.01$, *** $p < 0.001$). Sample numbers are listed in Supplemental Table 7-6 (modified from Smyrek & Mathew *et al.* 2017).

Drug concentration testing revealed appropriate cytochalasin D concentrations of 2.5 μM for HC11 and 4T1 cells, and 1 μM for T47D cells (Supplemental Figure 7-19). The appropriate concentration of para-nitroblebbistatin was 10 μM for all cell lines. At this concentration, cells showed strong morphological alterations of the cell shape and of the actin cytoskeleton. No increase of cell death was observed (Supplemental Figure 7-20). For HC11 and 4T1 cells, 5 μM nocodazole was required to affect microtubule polymerization, while for T47D cells 0.5 μM was sufficient (Supplemental Figure 7-21). To block FAK activity, the inhibitor PF-573228 has proven sufficiently at a concentration of 1 μM in the three cell lines (Supplemental Figure 7-16a).

3.5.3 Actin is indispensable for spheroid formation and reinforces cell adhesion

The actin cytoskeleton is known to be heavily involved in cell adhesion, cell shape regulation and migration (reviewed in Gardel *et al.*, 2010). In the three-dimensional context, it has been shown to

be an important contributor to spheroid formation (Tzanakakis et al., 2001; Gardel et al., 2010; Yoshii et al., 2011). However, these studies provide neither a high temporal resolution nor quantitative analysis. A detailed and temporally resolved investigation of actin in spheroid formation and a complementary analysis with the agent-based computational model were performed to gain knowledge about how actin contributes to this process.

When cytochalasin D was added to the cells, the first hours of spheroid formation were not influenced in HC11 and T47D cells, while 4T1 cells showed a larger projected area when the actin cytoskeleton was disrupted. At the onset of spheroid formation, HC11 and T47D cells showed a strong effect upon cytochalasin D treatment and on the long run, spheroids did not form (Figure 3-30a, b). The projected area was significantly larger in all cell lines at time points 12 hours, 24 hours, 36 hours, 48 hours and 7 days compared to the control (Figure 3-30b). The effect of actin disruption in T47D cells was severe. Cells stopped aggregating after 10 hours, while HC11 and 4T1 cells aggregated further to a certain extent. However, all cell lines failed to form compact spheroids after 48 hours and 7 days (Supplemental Figure 7-15b, Supplemental Figure 7-22a). Especially after 7 days upon cytochalasin D treatment, cellular aggregates were fragile while pipetting. After 7 days, HC11 cells showed a slightly increased projected area compared to the time point at 48 hours. Interestingly, 4T1 aggregates showed an increasing projected area from 30 hours of spheroid formation on, which was after 7 days as large as the initial size at time point 0 hours (Figure 3-30a, b). Investigation of the 4T1 cell morphology revealed that the size of the cell nuclei increased upon cytochalasin D treatment (Supplemental Figure 7-22b), which suggested that the increasing projected area was rather due to cell volume changes than due to increased cell division. Contrary to HC11 and 4T1 cells, T47D cells had a smaller projected area after 7 days compared to 48 hours (Figure 3-30a, b). To exclude that the disability to form spheroids upon cytochalasin D treatment was due to an induction of cell death, we performed a live-dead assay at various time points during the spheroid formation process. The results showed that cytochalasin D did not induce an excess of cell death. In the majority of investigated time points, the ratio between dead and living cells was similar to the control (Supplemental Figure 7-23).

To further investigate the influence of actin on the adhesive properties of the cells, the agent-based computational model was fitted to the experimental data to obtain quantitative data on the binding and unbinding probability of the cells. When the actin cytoskeleton was disrupted, the probability at which two cells bind decreased in T47D cells ($p_{\text{bindDMSO}} = 0.62 \pm 0.04$, $p_{\text{bindcytochalasinD}} = 0.57 \pm 0.04$), but it was not altered in HC11 and 4T1 cells (Figure 3-30c and Supplemental Figure 7-18). More prominent was the change of the unbinding probability when actin was depolymerized. It was at least doubled in each of the three cell lines (Figure 3-30c and Supplemental Figure 7-18), which indicated that a general mechanism of actin is to stabilize intercellular junctions in multicellular aggregates.

In comparison to the function-blocking antibody DECMA-1, which also inhibited spheroid formation and showed strong movement of cellular aggregates, the aggregating cells devoid of F-actin lacked these dynamic movements completely.

In summary, these data showed that the actin cytoskeleton is crucial driving the aggregation of isolated cells. Actin is necessary to ensure that connections, which have been formed, do not break again by enforcing the adhesion (Vasioukhin and Fuchs, 2001). In addition, actin may facilitate a certain agility of the cellular aggregates, which is necessary to form a three-dimensional cluster.

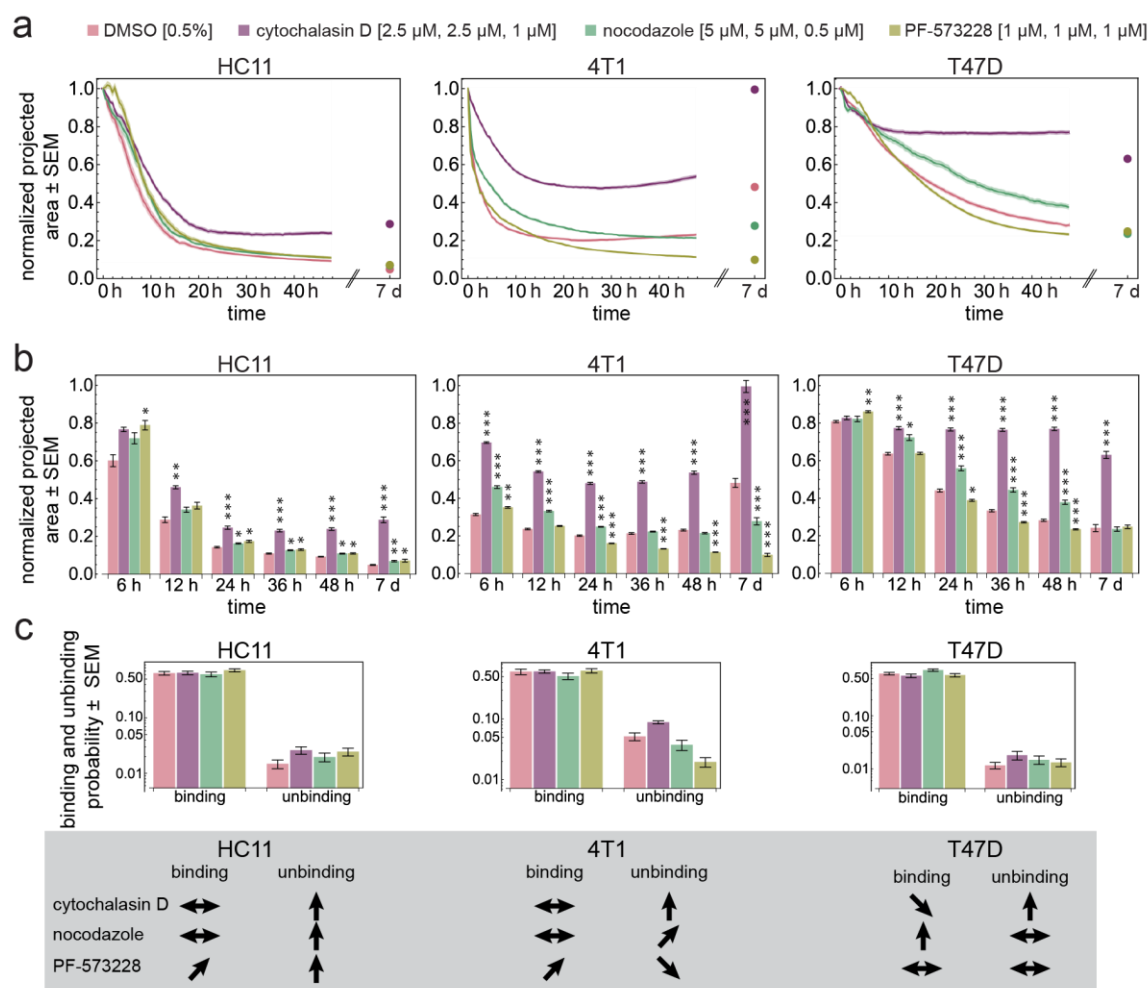


Figure 3-30 The cytoskeleton and FAK activity influence spheroid formation dynamics. (a) Cells were treated with either cytochalasin D, nocodazole or PF-573228 to destabilize or inhibit F-actin, microtubules and FAK, respectively. Spheroid formation was analyzed over 7 days, where the first 48 hours were studied extensively. The projected area occupied by HC11, 4T1 and T47D cells is normalized to the area at the first time point. The line shows the mean. Shaded regions show the standard error of the mean (SEM). Dots are the projected area measured after 7 days. (b) Bars show the normalized projected area after 6, 12, 24, 36, 48 hours and after 7 days in HC11, 4T1 and T47D cells. Hypothesis testing was performed using a Wilcoxon rank sum test with Holm correction for multiple testing. Asterisks show significant differences (* $p < 0.05$, ** $p < 0.01$, *** $p < 0.001$). Drugs were compared to the DMSO control. Sample numbers are listed in Supplemental Table 7-6. (c) Binding and unbinding probabilities obtained from fitting the agent-based computational model to the experimental data. The arrows show the difference of the binding and unbinding probability compared to the control. (modified from Smyrek & Mathew *et al.* 2017).

The actin cytoskeleton is not a stiff structure but rather exhibits high dynamic characteristics facilitated by actin-binding proteins. These dynamics ensure cellular tension, cell shape and control cell movement. Proteins of the class II myosins are motor proteins that associate with actin and actively move actin filaments relative to each other (Ouderkirk and Krendel, 2014). To investigate the function of actin filament dynamics, the microscopy-friendly derivative of blebbistatin, para-nitroblebbistatin was used (Supplemental Figure 7-24, Képiró et al., 2014). Both inhibit the ATPase activity of myosin II. In the spheroid formation assay, both components, blebbistatin as well as para-nitroblebbistatin showed strong cytotoxic effects when they were illuminated with blue light (470 nm) to detect EGFP-H2B (Supplemental Figure 7-25). The cytotoxic effect was more severe with blebbistatin than with para-nitroblebbistatin. Thus, the results could not be used for an interpretation.

3.5.4 Microtubule depolymerization decelerates spheroid formation and inhibits spheroid growth

The second investigated cytoskeletal component was the microtubule cytoskeleton. Microtubules are important for cell division, migration and influence the formation, maintenance and dissociation of cell adhesion to other cells and to the ECM (Etienne-Manneville, 2013; Mary et al., 2002). Upon depolymerization using the drug nocodazole, the aggregation and compaction phases were affected, but spheroids formed. The aggregation of the non-tumorigenic HC11 cells decelerated not significantly within the first 12 hours of spheroid formation. After 24 hours of spheroid formation, the aggregates were less compact when microtubules were destabilized. After 7 days of spheroid formation, HC11 spheroids condensed, but were not as compact as the controls (Figure 3-30a, b and Supplemental Figure 7-15b).

The highly invasive cell line 4T1 aggregated significantly slower during the initial 24 hours compared to the controls (Figure 3-30a, b and Supplemental Figure 7-15b). Spheroids devoid of functional microtubules further compacted and had the same projected area compared to the controls between 36 hours and 48 hours of spheroid formation. However, while the size of control spheroids increased presumably due to proliferation within 48 hours, growth was not present in nocodazole-treated spheroids. This effect was still prominent after 7 days of culture.

From 12 hours onwards, T47D spheroids treated with nocodazole had a larger projected area compared to the controls. After 7 days in culture, this effect was not anymore observable and the size of spheroids treated with nocodazole was similar to the controls (Figure 3-30a, b and Supplemental Figure 7-15b).

Further investigation of the binding behavior of the cells when the microtubule cytoskeleton was not functional revealed that the binding probability in HC11 cells was not affected but the unbinding probability was doubled compared to the controls ($p_{\text{unbindDMSO}} = 0.01 \pm 0.003$, $p_{\text{unbindnocodazole}}$

= 0.02 ± 0.003). This was also found in 4T1 cells, where the unbinding probability tended to be increased ($p_{\text{unbindDMSO}} = 0.03 \pm 0.006$, $p_{\text{unbindnocodazole}} = 0.04 \pm 0.006$). Contrary to HC11 and 4T1 cells, T47D cells, which also showed a decelerated aggregation, had an increased binding probability upon treatment with nocodazole ($p_{\text{bindDMSO}} = 0.62 \pm 0.04$, $p_{\text{bindnocodazole}} = 0.73 \pm 0.04$), and their unbinding probability was not changed (Figure 3-30c and Supplemental Figure 7-18).

Together, these data suggest a role for microtubules in the aggregation and compaction phases of spheroid formation. Unlike actin, the microtubules are not crucial for a successful accumulation of cells into spheroids and the way of action seems to be different among cell types.

3.5.5 FAK activity is crucial for spheroid growth but not for spheroid formation

External cues such as the binding of cells to the ECM often influence cytoskeleton remodeling. The cells from the three investigated cell lines synthesized ECM early in forming spheroids (section 3.3). This led to the hypothesis that ECM-mediated signaling into the cell impacts the aggregation of cells to form compact spheroids. A prominent mediator of such signals is FAK, a highly tyrosine-phosphorylated kinase that links integrin receptor signaling to intracellular pathways. It thereby influences cell proliferation, cell survival, migration, and adhesion. FAK induces cytoskeleton remodeling and transmits signals to the cell-cell adhesion and cell-ECM adhesion sites (Schlaepfer et al., 1999). Therefore, the influence of FAK activity in spheroid formation was investigated.

In HC11, 4T1 and T47D cells, the aggregation within the first 6 hours was decreased when FAK phosphorylation at Y397 ($p\text{FAK}^{\text{Y397}}$) was inhibited. After 12 hours of spheroid formation, the projected area of FAK inhibited cells was similar compared to the controls. Interestingly, after 24 hours, the projected area of HC11 cells was smaller compared to the controls, while it was larger in 4T1 and T47D cells (Figure 3-30a, b). This effect was also prominent after 48 hours of spheroid formation. After 7 days, HC11 spheroids were still larger compared to the controls and 4T1 spheroids were still smaller, while T47D spheroids were similar to the controls. Interestingly, while control spheroids of 4T1 cells showed an increasing projected area from approximately 24 hours onwards, the FAK inhibited spheroids did not show this increase of the projected area. In addition, when FAK was inhibited the alterations observed were more prominent in 4T1 cells compared to HC11 and T47D cells.

A comparison with the computational model revealed that the binding probability of HC11 cells was slightly increased compared to the control ($p_{\text{bindDMSO}} = 0.64 \pm 0.05$, $p_{\text{bindPF-573228}} = 0.72 \pm 0.05$) and the possibility that formed contacts break again was doubled in HC11 cells ($p_{\text{unbindDMSO}} = 0.01 \pm 0.003$, $p_{\text{unbindPF-573228}} = 0.02 \pm 0.004$) (Figure 3-30c and Supplemental Figure 7-18). In 4T1 cells, the impact of PF-573228 treatment on the binding and unbinding probability was a slight increase of the binding probability and a slight decrease of the unbinding

probability ($p_{\text{bindDMSO}} = 0.62 \pm 0.06$, $p_{\text{bindPF-573228}} = 0.69 \pm 0.05$ and $p_{\text{unbindDMSO}} = 0.03 \pm 0.006$, $p_{\text{unbindPF-573228}} = 0.02 \pm 0.005$) although the effects on the projected area of spheroids were the strongest. In T47D cells, PF-573228 treatment affected neither the binding nor the unbinding probability.

In summary, these data suggested that an intact FAK signaling is not crucial for the successful assembly of cellular aggregates but rather for their growth. These results showed that FAK affects spheroid formation in a cell type-dependent manner.

To investigate the origin of the differences in forming spheroids observed among the cell lines when FAK was inhibited, the basal levels of FAK pFAK^{Y397} were measured. Protein extracts from spheroids grown for 2 and 7 days were collected, separated with SDS-PAGE and analyzed with immunoblotting. The activity of FAK strongly depends on the activity of integrin receptor signaling (Cukierman et al., 2001). Since this is strongly increased in two-dimensional monolayer cultures, protein extracts from cells grown on plastic surfaces were used for further comparison. The protein level of FAK and pFAK^{Y397} varied strongly among the three cell lines and between the two-dimensional and the three-dimensional cultures. When HC11 cells grew as a monolayer culture, FAK and pFAK^{Y397} were detected. However, when these cells were used to form spheroids, FAK and pFAK^{Y397} protein levels were reduced to the detection minimum (Figure 3-31a, upper blot). This was different for 4T1 cells, which showed increased protein level of both, and pFAK^{Y397} in all culture conditions. Unlike HC11 cells, the protein level of FAK and pFAK^{Y397} remained high in 4T1 spheroids (Figure 3-31a, middle blot). In the human T47D cells, FAK and pFAK^{Y397} were detectable in the monolayer cultures. When T47D cells grew as spheroids, the protein level of FAK remained, but compared to that the level of active FAK decreased strongly to the detection minimum in 7 days old cultures (Figure 3-31a, lower blot).

FAK protein level and the phosphorylation at Y397 were high in 4T1 spheroids. In these cells, the effects of FAK inhibition on spheroid growth were prominent. FAK is essential for tumor growth (Wendt et al., 2011; Tanjoni et al., 2010; Tancioni et al., 2015) and its influence on cell proliferation can occur either in an integrin-dependent manner or independently from an association of integrin with the ECM. While in the first option FAK remains as a cytoplasmic relay for the signal coming from the integrins, the second option is marked by a nuclear trans-localization of FAK (Lim, 2013). To investigate the intracellular distribution of FAK, it was immunolabeled in spheroids of different age. In spheroids of all investigated time points (i.e. 24 hours, 48 hours and 7 days), the immunofluorescence staining of FAK showed a weak signal that was distributed in the cytoplasm of the cells and it was excluded from the cell nuclei (Figure 3-31b). Interestingly, although FAK inhibition had a strong effect on spheroid growth of 4T1 cells, the cell viability was not affected when these cell were cultured as a monolayer. Contrarily, when HC11 cells were cultured as a

monolayer, FAK inhibition had a positive effect on cell viability. In T47D monolayer cultures, FAK inhibition had no effect compared to the control (Supplemental Figure 7-23).

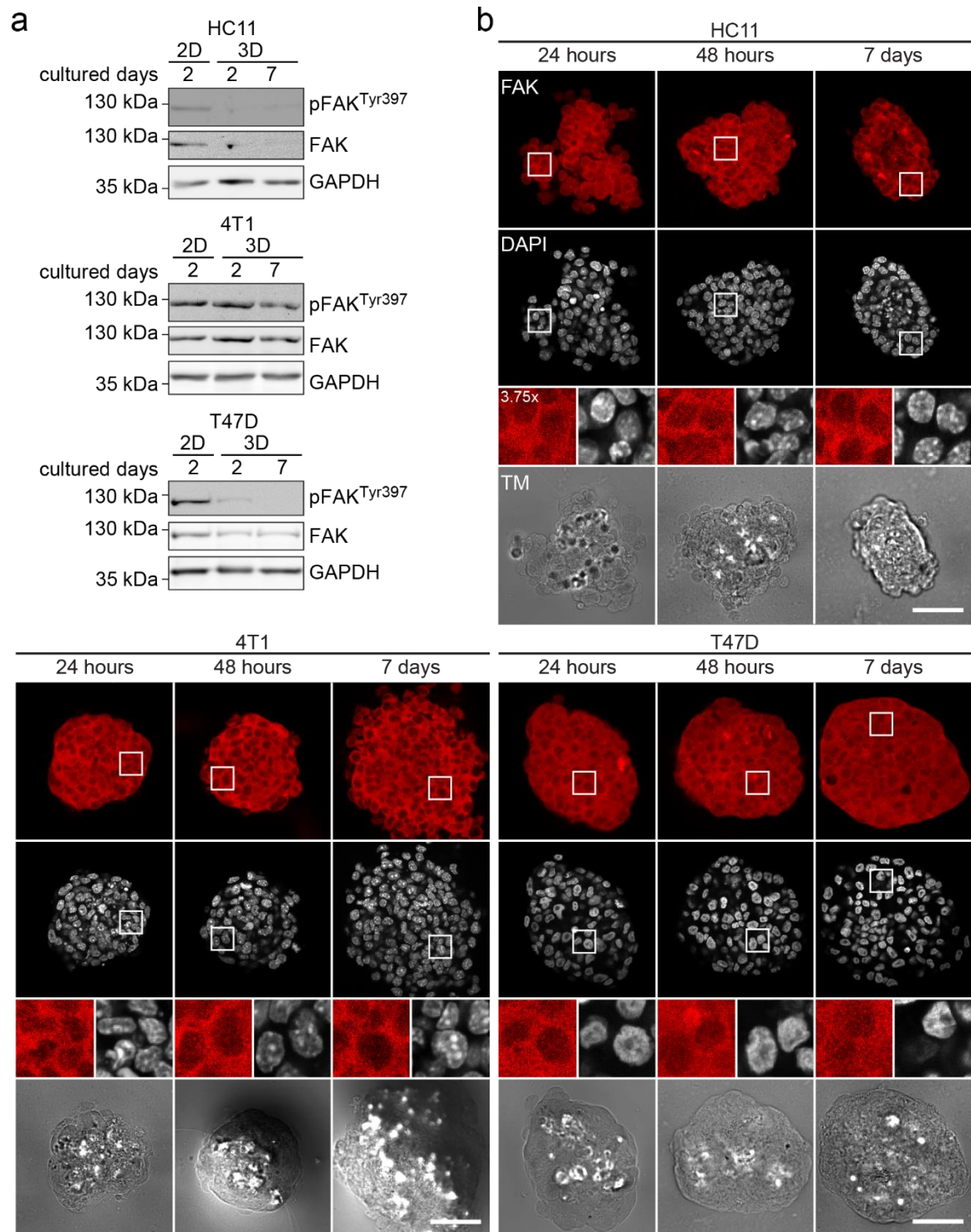


Figure 3-31 FAK synthesis and phosphorylation differs between cell lines and culturing methods. (a) Immunoblot analysis was performed with protein extracts from monolayer and spheroid culture. Cells were lysed with RIPA buffer and analyzed by SDS-PAGE. Antibodies against FAK and pFAK^{Y397} were used. GAPDH is shown as loading control. (b) Immunostaining against FAK shows a cytoplasmic distribution in spheroids formed from HC11, 4T1 and T47D cells at different time points of spheroid formation. The staining was excluded from the cell nuclei. DAPI was used to stain cell nuclei. A section from the central region of

the spheroid is shown. Microscope: Zeiss LSM780, objective lens: Plan-Neofluar 40x/NA 1.3 oil, scale bar: 50 μm . (modified from Smyrek & Mathew *et al.* 2017).

These results demonstrated that the synthesis of FAK strongly differed between the monolayer cultures and the spheroid cultures. Further, pFAK^{Y397} decreased in two of the three cell lines, when they grew as spheroids. This indicated that integrin-mediated activation of FAK strongly depends on the culture conditions. In 4T1 cells, which are highly invasive cancer cells, the culture conditions showed no effect, which presumably was due to deregulated signaling (McLean *et al.*, 2005). The intracellular location of FAK was cytoplasmic in the three cell lines indicating no nuclear translocation of FAK, which has been reported to be an alternative pathway of FAK on growth regulation.

3.5.6 BAG3 knockdown decelerates the aggregation phase and BAG3 knockout reduces cell viability in spheroids

The influence of BAG3, which was modulating cell migration and cell viability in HC11 monolayer cultures, was analyzed in the spheroid formation process. Therefore, BAG3 knockout and knockdown cells were used. As controls, the appropriate sgscr or shscr cells were used. Since the knockout cells were devoid of a fluorescence marker, the segmentation of the projected area was performed in the transmission channel. Spheroids formed from cells with BAG3 downregulation showed a larger projected area in the late aggregation phase. At time points 6 hours and 12 hours, the differences were statistically significant. From 15 hours on, the projected area of the BAG3 knockdown cells was similar to the controls. Interestingly, this was close to the time point when compaction was prominent. From then on until 48 hours, the size of the BAG3 knockdown spheroids was similar to the controls. However, at the last time point (48 hours), the knockdown cells showed a slightly enlarged projected area. At the long term (7 days), a downregulation of BAG3 had no effect on the spheroid size (Figure 3-32a). Interestingly, when BAG3 knockout cells were used, the effect on cell aggregation, which was observed in the knockdown, was not detected. BAG3 knockout cells showed a slightly smaller projected area after 6 hours of spheroid formation. After 7 days of formation, the BAG3 knockout spheroids projected a larger area compared to the controls (Figure 3-32b). Fitting the data obtained from the agent-based computational model to the experimental data revealed that neither the binding nor the unbinding probabilities changed upon either knockdown or knockout of BAG3 in the cells (Figure 3-32c, d). An examination of the segmentation showed that within the course of time the spheroids shed cells, which accumulated around the living spheroid (Figure 3-32e). Since the image segmentation was performed in the transmission images, the accumulation of dead cells was also segmented and accounted to the projected area (Supplemental Figure 7-26). Comparing the image data of BAG3 knockout cells with the control cells showed that after 7 days of formation, BAG3 knockout spheroids showed more

dead cells, indicating a reduction of cell survival on the long term. The quantification of dead cells further supported this. BAG3 knockout spheroids exhibited increased cell death after 7 days in culture ($p < 0.05$). Interestingly, this effect was not yet present in spheroids that were 2 days old (Figure 3-32f).

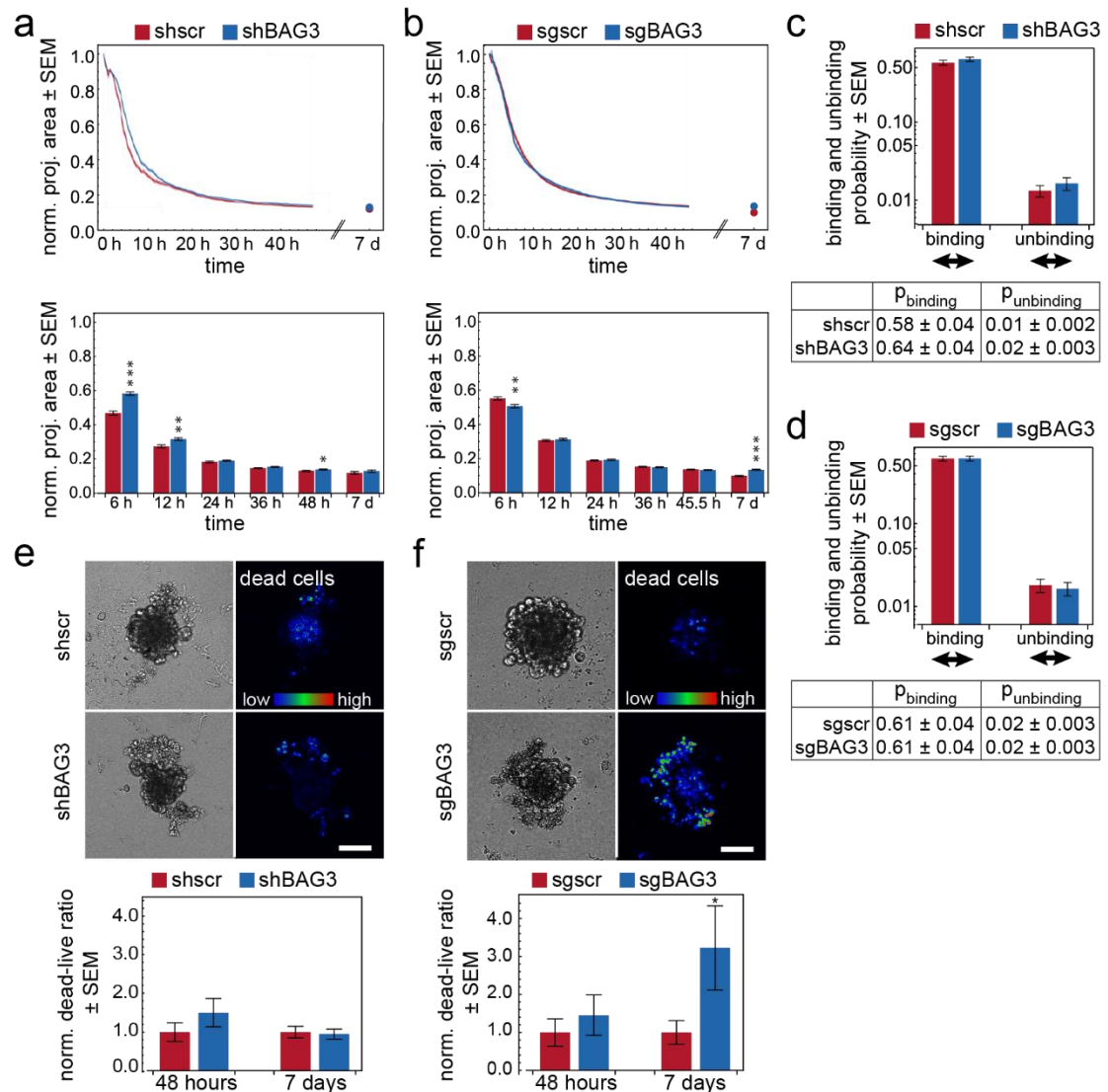


Figure 3-32 BAG3 knockdown but not knockout affects spheroid formation in the aggregation phase and BAG3 knockout but not knockdown induces cell death in spheroids in the long term. (a, b) The projected area of cells in the x,y-plane was segmented and plotted over time to show the spheroid formation dynamics. Spheroids were formed from (a) BAG3 knockdown and (b) BAG3 knockout cells. (c, d) Binding and unbinding probabilities obtained from fitting the agent-based computational model to the experimental data from the spheroid formation of (c) BAG3 knockdown or (d) knockout cells. The arrows show the difference of the binding and unbinding probability compared to the control. (e, f) Live-dead assay of spheroids with a (e) knockdown or (f) knockout for BAG3. Images show the transmission channel and the fluorescence channel of spheroids after 7 days of culture. The fluorescence intensities are mapped from low (blue) to high (red) signal intensities. The amount of dead cells was measured 48 hours and 7 days after spheroid formation. Sample numbers are listed in Supplemental Table 7-6 and Supplemental Table 7-7. Statistics: Mann-Whitney test with Holm correction for multiple testing (* $p < 0.05$, ** $p < 0.01$, *** $p < 0.001$).

In summary, these results demonstrated that a BAG3 knockdown provides different results than a knockout in a spheroid formation assay. The delay in the aggregation phase of BAG3 knockdown cells was not detectable in the knockout. Contrary, the long-term effects on cell survival were observed only in BAG3 knockout cells but not under knockdown conditions.

4 Discussion

4.1 Imaging large spheroids requires high labeling performance and an adapted imaging approach

4.1.1 Evaluation of the immunofluorescence staining performance in large specimens

Antibody-mediated specific labeling of the protein of interest is one of the driving forces in molecular, cell and developmental biology. However, the larger the specimen of interest, the more difficult is an appropriate staining result. Classical immunofluorescence staining approaches need to be optimized for three-dimensional specimens such as spheroids, which requires a suitable evaluation procedure. In a previous study, the staining efficacy has been evaluated by confocal fluorescence microscopy and FACS analysis, for which the spheroids had to be disassembled (Weiswald et al., 2010). We continued with the idea of having an objective estimation of the staining quality and introduced three aspects, which help to successfully rate a fluorescence stain. First, the stain specificity as a qualitative approach evaluates the data for the anticipated staining pattern. Immunofluorescence stains are generally prone to introduce artifacts such as speckles or the destruction of the epitopes, which results in not interpretable data (Schnell et al., 2012). Thus, a highly specific stain is necessary. When specificity is given, the signal intensity and the homogeneous dispersion of the fluorophores are assessed. For the latter two measures, an image analysis pipeline was implemented, which is quick and straightforward. It first translates the three-dimensional data set into a two-dimensional projection presenting the average signal intensity. Then, the intensity profile perpendicular to the light source, which was in this case the light sheet of a light sheet-based fluorescence microscope, is measured. High signal intensities usually increase contrast and thus, increase image quality, which is especially important for downstream applications like object segmentation (Mathew et al., 2015; Schmitz et al., 2017). High image quality further requires a homogeneous stain, which might not be provided in three-dimensional large specimen due to decreased diffusion of the fluorophores into the central region. To measure the stain homogeneity, we used a reference dye for comparison.

The more frequent researchers work with complex, three-dimensional specimens, the more required are standardized procedures, which are the fundament for reproducible experiments. The introduced evaluation criteria allow a standardization and reproducibility of immunofluorescence staining.

4.1.2 An increased antibody incubation temperature improves the staining

With the approach for immunofluorescence stain evaluation, classical immunostaining procedures were tested with the objective to find an optimized protocol for the use in large three-dimensional specimens. The appropriate models were cellular spheroids with an average diameter of about 600 μm . One feature of such large spheroids is that they will form morphologically distinct layers, which makes them comparable to avascular tumors *in vivo* (Sutherland, 1988; Bell et al., 2001). However, to avoid effects of the morphologically distinct zones on the outcome of the fluorescence stain, we used spheroids that were formed for 6 days, just prior layer development. To capture the entire spheroid, LSFM was combined with optical clearing. Murray's clear was chosen due to its inexpensiveness, reproducibility and the simple establishment. It successfully renders the specimens transparent and preserves organic fluorophores (Dodt et al., 2007).

The most positive effect on the signal intensity and signal homogeneity was achieved when the antibody incubation temperature was increased from the usual 4°C to 37°C. Further, a prolonged incubation time for the secondary antibodies increased the signal intensity but affected the dispersion of the fluorophores negatively. This indicates that the effect of the antibody concentration gradient from the surface to the center of the spheroid is reinforced when the incubation time for the secondary antibodies is prolonged. Thus, a shorter secondary antibody incubation time of 4 hours provides a more homogeneous staining signal.

The variation of other parameters affected various aspects of the immunofluorescence staining quality. Alcohols as fixative impaired the stain specificity especially of α -tubulin. However, alcohols have been used frequently as fixatives in two-dimensional cell cultures with a subsequent visualization of the cytoskeleton (Li et al., 1998). In addition, due to their strong permeabilizing effect, alcohols have been used reportedly successful to obtain a homogeneous antibody staining in thick biological specimens (Ott, 2008). In contrast, our results showed that the use of alcohol fixation affected not only the specificity, but also the signal intensity. The lowest signal intensities were measured when spheroids were fixed with methanol and acetone. They were about two to four times lower compared to spheroids that were fixed and permeabilized with PFA and Triton X-100, respectively. It is likely that due to structural differences the cytoskeleton in a spheroid is more sensitive compared to two-dimensional cell cultures, and that the harsh treatment with alcohols rapidly destabilizes it. In contrast, when alcohols were used following cross-linking fixation, the structure of the microtubules was preserved, which was demonstrated by the detection of the spindle apparatus in most of the samples.

The three aspects of immunostaining quality evaluation can be rated according to their importance. Most essential is the stain specificity, followed by the signal intensity and the stain homogeneity. According to this and to the adapted staining protocols for large spheroids, a cross-linker-based

fixation with PFA and a detergent-based permeabilization (i.e. Triton X-100) is suggested. Both provide the maintenance of the epitopes, contribute to high signal intensities and reasonable staining homogeneity. The increased antibody incubation temperature further improves antibody diffusion inside the specimens, and thereby the overall performance of the approach. A high specificity to detect α -tubulin and β -catenin was achieved. However, an evaluation of the immunostaining quality for any other type of antibody is suggested. The adapted immunofluorescence staining protocol takes about one and a half working days, which is temporally comparable to staining approaches of two-dimensional monolayer cultures or of thin tissue sections.

4.1.3 The advantages of optical clearing over multi-view image fusion

LSFM allows acquiring images of large three-dimensional specimens. However, large specimens scatter light; thereby inner regions are hardly resolved when they are imaged *in toto*. To enhance image quality, two approaches were studied. Optical clearing increases the transparency of the specimen. Consequently, regions at higher depth become accessible for light microscopy. However, optical clearing may produce artifacts such as morphological aberrations (Dodt et al., 2007). Multi-view image acquisition is a unique feature of LSFM (Swoger et al., 2007). It allows the acquisition of the specimen from multiple view angles, which can be fused subsequently into a single image with improved resolution. Multi-view image fusion increases image contrast and axial resolution compared to the data acquired from a single view (Preibisch et al., 2014). The advantages and disadvantages of both approaches were investigated for image acquisition of fluorescently labeled multicellular spheroids.

Multi-view image fusion requires a good choice of the registration and fusion parameter values. The registration and fusion parameters were empirically determined and the same parameter settings were used for all data sets. The sample preparation and image acquisition from four view angles and two fluorescence channels required approximately 15 minutes for one data set. The time required for the registration and fusion was approximately 21 minutes when deconvolution was used during the fusion process (eight iterations, two six-core CPUs [X5650, Intel Corporation], 96 Gigabyte DDR3 memory, seven Tesla M2070 [NVIDIA Corporation] graphics cards for GPU processing, running Windows Server 2012 R2). A reduction of time consumption can be achieved by simultaneous acquisition of the specimen from multiple views and the immediate fusion of the multiple views (Tomer et al., 2012; Krzic et al., 2012).

In comparison, optical clearing consumes time prior image acquisition. Using Murray's clear, spheroids were dehydrated, optically cleared and mounted inside the microscope within 30 minutes. Image acquisition from one view required about 5 minutes for two fluorescence channels. An image post-processing was not necessary. In conclusion, optical clearing has no temporal advancement over multi-view image fusion (Table 4-1).

The image quality of both, fused images and optically cleared images is good but the degree of light scattering depends on the molecular content of the specimen. High protein concentrations but also large molecules result in strong light scattering effects (Lorber et al., 2012). This indicates that 4T1 cells might contain more light scattering molecules than T47D cells since multi-view imaging did not provide fully resolved 4T1spheroids. This concludes that the specimen limits the performance of multi-view image fusion (i.e. molecular content and size). Two-photon excitation could improve the penetration of the illuminating light but it does not circumvent the diffraction of the emitted light at lower wavelengths (Helmchen and Denk, 2005).

To measure the morphological properties of the spheroids and to estimate the effect of optical clearing, cell nuclei segmentation was performed. The segmentation performance of cell nuclei in images of optically cleared spheroids was higher compared to fused images. For fused images, no appropriate segmentation parameter were found. Since the segmentation pipeline was developed with optically cleared specimens, it might be inappropriate for fused and deconvolved data.

Optical clearing involves a harsh treatment of the specimen by replacing the extracellular water with solutions having high refractive indices (D’Esposito et al., 2015; Seo et al., 2016). Dehydrating methods use alcohols at high concentrations, which result in shrinkage of the specimen (Dodt et al., 2007). This rules out measuring real quantities such as distances. Shrinkage effects, or in other optical clearing methods expansion effects (Hama et al., 2011), limit optical clearing by permitting only relative measurements. Even though the morphology of the specimen was affected by shrinkage, optical clearing did not induce distortion of the specimen, which enables to measure quantities as relatives. Nevertheless, optical clearing has developed remarkably within the past ten years, providing promising optical clearing protocols that are less harmful regarding the specimen’s morphology and the fluorophores (reviewed in Seo et al., 2016).

Table 4-1 Comparison between multi-view image fusion and optical clearing.

	multi-view image fusion (i.e. <i>ImageJ</i> plugin <i>Multiview Reconstruction</i>)	optical clearing (i.e. <i>Murray’s clear</i>)
time per sample	~ 36 minutes (can be improved by parallelization of imaging / fusion)	~ 35 minutes
image quality	high (but depends on the molecule density and composition of the specimen) gain of resolution (i.e. axial)	high no gain of resolution
other aspects	applicable for live specimens	morphological alterations (i.e. shrinkage) accessible for object segmentation

Which of the two approaches is best suitable strongly depends on the biological question and the experimental design. The multi-view imaging approach is highly suitable for small specimens and live imaging. The light penetration is sufficient in smaller samples and the imaging conditions can

be adapted to living specimens. Optical clearing is suitable when end-point images are generated and spatial detail is required. Further, images of optically cleared specimens provide constant image quality, which makes this technique accessible for segmentation approaches (Table 4-1).

4.2 Spheroids with epithelial characteristics are a reliable tissue model system

Epithelia are tissues that line the surfaces of the body, blood vessels and organs. They function as a barrier and are involved in the secretion and absorption of molecules. All epithelia reside on a layer of ECM with supportive tissue underneath (Alberts et al., 2008).

Epithelial cell lines, non-malignant as well as cancerous, form spheroids. However, to which extent the cells within a spheroid adopt epithelial characteristics, has to be investigated for each cell type.

HC11 cells grown as a spheroid retain the ability to establish an apico-basal membrane polarity, which was identified by the apical localization of F-actin and ezrin. However, the cells failed to establish a polarization of the Golgi. It has been shown previously that plasma membrane polarity can be established independently from the polarization of the Golgi (Bisel et al., 2013). In conjunction with other studies, this result suggests that the apico-basal membrane polarity and the polarization of the trafficking machinery are regulated by distinct cellular pathways (Wang et al., 2013; Bisel et al., 2013).

Originally, HC11 cells have been selected as a clone that undergoes lactogenic differentiation without any external addition of ECM or other cell types (Ball et al., 1988). Mammary epithelial cells require specific BM proteins to successfully secrete milk protein (Bissell et al., 2003). Spheroids formed from HC11 cells underwent lactogenic differentiation regardless of the external addition of collagen during spheroid formation. The experiments showed that the ability to differentiate retained when the cells were cultured in a non-adhesive three-dimensional context. This is further supported by a study with primary mammary epithelial cells from organ explants that undergo lactogenic differentiation when cultured as spheroids (Timmins et al., 2005). Thus, HC11 spheroids have proven as a suitable three-dimensional *in vitro* model, which allows the investigation of molecular and morphological aspects of lactogenesis in mammary gland development. In comparison to mammary epithelial cells from organ explants, the HC11 spheroid model is less time-consuming and has no need for wasting animals.

4.3 ECM in mammary epithelial cell spheroids is differently synthesized and distributed

As discussed above, the presence of ECM influences the phenotype of cells (i.e. the capability to differentiate). Thus, several studies have been interested regarding the synthesis of ECM in spheroids. These have shown that tumor cells assembled into spheroids synthesize ECM proteins like fibronectin, laminin and collagen (Nederman et al., 1984; Bjerkvig et al., 1989). Another study has examined spheroids formed from an osteosarcoma cell line. A strong abundance of glycoproteins and type I collagen has been described. The ECM in these spheroids further resembles structures of tissues *in vivo* (Gebhard et al., 2016). Besides studies on malignant, cancerous cell types, Bhang *et al.* have shown that primary cells from the benign human vein umbilical endothelium (HUVECs) synthesize fibronectin and laminin when cultured as spheroids (Bhang et al., 2012).

Most of the studies that have examined spheroids have shown that ECM expression is induced under these culture conditions. Moreover, we investigated the expression in both, monolayer and spheroid culture. In monolayer cultures, type I collagen and fibronectin were present in the three mammary epithelial cell lines. However, when spheroids were formed from the non-malignant HC11 cells, type I collagen mRNA decreased over time and only small amounts of protein were detected in the spheroids. Interestingly, a reduced synthesis of ECM proteins has been observed in hepatoma cells when cultured as spheroids compared to monolayer cultures (Chang and Hughes-Fulford, 2009). Paulus *et al.* described a reduced expression of laminin and collagens in spheroids that have been formed directly from biopsies (Paulus et al., 1994), which indicates that the origin and the previous culture conditions of the cells may affect the synthesis of ECM in the spheroids. Compared to this, the highly invasive cell line 4T1 showed strong amounts of type I collagen throughout the entire spheroid culture. In the *in vivo* context, type I collagen is not present in the mammary BM, but is rather found in the interstitial stromal ECM. Upon tumor development and invasion, type I collagen, and further type III and IV collagens are often upregulated (Frantz et al., 2010), which goes along with our findings.

Compared to type I collagen, fibronectin was synthesized in monolayer cultures and in spheroids from the three cell lines during the entire time of cultivation. It has to be noted that the relative expression of ECM was not examined. Thus, no conclusion could be drawn about whether an ECM protein was up- or downregulated in spheroid culture compared to monolayer culture. The experiments rather focused on the presence or absence of expression and resolved the ECM distribution in the spheroids. Therefore, spheroids of different age were examined for the appearance of ECM via immunofluorescence. This revealed that the aggregating cells induce ECM synthesis early during spheroid formation, latest after 24 hours, and that an active rearrangement of

the ECM occurs in the forming spheroids. This was highly abundant in 4T1 spheroids, which formed a fibronectin layer a few cell layers below the spheroid surface. It remains elusive why the cells assemble fibronectin at this position. One assumption is that the fibronectin layer is the result of having two metabolically different populations of cells within the spheroids: proliferative cells at the spheroid surface and dormant cells in the center of the spheroids (Wenzel et al., 2014). A study that has examined the influence of microRNA on ECM expression in quiescent fibroblasts indicates a difference of ECM protein synthesis in quiescent versus proliferative cells (Suh et al., 2012).

The distribution of several ECM proteins was cytoplasmic. The murine mammary cell lines, HC11 and 4T1, accumulated laminin in the cytoplasm of cells located at the spheroid surface. Laminin was distributed in the cytoplasm of highly invasive 4T1 cells at all investigated time points. In spheroids formed from the non-tumorigenic HC11 cells, it started to distribute extracellularly 24 hours after spheroid formation. The assembly of mature laminin from A and B subunits is a prerequisite for its secretion. A failure during the assembly results in cytoplasmic accumulation (Peters et al., 1985). The highly invasive cells thus may fail to produce mature laminin, whereas the non-tumorigenic HC11 cells overcome the cytoplasmic accumulation of immature laminin at later time points.

Apart from the abundance and organization of ECM proteins that differed between the three cell types, the capability of cells to interact with the ECM varied. Non-malignant HC11 cells barely attached to type I collagen, which is in conjunction with the absence of this protein in the spheroids and the BM of the mammary epithelium *in vivo* (Richert et al., 2000). Contrary, cells from 4T1 and T47D cell lines attached more frequently to type I collagen. Their tumorigenic character may cause this. The cells not only produce larger amounts of type I collagen but also have an increased attachment rate to this type of ECM compared to the non-malignant cells. This leads to the hypothesis that the amount and the types of integrins that are expressed to facilitate attachment to the ECM differ between these cell types. The formation of heterodimers upon binding to the ECM activates integrins. Consequently, downstream signaling pathways are stimulated. These engage in cell cycle progression, gene expression, focal adhesion turnover and regulation of cytoskeleton dynamics (Berrier and Yamada, 2007). An aberrant integrin expression and activity is implicated in tumor cell proliferation, migration and survival (Desgrosellier and David, 2015). Thus, the differences in cell attachment strength to ECM may serve as an indicator for abnormal integrin expression.

4.4 The differential expression of BAG3 implies an important role in mammary gland development

BAG3 is a co-chaperone involved in cell survival. Mutated BAG3 often correlates with severe diseases of the muscle apparatus, like myopathy and muscle dystrophy (Rosati et al., 2011). In the context of muscle tissues, it has been shown recently that BAG3 is highly involved in the turnover and expression of cytoskeletal proteins, which have been damaged upon excessive mechanical forces (Ulbricht and Höhfeld, 2013; Ulbricht et al., 2013a; b). The cellular processes, in which BAG3 is involved, are also present in different developmental stages of the mammary gland. This led to the hypothesis that BAG3 could also be an important player in mammary gland development. Therefore, the BAG3 mRNA expression was analyzed in different developmental stages of the mammary gland.

Already in 2003, the group around Christine Watson has performed expression analyses on the mammary gland from mice at different developmental stages (Clarkson and Watson, 2003). The microarray data has provided information about the expression of BAG3 in mammary gland development. It has shown that the amount of BAG3 mRNA at 24 hours of involution was 1.6 times higher compared to 7 days lactating mice (Clarkson and Watson, 2003). Compared to this, the qPCR revealed a 3.8-fold expression of BAG3 between day 8 of lactation and 24 hours of involution. Although the trend of BAG3 gene expression was similar in both methods, the values differed strongly.

The profile of c-Fos mRNA level from the microarray analysis and our qPCR analysis was similar. It was low during pregnancy and lactation, and increased with the onset of involution. Interestingly, while the maximum increase of c-Fos expression was 4.3-fold at day 4 of involution compared to day 7 of lactation, the qPCR analysis showed a 20.2-fold induction at involution day 3 compared to lactation at day 8. Poor hybridization of markers on microarrays may produce an insufficient representation of the actual transcripts. Therefore, a verification and reevaluation with other approaches is essential. It has been shown that the results obtained from microarray analysis and qPCR may deviate upon data quality (Morey et al., 2006). The different localizations of probes between microarray and qPCR, and genes with very high or very low levels of expression reduce the comparability between these two methods (Etienne et al., 2004).

Recent RNA-seq studies have shown that BAG3 expression during lactation increases compared to late pregnancy in the ovine mammary gland (Paten et al., 2015). Our data confirmed this trend for the murine mammary gland, however, the expression in the murine mammary gland was not as strong as described by Paten *et al.*. During pregnancy, the BAG3 mRNA level remained constant at a low level. Already 2 days after parturition, the amount of BAG3 mRNA rose and further increased with ongoing lactation. Paten *et al.* have suggested that the increased BAG3 expression

together with increased expression of other cell survival markers is involved in the maintenance of secretory alveolar cells during lactation (Paten et al., 2015). However, according to our data from the entire time course of mammary gland development, the cell survival mechanisms may not be that prominent and important in the lactation phase. Moreover, our data included the involution phase, in which the expression of BAG3 was strongly increased compared to the lactation phase. Our data comprised a detailed transcription analysis of BAG3 during involution. We analyzed the first phase of involution 12 hours and 24 hours following pup removal, and the beginning second phase at day 3 of involution, day 7 in the middle of this phase and day 14 as a very late time point in involution. Within this period of time, BAG3 expression varied. At the onset of involution, its expression increased, peaked at the early second phase and then decreased. Whether the real peak of BAG3 expression was before or after day 3 of involution remains elusive and should be investigated in a detailed follow-up expression analysis. The increasing expression, especially within the first 3 days of involution indicates that BAG3 is of high importance at this time point of mammary gland development. In this temporal window, different processes occur, in which BAG3 is presumably involved: (1) cell survival mechanisms are active in the first phase of involution. This is necessary to retain the mammary gland in a state, where a reoccurring suckling stimulus halts the advance of involution (Pensa et al., 2014). (2) Milk stasis delays alveoli and mechanical forces drastically increase in the first hours of involution (Wilde et al., 1999; Quaglino et al., 2009). When BAG3 was genetically depleted from non-malignant mammary epithelial cells, their viability was reduced by more than 20%. However, when BAG3 expression was downregulated by approximately 50%, cells were as viable as the control. The MTS assay to assess the cell viability of monolayer cultures does not distinguish between proliferation and cell survival as the underlying mechanisms. The experiments with the spheroids provide a more detailed insight. Spheroids formed from HC11 BAG3 knockout cells shed an increased number of dead cells after 7 days of culture compared to the controls. However, these results are different from what has been described for tumor cells. There, a reduced protein amount of BAG3 upon downregulation is sufficient to decrease cell viability in several tumor cell lines (Shi et al., 2016; Rapino et al., 2014). Most studies have investigated BAG3 expression and its role in cell survival in tumor cell lines (Rosati et al., 2011; Behl, 2016). However, their signaling pathways are often hyperactive or silenced. Thus, these results rather reflect pathological conditions than the physiological conditions of healthy tissues. Our results suggest that in non-malignant mammary epithelial cells BAG3 supports cell viability unless its expression does not fall below a certain threshold. This explains that a remaining BAG3 protein level of approximately 50% does not affect cell viability, while a knockout of BAG3 does. This is a strong indication for the supporting role of BAG3 in cell survival in non-malignant mammary epithelial cells. On the level of the mammary gland, it is of interest whether an increased BAG3 expression is sufficient to overcome death signals, as it may occur during early involution.

Despite the increased BAG3 mRNA level during involution, we found an increased BAG3 expression in the mammary glands of virgin mice. These mice were 8 weeks old and pubescent. During puberty, the ductal tree grows out and processes like proliferation and migration are abundant (Friedl and Gilmour, 2009). We think that the increased expression of BAG3 in this phase of mammary gland development could attribute to its role in cell migration. Whether the increased expression of BAG3 in mammary glands of pubescent mice affects the migration of the ductal cells, remains elusive. However, a controversy exists within the literature about BAG3 and cell migration. When BAG3 has been overexpressed in cancer cell lines, the migration rate has been shown to be increased, and a downregulation has been linked to decreased migration and invasion (Iwasaki et al., 2007; Fontanella et al., 2010; Suzuki et al., 2011; Shi et al., 2016). Other studies have reported that BAG3 downregulation induces cell migration and EMT-like processes (Meng et al., 2014). In human breast carcinoma cells, BAG3 overexpression results in poor migration through a reduced formation of focal adhesion in a FAK-dependent manner (Kassis et al., 2006). It can be inferred that BAG3 affects cell migration and invasion in a cell context-dependent manner. Our results assigned BAG3 an inhibitory role in cell migration in non-malignant mammary epithelial cells. Both, BAG3 knockdown and knockout cells affected cell migration in a wound healing assay. The reduced expression of BAG3 resulted in an increased migration of the cells into the wound area, and this effect was stronger when BAG3 was depleted genetically. It further showed that altering amounts of BAG3 in the cells affect cell migration. Thus, BAG3 expression must be tightly regulated to coordinate cell migration. Our results indicate the value of BAG3 in mammary gland development.

4.5 Mechanical stress activates caspases and alters the morphology in spheroids

Physical forces such as mechanical stress influence tissue integrity. The mechanical load during mammary gland development varies strongly but the contribution to the onset of developmental processes is only vague. Thus, we aimed to investigate the influence of mechanical stress on cell and tissue morphology as well as on signaling pathways that contribute to cell survival (i.e. autophagy and caspase-mediated cell death). The mechanical stress experiments conducted on monolayer cultures of HC11 cells were methodically instable and provided inconclusive results due to technically produced artifacts.

Thus, we commenced to apply mechanical stress on mammary epithelial spheroids. One aim of these experiments was to mimic the strain exerted on alveolar cells by the accumulation of milk during forced involution. However, the strain of the spheroids after compression was at least 100% lower compared to the strain that was exerted on the alveolar cells *in vivo*, where milk stasis was

induced by pup removal. Thus, the results from this experimental approach are unlikely to be comparable to the mechanical stress situation in the mammary gland at the onset of forced involution *in vivo*. Nevertheless, this approach takes the three-dimensionality of the specimen into account and allows a complete analysis of the spheroid morphology under compressive stress *in toto*. It provides insight into aspects of mechanical stresses influencing tissue morphology. Certainly, the experimental setup to apply mechanical stress has strong influence on the cellular response like the activation of survival pathways and the initiation of programmed cell death. Furthermore, one has to consider to which extent the experimentally applied mechanical stress reflects the physiological conditions. Most of the previous studies have applied passive mechanical load by increasing the stiffness of the surrounding substrate (Helmlinger et al., 1997), by growth in a confined environment (Desmaison et al., 2013) or by osmotic pressure (Montel et al., 2012). These approaches have aimed to mimic the stiffening of the surrounding tissue upon tumor growth. The difference of our experimental approach was that the mounting into the agarose capillary induced an immediate deformation of the spheroids to resemble the physiologically occurrences in the mammary gland (i.e. increasing pressure by milk accumulation and milk stasis). On the cellular level, all types of forces (i.e. compressive, tensile and shear stress) are present, which mimic the situation in the developing mammary gland.

At the short term (i.e. 1 hour), spheroid compression did not cause morphological changes. Apart from the shape change, the spheroid volume, the cell nuclei count and volumes were similar to the controls. However, after 24 hours of compression, the cell nuclei volumes decreased compared to the controls, while this effect disappeared after 96 hours. After 96 hours of compression, the cell nuclei volume was similar to the controls. This might originate from a compensatory mechanism, in which the cells structurally reorganize over time. The delayed volume reduction and the regeneration to the normal state strongly indicates that the nucleus volume regulation is an active process to adapt to the mechanical stress. Simulations have suggested that the shape changes of cell nuclei in endothelial cells minimize the forces experienced by the nuclei (Hazel and Pedley, 2000). *In vitro* experiments have shown that mechanically deformed cell nuclei increase their stiffness and retain this for multiple hours after the release of mechanical forces by active remodeling mechanisms of the nuclear shaping structures (Deguchi et al., 2005). It is known that the nuclear volume correlates with the proliferative activity of the cell. An increased volume correlates with increased expression of the proliferation marker Ki-67 (Smolle et al., 1989). Consequently, a reduction of the cell nucleus volume would indicate reduced cell proliferation. We investigated cell proliferation indirectly by measuring the number of cells and the amount of active caspase-3 in the spheroids, and found that proliferation was not affected 24 hours after spheroid compression. However, a detailed and direct analysis with cell proliferation markers would validate these results. Further, cell nucleus volume can be altered by the actin cytoskeleton, which associates with the

nuclear matrix and thereby can influence the cell nuclei structurally (Ingber et al., 1994; Chen et al., 2015). Nuclear shape changes are associated with changing function and phenotype of cells. This occurs when cells differentiate or mature, but it is also associated with cancer progression. Consequently, nuclear shape changes are associated with transcriptional alterations (Dahl et al., 2008; Chen et al., 2015). The decreased expression of BAG3 in compressed spheroids supports this and indicates that transcriptional regulation of other factors might be induced in the compressed spheroids.

BAG3 expression has been reported to protect cells from apoptosis (Rosati et al., 2011). Further, an increased expression of BAG3 has been shown in human periodontal ligament cells that were stretched for 6 hours but not in cells that were stretched for 24 hours (Xu et al., 2011). After 24 hours of compression, BAG3 expression decreased compared to the controls. Until this time point, the amount of active caspase-3 was increased, indicating reduced cell survival mechanisms. However, it remains elusive whether the decreased activity of caspase-3 corresponds to an increased BAG3 expression. Future work should therefore aim to characterize the time-dependent expression of BAG3 in compressed spheroids. It is likely that the initial mechanical stress induces an increase of apoptosis (i.e. by elevated activation of caspase-3), which in turn induces cell survival mechanisms that involve BAG3 expression. We hypothesize that BAG3 expression increases at later time points of compression to protect cells from death.

Increased physical forces are frequently associated with changes in cell proliferation and cell death. The compression of mammary epithelial cell spheroids did not induce cell division, which was indirectly measured by the number of cell nuclei in the spheroids. However, this does not necessarily mean that the cells remain mainly in a dormant state. Moreover, it has been reported that spheroids induce proliferation but fail to undergo successful mitotic division under confined growth conditions (Desmaison et al., 2013). Furthermore, cell death is affected by mechanical stress (Helmlinger et al., 1997; Cheng et al., 2009; Montel et al., 2011). The balance between cell proliferation and cell death is sensitive towards mechanical forces and an imbalance promotes tumor progression (Helmlinger et al., 1997; Montel et al., 2012; Delarue et al., 2014). Our results showed that caspase-mediated programmed cell death is regulated in a time-dependent manner in the compressed spheroids. While short-term compression increased the amounts of active caspase-3, long-term compression for 96 hours decreased the amounts of active caspase-3 compared to the respective controls. It is therefore important to distinguish between short-term reactions and the long-term adaption of cells to continuous mechanical stress. The decrease of cell death on the long-term may contribute to the maintenance and survival of the cells.

Mechanical stress damages cytoskeletal components (Ehrlicher et al., 2011), which are removed and replaced subsequently (Ulbricht et al., 2013a). CASA has been reported as a mechanism in cells that experience cytoskeleton damage upon mechanical stress. The co-chaperone BAG3 plays a key

role in this mechanism. It forms together with other proteins the CASA chaperone complex, binds damaged (i.e. ubiquitinated) proteins and transfers them to the autophagosome degradation machinery (Ulbricht et al., 2013a). In spheroids that were compressed for 24 hours, BAG3 expression was reduced. Since an induction of CASA is associated with an increased expression of BAG3 (Ulbricht et al., 2013a), it indicates that CASA is not induced when mechanical stress was applied. This is supported by the unchanged expression of filamin, an actin-binding protein with mechanosensing functions. Further, spheroids compressed for 24 hours showed no induction of the autophagy flux. However, it remains to be solved, how sensitive this assay is, as only strong changes in fluorescence intensity are measured. Previous studies that have examined CASA induction upon mechanical stress, have used muscle cells, which are exposed to a high mechanical load *in vivo*, grown on stiff substrates (Ulbricht et al., 2013b). *In vivo*, only high intensity exercise caused significantly increased expression of multiple CASA proteins in the muscle (Ulbricht et al., 2015). This suggests that only strong strain causes physical damage on cellular components such as the cytoskeleton and cytoskeleton-associated proteins and induces CASA. Low strain may not be sufficient to induce the CASA machinery. This assay did not induce strong strain by compressing spheroids, but it has to be considered that the strong deformation of mammary alveolar cells induces different mechanisms upon milk accumulation, in which CASA might play a role.

4.6 A spheroid formation assay reveals proteins that modulate tissue integrity

Apart from external factors, cellular processes like cell adhesion, growth and survival are important factors that contribute to the functionality of a tissue and to modulate tissue integrity (Gumbiner, 1996, 2000; Ewald et al., 2008). The mechanisms that facilitate adhesion and growth in three-dimensional cell aggregates are largely unknown and are likely to be different from what has been found in monolayer cultures. Cells in two-dimensional monolayer cultures form extensive numbers of focal adhesion compared to cells in three-dimensional cultures (Cukierman et al., 2001), which affect the internal distribution and structure of proteins such as the actin cytoskeleton (Pampaloni et al., 2010). The molecular mechanisms are influenced strongly by the attachment of the cells to a stiff, thus non-physiological substratum. As discussed above (section 4.2), cellular spheroids are appropriate model systems to study processes that are abundant in the tissue context. It is accepted that mature spheroids resemble properties of tissues like polarization, differentiation, and morphologically distinct zones. However, the investigation of mature spheroids will not truly reflect processes that occur during adhesion formation. Instead, investigation of the spheroid formation process offers a suitable platform to study those highly dynamic processes. In these non-adhesive conditions, mechanism that significantly contribute in the collective behavior of groups of cells were studied.

4.6.1 Spheroid formation is a reaction-controlled mechanism and is distinguishable into three phases

Two opposing concepts of spheroid formation exist. The first hypothesis regards spheroid formation as a diffusion-controlled process, where cells adhere when they collide (Neelamegham et al., 1997). Conflictingly, the second hypothesis regards spheroid formation as being reaction-controlled. It proposes that a connection between cells not necessarily occurs when cells contact each other upon collision (Enmon et al., 2001). Fitting the previously developed computational model (Garg et al., 2015) to the experimental data of spheroid formation showed that the cells exhibited a certain probability to bind and to unbind. For the three investigated cell lines, the binding probability was high but never exceeded 73%, meaning that when two cells collide, they likely but not necessarily form a connection. This strongly supports spheroid formation being a reaction-controlled mechanism.

When spheroids form, they pass through three distinct phases (Enmon et al., 2001; Lin and Chang, 2008). An intermediate delay phase has been proposed to exist between the aggregation and compaction phases (Lin et al., 2006). The abundance of a delay phase in the spheroid formation of HC11, 4T1 or T47D cells could not be confirmed. Lin and colleagues have observed this delay phase exclusively when collagen was added to support the spheroid formation process. Their negative control (i.e. no collagen added) did not display a delay in spheroid formation. This suggests that upon collagen addition, the cells have an excess of supportive material. A rearrangement of the excess ECM by expression and secretion of MMPs to incorporate this into the aggregating spheroid might be at the cost of the aggregation speed. This indicates that the intermediate delay phase is rather an artificial occurrence without relevance in the physiological context of adhesion formation.

The three distinct phases can be extracted from the area-time plot and the shrinkage rate. In the aggregation phase, cells rapidly contact each other, which results in a fast decrease of the projected area. This is marked by a steep decay in the area-time plot. When the slope decreases and the shrinkage rate drops below a threshold, the compaction phase is initiated in the three investigated cell lines. In this phase, cells have already formed clusters but start to rearrange, expand against gravity, and foster their connections. The growth phase begins when the slope in the area-time plot becomes positive. This is associated with the shrinkage rate dropping below zero. The phase transition does not occur abruptly. The characterization of the phases highlights that a certain behavior of the cells dominates in a particular phase. This can be exemplified on cell proliferation, which was present in the aggregation and compaction phases but did not dominate in these. Different cell lines vary substantially in the spheroid formation dynamics. The highly invasive cancer cell line 4T1 aggregated the fastest and displayed all three phases of spheroid formation within the period of 48 hours. The non-tumorigenic cell line HC11 showed a fast spheroid formation without displaying a growth phase within the first 48 hours. The cancer cell line T47D

formed spheroids very slowly. These did not form spherical but rather oblate cell cluster. However, the variations in spheroid formation dynamics cannot be assigned to the metastatic potential of the cells (HC11<T47D<4T1). One influencing factor could be that the species of origin of the cell lines differed. HC11 and 4T1 cells are murine, and T47D cells are human cells. To which extent this affects differences in the behavior of the cells remains elusive. Furthermore, the identification of molecular pathways or even single molecules that cause these variations is of high interest.

4.6.2 Cadherins are important to reinforce cell contacts

E-cadherin is reportedly crucial for successful spheroid formation (Ivascu and Kubbies, 2007; Li et al., 2007; Saias et al., 2015). Our results support these previous findings. Despite E-cadherin blocking, cells retain the ability to contact another, but the cell clusters fail to compact. Upon E-cadherin blocking, the two murine cell lines, HC11 and 4T1, exhibited strong fluctuations of the projected area in the loose aggregates suggesting that the connections are weak and break frequently. Contrarily, T47D cells did not show these strong fluctuations. A previous study has investigated the contribution of N-cadherin cell contact formation in L-cells, which naturally do not express N-cadherin. The wild-type cells fail to form compact spheroids but rather aggregate loosely. Interestingly, these cells show similar fluctuations of the projected area when they assemble (Garg et al., 2015). This suggests that cadherins in general are crucial for compaction of cell aggregates but are not solely essential for the contact formation between cells. It is likely that T47D cells, which upon E-cadherin blocking do not show the projected area fluctuations, exhibit a strong involvement of alternative factors to conduct spheroid formation. Saias and colleagues have shown that this is highly likely, also for the other two cell lines (i.e. HC11 and 4T1). Other adhesion molecules like desmosome proteins are involved in the spheroid formation process (Saias et al., 2015). This is strongly supported by the results from the computational model. It revealed that the probability of the cells to form connections is not altered when E-cadherin function was blocked. Moreover, the probability to lose the connections that have been formed already was increased. This is a rather unexpected result since E-cadherin is commonly believed as an important part in cell-cell contact formation (Takeichi, 1991; Ratheesh and Yap, 2012). Our results indicate that cadherins (i.e. E-cadherin) are not crucial for the contact formation between cells but rather enforce connections that have been formed already. Interestingly, in T47D cells, which showed a decelerated spheroid formation, neither the binding nor the unbinding probability was altered. So far, we cannot draw a conclusion from this result, but it suggests that another parameter might be affected, which was not yet considered in the computational model.

4.6.3 Actin stabilizes existing cell contacts

Among the proteins that are localized intracellularly, actin is highly involved in contact formation of cells. Additionally, it provides cell shape, promotes cell migration and forms a network of cells with their neighboring cells and the ECM via adhesion molecules. When actin assembly is abrogated, cells cannot form spheroids (Tzanakakis et al., 2001; Yoshii et al., 2011). This is confirmed by our results, which furthermore provide a detailed quantitative analysis.

Although a treatment with cytochalasin D inhibited spheroid formation in the investigated cell lines, the projected area of 4T1 aggregates increased in size. The cell viability analysis showed no cell proliferation inducing effect of cytochalasin D. A detailed view of single cells within the aggregates revealed that the cell nuclei volume was increased. This indicates that the increased projected area in 4T1 cells was rather due to cell swelling than to cell proliferation. Actin is involved in cell volume regulation (Mills et al., 1994) and a disintegrated actin cytoskeleton results in cell swelling (Blase et al., 2009). This effect strongly depends on the cell type (Pedersen et al., 2001). Our results supported this, since the other cell lines did not display cell or cell nucleus swelling, even though HC11 cells were treated with the same concentration of cytochalasin D as 4T1 cells.

Cells treated with cytochalasin D displayed a decreased (i.e. HC11 and 4T1) or even absent agility (i.e. T47D) when they aggregated. In comparison, blocked E-cadherin function had a similar impact on the dynamics of spheroid formation, but the cell aggregates displayed a high degree of agility. Consequently, the actin cytoskeleton promotes the agility of cellular aggregates to form a three-dimensional cluster. Future experiments should inhibit both, E-cadherin and actin polymerization in the cells to further manifest this hypothesis.

Actin is suggested to contribute to cell-cell adhesion formation by two mechanisms. First, it assembles to form filopodial extensions, which contact opposing cellular membranes to enlarge the area of contact between cells. Second, actin interacts with the adhesion complex to stabilize the contacts (Vasioukhin and Fuchs, 2001; Ratheesh and Yap, 2012). However, the cells cohered but the connections broke easily when actin was depolymerized. This is emphasized by the increased unbinding probability provided by the computational model. Hence, the actin cytoskeleton mainly reinforces cell contacts during spheroid formation. Since the binding probability was not, or only slightly altered, the actin cytoskeleton it is not essential for the formation of a connection between two cells. This leads to the suggestion that the filopodial, actin-rich extensions may assist cells to find potential binding partners but they are not required to form a connection between cells.

4.6.4 Microtubules strengthen cell adhesion, promote cell rearrangement and facilitate cell proliferation

The second investigated cytoskeletal component in spheroid formation were the microtubules. Their role in spheroid formation has been investigated only rarely and to the current state, no quantitative analysis of spheroid formation dynamics exists. The literature describes the impact of microtubules in spheroid formation differently. Tzanakakis *et al.* have not observed an effect of microtubule depolymerization using taxol or nocodazole in hepatocyte spheroid formation after 36 hours and 120 hours (Tzanakakis *et al.*, 2001). Contrary, Yoshii *et al.* have assigned microtubules an important role in the formation process of colon carcinoma spheroids (Yoshii *et al.*, 2011). In the latter study, the spheroid formation was inspected visually every 4 hours during the first 92 hours. Our approach investigated the first 48 hours of spheroid formation in detail and provided a quantitative analysis. Regardless of the cell line, a depolymerization of microtubules affected spheroid formation by a deceleration. Microtubules are crucial for cell division by forming the spindle apparatus during mitosis and a treatment of cells with nocodazole resulted in reduced cell viability by an inhibition of cell division (HC11 and 4T1). Spheroid growth is thus affected by the loss of microtubule integrity.

Nocodazole treatment differently affected the binding and unbinding probabilities from the computational model in the cell lines. The unbinding probability increased in HC11 and 4T1 cells, but the binding probability did not change. Microtubules have been found associated with cadherin-catenin adhesions (Stehbens *et al.*, 2006; Meng *et al.*, 2008). One mechanism of microtubules to contribute to adhesion is by facilitating transport of molecular mediators via vesicles to the plasma membrane (Mary *et al.*, 2002), which are important to promote the spheroid formation process (this study and Lin and Chang, 2008). Conflictingly, although the decreased aggregation speed in T47D cells was similar compared to the other two cell lines, the unbinding probability was not increased, but instead the binding probability was. T47D cells are known to exhibit strong cell-cell adhesions (Holliday and Speirs, 2011; Ivascu and Kubbies, 2007), thus a high amount of adhesion molecules might already be present at the plasma membrane so that a disrupted microtubule-driven vesicle transport does not drive spheroid formation in these cells. Another explanation is supported by a recent study. It has unveiled that a disruption of the microtubule cytoskeleton activates cadherins to form adhesion contacts. This is mediated by p120-catenin, which is dephosphorylated upon the loss of microtubules. Dephosphorylated p120-catenin binds cadherin to activate it (Maiden *et al.*, 2016). In this paper, the authors have shown that the degree of p120-catenin dephosphorylation depends strongly on the concentration of nocodazole (Maiden *et al.*, 2016). This may help to understand why the binding and unbinding probabilities differed that strongly between the cell lines, which were treated with different concentrations of nocodazole. Future investigations should focus on p120-catenin and its state of phosphorylation during spheroid formation. Whatever the

case is, a consequence of an increased binding probability is the assembly of the cells in one plane. The increased binding of the cells perturbs rearrangement against gravity into the third dimension. To facilitate a rearrangement of cells, cells need to remodel their connections and may change the position relative to another by migration. A prerequisite for cell migration is the presence of a substrate to move along. Cells attach to the ECM via integrins and a turnover of integrins paired with the formation of protrusions results in cell movement (Vicente-Manzanares and Horwitz, 2011). We showed that the cells in the spheroids synthesize ECM proteins. Thus, microtubules presumably have a dual role in the first two phases in spheroid formation: (1) they mediate the formation of adhesion sites in the aggregation phase and (2) promote migration in the compaction phase promoting the disassembly of adhesion sites (Lock et al., 2008). Finally, it depends on the biochemical composition of the cells, which of these processes dominate in spheroid formation.

4.6.5 Levels of FAK protein synthesis and activity vary among cell lines

The cytoskeleton appears to be important in the spheroid formation process. Cytoskeleton remodeling is affected by signals that originate from the adhesion of cells to the ECM. These signals induce the phosphorylation, and thereby activation of FAK. FAK is an important modulator of cytoskeleton remodeling and thus may influence spheroid formation. Beck and colleagues describe that FAK phosphorylation at Y397 is crucial for the formation of spheroids in human dental follicle cells (Beck et al., 2014). They induced spheroid formation under serum-free culture conditions and cultured the cells on dishes coated with poly-L-lysine. Under these circumstances, a strong phosphorylation of FAK is comprehensible. The cells attach to the culture dish and form islet-like cluster with a large portion of the cells remaining attached to the surface of the dish, which does not resemble a three-dimensional cell culture. The strong phosphorylation of FAK in these cell clusters are likely caused by massive integrin attachment to the surface. However, our approach to study spheroid formation avoids the attachment to any non-physiological surface. When the inhibitor of phosphorylation at Y397 was used to block FAK activity, spheroids formed to a certain extent exhibiting cell type specific effects.

The phosphorylation of FAK is promoted by integrin adhesion to substratum (Mitra et al., 2005), and an increased amount and activity of FAK is frequently associated with tumors (McLean et al., 2005). The amount of FAK as well as its Y397 phosphorylation varied between the cell lines. It was strong in the metastatic 4T1 cells and was weak in the non-tumorigenic HC11 cells. T47D cells contained less of both, FAK and pFAK^{Y397}, compared to 4T1 cells. However, the amount of FAK not only correlated with the metastatic potential of the cells. FAK was differently expressed and phosphorylated in two-dimensional cell cultures compared to spheroid cultures. In both, HC11 and T47D cells, FAK phosphorylation decreased strongly in spheroid cultures. In 4T1 spheroids, the amounts of FAK and pFAK^{Y397} in spheroids were similar to two-dimensional cell cultures. Tanjoni

et al. conducted similar experiments with 4T1 cells and have reported that an Y397 phosphorylation of FAK decreases when cells are cultured as spheroids (Tanjoni *et al.*, 2010). Differences in methodologies used may contribute to the diverging findings. One thing that was performed differently compared to Tanjoni *et al.*, was the seeded cell number of 2×10^5 cells to form spheroids, whereas we seeded a number of 2×10^3 cells per spheroid. Since FAK activation is sensitive towards external changes, an altered cell number with an altered surface-to-volume ratio might already affect its phosphorylation state.

In the metastatic 4T1 cells, an inhibition of FAK phosphorylation exhibited a strong effect on spheroid growth. These cells exhibit a strong basal phosphorylation of FAK. However, when the cells were cultured as monolayers, FAK inhibition did not affect cell viability. The diverging effect of FAK on cell viability in two- and three-dimensional cell cultures has been reported previously for 4T1 cells (Tanjoni *et al.*, 2010). FAK acts on cell proliferation in an integrin-dependent and integrin-independent manner. In the integrin-independent pathway, which is activated upon detachment from substratum, TNF α signaling, or stress signals such as chemical or oxidative stress, FAK translocates into the cell nucleus (Lim, 2013). In the forming spheroids, FAK was at no time point found in the cell nucleus. This strongly suggests that the effects of FAK on spheroid growth occur in an integrin-mediated fashion, which is further supported by the intrinsic expression of ECM molecules that facilitate integrin binding and activation of FAK in spheroids. However, the amount of integrin-to-ECM connections may differ between two- and three-dimensional cell cultures, which in turn affects integrin-mediated signaling through FAK. The inhibiting effects on spheroid growth were different among the cell lines. The metastatic 4T1 cells exhibited a strong growth inhibition upon FAK inhibition. These cells exhibited a strong expression and phosphorylation of FAK at Y397. Contrary, HC11 cells strongly reduced FAK in spheroids and showed a slightly increased projected area in forming spheroids compared to the control. In monolayer cultures, FAK inhibition increased proliferation in HC11 cells. Provided that there are no differences of FAK signaling in cell viability between two-dimensional compared to the three-dimensional culture conditions in HC11 cells (compare Figure 3-30a and Supplemental Figure 7-23b), the increased proliferation upon FAK inhibition may account for the increased spheroid size. In the tumorigenic T47D cells, FAK inhibition neither affected the proliferation in the monolayer nor the spheroid size. In these cells, the FAK activity was low in forming spheroids. Consequently, FAK activity correlates with the invasiveness of cells and strong FAK activity is associated with massive growth in spheroids.

FAK further transduces signals to promote cell migration and invasion (Slack *et al.*, 2001; Mitra *et al.*, 2006), but it also affects cadherin-mediated cell adhesion (Yano *et al.*, 2004). The computational model unveiled a slight increase of the binding probability when FAK was inhibited in HC11 and 4T1 cells. This suggests that, at least in these cell types, phosphorylated FAK counteracts the

contact formation between cells. The analysis further showed that the unbinding probability was affected differently in the cell lines. Thus, different levels of FAK and its activity might induce different subsets of FAK-activated signaling pathways in spheroid formation in different cell types. This is further supported by the diverging results obtained from spheroid formation of T47D cells. FAK inhibition accelerated spheroid formation but neither the binding nor the unbinding probabilities were affected. Further, T47D cells display a relatively weak adhesion to ECM proteins, making the cell-ECM interaction a less prominent factor in the progression of spheroid formation progression.

4.6.6 BAG3 promotes cell survival in spheroids

BAG3 has been shown reportedly to influence adhesion, cell migration, cell survival and its expression is stimulated upon mechanical stress (Kassis et al., 2006; Ulbricht et al., 2013a; Antonietti et al., 2017). These processes are abundant in the three phases in the spheroid formation process. We hypothesized that BAG3 affects important cellular mechanisms such as adhesion and cell survival in forming spheroids. Both, a knockdown and knockout for BAG3 were investigated in spheroid formation of HC11 cells. Different results were obtained for the two approaches. Only a downregulation decelerated the aggregation phase, while the knockout did not. This suggests that the contribution of BAG3 in this phase is compensated by another cellular mechanism when the protein is completely absent (i.e. knockout). However, when the expression is reduced, the remaining protein may sufficiently fulfill its task but with a delayed accomplishment of the process. We suggest that adhesion formation processes are prominent especially in the aggregation phase. The modes, in which BAG3 influences cell adhesion, are different. It is capable to regulate cell adhesion by interaction with multiple proteins and involvement in different adhesion-mediating processes (Fontanella et al., 2010; Iwasaki et al., 2010; Rosati et al., 2011).

BAG3 knockout affected cell survival negatively in 7 days old spheroids. However, the reduction of BAG3 expression (i.e. knockdown) did not affect cell survival in spheroids. This is another indication that the amount of protein is crucial for its function. In some cases, a reduced expression is sufficient to maintain cell function, whereas either a complete loss might induce an alternative process to compensate for the loss or, when this is not possible, cells adapt a distinct phenotype. Regarding BAG3, not only the presence or absence but also the concentration of the protein within a cell affects cellular processes.

4.6.7 Phases of spheroid formation reflect modalities of tissue integrity

The main benefit of a spheroid formation assay over conventional two-dimensional cell culture assays is that it allows studying cell interaction with its environment under non-adhesive and thus unbiased conditions. We dissected three temporally distinct phases in the spheroid formation

process. Specific cellular processes dominate the phases. Adhesion formation is of particular importance in the aggregation phase. It involves multiple molecules and does not depend on a single type of connection (i.e. E-cadherin-mediated adherens junction). Adhesion maturation and remodeling as well as cell rearrangement are processes that are present in the compaction phase. Cell proliferation is prominent in the growth phase. From our results, we hypothesize that spheroid formation displays three-dimensional cell migration. Cell migration could be prominent especially in the compaction phase, where a strong regulation of both, adhesion and rearrangement of the cells promotes the formation of a three-dimensional cluster. To which extend collective cell migration (Friedl and Gilmour, 2009) is present in spheroids, needs to be solved.

The three phases of spheroid formation reflect modalities of tissue integrity. Tissue integrity increases when adhesion of cells is promoted, when cells are able to rearrange to form structural and functional units and when cells reinforce their connections. The processes possess a bi-directionality, where the direction is emphasized according to the developmental requirements. Mammary gland ductal outgrowth during puberty aims to achieve full tissue integrity. Cells divide, rearrange their connections and move to form a ductal tree, which fills the mammary fat pad. Different is the post-lactational regression of the mammary gland, in which tissue integrity is temporally lost to accomplish the remodeling processes. In malignant diseases such as cancer, the increasing metastatic potential counteracts tissue integrity by destabilization of cell adhesion and excessive cell proliferation (Figure 4-1).

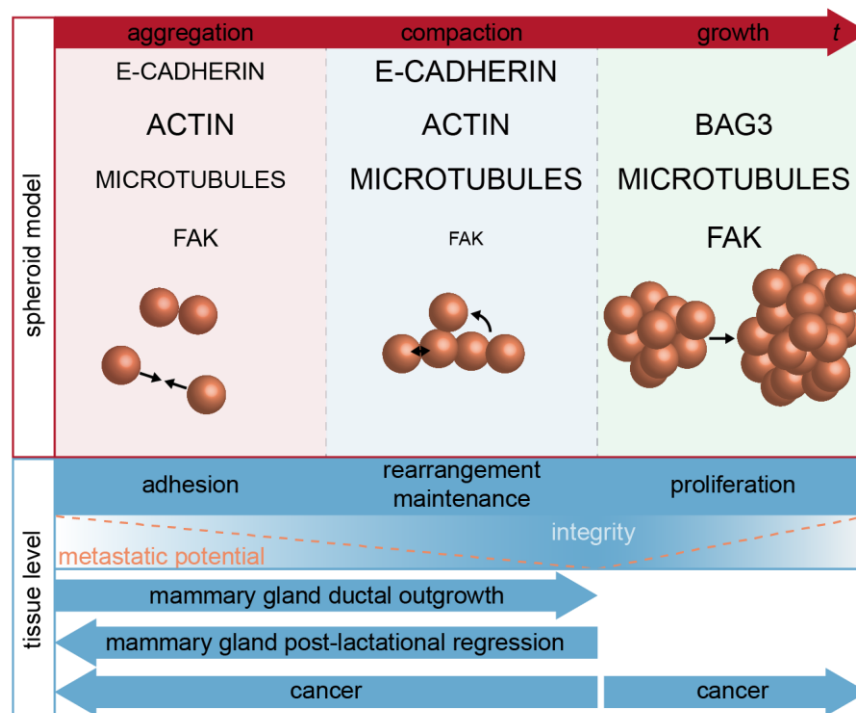


Figure 4-1 Results obtained from spheroid formation can be extrapolated to the tissue level. Spheroid formation on a non-adhesive surface subdivides into the three phases of aggregation, compaction and growth. The involvement of E-cadherin, actin, microtubules, FAK and BAG3 is indicated in each phase. The font size

of each component indicates its importance in the according phase regardless of having a positive or negative effect. The phases in spheroid formation can be translated to the tissue level to describe its features that contribute to tissue integrity. The integrity is high when cellular rearrangement is followed by the maintenance of cell adhesion by reinforcement. Excessive proliferation and loosely attached cells counteract tissue integrity and correlate with increased metastatic potential. Potential developmental contexts, which can be studied with spheroid formation, are mammary gland and cancer development.

5 Outlook and Conclusion

Studying dynamic three-dimensional models provides a physiological understanding of tissue development and the underlying cellular processes. This work contributes to an overall picture of how cellular aggregates develop, are maintained, and to which extent physical forces influence this homeostasis.

Methodically, this thesis contributes an immunofluorescence staining protocol for a stain of large spheroids *in toto*. Further, an evaluation is introduced that incorporates qualitative and quantitative aspects of the stain quality, i.e. (1) the stain specificity, (2) the stain intensity and (3) the stain homogeneity. For image acquisition of fixed cellular spheroids using LSM, optical clearing benefits from a strong reduction of light scattering effects, which multi-view image fusion does not provide.

In the context of the mammary gland, we learned that BAG3 is involved in mammary gland development and predominantly present in the phase of post-lactational remodeling. Its function in mammary epithelial cells is strongly associated with cell survival.

This work provides new insights on how cells form aggregates and how physical forces affect their morphology. We learned that the proteins E-cadherin and actin are associated with cell adhesion by being involved rather in enforcing existing connections than in building new ones. However, the formation of multicellular aggregates does not follow a universal procedure as certain molecules (i.e. microtubules) contribute differently in cells from different cell types. Cell aggregates certainly produce ECM but the attachment to it and the subsequently involved signaling pathways are not necessary for the aggregation of cells in a three-dimensional context.

Physical forces applied by compression induce morphological alterations of mammary epithelial cellular networks. While programmed cell death is induced as an immediate response, cells adapt to the changes of the environment on the long term.

5.1 Future research topics

5.1.1 Imaging large volumes of tissues will reveal cellular networks *in vivo*

Spheroids serve as an *in vitro* model system to study aspects of tissues. Nevertheless, studying real tissue is still necessary to understand the complexity of such a system. In this context, it is favorable to generate three- or even four-dimensional (i.e. time) image data of the cellular networks within tissues. This will help to understand not only the connection between subsets of cell populations

but also dynamic processes like cell migration. A first step of looking into tissue networks is imaging large volumes of tissue and organ samples. This in combination with the specific labeling of proteins of interest is a mayor future goal to support a magnitude of biomedical sciences.

However, tissues and organs are structurally more complex than spheroids, and thus require a further improvement of the immunofluorescence staining procedure. One option is the improvement of the labels. Antibodies are large and charged, and therefore diffuse only poorly into tissue. The use of smaller components such as nanobodies (Ries et al., 2012) will improve the penetration into large and dense tissues.

In the past years, much effort has been put in the development of novel optical clearing techniques. The aim is to improve the transparency of the sample while maintaining the architecture of the tissue and the function of the fluorophores. Promising techniques use polymers and novel staining procedures, which facilitate stain homogeneity (Chung and Deisseroth, 2013; Murray et al., 2015).

With reliable staining, optical clearing and imaging workflows available, the obtained data will be valid and valuable for subsequent quantitative analysis. The recognition of individual cells and the connection with their neighboring cells can provide information about the complex architecture and communication networks of tissues.

5.1.2 The mechanism of BAG3 function in mammary gland development

Mammary gland development is highly complex. Especially the involution phase requires synergy of multiple pathways and cellular mechanisms. The loss of synergy results in inappropriate clearance mechanisms and implicates the development of tumors (Silanikove, 2014). Thus, an understanding of the initial cues and mechanisms that initiate involution is important. This thesis points out that BAG3 and its interaction partners are targets for further investigation. Its expression increases at the onset of involution and it is implicated in the development of breast cancer. The *in vitro* experiments showed that BAG3 is involved in cell migration but more importantly in cell survival in mammary epithelial cells. From this point of view, new research questions could address to which extent the initiation of mammary gland involution requires BAG3 expression, and in what exact cellular mechanism BAG3 is involved. A conditional knockout of BAG3 in the murine mammary gland would unveil its function *in vivo*. In the context of breast cancer, it has been shown that inflammation during mammary gland involution induces epigenetic alterations, which increase the risk of developing cancer with increasing age (Chung et al., 2017). Whether epigenetic mutations alter BAG3 expression is unknown but might help to understand the development of breast cancer.

5.1.3 The effect of ECM on the diffusion of small molecules in spheroids

The ECM has supportive and signaling character, but may also function as a barrier for diffusing small molecules. The massive production of ECM in tumors could further protect against exogenous factors like chemotherapeutics. The investigation of the ECM organization in tumor spheroids with regard to the diffusion of molecules into the center of the spheroids (Goodman et al., 2008) may help to understand why certain chemotherapeutics are more effective in monolayer cultures compared to tumor spheroid cultures.

5.1.4 The influence of mechanical stress on mammary gland involution

The physical forces within the regressing mammary gland are by far greater than in the *in vitro* experiments. The lateral strain in mammary glands (117%-218%) is much larger compared to the lateral strain in the compressed spheroids (12.6% after 24 hours of compression). Consequently, the mechanical load is different. Hypothetically, the forces executed upon milk stasis cause severe cell stretching in the *in vivo* tissue that induce activation of the cell survival machineries, repair mechanisms and mechanosignaling pathways (Watson and Kreuzaler, 2011; Pensa et al., 2014). In the *in vitro* assay, cells were not sufficiently deformed such that a comparable answer was induced. However, the compression exerted on the spheroids is limited by the minimum inner diameter of the agarose capillaries of 200 μm . Agarose capillaries with smaller inner diameters tend to collapse. Alternative methods are required to reflect the *in vivo* situation. Spheroids could be placed in-between two flat surfaces (i.e. glass slides) that are separated by beads with a defined diameter. This approach is successfully used to compress *Caenorhabditis elegans* embryos (Murray et al., 2006). To reflect the deformation occurring in the mammary gland *in vivo*, the strain in the spheroids could be varied by using beads of different diameters.

5.1.5 Cell migration and agility during spheroid formation and in mature spheroids

Spheroid formation is a promising tool to study tissue-forming processes in four dimensions (i.e. spatial and temporal). In our experiments, we used two-dimensional images to describe the spheroid formation process. First promising approaches of acquiring three-dimensional images of spheroid formation have been conducted (Pampaloni et al., 2015). An elaborated microscopy approach will provide insight into the cellular rearrangements in spheroids. Of special interest is cell migration during spheroid formation and in mature spheroids (initial work on the latter one has been done by Till Moreth). Research on three-dimensional cell migration will be further promoted by adding a fluorescent label for the plasma membrane. Its labeling will provide information about the cell morphology and the formation of protrusions.

5.1.6 Proteins involved in the formation of cell contacts upon collision of cells

Our results showed that the adherens junction protein E-cadherin is not primarily involved in the formation of cell contacts. The chance of cells to form a connection was not altered when E-cadherin function was blocked. A previous study has postulated that desmosomal proteins are necessary to form contacts between cells (Saias et al., 2015). Future investigations of desmosomal proteins in spheroid formation and the analysis with the computational model will unveil whether the binding probability of cells is altered.

5.2 Concluding remarks

The results of this thesis identified and characterized survival- and adhesion-associated proteins that are important for tissue integrity. The broader perspective of this research area is to explain how cells within tissues are connected, and what factors and processes induce cells to break out of their niche.

This thesis unveiled that a BAG3-dependent cell survival mechanism is prominent at the beginning of mammary gland involution. Based on these results, future studies will have to identify the related factors and the inducers of the loss of tissue integrity in the mammary gland. This will help to understand the physiology of this organ and disorders that destroy its tissue integrity.

In addition, the results of this thesis contribute to a better understanding of spontaneous cell aggregation and organization. The results of this thesis raise the question about the role of cell migration in this process. Based on these results, future studies will have to focus on three-dimensional cell migration, how it is promoted and to which extent it supports tissue integrity.

6 References

- Abu-Absi, S.F., J.R. Friend, L.K. Hansen, and W.-S. Hu. 2002. Structural Polarity and Functional Bile Canaliculi in Rat Hepatocyte Spheroids. *Exp. Cell Res.* 274:56–67. doi:10.1006/excr.2001.5467.
- Alberts, B., A. Johnson, J. Lewis, M. Raff, K. Roberts, and P. Walter. 2008. Molecular biology of the cell - Fifth edition. 5th ed. Garland Science, New York and Abingdon.
- Alessandri, K., B.R. Sarangi, V.V. Gurchenkov, B. Sinha, T.R. Kießling, L. Fetler, F. Rico, S. Scheuring, C. Lamaze, A. Simon, S. Geraldo, D. Vignjevic, H. Doméjean, L. Rolland, A. Funfak, J. Bibette, N. Bremond, and P. Nassoy. 2013. Cellular capsules as a tool for multicellular spheroid production and for investigating the mechanics of tumor progression in vitro. *Proc. Natl. Acad. Sci. U. S. A.* 110:14843–8. doi:10.1073/pnas.1309482110.
- Antonietti, P., B. Linder, S. Hehlhans, I.C. Mildenerger, M.C. Burger, S. Fulda, J.P. Steinbach, F. Gessler, F. Rodel, M. Mittelbronn, D. Kogel, F. Rödel, M. Mittelbronn, and D. Kögel. 2017. Interference with the HSF1/HSP70/Bag3 pathway primes glioma cells to matrix detachment and BH3 mimetic-induced apoptosis. *Mol. Cancer Ther.* 16:156–168.
- Arndt, V., N. Dick, R. Tawo, M. Dreiseidler, D. Wenzel, M. Hesse, D.O. Fürst, P. Saftig, R. Saint, B.K. Fleischmann, M. Hoch, and J. Höhfeld. 2010. Chaperone-assisted selective autophagy is essential for muscle maintenance. *Curr. Biol.* 20:143–148. doi:10.1016/j.cub.2009.11.022.
- Aslakson, C.J., and F.R. Miller. 1992. Selective events in the metastatic process defined by analysis of the sequential dissemination of subpopulations of a mouse mammary tumor. *Cancer Res.* 52:1399–1405.
- Ball, R.K., R.R. Friis, C.A. Schoeneberger, W. Doppler, and B. Groner. 1988. Prolactin regulation of beta-casein gene expression and of a cytosolic 120-kd protein in a cloned mouse mammary epithelial cell line. *EMBO J.* 7:2089–2095.
- Barltrop, J.A., T.C. Owen, A.H. Cory, and J.G. Cory. 1991. 5-(3-carboxymethoxyphenyl)-2-(4,5-dimethylthiazolyl)-3-(4-sulfophenyl)tetrazolium, inner salt (MTS) and related analogs of 3-(4,5-dimethylthiazolyl)-2,5-diphenyltetrazolium bromide (MTT) reducing to purple water-soluble formazans As cell-viability indicators. *Bioorganic Med. Chem. Lett.* 1:611–614. doi:10.1016/S0960-894X(01)81162-8.
- Beck, H.C., M. Gosau, L.P. Kristensen, and C. Morszeck. 2014. A site-specific phosphorylation of the focal adhesion kinase controls the formation of spheroid cell clusters. *Neurochem. Res.* 39:1199–1205. doi:10.1007/s11064-014-1298-y.
- Behl, C. 2016. Breaking BAG: The co-chaperone BAG3 in health and disease. *Trends Pharmacol. Sci.* 37:672–688. doi:10.1016/j.tips.2016.04.007.
- Bell, H.S., I.R. Whittle, M. Walker, H.A. Leaver, and S.B. Wharton. 2001. The Development of necrosis and apoptosis in glioma: experimental findings using spheroid culture systems. *Neuropathol. Appl. Neurobiol.* 27:291–304.
- Berrier, A.L., and K.M. Yamada. 2007. Cell-matrix adhesion. *J. Cell. Physiol.* 213:565–573. doi:10.1002/jcp.21237.
- Bershadsky, A. 2004. Magic touch: How does cell-cell adhesion trigger actin assembly? *Trends Cell Biol.* 14:589–593. doi:10.1016/j.tcb.2004.09.009.
- Bhang, S.H., S. Lee, T.-J. Lee, W.-G. La, H.-S. Yang, S.-W. Cho, and B.-S. Kim. 2012. Three-dimensional cell grafting enhances the angiogenic efficacy of human umbilical vein endothelial cells. *Tissue Eng. Part A.* 18:310–9. doi:10.1089/ten.TEA.2011.0193.
- Bisel, B., M. Calamai, F. Vanzi, and F.S. Pavone. 2013. Decoupling polarization of the Golgi apparatus and GM1 in the plasma membrane. *PLoS One.* 8:e80446. doi:10.1371/journal.pone.0080446.
- Bissell, M.J., A. Rizki, and I.S. Mian. 2003. Tissue architecture: the ultimate regulator of breast epithelial function. *Curr. Opin. Cell Biol.* 15:753–762.

- Bjerkvig, R., O.D. Laerum, and G.J. Rucklidge. 1989. Immunocytochemical characterization of extracellular matrix proteins expressed by cultured glioma cells. *Cancer Res.* 49:5424–5428.
- Blase, C., D. Becker, S. Kappel, and J. Bereiter-Hahn. 2009. Microfilament dynamics during HaCaT cell volume regulation. *Eur. J. Cell Biol.* 88:131–139. doi:10.1016/j.ejcb.2008.10.003.
- BMEL. 2013. Stillen - Die beste Ernährung in den ersten Lebensmonaten. https://www.bmel.de/DE/Ernaehrung/GesundeErnaehrung/SchwangerschaftBaby/_Texte/DossierSchwangerschaftUndBaby.html?docId=635206.
- Bork, P., and M. Sudol. 1994. The WW domain: A signalling site in dystrophin? *Trends Biochem. Sci.* 19:531–533. doi:10.1016/0968-0004(94)90053-1.
- Bradford, M.M. 1976. A rapid and sensitive method for the quantitation of microgram quantities of protein utilizing the principle of protein-dye binding. *Anal. Biochem.* 254:248–254. doi:10.1016/0003-2697(76)90527-3.
- Brandtzaeg, P. 1998. The increasing power of immunohistochemistry and immunocytochemistry. *J. Immunol. Methods.* 216:49–67. doi:10.1016/S0022-1759(98)00070-2.
- Brasch, J., O.J. Harrison, B. Honig, and L. Shapiro. 2012. Thinking outside the cell: How cadherins drive adhesion. *Trends Cell Biol.* 22:299–310. doi:10.1016/j.tcb.2012.03.004.
- Broutier, L., A. Andersson-Rolf, C.J. Hindley, S.F. Boj, H. Clevers, B.-K. Koo, and M. Huch. 2016. Culture and establishment of self-renewing human and mouse adult liver and pancreas 3D organoids and their genetic manipulation. *Nat. Protoc.* 11:1724–43. doi:10.1038/nprot.2016.097.
- Butcher, D.T., T. Alliston, and V.M. Weaver. 2009. A tense situation: forcing tumour progression. *Nat. Rev. Cancer.* 9:108–122. doi:10.1038/nrc2544.
- Campinho, P., M. Behrndt, J. Ranft, T. Risler, N. Minc, and C.-P. Heisenberg. 2013. Tension-oriented cell divisions limit anisotropic tissue tension in epithelial spreading during zebrafish epiboly. *Nat. Cell Biol.* 15:1405–14. doi:10.1038/ncb2869.
- Carlsson, J., and J. Yuhas. 1984. Liquid-overlay culture of cellular spheroids. *Recent Results Cancer Res.* 95:1–23.
- Casey, R.C., K.M. Bureson, K.M. Skubitz, S.E. Pambuccian, T.R. Oegema, L.E. Ruff, and A.P. Skubitz. 2001. Beta 1-integrins regulate the formation and adhesion of ovarian carcinoma multicellular spheroids. *Am. J. Pathol.* 159:2071–80. doi:10.1016/S0002-9440(10)63058-1.
- CDC. 2013. U.S. National Breastfeeding Rates, 2013 Births. https://www.cdc.gov/breastfeeding/data/NIS_data/index.htm#modalIdString_CDCTable_2.
- Chang, B.-J., V. Didier Perez Meza, and E.H.K. Stelzer. 2017. csiLSFM combines light-sheet fluorescence microscopy and coherent structured illumination for a lateral resolution below 100 nm. *PNAS.* 114:4869–4874. doi:10.1073/pnas.1609278114.
- Chang, T.T., and M. Hughes-Fulford. 2009. Monolayer and spheroid culture of human liver hepatocellular carcinoma cell line cells demonstrate distinct global gene expression patterns and functional phenotypes. *Tissue Eng. Part A.* 15:559–567. doi:10.1089/ten.tea.2007.0434.
- Chen, B., C. Co, and C.-C. Ho. 2015. Cell shape dependent regulation of nuclear morphology. *Biomaterials.* 67:129–136. doi:10.1016/j.biomaterials.2015.07.017.
- Cheng, G., J. Tse, R.K. Jain, and L.L. Munn. 2009. Micro-Environmental Mechanical Stress Controls Tumor Spheroid Size and Morphology by Suppressing Proliferation and Inducing Apoptosis in Cancer Cells. *PLoS One.* 4:e4632. doi:10.1371/journal.pone.0004632.
- Chiappetta, G., M. Ammirante, A. Basile, A. Rosati, M. Festa, M. Monaco, E. Vuttariello, R. Pasquinelli, C. Arra, M. Zerilli, M. Todaro, G. Stassi, L. Pezzullo, A. Gentilella, A. Tosco, M. Pascale, L. Marzullo, M.A. Belisario, M.C. Turco, and A. Leone. 2007. The antiapoptotic protein BAG3 is expressed in thyroid carcinomas and modulates apoptosis mediated by tumor necrosis factor-related apoptosis-inducing ligand. *J. Clin. Endocrinol. Metab.* 92:1159–1163. doi:10.1210/jc.2006-1712.
- Chiappetta, G., A. Basile, A. Barbieri, A. Falco, A. Rosati, M. Festa, R. Pasquinelli, D. Califano, G. Palma, R. Costanzo, D. Barcaroli, M. Capunzo, G. Rocco, M. Pascale, M.C. Turco, V. De, and C. Arra. 2014. The anti-apoptotic BAG3 protein is expressed in lung carcinomas and regulates small cell lung carcinoma (SCLC) tumor growth. *Oncotarget.* 5. doi:10.18632/oncotarget.2261.

- Chung, H.H., Y.Z. Or, S. Shrestha, J.T. Loh, C.L. Lim, Z. Ong, A.R.E. Woo, I.-H. Su, and V.C.L. Lin. 2017. Estrogen reprograms the activity of neutrophils to foster protumoral microenvironment during mammary involution. *Sci. Rep.* 7:46485. doi:10.1038/srep46485.
- Chung, K., and K. Deisseroth. 2013. CLARITY for mapping the nervous system. *Nat. Methods.* 10:508–13. doi:10.1038/nmeth.2481.
- Clarkson, R.W.E., and C.J. Watson. 2003. Microarray Analysis of the Involution Switch. *J. Mammary Gland Biol. Neoplasia.* 8:309–319.
- Coons, A.H., and M.H. Kaplan. 1950. Localization of antigen in tissue cells; improvements in a method for the detection of antigen by means of fluorescent antibody. *J. Exp. Med.* 91:1–13. doi:10.1084/jem.91.1.1.
- Cukierman, E., R. Pankov, D.R. Stevens, and K.M. Yamada. 2001. Taking cell-matrix adhesions to the third dimension. *Science (80-.).* 294:1708–1712. doi:10.1126/science.1064829.
- D’Esposito, A., D. Nikitichev, A. Desjardins, S. Walker-Samuel, and M.F. Lythgoe. 2015. Optical clearing of the mouse brain and light attenuation quantification. *Proc. SPIE, Photons Plus Ultrasound Imaging Sens.* 9321:93210R. doi:10.1117/12.2075580.
- Dahl, K.N., A.J.S. Ribeiro, and J. Lammerding. 2008. Nuclear shape, mechanics, and mechanotransduction. *Circ. Res.* 102:1307–1318. doi:10.1161/CIRCRESAHA.108.173989.
- Danielson, K.G., C.J. Oborn, E.M. Durban, J.S. Butel, H.A. Bern, and D. Medina. 1984. Epithelial mouse mammary cell line exhibiting normal morphogenesis in vivo and functional differentiation in vitro. *Proc. Natl. Acad. Sci. U. S. A.* 81:3756–3760. doi:10.1073/pnas.81.12.3756.
- Debnath, J., S.K. Muthuswamy, and J.S. Brugge. 2003. Morphogenesis and oncogenesis of MCF-10A mammary epithelial acini grown in three-dimensional basement membrane cultures. *Methods.* 30:256–268. doi:10.1016/s1046-2023(03)00032-x.
- Deguchi, S., K. Maeda, T. Ohashi, and M. Sato. 2005. Flow-induced hardening of endothelial nucleus as an intracellular stress-bearing organelle. *J. Biomech.* 38:1751–1759. doi:10.1016/j.jbiomech.2005.06.003.
- Delarue, M., F. Montel, D. Vignjevic, J. Prost, G. Cappello, M. Curie, I. Curie, C. De Recherche, J.-F. Joanny, and G. Cappello. 2014. Compressive Stress Inhibits Proliferation in Tumor Spheroids through a Volume Limitation. *Biophys. J.* 107:1821–1828. doi:10.1016/j.bpj.2014.08.031.
- Dent, J. a, A.G. Polson, and M.W. Klymkowsky. 1989. A whole-mount immunocytochemical analysis of the expression of the intermediate filament protein vimentin in *Xenopus*. *Development.* 105:61–74.
- Desgrosellier, J., and C. David. 2015. Integrins in cancer: biological implications in therapeutic opportunities. *Cancer, Nat Rev.* 10:9–22. doi:10.1038/nrc2748.Integrins.
- Desmaison, A., C. Frongia, K. Grenier, B. Ducommun, and V. Lobjois. 2013. Mechanical stress impairs mitosis progression in multi-cellular tumor spheroids. *PLoS One.* 8:4–13. doi:10.1371/journal.pone.0080447.
- Dewey, K. 2003. Guiding Principles for Complementary Feeding of the Breastfed (PAHO and WHO). *Pan Am. Heal. Organ. World Heal. Organ.* doi:10.1017/S1368980011002485.
- Dotdt, H.U., U. Leischner, A. Schierloh, N. Jaehrling, C.P. Mauch, K. Deininger, J.M. Deussing, M. Eder, W. Zieglergaensberger, and K. Becker. 2007. Ultramicroscopy: three-dimensional visualization of neuronal networks in the whole mouse brain. *Nat. Methods.* 4:331–336. doi:10.1038/nmeth1036.
- DuFort, C.C., M.J. Paszek, and V.M. Weaver. 2011. Balancing forces: architectural control of mechanotransduction. *Nat. Rev. Mol. Cell Biol.* 12:308–319. doi:10.1038/nrm3112.
- Dull, T.O.M., R. Zufferey, M. Kelly, R.J. Mandel, M. Nguyen, D. Trono, L. Naldini, and J. V Irol. 1998. A Third-Generation Lentivirus Vector with a Conditional Packaging System. *J. Virol.* 72:8463–8471.
- Ehrlicher, A.J., F. Nakamura, J.H. Hartwig, D.A. Weitz, and T.P. Stossel. 2011. Mechanical strain in actin networks regulates FilGAP and integrin binding to filamin A. *Nature.* 478:260–263. doi:10.1038/nature10430.
- Enmon, R.M., K.C. O’Connor, D.J. Lacks, D.K. Schwartz, and R.S. Dotson. 2001. Dynamics of spheroid self-assembly in liquid-overlay culture of DU 145 human prostate cancer cells. *Biotechnol. Bioeng.* 72:579–591. doi:10.1002/1097-0290(20010320)72:6<579::AID-BIT1023>3.0.CO;2-L.

- Estrada, M.F., S.P. Rebelo, E.J. Davies, M.T. Pinto, H. Pereira, V.E. Santo, M.J. Smalley, S.T. Barry, E.J. Gualda, P.M. Alves, E. Anderson, and C. Brito. 2016. Modelling the tumour microenvironment in long-term microencapsulated 3D co-cultures recapitulates phenotypic features of disease progression. *Biomaterials*. 78:50–61. doi:10.1016/j.biomaterials.2015.11.030.
- Etienne-Manneville, S. 2013. Microtubules in cell migration. *Annu. Rev. Cell Dev. Biol.* 29:471–499. doi:10.1146/annurev-cellbio-101011-155711.
- Etienne, W., M.H. Meyer, J. Peppers, and R.A. Meyer. 2004. Comparison of mRNA gene expression by RT-PCR and DNA microarray. *Biotechniques*. 36:618–626.
- Ewald, A.J., A. Brenot, M. Duong, B.S. Chan, and Z. Werb. 2008. Collective epithelial migration and cell rearrangements drive mammary branching morphogenesis. *Dev. Cell*. 14:570–581. doi:10.1016/j.devcel.2008.03.003.
- Fahrbach, F.O., and A. Rohrbach. 2010. A line scanned light-sheet microscope with phase shaped self-reconstructing beams. *Opt. Express*. 18:24229–24244. doi:10.1038/nphoton.2010.204.J.
- Fata, J.E., Z. Werb, and M.J. Bissell. 2004. Regulation of mammary gland branching morphogenesis by the extracellular matrix and its remodeling enzymes. *Breast Cancer Res.* 6:1–11. doi:10.1186/bcr634.
- Fontanella, B., L. Birolo, G. Infusini, C. Cirulli, L. Marzullo, P. Pucci, M.C. Turco, and A. Tosco. 2010. The co-chaperone BAG3 interacts with the cytosolic chaperonin CCT: New hints for actin folding. *Int. J. Biochem. Cell Biol.* 42:641–650. doi:10.1016/j.biocel.2009.12.008.
- Fox, J., and D. Phillips. 1981. Inhibition of actin polymerization in blood platelets by cytochlasins. *Nature*. 292:650–652.
- Frantz, C., K.M. Stewart, and V.M. Weaver. 2010. The extracellular matrix at a glance. *J. Cell Sci.* 123:4195–4200. doi:10.1242/jcs.023820.
- Friedl, P., and D. Gilmour. 2009. Collective cell migration in morphogenesis, regeneration and cancer. *Nat. Rev. Mol. Cell Biol.* 10:445–457. doi:10.1038/nrm2720.
- Frisch, S., and H. Francis. 1994. Disruption of epithelial cell-matrix interactions induces apoptosis. *J. Cell Biol.* 124:619–626.
- Fung, Y. 1993. Biomechanics: mechanical properties of living tissues. 2nd ed. Springer, New York.
- Gajewska, M., K. Zielniok, and T. Motyl. 2013. Autophagy in Development and Remodelling of Mammary Gland. doi:10.5772/54558.
- Gardel, M.L., I.C. Schneider, Yvonne Aratyn-Schaus, and C.M. Waterman. 2010. Mechanical integration of actin and adhesion dynamics in cell migration. *Annu. Rev. Cell Dev. Biol.* 26:315–333. doi:10.1146/annurev.cellbio.011209.122036.
- Garg, S., S.C. Fischer, E.M. Schuman, and E.H.K. Stelzer. 2015. Lateral assembly of N-cadherin drives tissue integrity by stabilizing adherens junctions. *J. R. Soc. Interface.* 12:20141055. doi:10.1098/rsif.2014.1055.
- Gebhard, C., C. Gabriel, and I. Walter. 2016. Morphological and Immunohistochemical Characterization of Canine Osteosarcoma Spheroid Cell Cultures. *Anat. Histol. Embryol.* 45:1–12. doi:10.1111/ahc.12190.
- Goodman, T.T., J. Chen, K. Matveev, and S.H. Pun. 2008. Spatio-temporal modeling of nanoparticle delivery to multicellular tumor spheroids. *Biotechnol. Bioeng.* 101:388–399. doi:10.1002/bit.21910.
- Gordon, K.E., B. Binas, R.S. Chapman, K.M. Kurian, R.W.E. Clarkson, A.J. Clark, E.B. Lane, and C.J. Watson. 2000. A novel cell culture model for studying differentiation and apoptosis in the mouse mammary gland. *Breast Cancer Res.* 2:222–235. doi:10.1186/bcr57.
- Groebe, K., and W. Mueller-Klieser. 1996. On the relation between size of necrosis and diameter of tumor spheroids. *Int. J. Radiat. Oncol. Biol. Phys.* 34:395–401. doi:10.1016/0360-3016(95)02065-9.
- Guilak, F., J.R. Tedrow, and R. Burgkart. 2000. Viscoelastic properties of the cell nucleus. *Biochem. Biophys. Res. Commun.* 269:781–786. doi:10.1006/bbrc.2000.2360.
- Gumbiner, B.M. 1992. Epithelial morphogenesis. *Cell*. 69:385–387. doi:10.1016/0092-8674(92)90440-N.
- Gumbiner, B.M. 1996. Cell adhesion: The molecular basis of tissue architecture and morphogenesis. *Cell*. 84:345–357. doi:10.1016/S0092-8674(00)81279-9.

- Gumbiner, B.M. 2000. Regulation of Cadherin Adhesive Activity. *J. Cell Biol.* 148:399–403.
- Hama, H., H. Kurokawa, H. Kawano, R. Ando, T. Shimogori, H. Noda, K. Fukami, A. Sakaue-sawano, and A. Miyawaki. 2011. Scale: a chemical approach for fluorescence imaging and reconstruction of transparent mouse brain. *Nat. Neurosci.* 14:1481–1488. doi:10.1038/nn.2928.
- Han, L.Q., G.Y. Yang, H.S. Zhu, Y.Y. Wang, L.F. Wang, Y.J. Guo, W.F. Lu, H.J. Li, and Y.L. Wang. 2010. Selection and use of reference genes in mouse mammary glands. *Genet. Mol. Res.* 9:449–456. doi:10.4238/vol9-1gmr724.
- Hazel, A.L., and T.J. Pedley. 2000. Vascular endothelial cells minimize the total force on their nuclei. *Biophys. J.* 78:47–54. doi:10.1016/S0006-3495(00)76571-4.
- Helmchen, F., and W. Denk. 2005. Deep tissue two-photon microscopy. *Nat. Methods.* 2:932–940. doi:10.1038/nmeth818.
- Helmlinger, G., P.A. Netti, H.C. Lichtenbeld, R.J. Melder, and R.K. Jain. 1997. Solid stress inhibits the growth of multicellular tumor spheroids. *Nat. Biotechnol.* 15:778–783. doi:10.1038/nbt0897-778.
- Hennighausen, L., and G.W. Robinson. 2005. Information networks in the mammary gland. *Nat. Rev. Mol. Cell Biol.* 6:715–725. doi:10.1038/nrm1714.
- Heppner, G.H., F.R. Miller, and P.M. Shekhar. 2000. Nontransgenic models of breast cancer. *Breast Cancer Res.* 2:331. doi:10.1186/bcr77.
- Holliday, D.L., and V. Speirs. 2011. Choosing the right cell line for breast cancer research. *Breast Cancer Res.* 13:215. doi:10.1186/bcr2889.
- Homma, S., M. Iwasaki, G.D. Shelton, E. Engvall, J.C. Reed, and S. Takayama. 2006. BAG3 deficiency results in fulminant myopathy and early lethality. *Am. J. Pathol.* 169:761–773. doi:10.2353/ajpath.2006.060250.
- Huisken, J., J. Swoger, F. Del Bene, J. Wittbrodt, and E.H.K. Stelzer. 2004. Optical sectioning deep inside live embryos by selective plane illumination microscopy. *Science (80-)*. 305:1007–1009. doi:10.1126/science.1100035.
- Humphries, J.D., A. Byron, and M.J. Humphries. 2006. Integrin ligands at a glance. *J. Cell Sci.* 119:3901–3903. doi:10.1242/jcs.03098.
- Ingber, D.E., L. Dike, L. Hansen, S. Karp, H. Liley, A. Maniotis, H. McNamee, D. Mooney, G. Plopper, J. Sims, and N. Wang. 1994. Cellular tensegrity: exploring how mechanical changes in the cytoskeleton regulate cell growth, migration, and tissue pattern during morphogenesis. *Int. Rev. Cytol.* 150:173–224. doi:10.1016/S0074-7696(08)61542-9.
- Iorio, V., M. Festa, a Rosati, M. Hahne, C. Tiberti, M. Capunzo, V. De Laurenzi, and M.C. Turco. 2015. BAG3 regulates formation of the SNARE complex and insulin secretion. *Cell Death Dis.* 6:e1684. doi:10.1038/cddis.2015.53.
- Iqbal, J., and M. Zaidi. 2005. Molecular regulation of mechanotransduction. *Biochem. Biophys. Res. Commun.* 328:751–755. doi:10.1016/j.bbrc.2004.12.087.
- Ivascu, A., and M. Kubbies. 2007. Diversity of cell-mediated adhesions in breast cancer spheroids. *Int. J. Oncol.* 31:1403–1413. doi:10.3892/ijco.31.6.1403.
- Iwasaki, M., S. Homma, A. Hishiya, S.J. Dolezal, J.C. Reed, and S. Takayama. 2007. BAG3 regulates motility and adhesion of epithelial cancer cells. *Cancer Res.* 67:10252–10259. doi:10.1158/0008-5472.CAN-07-0618.
- Iwasaki, M., R. Tanaka, A. Hishiya, S. Homma, J.C. Reed, and S. Takayama. 2010. BAG3 directly associates with guanine nucleotide exchange factor of Rap1, PDZGEF2, and regulates cell adhesion. *Biochem. Biophys. Res. Commun.* 400:413–418. doi:10.1016/j.bbrc.2010.08.092.
- Jorge, S., S. Chang, J.J. Barzilai, P. Leppert, and J.H. Segars. 2014. Mechanical Signaling in Reproductive Tissues: Mechanisms and Importance. *Reprod. Sci.* 21:1933719114542023-. doi:10.1177/1933719114542023.
- Kass, L., J.T. Erler, M. Dembo, and V.M. Weaver. 2007. Mammary epithelial cell: influence of extracellular matrix composition and organization during development and tumorigenesis. *Int. J. Biochem. Cell Biol.* 39:1987–1994. doi:10.1016/j.biocel.2007.06.025.

- Kassis, J.N., E.A. Guancial, H. Doong, V. Virador, and E.C. Kohn. 2006. CAIR-1/BAG-3 modulates cell adhesion and migration by downregulating activity of focal adhesion proteins. *Exp. Cell Res.* 312:2962–2971. doi:10.1016/j.yexcr.2006.05.023.
- Kassis, J.N., V.M. Virador, E.A. Guancial, D. Kimm, A.S. Ho, M. Mishra, E.Y. Chuang, J. Cook, D. Gius, and E.C. Kohn. 2009. Genomic and phenotypic analysis reveals a key role for CCN1 (CYR61) in BAG3 - modulated adhesion and invasion. *J. Pathol.* 218:495–504. doi:10.1002/path.
- Ke, M.-T., S. Fujimoto, and T. Imai. 2013. SeeDB: a simple and morphology-preserving optical clearing agent for neuronal circuit reconstruction. *Nat. Neurosci.* 16:1154–1161. doi:10.1038/nn.3447.
- Keller, P.J., A.D. Schmidt, A. Santella, K. Khairy, Z. Bao, J. Wittbrodt, and E.H.K. Stelzer. 2010. Fast, high-contrast imaging of animal development with scanned light sheet-based structured-illumination microscopy. *Nat. Methods.* 7:637–642. doi:10.1038/nmeth.147610.1038/NMETH.1476.
- Keller, P.J., A.D. Schmidt, J. Wittbrodt, and E.H.K. Stelzer. 2008. Reconstruction of zebrafish early embryonic development by scanned light sheet microscopy. *Science.* 322:1065–1069. doi:10.1126/science.1162493.
- Képiró, M., B.H. Várkuti, L. Végner, G. Vörös, G.G. Hegyi, M.M. Varga, and A. Málnási-Csizmadia. 2014. Para-nitroblebbistatin, the non-cytotoxic and photostable myosin II inhibitor. *Angew. Chemie - Int. Ed.* 53:8211–8215. doi:10.1002/anie.201403540.
- Keydar, I., L. Chen, S. Karby, F.R. Weiss, J. Delarea, M. Radu, S. Chaitcik, and H.J. Brenner. 1979. Establishment and characterization of a cell line of human breast carcinoma origin. *Eur. J. Cancer.* 15:659–670. doi:10.1016/0014-2964(79)90139-7.
- Kimura, S., T. Noda, and T. Yoshimori. 2007. Dissection of the autophagosome maturation process by a novel reporter protein, tandem fluorescent-tagged LC3. *Autophagy.* 3:452–460.
- King, J.S., D.M. Veltman, and R.H. Insall. 2011. The induction of autophagy by mechanical stress. *Autophagy.* 7:1490–1499. doi:10.4161/auto.7.12.17924.
- Komuro, I., T. Kaida, Y. Shibazaki, M. Kurabayashi, Y. Katoh, E. Hoh, F. Takaku, and Y. Yazaki. 1990. Stretching cardiac myocytes stimulates protooncogene expression. *J. Biol. Chem.* 265:3595–3598.
- Kreuzaler, P.A., A.D. Staniszevska, W. Li, N. Omidvar, B. Kedjouar, J. Turkson, V. Poli, R.A. Flavell, R.W.E. Clarkson, and C.J. Watson. 2011. Stat3 controls lysosomal-mediated cell death in vivo. *Nat. Cell Biol.* 13:303–309. doi:10.1038/ncb2171.
- Kritikou, E.A., A. Sharkey, K. Abell, P.J. Came, E. Anderson, R.W.E. Clarkson, and C.J. Watson. 2003. A dual, non-redundant, role for LIF as a regulator of development and STAT3-mediated cell death in mammary gland. *Development.* 130:3459–3468. doi:10.1242/dev.00578.
- Krzic, U., S. Gunther, T.E. Saunders, S.J. Streichan, and L. Hufnagel. 2012. Multiview light-sheet microscope for rapid in toto imaging. *Nat. Methods.* 9:730–733. doi:10.1038/nmeth.2064.
- Kuwajima, T., A. a Sitko, P. Bhansali, C. Jurgens, W. Guido, and C. Mason. 2013. ClearT: a detergent- and solvent-free clearing method for neuronal and non-neuronal tissue. *Development.* 140:1364–8. doi:10.1242/dev.091844.
- Laemmli, U.K. 1970. Cleavage of structural proteins during the assembly of the head of bacteriophage T4. *Nature.* 227:680–685. doi:10.1038/227680a0.
- Lancaster, M. a., and J. a. Knoblich. 2014. Organogenesis in a dish: modeling development and disease using organoid technologies. *Science.* 345:1247125. doi:10.1126/science.1247125.
- Li, F., G. Ambrosini, E.Y. Chu, J. Plescia, S. Tognin, P.C. Marchisio, and D.C. Altieri. 1998. Control of apoptosis and mitotic spindle checkpoint by survivin. *Nature.* 396:580–584. doi:10.1038/25141.
- Li, L., X. Lin, A. Khvorova, S.W. Fesik, and Y.U. Shen. 2007. Defining the optimal parameters for hairpin-based knockdown constructs. *RNA.* 13:1765–1774. doi:10.1261/rna.599107.
- Liao, Q., F. Ozawa, H. Friess, A. Zimmermann, S. Takayama, J.C. Reed, J. Kleeff, and M.W. Büchler. 2001. The anti-apoptotic protein BAG-3 is overexpressed in pancreatic cancer and induced by heat stress in pancreatic cancer cell lines. *FEBS Lett.* 503. 503:151–157.
- Lim, S.T.S. 2013. Nuclear FAK: A new mode of gene regulation from cellular adhesions. *Mol. Cells.* 36:1–6. doi:10.1007/s10059-013-0139-1.

- Lin, R.-Z., L.-F. Chou, C.-C.M. Chien, and H.-Y. Chang. 2006. Dynamic analysis of hepatoma spheroid formation: roles of E-cadherin and β 1-integrin. *Cell Tissue Res.* 324:411–422. doi:10.1007/s00441-005-0148-2.
- Lin, R.Z., and H.Y. Chang. 2008. Recent advances in three-dimensional multicellular spheroid culture for biomedical research. *Biotechnol. J.* 3:1172–1184. doi:10.1002/biot.200700228.
- Lock, J.G., B. Wehrle-Haller, and S. Strömblad. 2008. Cell-matrix adhesion complexes: Master control machinery of cell migration. *Semin. Cancer Biol.* 18:65–76. doi:10.1016/j.semcancer.2007.10.001.
- Loessner, D., J. Flegg, H. Byrne, J. Clements, and D. Hutmacher. 2013. Growth of confined cancer spheroids: a combined experimental and mathematical modelling approach. *Integr. Biol. (Camb).* 5:597–605. doi:10.1039/c3ib20252f.
- Lorber, B., F. Fischer, M. Bailly, H. Roy, and D. Kern. 2012. Protein analysis by dynamic light scattering: Methods and techniques for students. *Biochem. Mol. Biol. Educ.* 40:372–382. doi:10.1002/bmb.20644.
- Luo, T.Z., K. Mohan, P.A. Iglesias, and D.N. Robinson. 2013. Molecular mechanisms of cellular mechanosensing. *Nat. Mater.* 12:1063–1070. doi:Doi 10.1038/Nmat3772.
- Macias, H., and L. Hinck. 2012. Mammary gland development. *Wiley Interdiscip. Rev. Dev. Biol.* 1:533–557. doi:10.1002/wdev.35.Mammary.
- Maiden, S.L., Y.I. Petrova, and B.M. Gumbiner. 2016. Microtubules inhibit E-cadherin adhesive activity by maintaining phosphorylated p120-catenin in a colon carcinoma cell model. *PLoS One.* 11:1–18. doi:10.1371/journal.pone.0148574.
- Marti, A., H. Lazar, P. Ritter, and R. Jaggi. 1999. Transcription factor activities and gene expression during mouse mammary gland involution. *J Mammary Gland Biol Neoplasia.* 4:145–152.
- Mary, S., S. Charrasse, M. Meriane, F. Comunale, P. Travo, A. Blangy, and C. Gauthier-Rouvière. 2002. Biogenesis of N-cadherin-dependent cell-cell contacts in living fibroblasts is a microtubule-dependent kinesin-driven mechanism. *Mol. Biol. Cell.* 13:285–301. doi:10.1091/mbc.01.
- Mathew, B., A. Schmitz, S. Muñoz-Descalzo, N. Ansari, F. Pampaloni, E.H.K. Stelzer, and S.C. Fischer. 2015. Robust and automated three-dimensional segmentation of densely packed cell nuclei in different biological specimens with Lines-of-Sight decomposition. *BMC Bioinformatics.* 16:187. doi:10.1186/s12859-015-0617-x.
- McLean, G.W., N.O. Carragher, E. Avizienyte, J. Evans, V.G. Brunton, and M.C. Frame. 2005. The role of focal-adhesion kinase in cancer - a new therapeutic opportunity. *Nat. Rev. Cancer.* 5:505–515. doi:10.1038/nrc1647.
- Meng, W., Y. Mushika, T. Ichii, and M. Takeichi. 2008. Anchorage of microtubule minus ends to adherens junctions regulates epithelial cell-cell contacts. *Cell.* 135:948–959. doi:10.1016/j.cell.2008.09.040.
- Meng, W., and M. Takeichi. 2009. Adherens junction: molecular architecture and regulation. *Cold Spring Harb. Perspect. Biol.* 1:a002899. doi:10.1101/cshperspect.a002899.
- Meng, X., D.-H. Kong, N. Li, Z.-H. Zong, B.-Q. Liu, Z.-X. Du, Y. Guan, L. Cao, and H.-Q. Wang. 2014. Knockdown of BAG3 induces epithelial-mesenchymal transition in thyroid cancer cells through ZEB1 activation. *Cell Death Dis.* 5:e1092. doi:10.1038/cddis.2014.32.
- Millard, M., S. Odde, and N. Neamati. 2011. Integrin targeted therapeutics. *Theranostics.* 1:154–88.
- Mills, J.W., E.M. Schwiebert, and B.A. Stanton. 1994. Evidence for the role of actin filaments in regulating cell swelling. *J. Exp. Zool.* 268:111–120. doi:10.1002/jez.1402680207.
- Mitra, S., S.-T. Lim, A. Chi, and D. Schlaepfer. 2006. Intrinsic focal adhesion kinase activity controls orthotopic breast carcinoma metastasis via the regulation of urokinase plasminogen activator expression in a syngeneic. *Oncogene.* 25:4429–4440. doi:10.1038/sj.onc.
- Mitra, S.K., D.A. Hanson, and D.D. Schlaepfer. 2005. Focal adhesion kinase: in command and control of cell motility. *Nat. Rev. Mol. Cell Biol.* 6:56–68. doi:10.1038/nrm1549.
- Miyoshi, H., U. Blömer, M. Takahashi, F.H. Gage, and I.M. Verma. 1998. Development of a self-inactivating lentivirus vector. *J. Virol.* 72:8150–8157.
- Monks, J., and P.M. Henson. 2009. Differentiation of the mammary epithelial cell during involution: implications for breast cancer. *J. Mammary Gland Biol. Neoplasia.* 14:159–170. doi:10.1007/s10911-

- 009-9121-0.
- Montel, F., M. Delarue, J. Elgeti, L. Malaquin, M. Basan, T. Risler, B. Cabane, D. Vignjevic, J. Prost, G. Cappello, and J.-F. Joanny. 2011. Stress clamp experiments on multicellular tumor spheroids. *Phys. Rev. Lett.* 107:188102. doi:10.1103/PhysRevLett.107.188102.
- Montel, F., M. Delarue, J. Elgeti, D. Vignjevic, G. Cappello, and J. Prost. 2012. Isotropic stress reduces cell proliferation in tumor spheroids. *New J. Phys.* 14:55008. doi:10.1088/1367-2630/14/5/055008.
- Morey, J.S., J.C. Ryan, and F.M. Van Dolah. 2006. Microarray validation: factors influencing correlation between oligonucleotide microarrays and real-time PCR. *Biol. Proced. Online.* 8:175–93. doi:10.1251/bpo126.
- Mueller-Klieser, W. 1984. Method for the determination of oxygen consumption rates and diffusion coefficients in multicellular spheroids. *Biophys. J.* 46:343–348. doi:10.1016/S0006-3495(84)84030-8.
- Murray, E., J.H. Cho, D. Goodwin, T. Ku, J. Swaney, S.Y. Kim, H. Choi, Y.G. Park, J.Y. Park, A. Hubbert, M. McCue, S. Vassallo, N. Bakh, M.P. Frosch, V.J. Wedeen, H.S. Seung, and K. Chung. 2015. Simple, scalable proteomic imaging for high-dimensional profiling of intact systems. *Cell.* 163:1500–1514. doi:10.1016/j.cell.2015.11.025.
- Murray, J.I., Z. Bao, T.J. Boyle, and R.H. Waterston. 2006. The lineaging of fluorescently-labeled *Caenorhabditis elegans* embryos with StarryNite and AceTree. *Nat. Protoc.* 1:1468–1476. doi:10.1038/nprot.2006.222.
- Naldini, L., U. Blomer, P. Gally, D. Ory, R. Mulligan, F.H. Gage, I.M. Verma, and D. Trono. 1996. In vivo gene delivery and stable transduction of post mitotic cells by a lentiviral vector. *Science (80-).* 272:263–267.
- Nederman, T., B. Glimelius, B. Norling, J. Carlsson, and U. Brunk. 1984. Demonstration of an extracellular matrix in multicellular tumor spheroids. *Cancer Res.* 44:3090–3097.
- Neelamegham, S., L.L. Munn, and K. Zygourakis. 1997. A model for the kinetics of homotypic cellular aggregation under static conditions. *Biophys. J.* 72:51–64. doi:10.1016/S0006-3495(97)78646-6.
- Nichols, M.G., and T.H. Foster. 1994. Oxygen diffusion and reaction kinetics in the photodynamic therapy of multicell tumour spheroids. *Phys. Med. Biol.* 39:2161–2181. doi:10.1088/0031-9155/39/12/003.
- Nourashrafeddin, S., M. Aarabi, M.H. Modarressi, M. Rahmati, and M. Nouri. 2015. The evaluation of WBP2NL-related genes expression in breast cancer. *Pathol. Oncol. Res.* 21:293–300. doi:10.1007/s12253-014-9820-8.
- O'Brien, L.E., T.S. Jou, A.L. Pollack, Q. Zhang, S.H. Hansen, P. Yurchenco, and K.E. Mostov. 2001. Rac1 orientates epithelial apical polarity through effects on basolateral laminin assembly. *Nat. Cell Biol.* 3:831–838. doi:10.1038/ncb0901-831.
- Oldenhof, A.D., O.P. Shynlova, M. Liu, B.L. Langille, and S.J. Lye. 2002. Mitogen-activated protein kinases mediate stretch-induced c-fos mRNA expression in myometrial smooth muscle cells. *Am J Physiol Cell Physiol.* 283:C1530–C1539. doi:10.1152/ajpcell.00607.2001.
- Otsu, N. 1979. A threshold selection method from gray-level histograms. *IEEE Trans. Syst. Man. Cybern.* 9:62–66. doi:10.1109/TSMC.1979.4310076.
- Ott, S.R. 2008. Confocal microscopy in large insect brains: Zinc–formaldehyde fixation improves synapsin immunostaining and preservation of morphology in whole-mounts. *J. Neurosci. Methods.* 172:220–230. doi:10.1016/j.jneumeth.2008.04.031.
- Ouderkirk, J.L., and M. Krendel. 2014. Non-muscle myosins in tumor progression, cancer cell invasion, and metastasis. *Cytoskeleton.* 71:447–463. doi:10.1002/cm.21187.
- Page-McCaw, A., A.J. Ewald, and Z. Werb. 2007. Matrix metalloproteinases and the regulation of tissue remodelling. *Nat. Rev. Mol. Cell Biol.* 8:221–233. doi:10.1038/nrm2125.
- Pampaloni, F., N. Ansari, and E.H. Stelzer. 2013. High-resolution deep imaging of live cellular spheroids with light-sheet-based fluorescence microscopy. *Cell Tissue Res.* 352:161–177. doi:10.1007/s00441-013-1589-7.
- Pampaloni, F., B. Mayer, K. Kabat Vel-Job, N. Ansari, K. Hötte, D. Kögel, and E.H.K. Stelzer. 2017. A novel cellular spheroid-based autophagy screen applying live fluorescence microscopy identified nonactin as

- a strong inducer of autophagosomal turnover. *SLAS Discov.* doi:10.1177/2472555217696798.
- Pampaloni, F., E.G. Reynaud, and E.H.K. Stelzer. 2007. The third dimension bridges the gap between cell culture and live tissues. *Nat. Rev. Mol. Cell Biol.* 8:839–845.
- Pampaloni, F., R. Richa, N. Ansari, and E.H.K. Stelzer. 2015. Live Spheroid Formation Recorded with Light Sheet-Based Fluorescence Microscopy. In *Advanced Fluorescence Microscopy*. Humana Press, New York, NY. 43–57.
- Pampaloni, F., E.H.K. Stelzer, S. Leicht, and M. Marcello. 2010. Madin-Darby canine kidney cells are increased in aerobic glycolysis when cultured on flat and stiff collagen-coated surfaces rather than in physiological 3-D cultures. *Proteomics*. 10:3394–3413. doi:10.1002/pmic.201000236.
- Paszek, M.J., N. Zahir, K.R. Johnson, J.N. Lakins, G.I. Rozenberg, A. Gefen, C.A. Reinhart-King, S.S. Margulies, M. Dembo, D. Boettiger, D.A. Hammer, and V.M. Weaver. 2005. Tensional homeostasis and the malignant phenotype. *Cancer Cell*. 8:241–254. doi:10.1016/j.ccr.2005.08.010.
- Paten, A.M., E.J. Duncan, S.J. Pain, S.W. Peterson, P.R. Kenyon, H.T. Blair, and P.K. Dearden. 2015. Functional development of the adult ovine mammary gland—insights from gene expression profiling. *BMC Genomics*. 16:748. doi:10.1186/s12864-015-1947-9.
- Paulus, W., C. Huettner, and J.C. Tonn. 1994. Collagens, integrins and the mesenchymal drift in glioblastomas: A comparison of biopsy specimens, spheroid and early monolayer cultures. *Int. J. Cancer*. 58:841–846. doi:10.1002/ijc.2910580616.
- Pawson, T., and J. Schlessinger. 1993. SH2 and SH3 domains. *Curr. Opin. Struct. Biol.* 3:434–442. doi:10.1016/0959-440X(92)90235-Y.
- Pedersen, S., E. Hoffmann, and J. Mills. 2001. The cytoskeleton and cell volume regulation. *Comp. Biochem. Physiol. Part A Mol. Integr. Physiol.* 130:385–399. doi:10.1016/S1095-6433(01)00429-9.
- Pensa, S., B. Lloyd-Lewis, T.J. Sargeant, H.K. Resemann, C.R. Kahn, and C.J. Watson. 2014. Signal transducer and activator of transcription 3 and the phosphatidylinositol 3-kinase regulatory subunits p55alpha and p50alpha regulate autophagy in vivo. *FEBS J.* 281:4557–4567. doi:10.1111/febs.13035.
- Peters, B.P., R.J. Hartle, R.F. Krzesicki, T.G. Kroll, F. Perini, J.E. Balun, I.J. Goldstein, and R.W. Ruddon. 1985. The biosynthesis, processing, and secretion of laminin by human choriocarcinoma cells. *J. Biol. Chem.* 260:14732–42.
- Philip, J.T., and K.N. Dahl. 2008. Nuclear mechanotransduction: Response of the lamina to extracellular stress with implications in aging. *J. Biomech.* 41:3164–3170. doi:10.1016/j.jbiomech.2008.08.024.
- Playford, M.P., K. Vadali, X. Cai, K. Burrige, and M.D. Schaller. 2008. Focal Adhesion Kinase regulates cell-cell contact formation in epithelial cells via modulation of Rho. *Exp. Cell Res.* 314:3187–3197. doi:10.1016/j.yexcr.2008.08.010.
- Pollard, T.D., W.C. Earnshaw, J. Lippincott-Schwartz, and G.T. Johnson. 2017. *Cell biology*. Elsevier, Philadelphia.
- Porter, K.M., N. Jeyabalan, and P.B. Liton. 2014. MTOR-independent induction of autophagy in trabecular meshwork cells subjected to biaxial stretch. *Biochim. Biophys. Acta.* 1843:1054–1062. doi:10.1016/j.bbamcr.2014.02.010.
- Preibisch, S., F. Amat, E. Stamatakis, M. Sarov, R.H. Singer, E. Myers, and P. Tomancak. 2014. Efficient Bayesian-based multiview deconvolution. *Nat. Methods*. 11:645–8. doi:10.1038/nmeth.2929.
- Preibisch, S., S. Saalfeld, J. Schindelin, and P. Tomancak. 2010. Software for bead-based registration of selective plane illumination microscopy data. *Nat. Methods*. 7:418–419. doi:10.1038/nmeth0610-418 10.1038/NMETH.F.304.
- Quaglino, A., M. Salierno, J. Pellegrotti, N. Rubinstein, and E.C. Kordon. 2009. Mechanical strain induces involution-associated events in mammary epithelial cells. *BMC Cell Biol.* 10:55. doi:10.1186/1471-2121-10-55.
- Quarrie, L.H., C.V.P. Addey, and C.J. Wilde. 1996. Programmed cell death during mammary tissue involution induced by weaning, litter removal, and milk stasis. *J. Cell. Physiol.* 168:559–569.
- Rapino, F., M. Jung, and S. Fulda. 2014. BAG3 induction is required to mitigate proteotoxicity via selective autophagy following inhibition of constitutive protein degradation pathways. *Oncogene*. 33:1713–

1724. doi:10.1038/onc.2013.110.
- Ratheesh, A., and A.S. Yap. 2012. A bigger picture: classical cadherins and the dynamic actin cytoskeleton. *Nat. Rev. Mol. Cell Biol.* 13:673–679. doi:10.1038/nrm3431.
- Redlich, M., H. Roos, E. Reichenberg, B. Zaks, A. Grosskop, I. Bar Kana, S. Pitaru, and A. Palmon. 2004. The effect of centrifugal force on mRNA levels of collagenase, collagen type-I, tissue inhibitors of metalloproteinases and beta-actin in cultured human periodontal ligament fibroblasts. *J. Periodontal Res.* 39:27–32. doi:10.1111/j.1600-0765.2004.00700.x.
- Ricca, B.L., G. Venugopalan, and D.A. Fletcher. 2013. To pull or be pulled: Parsing the multiple modes of mechanotransduction. *Curr. Opin. Cell Biol.* 25:558–564. doi:10.1016/j.ceb.2013.06.002.
- Richert, M.M., K.L. Schwertfeger, J.W. Ryder, and S.M. Anderson. 2000. An atlas of mouse mammary gland development. *J. Mammary Gland Biol. Neoplasia.* 5:227–241.
- Ridley, A.J., M.A. Schwartz, K. Burridge, R.A. Firtel, M.H. Ginsberg, G. Borisy, J.T. Parsons, and A.R. Horwitz. 2003. Cell migration: integrating signals from front to back. *Science.* 302:1704–9. doi:10.1126/science.1092053.
- Ries, J., C. Kaplan, E. Platonova, H. Eghlidi, and H. Ewers. 2012. A simple, versatile method for GFP-based microscopy via nanobodies. *Nat. Methods.* 9:582–584. doi:10.1038/nmeth.1991.
- Rodriguez-Boulan, E., and I.G. Macara. 2014. Organization and execution of the epithelial polarity programme. *Nat. Rev. Mol. Cell Biol.* 15:225–242. doi:10.1038/nrm3775.
- Rosati, A., V. Graziano, V. De Laurenzi, M. Pascale, and M.C. Turco. 2011. BAG3: a multifaceted protein that regulates major cell pathways. *Cell Death Dis.* 2:e141. doi:10.1038/cddis.2011.24.
- Rossi, A., Z. Kontarakis, C. Gerri, H. Nolte, S. Hölper, M. Krüger, and D.Y.R. Stainier. 2015. Genetic compensation induced by deleterious mutations but not gene knockdowns. *Nature.* Aug 13:230–3. doi:10.1038/nature14580.
- Rothbauer, U., K. Zolghadr, S. Tillib, D. Nowak, L. Schermelleh, A. Gahl, N. Backmann, K. Conrath, S. Muyltermans, M.C. Cardoso, and H. Leonhardt. 2006. Targeting and tracing antigens in live cells with fluorescent nanobodies. *Nat. Methods.* 3:887–9. doi:10.1038/nmeth953.
- Rubio-Guivernau, J.L., V. Gurchenkov, M.A. Luengo-Oroz, L. Duloquin, P. Bourguine, A. Santos, N. Peyrieras, and M.J. Ledesma-Carbayo. 2012. Wavelet-based image fusion in multi-view three-dimensional microscopy. *Bioinformatics.* 28:238–245. doi:10.1093/bioinformatics/btr609.
- Russo, I.H., and J. Russo. 1996. Mammary Gland Neoplasia in Long-Term Rodent Studies. *Environ. Health Perspect.* 104:938–967.
- Saias, L., A. Gomes, M. Cazales, B. Ducommun, and V. Lobjois. 2015. Cell-cell adhesion and cytoskeleton tension oppose each other in regulating tumor cell aggregation. *Cancer Res.* 75:2426–2433. doi:10.1158/0008-5472.CAN-14-3534.
- Samson, F., J.A. Donoso, I. Heller-Bettinger, D. Watson, and R.H. Himes. 1979. Nocodazole action on tubulin assembly, axonal ultrastructure and fast axoplasmic transport. *J. Pharmacol. Exp. Ther.* 208:411–417.
- Schedin, P., and P.J. Keely. 2011. Mammary gland ECM remodelling, stiffness, and mechanosignaling in normal development and tumor progression. *Cold Spring Harb. Perspect. Biol.* 3:a003228. doi:10.1101/cshperspect.a003228.
- Schlaepfer, D., C. Hauck, and D. Sieg. 1999. Signaling through focal adhesion kinase. *Prog. Biophys. Mol. Biol.* 71:435–478.
- Schmitz, A., S.C. Fischer, C. Mattheyer, F. Pampaloni, and E.H.K. Stelzer. 2017. Multiscale image analysis reveals structural heterogeneity of the cell microenvironment in homotypic spheroids. *Sci. Rep.* 7:43693. doi:10.1038/srep43693.
- Schnell, U., F. Dijk, K.A. Sjollem, and B.N.G. Giepmans. 2012. Immunolabeling artifacts and the need for live-cell imaging. *Nat. Methods.* 9:152–8. doi:10.1038/nmeth.1855.
- Semino, C.E., J.R. Merok, G.G. Crane, G. Panagiotakos, and S. Zhang. 2003. Functional differentiation of hepatocyte-like spheroid structures from putative liver progenitor cells in three-dimensional peptide scaffolds. *Differentiation.* 71:262–270. doi:10.1046/j.1432-0436.2003.7104503.x.

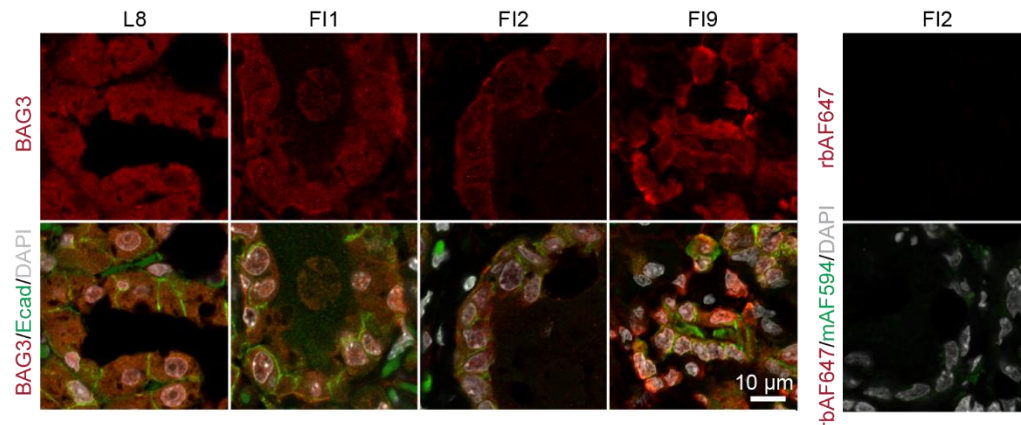
- Seo, J., M. Choe, and S.-Y. Kim. 2016. Clearing and labeling techniques for large-scale biological tissues. *Mol. Cells*. 39:439–446. doi:10.14348/molcells.2016.0088.
- Shapiro, a L., E. Viñuela, and J. V Maizel. 1967. Molecular weight estimation of polypeptide chains by electrophoresis in SDS-polyacrylamide gels. *Biochem. Biophys. Res. Commun.* 28:815–820. doi:10.1016/0006-291X(67)90391-9.
- Shi, H., H. Xu, Z. Li, Y. Zhen, B. Wang, S. Huo, R. Xiao, and Z. Xu. 2016. BAG3 regulates cell proliferation, migration, and invasion in human colorectal cancer. *Tumor Biol.* 37:5591–5597. doi:10.1007/s13277-015-4403-1.
- Sieminski, A.L., A.S. Was, G. Kim, H. Gong, and R.D. Kamm. 2007. The stiffness of three-dimensional ionic self-assembling peptide gels affects the extent of capillary-like network formation. *Cell Biochem. Biophys.* 49:73–83. doi:10.1007/s12013-007-0046-1.
- Silanikove, N. 2014. Natural and abrupt involution of the mammary gland affects differently the metabolic and health consequences of weaning. *Life Sci.* 102:10–15. doi:10.1016/j.lfs.2014.02.034.
- Slack-Davis, J.K., K.H. Martin, R.W. Tilghman, M. Iwanicki, E.J. Ung, C. Autry, M.J. Luzzio, B. Cooper, J.C. Kath, W.G. Roberts, and J.T. Parsons. 2007. Cellular characterization of a novel focal adhesion kinase inhibitor. *J. Biol. Chem.* 282:14845–14852. doi:10.1074/jbc.M606695200.
- Slack, J.K., R.B. Adams, J.D. Rovin, E.A. Bissonette, C.E. Stoker, and J.T. Parsons. 2001. Alterations in the focal adhesion kinase/Src signal transduction pathway correlate with increased migratory capacity of prostate carcinoma cells. *Oncogene.* 20:1152–1163. doi:10.1038/sj.onc.1204208.
- Smalley, M.J., J.S. Reis-Filho, and A. Ashworth. 2008. BRCA1 and stem cells: tumour typecasting. *Nat. Cell Biol.* 10:377–379. doi:10.1038/ncb0408-377.
- Smolle, J., R. Hofmann-Wellenhof, H.P. Soyer, H. Stettner, and H. Kerl. 1989. Nuclear size and shape parameters correlate with proliferative activity in cutaneous melanocytic tumors. *J. Invest. Dermatol.* 93:178–82. doi:10.1111/1523-1747.ep12277396.
- Smyrek, I., and E.H.K. Stelzer. 2017. Quantitative three-dimensional evaluation of immunofluorescence staining for large whole mount spheroids with light sheet microscopy. *Biomed. Opt. Express.* 8:484–499. doi:10.1364/BOE.8.000484.
- Stehbens, S.J., A.D. Paterson, M.S. Crampton, A.M. Shewan, C. Ferguson, A. Akhmanova, R.G. Parton, and A.S. Yap. 2006. Dynamic microtubules regulate the local concentration of E-cadherin at cell-cell contacts. *J Cell Sci.* 119:1801–1811. doi:10.1242/jcs.02903.
- Stelzer, E.H.K. 2015. Light-sheet fluorescence microscopy for quantitative biology. *Nat. Publ. Gr.* 12:23–26. doi:10.1038/nmeth.3219.
- Strobl, F., S. Klees, and E.H.K. Stelzer. 2017. Light sheet-based fluorescence microscopy of living or fixed and stained *Tribolium castaneum* embryos. *J. Vis. Exp.* e55629–e55629. doi:10.3791/55629.
- Strobl, F., A. Schmitz, and E.H.K. Stelzer. 2015. Live imaging of *Tribolium castaneum* embryonic development using light-sheet-based fluorescence microscopy. *Nat. Protoc.* 10:1486–1507. doi:10.1038/nprot.2015.093.
- Suh, E.J., M.Y. Remillard, A. Legesse-Miller, E.L. Johnson, J.M.S. Lemons, T.R. Chapman, J.J. Forman, M. Kojima, E.S. Silberman, and H.A. Collier. 2012. A microRNA network regulates proliferative timing and extracellular matrix synthesis during cellular quiescence in fibroblasts. *Genome Biol.* 13:R121. doi:10.1186/gb-2012-13-12-r121.
- Susaki, E.A., K. Tainaka, D. Perrin, F. Kishino, T. Tawara, T.M. Watanabe, C. Yokoyama, H. Onoe, M. Eguchi, S. Yamaguchi, T. Abe, H. Kiyonari, Y. Shimizu, A. Miyawaki, H. Yokota, and H.R. Ueda. 2014. Whole-brain imaging with single-cell resolution using chemical cocktails and computational analysis. *Cell.* 157:726–739. doi:10.1016/j.cell.2014.03.042.
- Sutherland, R.M. 1988. Cell and environment interactions in tumor microregions: the multicell spheroid model. *Science (80-)*. 240:177–240.
- Sutherland, R.M., B. Sordat, J. Bamat, H. Gabbert, B. Bourrat, and W. Mueller-Klieser. 1986. Oxygenation and differentiation in multicellular spheroids of human colon carcinoma. *Cancer Res.* 46:5320–5329.
- Suzuki, M., M. Iwasaki, A. Sugio, A. Hishiya, R. Tanaka, T. Endo, S. Takayama, and T. Saito. 2011. BAG3 (BCL2-associated athanogene 3) interacts with MMP-2 to positively regulate invasion by ovarian

- carcinoma cells. *Cancer Lett.* 303:65–71. doi:10.1016/j.canlet.2011.01.019.
- Swoger, J., P. Verveer, K. Greger, J. Huisken, and E.H.K. Stelzer. 2007. Multi-view image fusion improves resolution in three-dimensional microscopy. *Opt. Express.* 15:8029. doi:10.1364/OE.15.008029.
- Takeichi, M. 1991. Cadherin cell adhesion receptors as a morphogenetic regulator. *Science.* 251:1451–1455. doi:10.1126/science.2006419.
- Tancioni, I., N.L.G. Miller, S. Uryu, C. Lawson, C. Jean, X.L. Chen, E.G. Kleinschmidt, and D.D. Schlaepfer. 2015. FAK activity protects nucleostemin in facilitating breast cancer spheroid and tumor growth. *Breast Cancer Res.* 17:47. doi:10.1186/s13058-015-0551-x.
- Tanjoni, I., C. Walsh, S. Uryu, A. Tomar, J.-O. Nam, A. Mielgo, S.-T. Lim, C. Liang, M. Koenig, N. Patel, C. Kwok, G. McMahon, D.G. Stupack, and D.D. Schlaepfer. 2010. PND-1186 FAK inhibitor selectively promotes tumor cell apoptosis in three-dimensional environments. *Cancer Biol. Ther.* 9:746–777. doi:10.1038/nature09421.Oxidative.
- Teplova, I., F. Lozy, S. Price, S. Singh, N. Barnard, R.D. Cardiff, R.B. Birge, and V. Karantza. 2013. ATG proteins mediate efferocytosis and suppress inflammation in mammary involution. *Autophagy.* 9:459–475. doi:10.4161/auto.23164.
- Timmins, N.E., F.J. Harding, C. Smart, M.A. Brown, and L.K. Nielsen. 2005. Method for the generation and cultivation of functional three-dimensional mammary constructs without exogenous extracellular matrix. *Cell Tissue Res.* 320:207–210. doi:10.1007/s00441-004-1064-6.
- Tomer, R., K. Khairy, F. Amat, and P.J. Keller. 2012. Quantitative high-speed imaging of entire developing embryos with simultaneous multiview light-sheet microscopy. *Nat. Methods.* 9:755–63. doi:10.1038/nmeth.2062.
- Tomer, R., L. Ye, B. Hsueh, and K. Deisseroth. 2014. Advanced CLARITY for rapid and high-resolution imaging of intact tissues. *Nat. Protoc.* 9:1682–97. doi:10.1038/nprot.2014.123.
- Truong, T. V., W. Supatto, D.S. Koos, J.M. Choi, and S.E. Fraser. 2011. Deep and fast live imaging with two-photon scanned light-sheet microscopy. *Nat. Methods.* 8:757–760. doi:10.1038/nmeth.1652.
- Tuchin, V. V. 2015. Tissue optics and photonics: light-tissue interaction. *J. Biomed. Photonics Eng.* 1:98–134. doi:10.18287/JBPE-2015-1-2-98.
- Tzanakakis, E.S., L.K. Hansen, and W.S. Hu. 2001. The role of actin filaments and microtubules in hepatocyte spheroid self-assembly. *Cell Motil. Cytoskeleton.* 48:175–189. doi:10.1002/1097-0169(200103)48:3<175::AID-CM1007>3.0.CO;2-2.
- Ulbricht, A., V. Arndt, and J. Höhfeld. 2013a. Chaperone-assisted proteostasis is essential for mechanotransduction in mammalian cells. *Commun. Integr. Biol.* 6:e24925. doi:10.4161/cib.24925.
- Ulbricht, A., F.J. Eppler, V.E. Tapia, P.F.M. Van Der Ven, N. Hampe, N. Hersch, P. Vakeel, D. Stadel, A. Haas, P. Saftig, C. Behrends, D.O. Fürst, R. Volkmer, B. Hoffmann, W. Kolanus, and J. Höhfeld. 2013b. Cellular mechanotransduction relies on tension-induced and chaperone-assisted autophagy. *Curr. Biol.* 23:430–435. doi:10.1016/j.cub.2013.01.064.
- Ulbricht, A., S. Gehlert, B. Leciejewski, T. Schiffer, W. Bloch, and J. Höhfeld. 2015. Induction and adaptation of chaperone-assisted selective autophagy CASA in response to resistance exercise in human skeletal muscle. *Autophagy.* 11:538–546. doi:10.1080/15548627.2015.1017186.
- Ulbricht, A., and J. Höhfeld. 2013. Tension-induced autophagy: May the chaperone be with you. *Autophagy.* 9:920–922. doi:10.4161/auto.24213 10.1016/j.cub.2013.01.064.
- Vasioukhin, V., and E. Fuchs. 2001. Actin dynamics and cell-cell adhesion in epithelia. *Curr. Opin. Cell Biol.* 13:76–84. doi:10.1016/S0955-0674(00)00177-0.
- Vestweber, D., and R. Kemler. 1985. Identification of a putative cell adhesion domain of uvomorulin. *EMBO J.* 4:3393–3398.
- Vicente-Manzanares, M., and a. R. Horwitz. 2011. Adhesion dynamics at a glance. *J. Cell Sci.* 124:3923–3927. doi:10.1242/jcs.095653.
- Wang, H., S. Lacoche, L. Huang, B. Xue, and S.K. Muthuswamy. 2013. Rotational motion during three-dimensional morphogenesis of mammary epithelial acini relates to laminin matrix assembly. *Proc. Natl. Acad. Sci. U. S. A.* 110:163–168. doi:10.1073/pnas.1201141110.

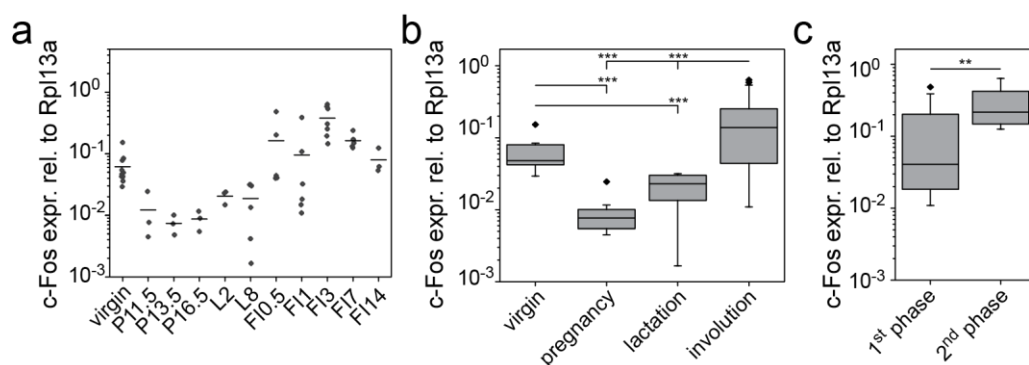
- Waterman-Storer, C.M., W.C. Salmon, and E.D. Salmon. 2000. Feedback interactions between cell-cell adherens junctions and cytoskeletal dynamics in newt lung epithelial cells. *Mol. Biol. Cell.* 11:2471–2483. doi:10.1091/mbc.11.7.2471.
- Watson, C.J. 2006. Key stages in mammary gland development Involution : apoptosis and tissue remodelling that convert the mammary gland from milk factory to a quiescent organ. 5:1–5. doi:10.1186/bcr1401.
- Watson, C.J., and W.T. Khaled. 2008. Mammary development in the embryo and adult: a journey of morphogenesis and commitment. *Development.* 135:995–1003. doi:10.1242/dev.005439.
- Watson, C.J., and P.A. Kreuzaler. 2011. Remodeling mechanisms of the mammary gland during involution. *Int. J. Dev. Biol.* 55:757–762. doi:10.1387/ijdb.113414cw.
- Weber, K., U. Bartsch, C. Stocking, and B. Fehse. 2008. A multicolor panel of novel lentiviral “gene ontology” (LeGO) vectors for functional gene analysis. *Mol. Ther.* 16:698–706. doi:10.1038/mt.2008.6.
- Weiswald, L.-B., D. Bellet, and V. Dangles-Marie. 2015. Spherical cancer models in tumor biology. *Neoplasia.* 17:1–15. doi:10.1016/j.neo.2014.12.004.
- Weiswald, L.B., J.M. Guinebretiere, S. Richon, D. Bellet, B. Saubamea, and V. Dangles-Marie. 2010. In situ protein expression in tumour spheres: development of an immunostaining protocol for confocal microscopy. *BMC Cancer.* 10:106. doi:10.1186/1471-2407-10-106.
- Wendt, M.K., M.A. Taylor, B.J. Schieman, and W.P. Schieman. 2011. Down-regulation of epithelial cadherin is required to initiate metastatic outgrowth of breast cancer. *Mol. Biol. Cell.* 22:2423–2435. doi:10.1091/mbc.E11-04-0306.
- Wenzel, C., B. Riefke, S. Gründemann, A. Krebs, S. Christian, F. Prinz, M. Osterland, S. Golfier, S. Räse, N. Ansari, M. Esner, M. Bickle, F. Pampaloni, C. Mattheyer, E.H. Stelzer, K. Parczyk, S. Prechtel, and P. Steigemann. 2014. 3D high-content screening for the identification of compounds that target cells in dormant tumor spheroid regions. *Exp. Cell Res.* 323:131–143. doi:10.1016/j.yexcr.2014.01.017.
- Wilde, C.J., C.H. Knight, and D.J. Flint. 1999. Control of milk secretion and apoptosis during mammary involution. *J. Mammary Gland Biol. Neoplasia.* 4:129–136.
- Xian, W., K.L. Schwertfeger, T. Vargo-gogola, and J.M. Rosen. 2005. Pleiotropic effects of FGFR1 on cell proliferation, survival, and migration in a 3D mammary epithelial cell model. *J. Cell Biol.* 171:663–673. doi:10.1083/jcb.200505098.
- Xu, C., Y. Hao, B. Wei, J. Ma, J. Li, Q. Huang, and F. Zhang. 2011. Apoptotic gene expression by human periodontal ligament cells following cyclic stretch. *J. Periodontal Res.* 46:742–748. doi:10.1111/j.1600-0765.2011.01397.x.
- Yamada, K.M., R. Pankov, and E. Cukierman. 2003. Dimensions and dynamics in integrin function. *Brazilian J. Med. Biol. Res.* 36:959–966. doi:10.1590/S0100-879X2003000800001.
- Yano, H., Y. Mazaki, K. Kurokawa, S.K. Hanks, M. Matsuda, and H. Sabe. 2004. Roles played by a subset of integrin signaling molecules in cadherin-based cell-cell adhesion. *J. Cell Biol.* 166:283–295. doi:10.1083/jcb.200312013.
- Ying, B., H. Fan, F. Wen, D. Xu, D. Liu, D. Yang, G. Chen, L. Dou, and F. Jiang. 2006. Mechanical strain-induced c-fos expression in pulmonary epithelial cell line A549. *Biochem. Biophys. Res. Commun.* 347:369–372. doi:10.1016/j.bbrc.2006.06.105.
- Yoshii, Y., A. Waki, K. Yoshida, A. Kakezuka, M. Kobayashi, H. Namiki, Y. Kuroda, Y. Kiyono, H. Yoshii, T. Furukawa, T. Asai, H. Okazawa, J.G. Gelovani, and Y. Fujibayashi. 2011. The use of nanoimprinted scaffolds as 3D culture models to facilitate spontaneous tumor cell migration and well-regulated spheroid formation. *Biomaterials.* 32:6052–6058. doi:10.1016/j.biomaterials.2011.04.076.

7 Supplement

7.1 BAG3 in the mammary gland and in mammary epithelial cells

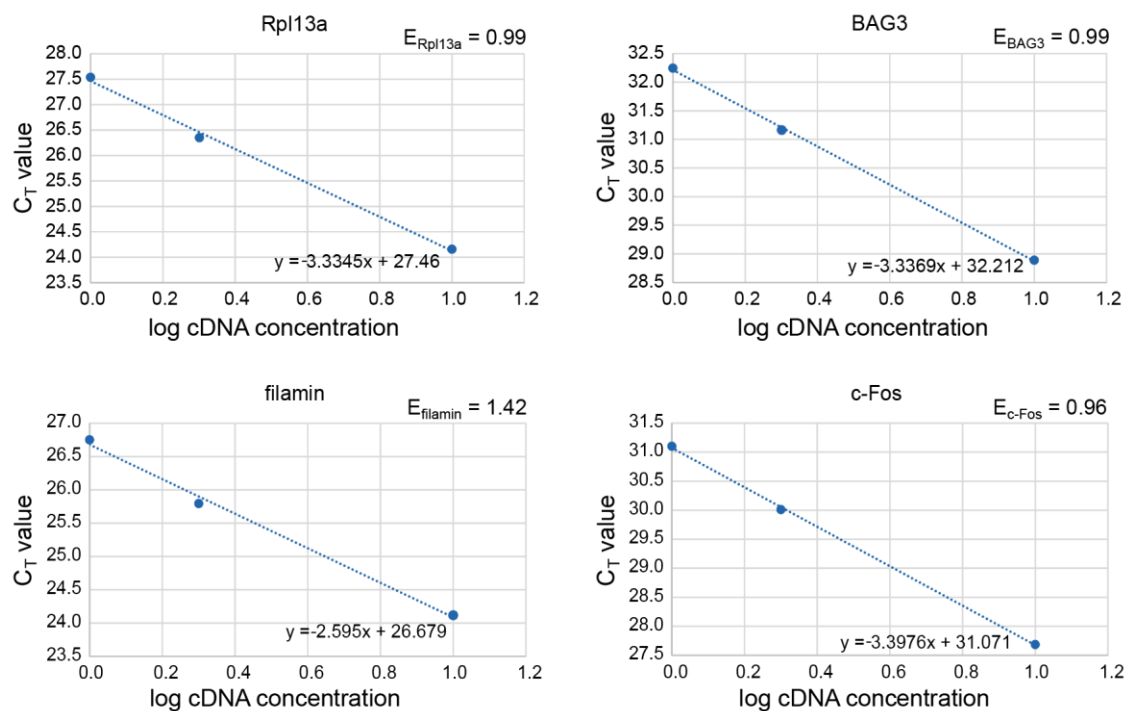


Supplemental Figure 7-1 BAG3 localization in the mammary gland. BAG3 shows a cytoplasmic localization during lactation (L8), early (F11 and F12) and late (F19) forced involution. Histological sections of murine mammary glands were stained with BAG3 and anti-rabbit AF647, and E-cadherin and anti-mouse AF594 antiserum. The right panel shows the negative control without primary antibody. Cell nuclei were stained with DAPI. Microscope: Zeiss LSM780, objective lens: Plan-Apochromat 63x/NA 1.4, scale bar: 10 μ m.



Supplemental Figure 7-2 Gene expression analysis of c-Fos in the developing mammary gland. RNA was extracted from mammary gland #4 of mice in different developmental stages. RNA was transcribed into cDNA, which was then used for qPCR with Taqman primer to detect c-Fos mRNA expression in all investigated time points of development. (a) The dots represent data from individual mice, and the lines show the mean values. (b) c-Fos mRNA expression in four phases of mammary gland development. Data were pooled from the time points that contribute to a developmental phase. (c) c-Fos expression in the first and second phase of involution. FI0.5 and FI1 were pooled to represent the first phase, and FI2 and FI7 are within the second phase of forced involution. Boxplot parameters: the box contains 50% of the data points, the middle line is the median, whiskers and outliers represent the upper and lower 25% of the data. Outliers are outside the 1.5x interquartile range. \blacklozenge , outliers. Statistics: Mann-Whitney test with Bonferroni correction for multiple comparison (** $p < 0.01$, *** $p < 0.001$). P: pregnancy, L: lactation, FI: forced involution.

In addition to BAG3, c-Fos expression levels were analyzed. The proto-oncogene c-Fos is involved in both processes, mammary gland involution (Marti et al., 1999) and the cellular response to mechanical stress (Komuro et al., 1990; Ying et al., 2006). The relative quantification of c-Fos expression in mammary gland samples served as a positive control for the entire experiment. The expression profile of c-Fos resembled the BAG3 profile. During virginity, its mean expression was 0.06, which dropped by a factor of about six to eight during pregnancy. C-Fos expression increased during the lactation phase (0.02 in L2 and L8), but did not reach the values of the virgin mammary gland. When involution was induced, c-Fos expression rapidly increased within the first 12 hours and was about 13.5-fold stronger compared to 8 days lactating mice. This peaked at day 3 of involution with a 28-fold induction compared to the lactating mice. Compared to the virgin gland, however, the induction at day 3 of involution was approximately six-fold less compared to the lactation phase. After 14 days of involution, the relative c-Fos expression decreased to a value of about 0.08, which was similar to the virgin mammary gland (Supplemental Figure 7-2a). Analysis of c-Fos expression in the four developmental stages revealed that the drop of c-Fos expression between virgin and pregnant glands was significant ($p < 0.001$). The reoccurring expression during lactation was still lower compared to the virgin gland ($p < 0.001$). The expression of c-Fos during the involution phases was comparable to the virgin gland but was significantly increased compared to pregnant and lactating glands ($p < 0.001$, Supplemental Figure 7-2b). The discrimination of c-Fos expression in the two phases of mammary gland involution showed a significant expression in the second phase compared to the first phase ($p < 0.01$, Supplemental Figure 7-2c).



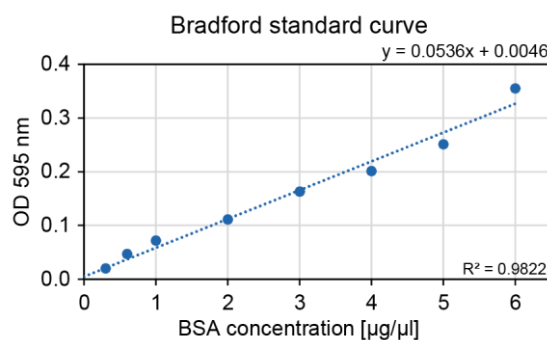
Supplemental Figure 7-3 Efficiency of Taqman primer for qPCR. Murine cDNA was used in three different concentrations with the respective Taqman primer. Samples ran in duplicates. The efficiency is

calculated from the slope of the linear fit when the threshold values (CT) is plotted against the logarithm of the cDNA concentration. $E = 10^{\left(\frac{1}{-slope}\right)} - 1$.

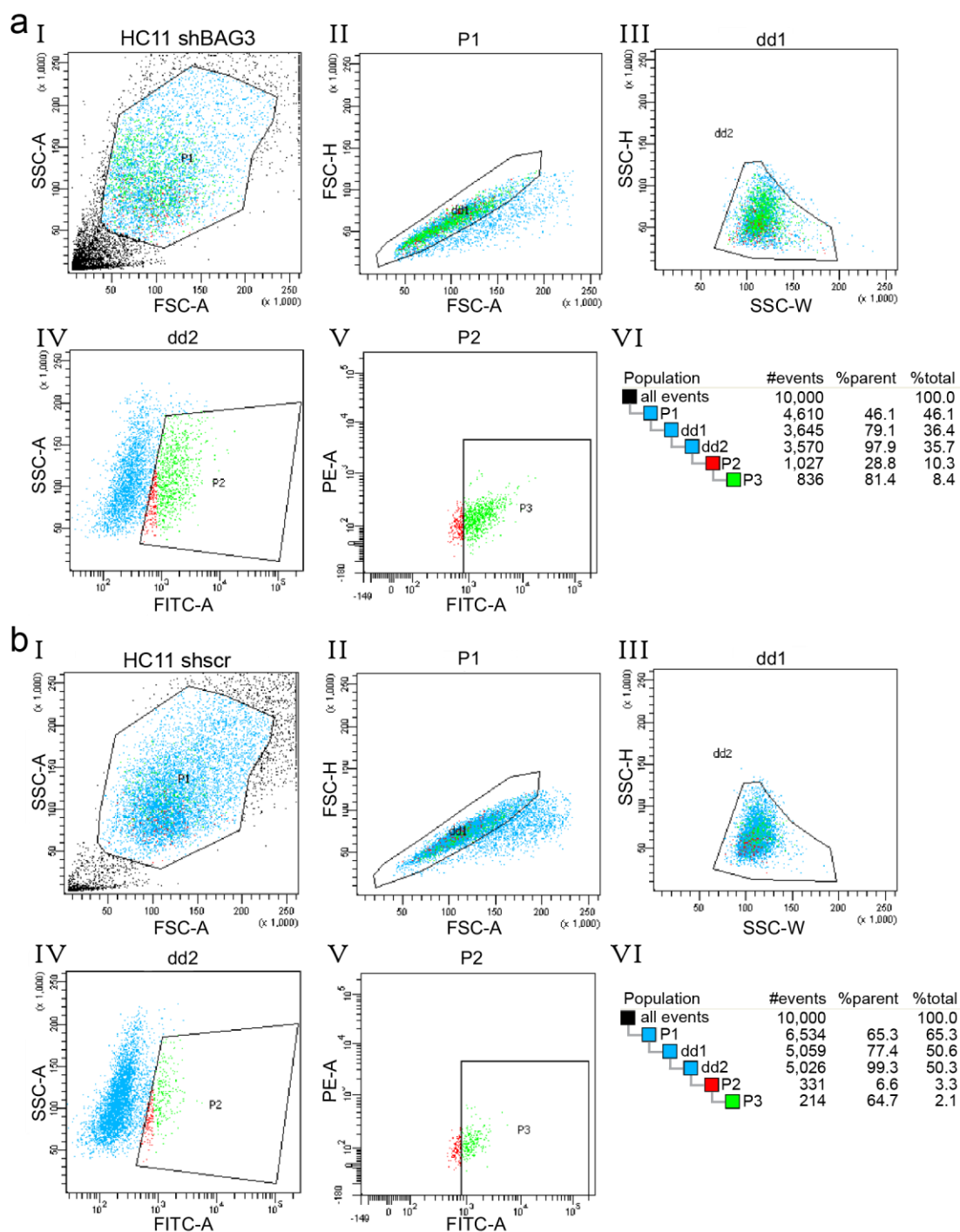
Supplemental Table 7-1 Descriptive statistics of the relative mRNA expression data from murine mammary glands. Experiments were run in triplicates from the indicated number of mice (n). The mean, median, standard deviation and SEM are shown for BAG3 and c-Fos for each developmental time point.

	n	BAG3				c-Fos			
		mean	median	SD	SEM	mean	median	SD	SEM
Virgin	12	0.192	0.137	0.118	0.034	0.062	0.048	0.034	0.010
P11.5	3	0.032	0.036	0.016	0.009	0.012	0.008	0.011	0.006
P13.5	3	0.022	0.022	0.001	0.001	0.007	0.007	0.003	0.002
P16.5	3	0.020	0.016	0.010	0.006	0.009	0.009	0.003	0.002
L2	3	0.050	0.048	0.007	0.004	0.021	0.023	0.005	0.003
L8	6	0.079	0.082	0.073	0.030	0.019	0.022	0.014	0.006
FI 0.5	5	0.207	0.144	0.212	0.095	0.162	0.044	0.193	0.086
FI 1	6	0.299	0.195	0.275	0.112	0.096	0.025	0.148	0.061
FI 3	7	0.425	0.356	0.193	0.073	0.380	0.305	0.202	0.076
FI 7	5	0.233	0.212	0.056	0.025	0.163	0.149	0.046	0.020
FI 14	3	0.142	0.161	0.052	0.030	0.080	0.062	0.038	0.022

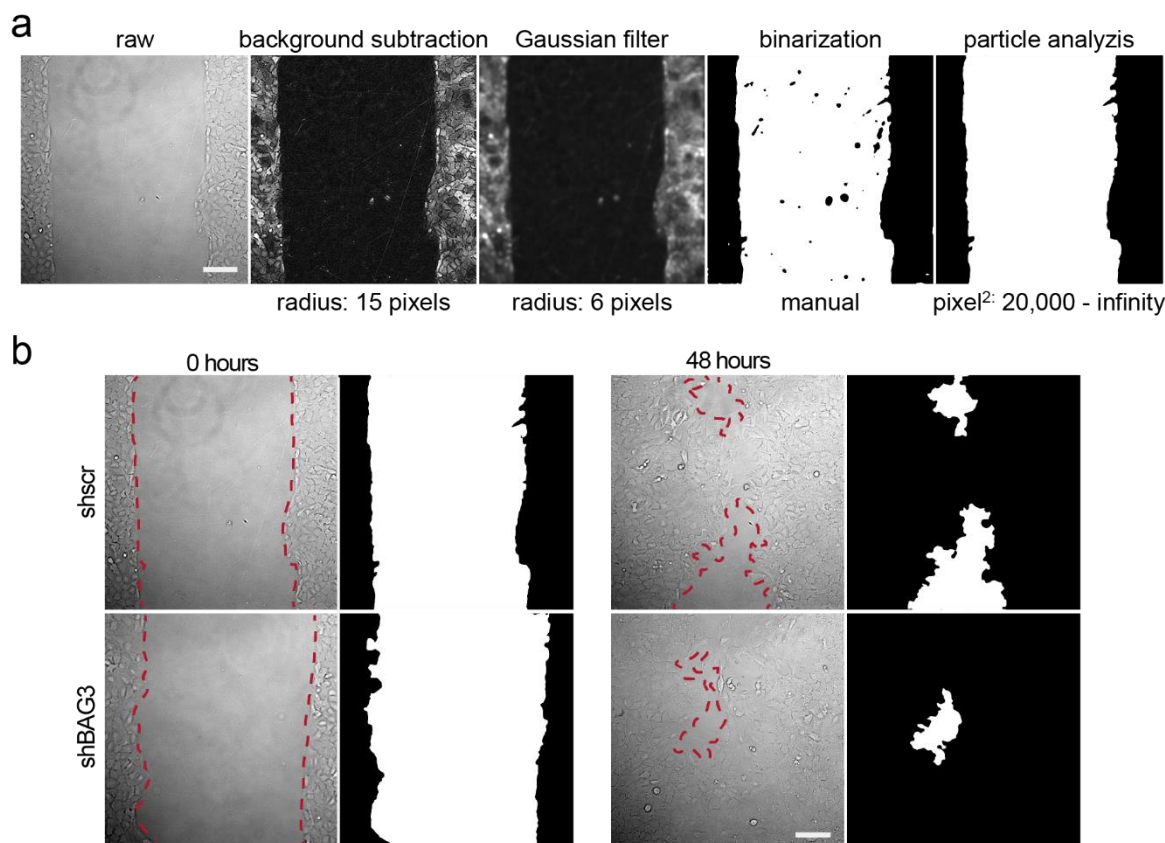
SD: standard deviation, SEM: standard error of the mean



Supplemental Figure 7-4 Standard curve for the protein concentration determination. The Bradford assay is a colorimetric assay and allows to measure the protein concentration of samples. The standard curve was generated using different concentrations of BSA diluted in RIPA buffer. The absorbance was measured at 595 nm.

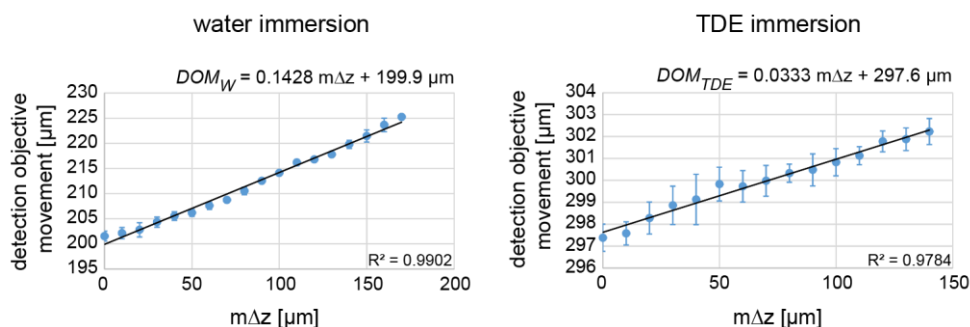


Supplemental Figure 7-5 FACS gating strategy for sorting HC11 EGFP⁺ cells. (a) HC11 shBAG3. (b) HC11 shscr. (I) Healthy cells were discriminated against damaged or dying cells, side scatter (SSC-A, log) and forward scatter (FSC-A, log) are plotted. Higher SSC-A signals indicate increased granularity and therefore likely show dying cells. Thus, the population with the lower SSC-A signal was chosen (P1). (II) To exclude cell clusters or doublets, the FSC-H was plotted against FSC-A and only the population that would fit a linear crossing zero was selected (dd1). (III) A second method was used to discriminate clusters of cells. Here, the SSC-H was plotted against the SSC-W. The population with the lower SSC-W was used (dd2). (IV) The signals from the side scatter (SSC-A, log) and the 488 nm laser (FITC-A, log) were plotted and the population with high FITC signal was selected. (V) To gate EGFP⁺ cells over autofluorescent cells, signals from the 488 nm laser (FITC-A, log) and from the PE laser (PE-A, log) were plotted. The population with the higher FITC-A signal was chosen for sorting (P3). (VI) Gating hierarchy with number of events, the percentage of the according parental population (%parent) and the percentage of the initial population (%total). A: area of the voltage pulse, H: height of the voltage pulse, W: width of the voltage pulse.



Supplemental Figure 7-6 Semi-automated image analysis pipeline for wound-healing assays. (a) Background is subtracted from raw images using a radius of 15 pixels. This is followed by applying a Gaussian filter with a radius of 6 pixels. The image is binarized with manual thresholding. The minimum values are between 15-20 for 16-bit images. Particles that have a minimum size of 20,000 pixels² are analyzed. (b) The semi-automated image analysis allows for an estimation of the wound area. The red-dashed lines in the raw images show the area of the wound. The white area in the binary images show the wound area following particle analysis. Microscope: Zeiss Axio Observer.Z1, objective lens: 10x/NA 0.5, scale bar: 100 μ m.

7.2 Immunofluorescence staining and optical clearing



Supplemental Figure 7-7 The detection objective focus shift in a BABB optical clearing microscope setup follows a linear equation. The detection objective movement (DOM) was measured as a function of the specimen movement ($m\Delta z$). The specimen was a spheroid, which was optically cleared with BABB and mounted inside a rectangular capillary. The capillary was filled with BABB, and the microscope chamber was filled with either water or TDE as an immersion medium. The specimen was then moved along z and the movement necessary to refocus the detection objective was measured. Points are average of three (water

immersion) or four (TDE immersion) measurements. Error bars show the standard deviation. R^2 is the coefficient of determination for the linear fit (this analysis was performed together with Victor Didier Perez Meza).

Supplemental Table 7-2 Immunofluorescence staining protocols used to improve the stain quality in spheroids *in toto*.

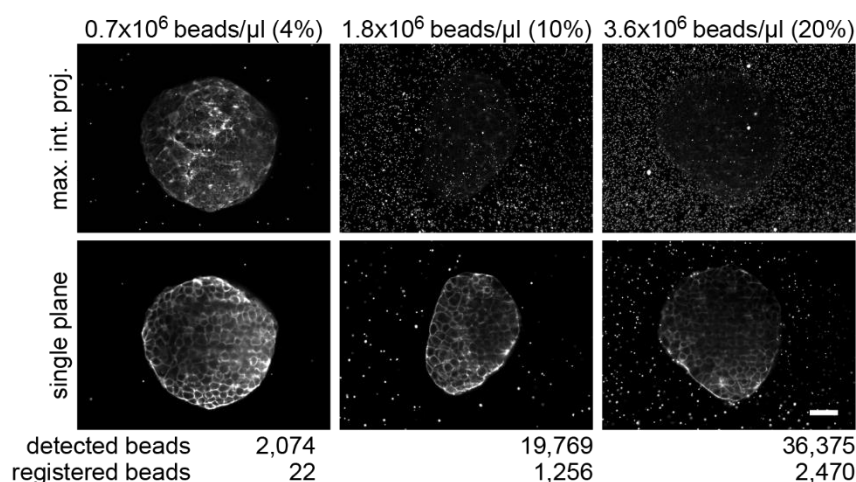
	fixation	permeabilization	block	1 st antibody	2 nd antibody
PFA-Triton	4% PFA for 15 min, RT	0.3% Triton X-100 for 15 min			in block sol. for 4h or o.n., 37°C
PFA-EtOH	4% PFA for 15 min, RT	dehydration (30%, 50%, 70%, 80%, 90%, 96%, 100% EtOH), rehydration (reverse order) for 2 min each, RT	0.1% BSA, 0.2% Triton X-100, 0.05% Tween-20, 10% goat serum for 1 hour, RT	in block sol. o.n., 37°C	in block sol. for 4h or o.n., 37°C
PFA-MetOH	4% PFA for 15 min, RT	MetOH for 5 min, -20°C			in block sol. for 4h or o.n., 37°C
MetOH-Ac	MetOH for 5 min, Ac for 1 min, -20°C	-			in block sol. for 4h or o.n., 37°C
EtOH	70% EtOH o.n., -20°C	-			in block sol. for 4h or o.n., 37°C
PFA-Triton 4°C	4% PFA for 15 min, RT	0.3% Triton X-100 for 15 min		in block sol. o.n., 4°C	in block sol. o.n., 4°C

Supplemental Table 7-3 Raw data from antibody dispersion measurement.

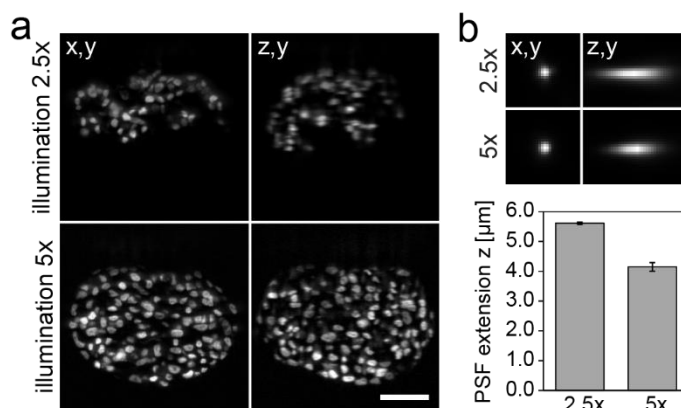
protocol antibody	PFA-Triton-o.n.-4°C		PFA-Triton-4h		PFA-Triton-o.n.		PFA-dehyd.-4h	
	α -tubulin	β -catenin	α -tubulin	β -catenin	α -tubulin	β -catenin	α -tubulin	β -catenin
R-value	0.563	0.211	0.893	0.660	0.597	0.294	0.833	0.688
	0.705	0.523	0.792	0.654	0.878	0.671	0.711	0.660
	0.911	0.858	0.755	0.154	0.599	0.137	0.700	0.483
	0.473	0.314	0.854	0.613	0.797	0.492	0.527	0.376
	0.568	0.501	0.767	0.492	0.798	0.375	0.633	0.479
			0.876	0.731	0.907	0.669	0.809	0.635
median	0.568	0.501	0.823	0.633	0.797	0.433	0.706	0.559

protocol antibody	PFA-dehyd.-o.n.		PFA-MetOH-4h		PFA-MetOH-o.n.		MetOH-Ac-4h	
	α -tubulin	β -catenin						
R-value	0.875	0.642	0.748	0.276	0.838	0.478	0.949	0.897
	0.782	0.437	0.853	0.702	0.687	0.866	0.850	0.714
	0.543	0.456	0.330	0.389	0.761	0.325	0.962	0.926
	0.550	0.214	0.876	0.693	0.857	0.648	0.971	0.843
	0.560	0.525	0.776	0.482	0.963	0.895	0.939	0.723
	0.618	0.521	0.484	0.299	0.917	0.713	0.979	0.963
					0.932	0.864		
median	0.589	0.488	0.762	0.435	0.857	0.713	0.956	0.870

protocol	MetOH-Ac-o.n.		ethanol-4h		ethanol-o.n.	
antibody	α -tubulin	β -catenin	α -tubulin	β -catenin	α -tubulin	β -catenin
R-value	0.947	0.716	0.966	0.899	0.780	0.851
	0.853	0.884	0.357	0.613	0.939	0.885
	0.715	0.408	0.974	0.949	0.885	0.864
	0.966	0.831	0.435	0.770	0.675	0.746
	0.899	0.703	0.973	0.879	0.884	0.825
	0.853	0.577	0.928	0.870	0.929	0.842
median	0.876	0.709	0.947	0.875	0.884	0.846

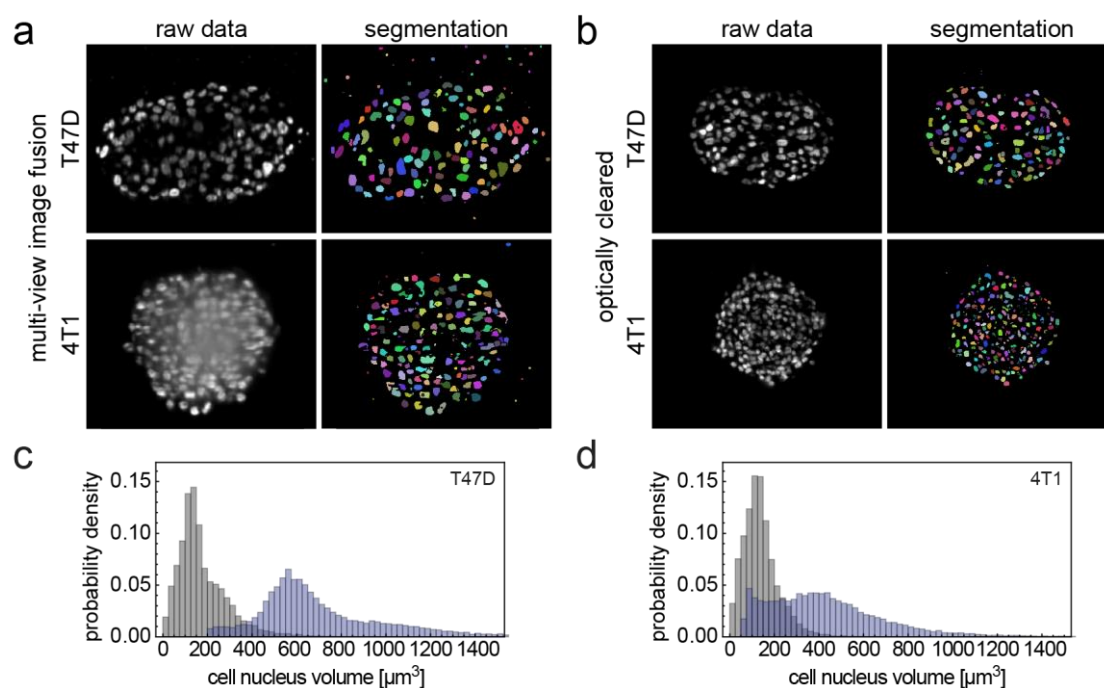


Supplemental Figure 7-8 Identification of the appropriate bead concentration for bead-based registration. Maximum intensity projections along z and single planes show the amount and distribution of fluorescent beads in the image data. Beads were dissolved in 1% low-melt agarose. T47D spheroids were stained with phalloidin AF546. The amount of detected beads and registered beads is listed for each tested condition. Microscope: mDSLML, illumination lens: Epiplan-Neofluar 2.5x/NA 0.06, detection lens: N-Achroplan 20x/NA 0.5, laser – filter (phalloidin): 561 nm - bandpass filter 607/70, 0.09 mW, scale bar: 50 μ m.



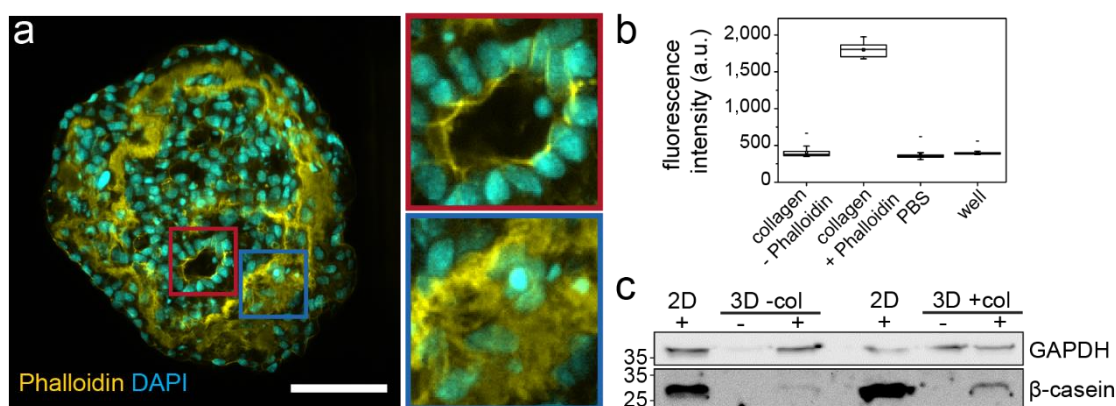
Supplemental Figure 7-9 Axial resolution is improved when a thinner light sheet is used. (a) Optical sections of T47D spheroids along two spatial directions (x,y and z,y) when a 2.5x or 5x illumination objective was used to generate the light sheet. Microscope: mDSLML, illumination lens: Epiplan-Neofluar 2.5x/NA 0.06 or Plan-Neofluar 5x/NA 0.16, laser-filter (DAPI): 405 nm – bandpass 447/55, scale bar: 50 μ m. (b) The PSF for the illumination objective lenses is shown for two spatial directions. Fluorescent beads with a diameter of 1 μ m were illuminated with a wavelength of 561 nm. For the 2.5x objective lens, the PSF was averaged from

106 beads from nine datasets. The average z-extension was 5.6 μm . For the 5x objective lens, the PSF was averaged from 80 beads from ten datasets. The average z-extension was 4.1 μm . Error bars show the standard error of the mean.



Supplemental Figure 7-10 Single planes of central spheroid regions indicate the performance of cell nuclei segmentation for fused and optically cleared data sets. (a) Segmentation of cell nuclei in fused image data sets of T47D and 4T1. The different colors represent individual, detected cell nuclei. The segmentation fails in regions of low contrast (e.g. in the central region of 4T1 spheroids). (b) Segmentation of cell nuclei in optically cleared T47D and 4T1 spheroids. The high contrast in the entire sample results in high cell nuclei segmentation performance. (c, d) Histograms of cell nuclei volume in T47D and 4T1 spheroids when data was (c) acquired by multi-view image fusion or (d) spheroids were optically cleared and imaged in a rectangular capillary.

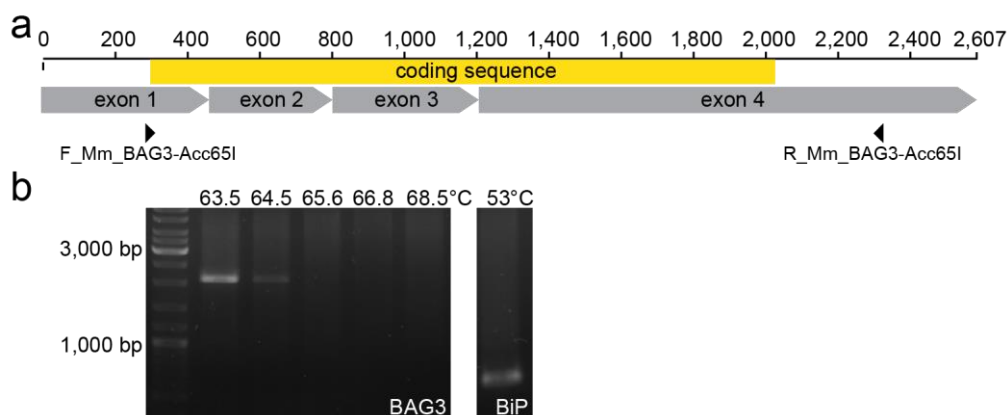
7.3 Characterization of mammary epithelial cell spheroids



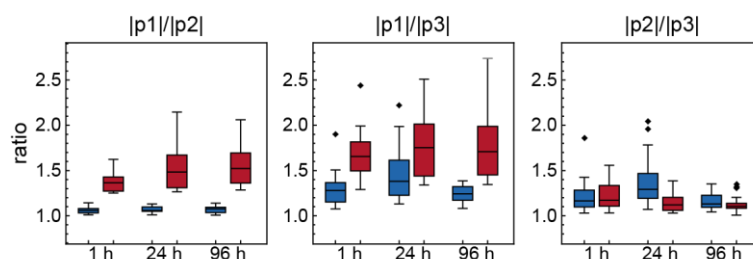
Supplemental Figure 7-11 Phalloidin cross-reacts with extracellular matrix. HC11 spheroids differentiate regardless external collagen addition. (a) Spheroids formed from 5,000 HC11 cells in presence of type I collagen were stained with phalloidin AF488 and DAPI and were subsequently optically cleared. The single slide shows that besides binding to F-actin, phalloidin also binds to non-cellular structures

within the spheroid (image detail). Microscope: mDSLM, illumination lens: Zeiss Epiplan-Neofluar 2.5x/NA 0.06, detection lens: Zeiss N-Achroplan 20x/NA 0.5, spacing: 1.29 μm , camera: Andor Clara, laser - filter (phalloidin AF488): 488 nm - 525/50; laser - filter (DAPI): 405 nm - 447/55; scale bar: 50 μm . (b) Wells were coated with type I collagen and incubated either with phalloidin (+) or without phalloidin (-). After several washing steps, the fluorescence intensity was measured (excitation: 488 nm, emission: 525 nm). (c) Spheroids formed from HC11 cells differentiated to express β -casein. Spheroids were formed either in presence (+) or in absence (-) of externally added collagen I. GAPDH served as the loading control.

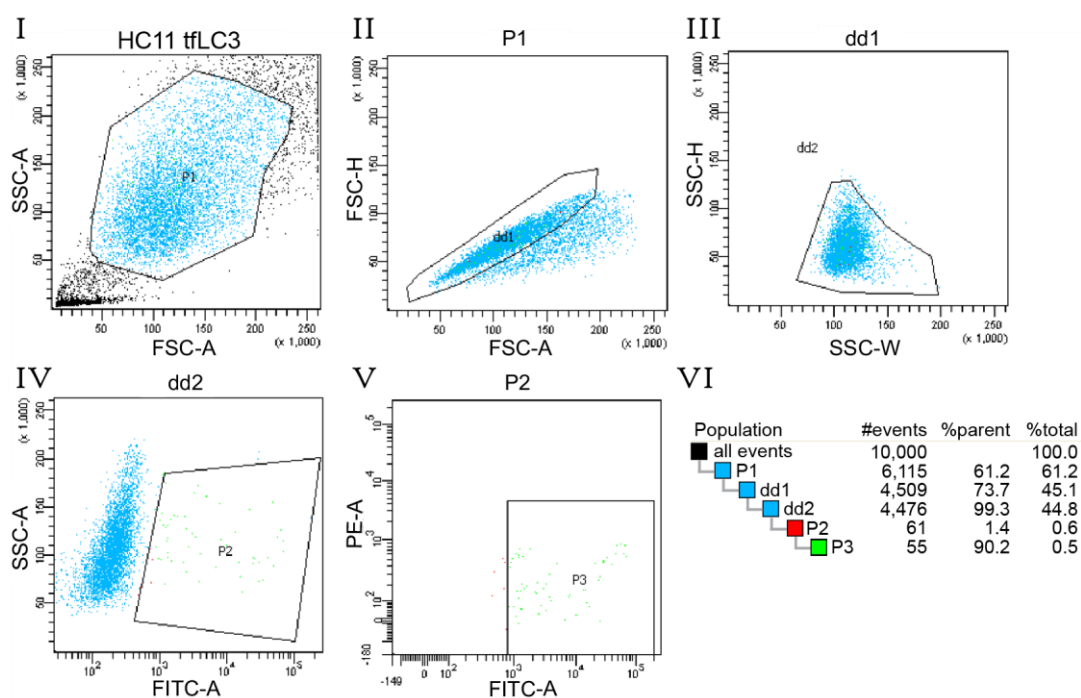
7.4 Mechanical stress



Supplemental Figure 7-12 BAG3 transcript variants with alternative exon usage between exon 1 and exon 4 are not present in murine mammary epithelial cells. (a) A primer pair was used to flank the coding sequence of full-length BAG3. Potential transcript variants with an alternative exon usage between exon 1 and exon 4 can thus be identified. (b) Amplification of BAG3 mRNA. RNA was extracted from KIM-2 cells. Following reverse transcription, BAG3 was amplified using the primer depicted in (a). The annealing temperature (indicated for each lane) was varied. BiP was amplified as a positive control.



Supplemental Figure 7-13 Pairwise ratios between the principal directions p1, p2 and p3 along the spheroids. Boxplot parameters: the box contains 50% of the data, the whiskers and outliers show the uppermost and lowermost 25% of the data. Outliers are outside the 1.5x interquartile range. The line in the box is the median. \blacklozenge : outliers, h: hours.



Supplemental Figure 7-14 FACS gating strategy for sorting HC11 GFP⁺ and mRFP⁺ cells. HC11 tFLC3 cells were enriched. (I) Healthy cells were discriminated against damaged or dying cells, side scatter (SSC-A, log) and forward scatter (FSC-A, log) are plotted. Higher SSC-A signals indicate increased granularity and are therefore likely to show dying cells. Thus, the population with the lower SSC-A signal was chosen (P1). (II) To exclude cell clusters or doublets, the FSC-H was plotted against FSC-A and only the population that would fit a linear crossing zero was selected (dd1). (III) A second method was used to discriminate clusters of cells. Here, the SSC-H was plotted against the SSC-W. The population with the lower SSC-W was used (dd2). (IV) The signals from the side scatter (SSC-A, log) and the 488 nm laser (FITC-A, log) were plotted and the population with high FITC signal was selected. (V) To gate EGFP⁺ and mRFP⁺ cells, signals from the 488 nm laser (FITC-A, log) and from the PE laser (PE-A, log) were plotted. The population with higher FITC-A and PE-A signal was chosen for sorting (P3). (VI) Gating hierarchy with number of events, the percentage of the according parental population (%parent) and the percentage of the initial population (%total). A: area of the voltage pulse, H: height of the voltage pulse, W: width of the voltage pulse.

Supplemental Table 7-4 Sample number for spheroid compression experiments. The number of spheroids used for the morphological analysis. The number of spheroids before the application of selection criteria is listed in the brackets. The total numbers of segmented cell nuclei for all spheroids in a condition are listed, from which the cell nuclei volume was measured.

	sample number					
	1h		24 h		96 h	
	control (input)	compressed (input)	control (input)	compressed (input)	control (input)	compressed (input)
spheroids	20 (28)	17 (37)	19 (20)	13 (20)	21 (29)	22 (30)
cell nuclei	86,585	93,156	79,006	61,248	98,243	121,128

7.5 Spheroid formation

Supplemental Table 7-5 The effect of light exposure on the projected area during the time-lapse. The second column (control TL) shows the normalized projected area of spheroids that were illuminated every 30 minutes for 48 hours. The last column (control MC) shows the normalized projected area of spheroids that

were been illuminated continuously but only at time point 0 hours and 48 hours. Values are the mean and the standard error of the mean.

HC11	control TL ± SEM	control MC ± SEM
DMSO (0.5%)	0.09 ± 0.01	0.12 ± 0.03
DECMA-1 (10 µg/ml)	0.41 ± 0.06	0.45 ± 0.09
IgG1 (10 µg/ml)	0.13 ± 0.03	0.15 ± 0.03
cytochalasin D (2.5µM)	0.25 ± 0.05	0.26 ± 0.06
nocodazole (5 µM)	0.10 ± 0.02	0.11 ± 0.02
PF-573228 (1 µM)	0.11 ± 0.02	0.12 ± 0.04
shscr	0.12 ± 0.02	0.21 ± 0.08
shBAG3	0.14 ± 0.02	0.27 ± 0.14
sgscr	0.13 ± 0.02	0.21 ± 0.11
sgBAG3	0.13 ± 0.02	0.21 ± 0.11
4T1	control TL ± SEM	control MC ± SEM
DMSO (0.5%)	0.23 ± 0.03	0.25 ± 0.04
DECMA-1 (10 µg/ml)	0.52 ± 0.09	0.49 ± 0.05
IgG1 (10 µg/ml)	0.18 ± 0.02	0.18 ± 0.03
cytochalasin D (2.5µM)	0.55 ± 0.06	0.56 ± 0.10
nocodazole (5 µM)	0.21 ± 0.02	0.21 ± 0.01
PF-573228 (1 µM)	0.11 ± 0.01	0.11 ± 0.01
T47D	control TL ± SEM	control MC ± SEM
DMSO (0.5%)	0.28 ± 0.04	0.26 ± 0.03
DECMA-1 (10 µg/ml)	0.43 ± 0.03	0.44 ± 0.04
IgG1 (10 µg/ml)	0.25 ± 0.04	0.24 ± 0.03
cytochalasin D (1 µM)	0.77 ± 0.06	0.73 ± 0.05
nocodazole (0.5 µM)	0.38 ± 0.08	0.37 ± 0.10
PF-573228 (1 µM)	0.23 ± 0.03	0.21 ± 0.02

MC: microscope control, TL: time-lapse

Supplemental Table 7-6 Spheroid formation sample numbers. The total numbers of samples from all experiments are listed. All plots and statistics are based on the values obtained from these samples.

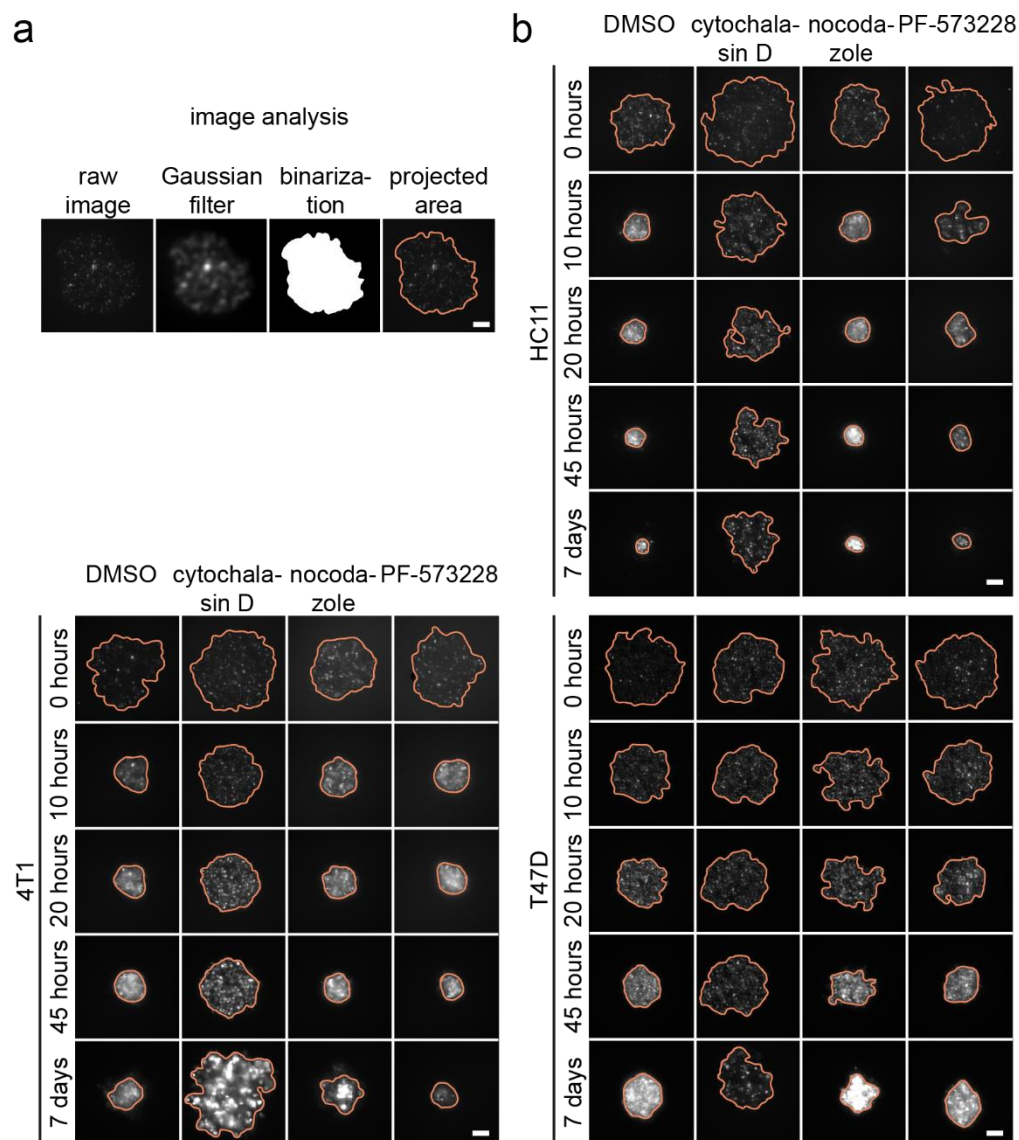
spheroid formation (48 h TL)	HC11	4T1	T47D
DMSO	30	40	30
DECMA-1	22	15	18
IgG1	19	23	24
cytochalasin D	12	23	21
nocodazole	25	14	26
PF-573228	38	22	35
shscr	30	-	-
shBAG3	27	-	-
sgscr	74	-	-
sgBAG3	82	-	-
spheroid formation (7 d EP)	HC11	4T1	T47D
DMSO	21	31	21
DECMA-1	20	6	18
IgG1	19	23	24
cytochalasin D	12	23	21
nocodazole	21	13	26
PF-573228	29	19	32

shscr	33	-	-
shBAG3	27	-	-
sgscr	50	-	-
sgBAG3	60	-	-

d: days, EP: end-point measurement, h: hours, TL: time-lapse

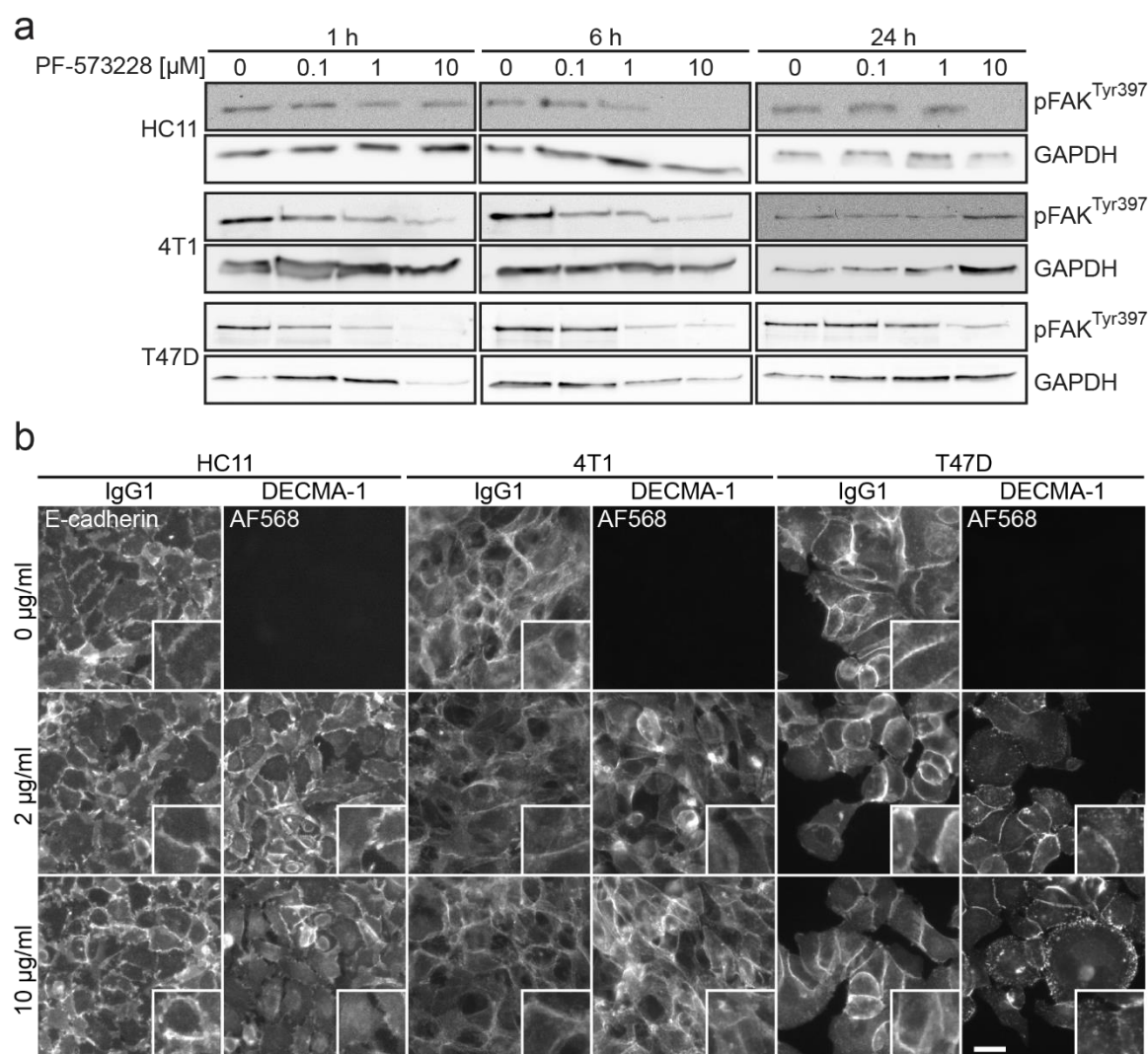
Supplemental Table 7-7 Sample numbers of the live-dead assay performed with HC11 BAG3 knockdown and knockout cells. The live-dead assay was performed at 48 hours and 7 days of spheroid formation. Listed are the total numbers of all experiments.

live-dead assay condition	48 hours	7 days
Triton X-100 (for knockdown experiments)	6	6
shscr	5	6
shBAG3	6	3
Triton X-100 (for knockout experiments)	4	6
sgscr	15	15
sgBAG3	15	19

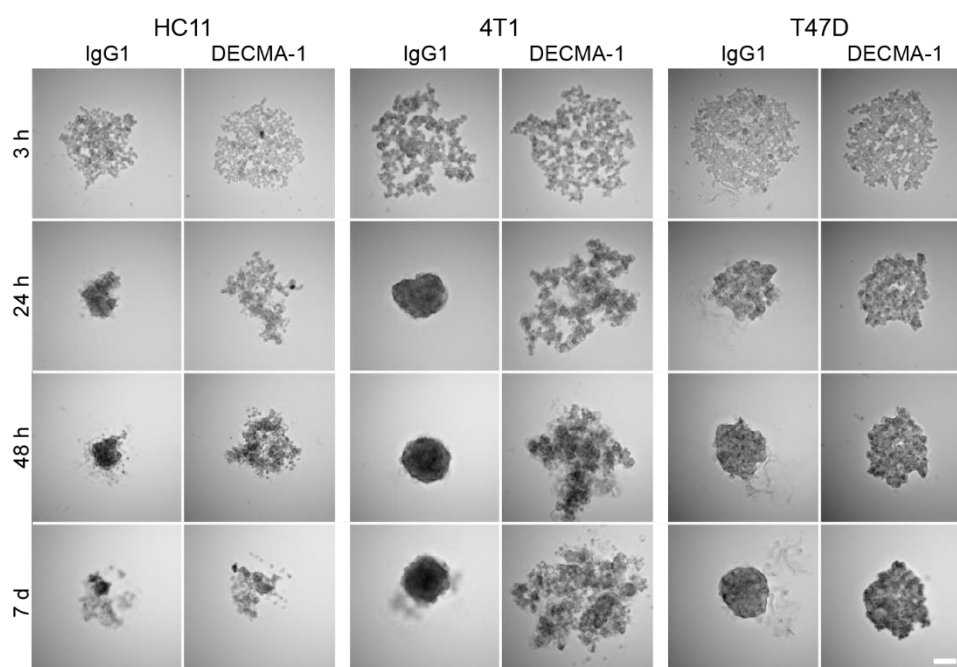


Supplemental Figure 7-15 Spheroid formation is analyzed by segmentation of the projected area of the cells. (a) Image analysis was performed by Biena Mathew. A Gaussian filter with a large Kernel was applied

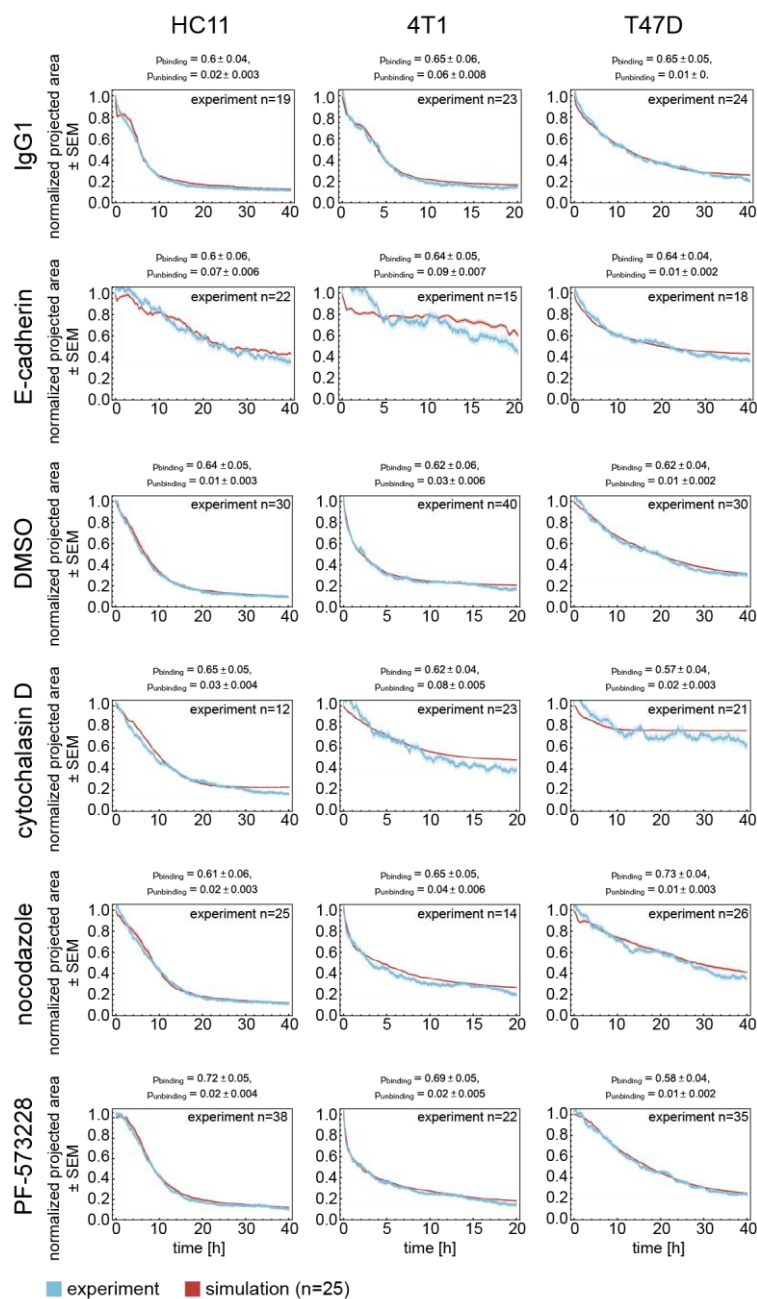
to fluorescence raw images. Images were binarized and the projected area was measured. (b) Representative images of spheroid formation for HC11, 4T1 and T47D cells at different time points. Images show cell nuclei labeled with EGFP-H2B. The orange outline shows the segmented area. Microscope: Zeiss Axio Observer.Z1, objective lens: Fluar 10x/NA 0.5, scale bar: 100 μm . (modified from Smyrek & Mathew *et al.* 2017).



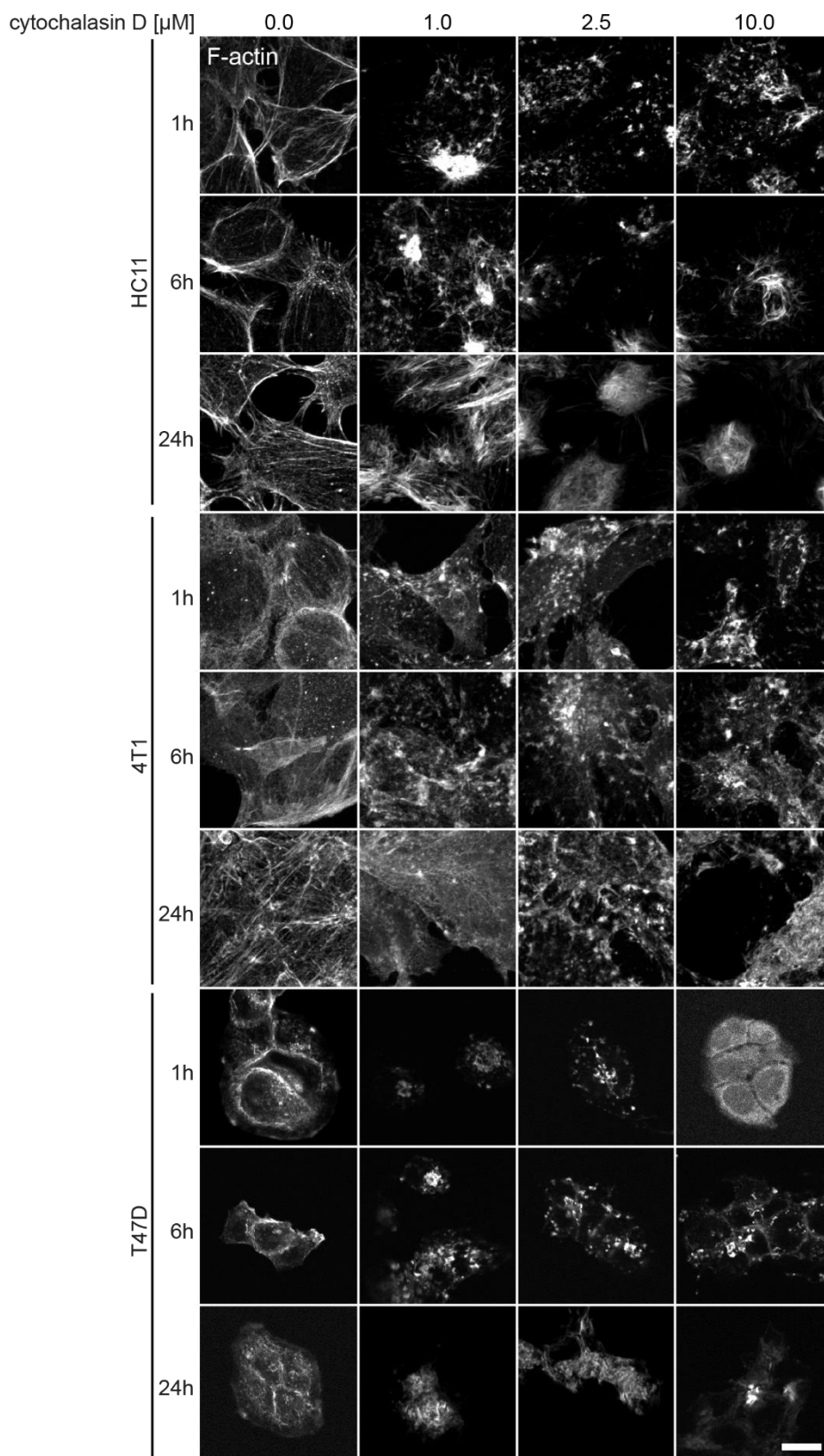
Supplemental Figure 7-16 Determination of PF-573228 and DECMA-1 concentration. (a) PF-573228 blocks FAK phosphorylation at Y397 sufficiently at 1 μM . Inhibition is stable for at least 24 hours. (b) DECMA-1 anti-E-cadherin antibody disassembles cadherin-cadherin contacts. Following attachment of the cells to the surface, cells were treated with DECMA-1 antibody. Cells were incubated with the antibody for 8 hours. Image details show a 2x magnification of a region of the original image. E-cadherin is less prominent at the cell surface in HC11 cells when 10 $\mu\text{g/ml}$ DECMA-1 antibody were used. 4T1 cells show a more diffuse signal compared to the control. Already 2 $\mu\text{g/ml}$ DECMA-1 affects E-cadherin in T47D cells. E-cadherin gets internalized (puncta) by the cells. The effect is more prominent at an antibody concentration of 10 $\mu\text{g/ml}$. Microscope: Zeiss Axiovert, objective lens: 32x, scale bar: 25 μm .



Supplemental Figure 7-17 Cells require E-cadherin to form compact spheroids. Transmission images show cellular spheroids at different time points of spheroid formation. Cells were treated with 10 $\mu\text{g/ml}$ DECMA-1 to block E-cadherin function, or with IgG1 as control. Microscope: Zeiss Axio Observer.Z1, objective lens: Fluar 10x/NA 0.5, time-lapse duration: 48 hours, time-lapse interval: 30 minutes, scale bar: 100 μm .

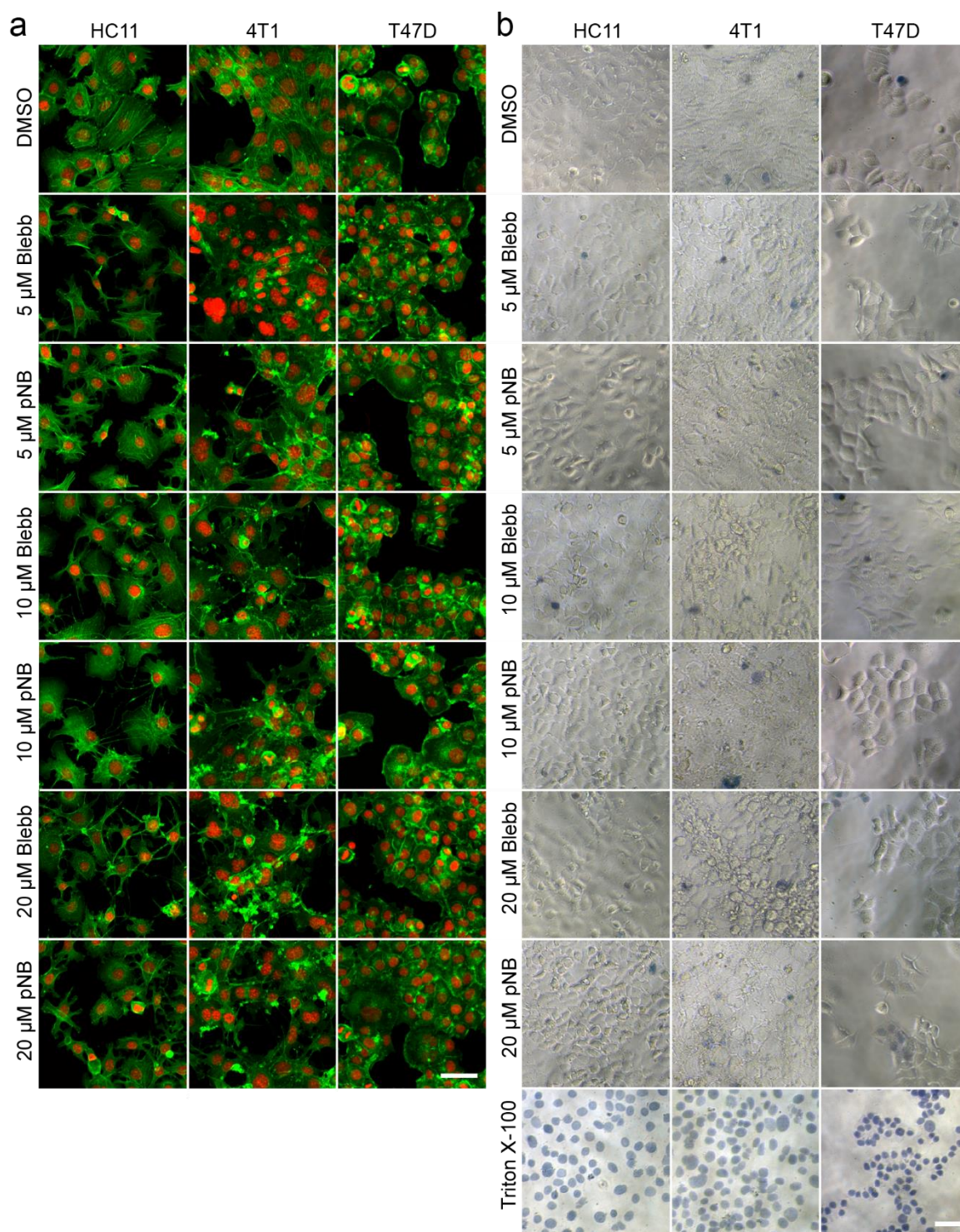


Supplemental Figure 7-18 Fit of the computational model simulations to the experimental data. Simulations were run 25 times. The number of experimental samples is indicated for each condition. The blue line is the mean of the experimental measurements. The light blue shaded region is the SEM. The red line shows the simulations. (modified from Smyrek & Mathew *et al.* 2017).



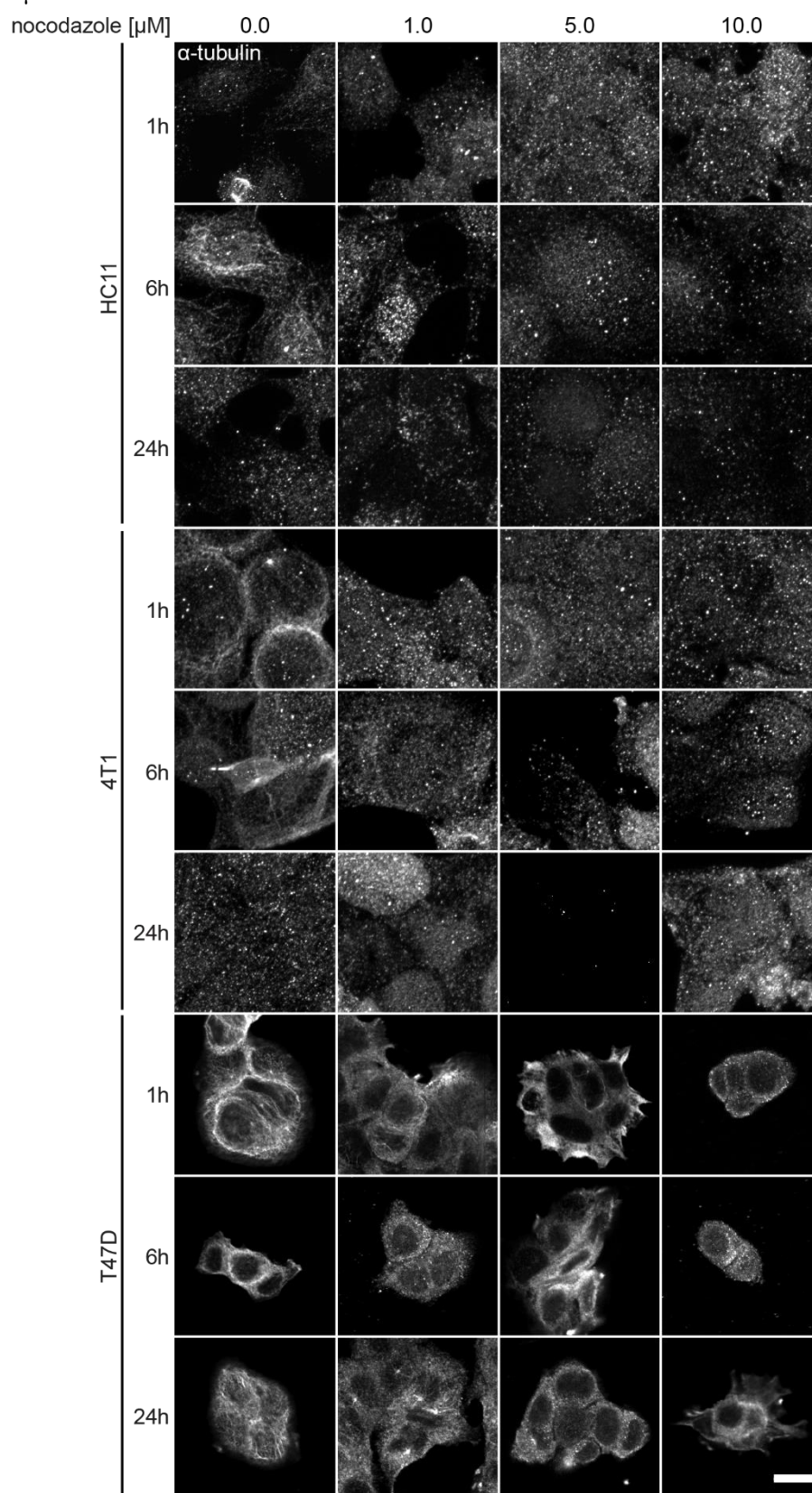
Supplemental Figure 7-19 Determination of cytochalasin D concentration. Cytochalasin D disassembles F-actin. In HC11 and 4T1 cells, F-actin is prominent in stress fibers. In T47D cells F-actin appears as a circumferential belt. A concentration of 2.5 μM is sufficient to disassemble F-actin in HC11 and 4T1 cells. In T47D cells, already 1 μM disassembles F-actin. F-actin is visualized by a stain with phalloidin AF488.

Maximum intensity projections are shown. Microscope: Zeiss LSM780, objective lens: Plan-Apochromat 63x/NA 1.4 oil, scale bar: 10 μ m.



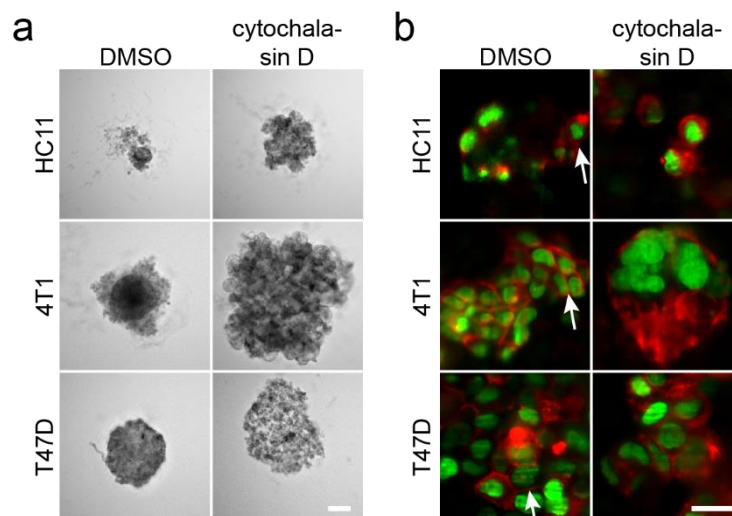
Supplemental Figure 7-20 Determination of blebbistatin and para-nitroblebbistatin concentration. Cells grown as a monolayer were treated with blebbistatin (Blebb) or para-nitroblebbistatin (pNB) at different concentrations for 20 hours. (a) Following drug treatment, cells were fixed and stained with phalloidin AF546 (green) and DAPI (red) to label the F-actin network and the cell nuclei, respectively. Microscope: Zeiss LSM780, objective: Plan-Apochromat 10x/NA 0.3, scale bar: 50 μ m. (b) Trypan blue exclusion assay. Following 20 hours drug treatment, cells were stained with Trypan blue to label dead cells. As positive

control, cells were treated with Triton X-100 prior staining. Microscope: Zeiss Axiovert, objective lens: 20x, scale bar: 50 μm .

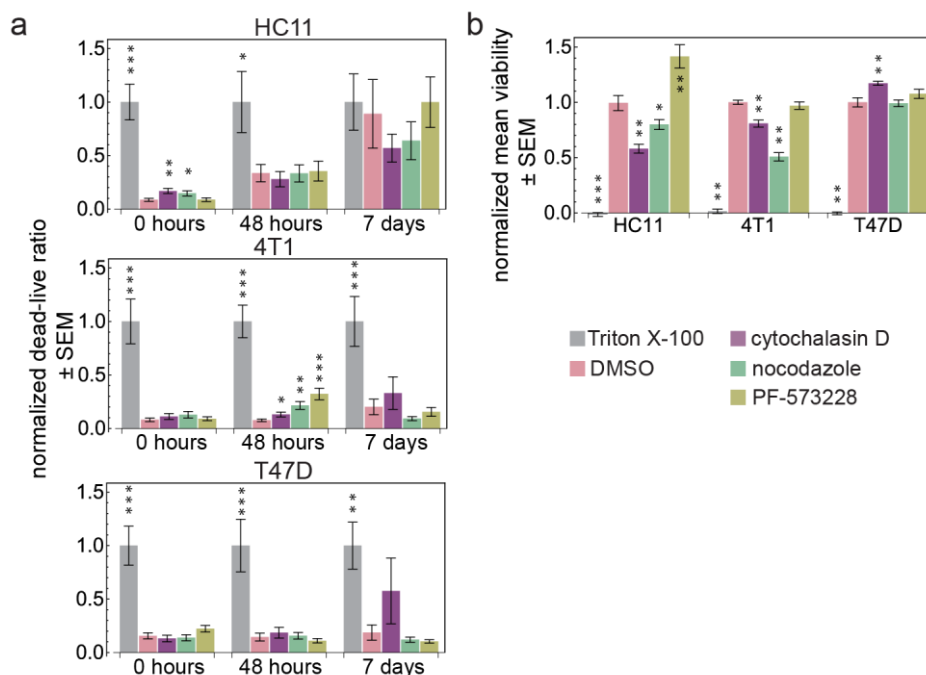


Supplemental Figure 7-21 Determination of nocodazole concentration. Nocodazole blocks microtubule polymerization. Maximum intensity projections show that microtubules are disassembled in cells already at

low concentrations. Anti- α -tubulin primary and anti-rabbit AF568 secondary antibodies were used. Microscope: Zeiss LSM780, objective lens: Plan-Apochromat 63x/NA 1.4 oil, scale bar: 10 μ m.

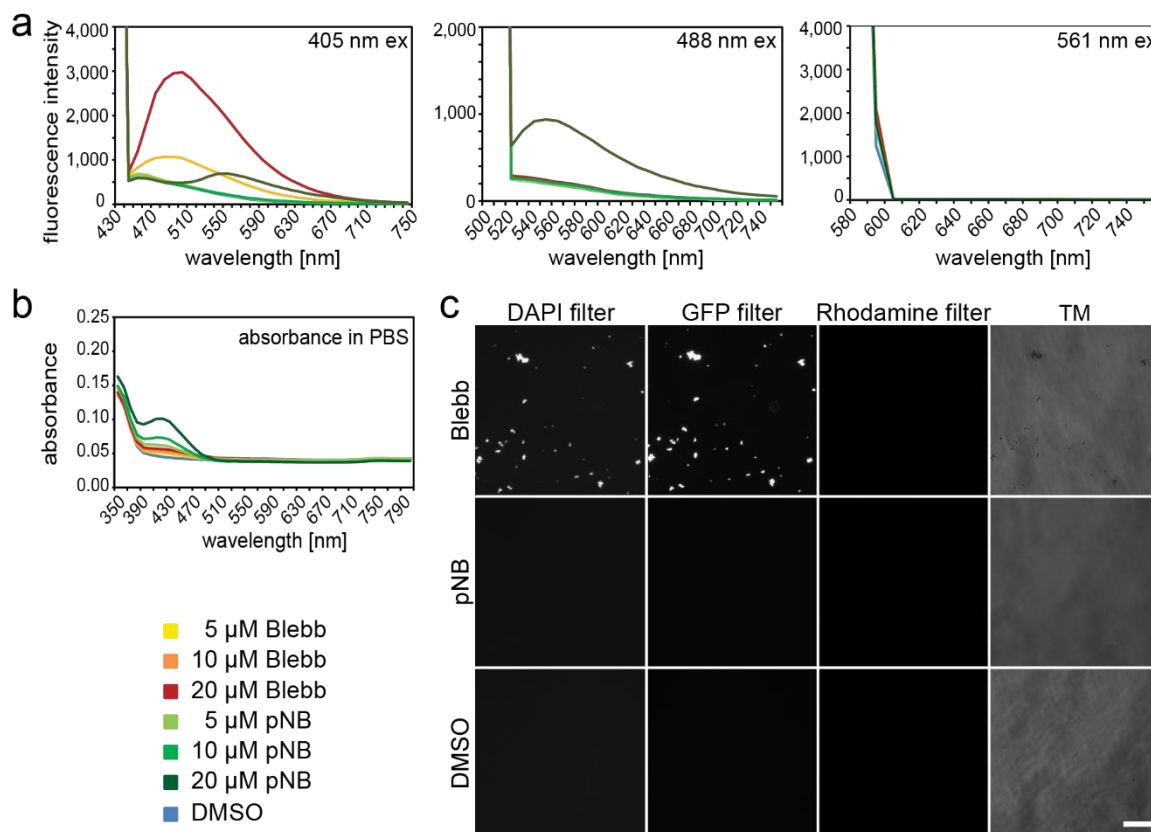


Supplemental Figure 7-22 Actin disruption inhibits spheroid formation and affects cell nuclei volume. (a) Transmission images show that cytochalasin D-treated cells fail to form compact spheroids after 7 days. Microscope: Zeiss Axio Observer.Z1, objective lens: Fluar 10x/NA 0.5, scale bar: 100 μ m. (b) In cytochalasin D-treated cells, the actin cytoskeleton (red, LifeAct-tagRFP) was still disintegrated 7 days after spheroid formation. Compared to the control (DMSO), 4T1 cells showed an increased cell nuclei (green, EGFP-H2B) size when cells were treated with cytochalasin D for 7 days. Image post-processing: background was subtracted and a median filter was applied. Microscope: mDSLML, illumination lens: Epiplan-Neofluar 2.5x/NA 0.06, detection lens: N-Achroplan 20x/NA 0.5, scale bar: 20 μ m. (modified from Smyrek & Mathew *et al.* 2017).



Supplemental Figure 7-23 The effect of drug treatment on cell death and cell viability. (a) Live-dead assay at time points 0 h, 48 h and 7 d of spheroid formation. Dead cells were labeled with SytoxBlue and live cells with EGFP-H2B. The dead-live ratio was calculated. As a positive control, cells were treated with Triton

X-100 to permeabilize all cells. (b) Cell viability assay of cells grown as monolayer culture. Cells were treated with the according drug for 24 hours. Hypothesis testing: Wilcoxon rank sum test with Holm correction for multiple testing. Asterisks show significant differences (* $p < 0.05$, ** $p < 0.01$, *** $p < 0.001$). (modified from Smyrek & Mathew *et al.* 2017).

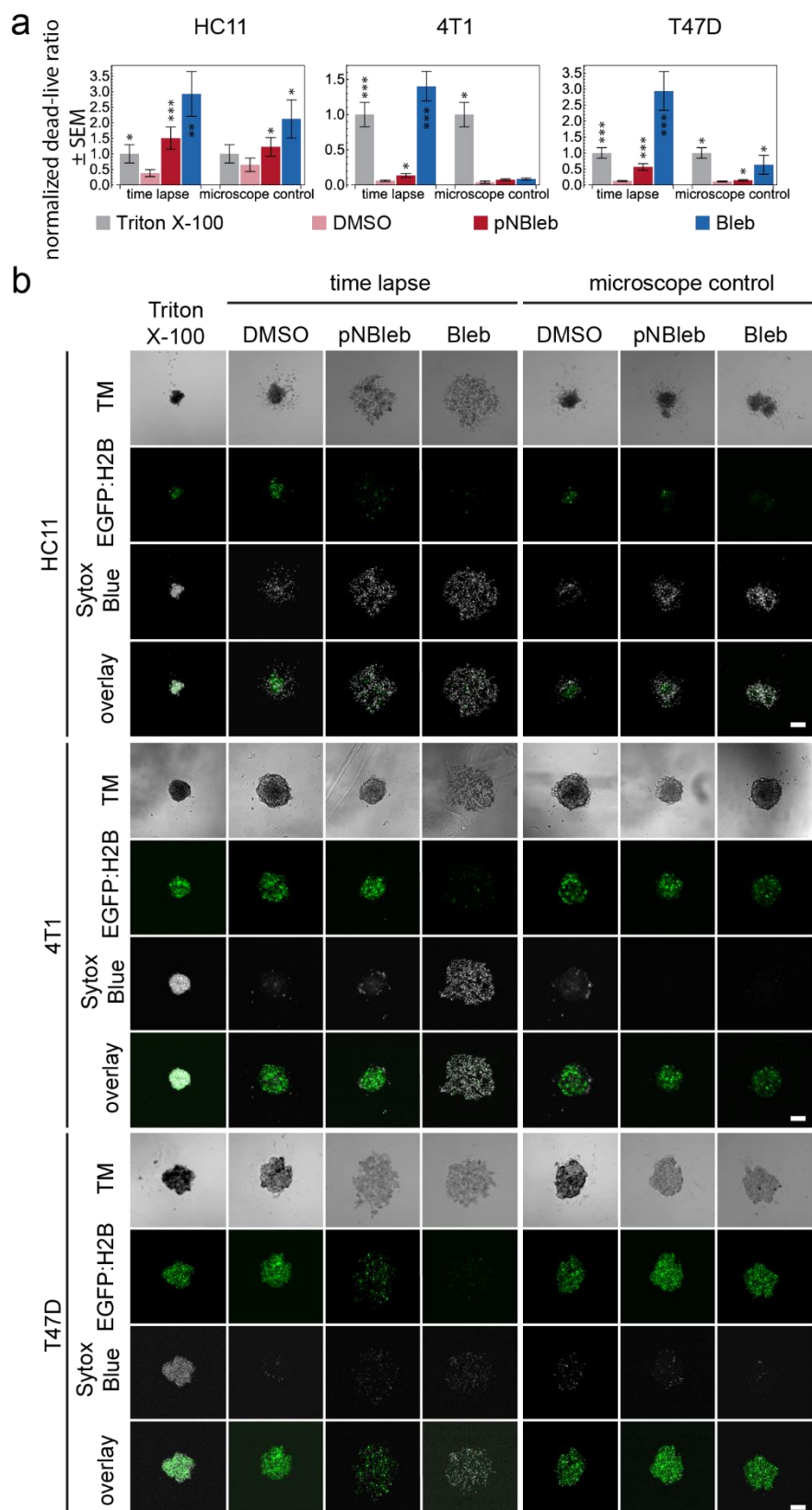


Supplemental Figure 7-24 Optical properties of blebbistatin and para-nitroblebbistatin. (a) Fluorescence intensity scan at different excitation wavelengths. Blebbistatin (Blebb) and para-nitroblebbistatin (pNB) were diluted in PBS and analyzed in the microplate reader M200 (Tecan). (b) Absorbance scan at different wavelengths spanning the visible spectrum. Drugs were diluted in PBS and measurements were performed with a microplate reader. (c) Blebbistatin but not para-nitroblebbistatin precipitates in PBS. Microscope: Zeiss Axiovert, Objective lens: 20x, scale bar: 50 μm .

Supplemental Table 7-8 Spheroid formation upon myosin-II inhibition. The total number of samples from all experiments is listed. Plots and statistics rely on the values obtained from these samples.

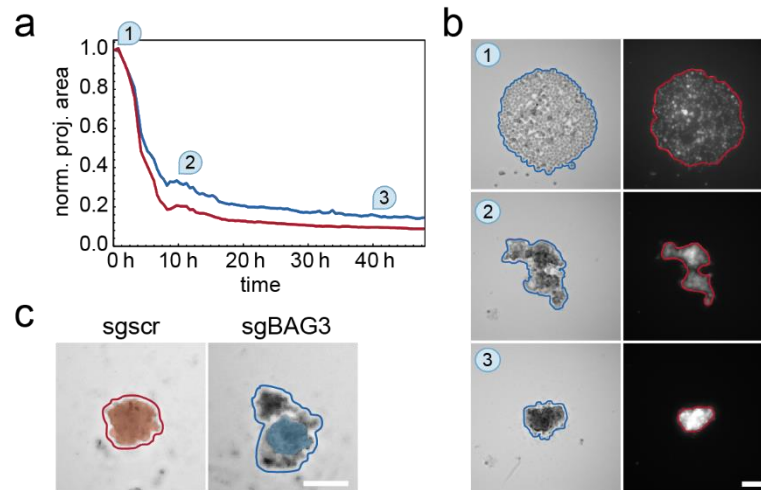
	HC11		4T1		T47D	
	TL	MC	TL	MC	TL	MC
Triton X-100		9		11		9
DMSO	8	6	9	3	9	4
blebbistatin	9	6	8	8	8	6
para-nitroblebbistatin	14	12	9	8	9	8

TL: time-lapse, MC: microscope control



Supplemental Figure 7-25 Blebbistatin and para-nitroblebbistatin are cytotoxic upon illumination with blue light. (a) Live-dead assay (LDA) of the three cell lines after 48 hours of spheroid formation. Dead cells were labeled with SytoxBlue and live cells expressed EGFP-H2B. The assay was performed with samples, which were imaged every 30 minutes for 48 hours (time-lapse) and samples, which were only imaged at the beginning and the end of the spheroid formation assay (microscope control). Asterisks show significant

differences (* $p < 0.05$, ** $p < 0.01$, *** $p < 0.001$). Sample numbers are listed in Supplemental Table 7-8. (b) Representative images of a live-dead assay after 2 days of spheroid formation for HC11, 4T1 and T47D cells. Triton X-100 was used as a positive control. Microscope: Zeiss LSM780, objective lens: Plan-Apochromat 10x/NA 0.3; scale bar: 100 μm . Blebb: blebbistatin, TM: transmission, pNBleb: para-nitroblebbistatin. (modified from Smyrek & Mathew *et al.* 2017).



Supplemental Figure 7-26 Area segmentation differs between transmission and fluorescence image data. (a) Segmented area in transmission images (blue) is larger than in fluorescence images (red) exemplified on one spheroid formed from HC11 cells. (b) Microscopy images the area segmentation at different time points (0 h, 10 h and 40 h). Cells expressed EGFP-H2B. Microscope: Zeiss Axio Observer.Z1, objective lens: Fluor 10x/NA 0.5, scale bar: 100 μm . (c) Segmentation in the transmission channel captures dead cells. The segmented area is marked in dark red or dark blue, and the area of the spheroid is shown in the red or blue overlay, respectively. Microscope: Zeiss LSM780, objective lens: Plan-Apochromat 10x/NA 0.3, scale bar: 100 μm .

Publications

Peer-reviewed in relation to this thesis

- [1] Fischer, S.C., Mathew, B., Hötte, K., Smyrek, I., Stelzer, E.H.K. 2017. Review: Image-based systems biology in spheroids (in preparation)
- [2] Smyrek, I.*, Mathew, B.*, Fischer, S.C., Lissek, S., Becker, S., Stelzer, E.H.K. 2017. Spheroid formation (under revision)
- [3] Smyrek, I., Stelzer, E.H.K. 2017. Quantitative three-dimensional evaluation of immunofluorescence staining for large whole mount spheroids with light sheet microscopy. *Biomedical Optics Express*. **8** (2): 484-499

Peer-reviewed in relation to the teaching activities

- [4] Hötte, K.*, Smyrek, I.*, Starzinski-Powitz, A., Stelzer, E.H.K. 2017. Endogenous AJAP1 associates with the cytoskeleton and attenuates angiogenesis in endothelial cells. *Biology Open*. **6** (6): 723-731

Non-peer-reviewed

- [5] Smyrek, I.*, Hötte, K.*, Schmitz, A.*, Strobl, F.*, Stelzer, E.H.K. 2015. Die Macht der dunklen Seite - Die Chancen der Lichtscheiben-Fluoreszenzmikroskopie in der modernen Zell- und Entwicklungsbiologie. *Forschung Frankfurt*. **2**: 17-20
- [6] Smyrek, I.*, Hötte, K.*, Strobl, F.*, Schmitz, A.*, Stelzer, E.H.K. (2015) Scheibchenweise statt am Stück. *Laborjournal*, **9**: 72-74

* authors contributed equally

Erklärung

Ich erkläre hiermit, dass ich mich bisher keiner Doktorprüfung im Mathematisch-Naturwissenschaftlichen Bereich unterzogen habe.

Frankfurt am Main, den _____

Isabell Smyrek

Versicherung

Ich erkläre hiermit, dass ich die vorgelegte Dissertation über „*The contribution of proteins associated with cell adhesion and survival to tissue integrity in the mammary gland*“ selbständig angefertigt und mich anderer Hilfsmittel als der in ihr angegebenen nicht bedient habe, insbesondere, dass alle Entlehnungen aus anderen Schriften mit Angabe der betreffenden Schrift gekennzeichnet sind.

Ich versichere, die Grundsätze der guten wissenschaftlichen Praxis beachtet, und nicht die Hilfe einer kommerziellen Promotionsvermittlung in Anspruch genommen zu haben.

Frankfurt am Main, den _____

Isabell Smyrek